EASIER: Extensive Air Shower Identification using Electron Radiometer

Romain Gaïor

► To cite this version:

Romain Gaïor. EASIER: Extensive Air Shower Identification using Electron Radiometer. Instrumentation and Methods for Astrophysic [astro-ph.IM]. Université Paris 6, 2013. English. ⟨NNT : ⟩. ⟨tel-01826441⟩

HAL Id: tel-01826441
https://hal.science/tel-01826441v1

Submitted on 6 Feb 2019

THÈSE DE DOCTORAT
DE L'UNIVERSITÉ PIERRE ET MARIE CURIE (UPMC)

présentée par

Romain Gaïor

Pour obtenir le grade de

DOCTEUR ÈS SCIENCES DE L'UNIVERSITÉ PIERRE ET MARIE CURIE

Spécialité :

La Physique de la Particule à la Matière Condensée (ED 389)

EASIER: Extensive Air Shower Identification using Electron Radiometer

Giuseppe	BATTISTONI	Examinateur
Jean-Pierre	LEES	Rapporteur
Antoine	LETESSIER-SELVON	Directeur de thèse
Paolo	PRIVITERA	Rapporteur
Pascal	VINCENT	Examinateur

Thèse soutenue le 24/09/2013

PhD THESIS
OF THE UNIVERSITÉ PIERRE ET MARIE CURIE (UPMC)

presented by

Romain Gaïor

Submitted in fulfillment of the requirements for the degree of

DOCTEUR ÈS SCIENCES DE L'UNIVERSITÉ PIERRE ET MARIE CURIE

Spéciality :

La Physique de la Particule à la Matière Condensée (ED 389)

EASIER: Extensive Air Shower Identification using Electron Radiometer

Giuseppe	BATTISTONI	Examiner
Jean-Pierre	LEES	Referee
Antoine	LETESSIER-SELVON	Supervisor
Paolo	PRIVITERA	Referee
Pascal	VINCENT	Examiner

Summary

More than a hundred years after the discovery of cosmic rays, the origin of Ultra High Energy Cosmic Rays (UHECR) remains uncertain. Nowadays several experiments agree on the shape of the energy spectrum above 10^{18} eV [1]. The ankle, a flattening of the spectrum at about 4×10^{18} eV and a decade higher in energy a cut off, are observed by all recent experiments. The origin of those spectral features remains unknown. In both cases, it can be due to the source distribution and acceleration mechanisms or be the signature of energy losses during transport from the distant sources to the Earth. Indeed, the ankle could reflect the transition from a Galactic dominated cosmic ray sky to an extragalactic one, or the energy loss via e^+/e^- pair production of proton against the cosmic microwave background. Similarly the cut off could either sign the GZK effect (the energy loss via pion production of protons against the cosmic microwave background) or indicate an exhaustion of sources at the highest energies.
To distinguish between these scenarios, the knowledge of cosmic ray composition and anisotropies is crucial. If the ankle is due to the Galactic to extragalactic transition, this should be visible in terms of anisotropies, while if it is a consequence of the e^+/e^- pair production, a proton composition should be clearly dominant over the ankle energy range. In the same way, if the cut off is due to the GZK effect, the composition should be dominated by protons at the corresponding energy, while if it is the sign of the source acceleration limitation, with a maximum energy proportional to the atomic number Z, the composition should become increasingly heavy with energy.
The Pierre Auger Observatory [2] detects UHECRs via the Extensive Air Shower (EAS) they induce in the atmosphere, using two detection techniques: a surface detector array (SD) and fluorescence telescopes (FD). The SD is composed of 1660 water Cherenkov detectors that sample the air shower at the ground. The FD consists of 27 telescopes installed at five sites and measures the shower development in the atmosphere by observing the fluorescence light from the decay of ionized nitrogen atoms. The SD measures the lateral distribution of the shower at one stage of its development, and is weakly sensitive to the primary mass. In contrast, the FD reconstructs the longitudinal profile of the air shower and thus observes the maximum development of the shower which is strongly related to the cosmic ray cross section (hence its composition). However, FD only operates on clear moonless nights, that is about 10% of the time, limiting its total exposure.

The detection of radio waves from the EAS holds the promises to combine a 100% duty cycle with a mass sensitivity comparable to the FD. I describe in this thesis, the developments, the installations and the data analysis of a special radio detection system called EASIER for Extensive Air Shower Identification using Electron Radiometer. Before explaining the detection setups, I briefly describe the potential emission mechanisms EASIER could be sensitive to.

Radio emissions

The radio detection of EAS was already developed with some success in the 1960s, and several experiments detected strong pulses in coincidence with EAS at frequencies from a few MHz to hundreds of MHz. The radio pulses were explained by a coherent emission of shower particles due to charge separation in the geomagnetic field and a "Cherenkov like" emission from an excess of negative charges in the shower. The dependence of the radio signal was summarized by Allan [3] in the following expression:

$$E_\nu = 20\,\left(\frac{E_p}{10^{17}}\right)\,\sin\alpha\cos\theta\exp\left(-\frac{R}{R_0(\nu,\theta)}\right)\quad[\mu\mathrm{V/m/MHz}] \tag{0.0.1}$$

where α is the angle between the arrival direction and the geomagnetic field direction, θ is the zenith angle, and R is the distance to the shower axis. The parameter R_0 was found to be (110 ± 10) m at the frequency $\nu = 55\,\mathrm{MHz}$ and with rather vertical shower $\theta \leq 35°$. At that time, the limited extension of the signal with distance, the difficult interpretation of its amplitude and the development of other techniques such as the fluorescence technique slowed down the developments of radio detection. A renewed interest started at the beginning of the years 2000 with the need for an increased aperture at ultra high energy and the progress in low noise electronics and data processing. Recent experiments like CODALEMA [4], LOPES [5] or AERA [6] confirmed the potential of this technique at energies around 10^{17} eV by instrumenting radio detector arrays with a spacing of about one hundred meters.
In addition to these recent developments in the VHF band, in 2008, a beam experiment was designed to observe the continuum emission in the band [1.5-6]GHz upon the passage of an electron beam in an anechoic chamber [7]. The emission, interpreted as Molecular Bremsstrahlung Radiation (MBR) produced by low energy electrons of the plasma induced after the passage of the shower, was reported sufficient to be observed from EAS. This radiation is emitted isotropically and the expected flux from air shower deduced from the measurement in laboratory is expressed as:

$$F(t) \propto F_{ref}\cdot\left(\frac{d}{R(t)}\right)^2\cdot\left(\frac{N(t)}{N_{ref}}\right)^\alpha\quad[\mathrm{W/m^2/Hz}] \tag{0.0.2}$$

where the $F_{ref} = 4\times10^{-16}\,\mathrm{W/m^2/Hz}$ and $N_{ref} \simeq 2\times10^8$ are a reference flux and the number of particles of a 3.36×10^{17} eV reference shower as deduced from the laboratory measurement. The parameter α indicates the level of coherence of the emission, i.e. its dependence with the number of particles. The beam measurements seem to indicate a full coherence that is $\alpha = 2$.

EASIER

The EASIER detectors are developed to detect extensive air shower radio signal in a complementary way to the Pierre Auger Observatory surface detector. It is flexible in terms of the frequency it is sensitive to. The radio detector is integrated with the water Cherenkov tank, and while the latter triggers at the passage of particles at ground, the former is recording the radio emission from the air shower. The measured radio profile will provide a calorimetric measurement of the electromagnetic shower by integration of the signal and two key informations for mass discrimination: firstly the depth of shower maximum development directly related to the primary composition can be deduced from the position in time of the maximum in the radio trace, secondly the muonic signal at ground can be inferred by subtraction of the electromagnetic component, as estimated from the radio, to the total signal recorded by the water Cherenkov detector.

The EASIER design includes a wide field of view antenna pointing at the zenith followed by an amplification and a filtering stage to select a bandwidth free from RFI (Radio Frequencies Interferences). Then, a power detection stage transforms the RF signal in its power envelope. Finally, a dedicated electronics adapts the power detector signal to the electronics input of the Auger SD detector unit which performs the acquisition. This scheme has been applied successfully to the VHF band and at microwave frequency where MBR from EAS is expected.

VHF band

The purpose of EASIER in this band is to explore a possible emission that could be detectable at further distances and higher energies than the coherent radiation reported by previous experiments. In this band the sensitive part of the detector, the antenna and the amplifier are the one developed for the CODALEMA experiment. The antenna is a fat dipole made of two aluminum blades of 0.6 m each and 0.1 m wide. It is tuned to a resonance frequency of $\sim$ 113 MHz and is matched with an amplifier to obtain an approximately flat frequency response from 1 kHz to 90 MHz. We developed an electronic board whose function is a filtering between 30 and 80 MHz, and to adapt the signal to the Auger SD electronics. This last function is performed by the power detector, that transforms the RF signal to a DC voltage proportional to its power in logarithmic scale, and by an amplification that allows us to select a dynamic range of around a factor 10000 in power.

The calibration of the electronic boards was performed in laboratory, however, due to the large amount of background noise at these frequencies in urban conditions the whole setup could not be tested completely until the installation on site. The installation of seven of these detectors was carried out at the Pierre Auger Observatory in March 2011 and several modifications were brought to the initial setup to guarantee a good data taking.

After a selection to reject noisy radio traces, we reported the detection of 36 radio events in coincidence with air shower detected by the SD with energy ranging from a few 10^{17} eV to more than 3×10^{19} eV. The main characteristics of these events are a short distance to the shower axis, a large zenith angle and an excess of detection from the southern direction.

The effect of the water Cherenkov detector on the radio sensor, crucial to perform the coincident detection, has been explored in detail. A study of the noise induced by the tank was achieved by emitting fake signal in the water Cherenkov tank and estimating the resulting amount of noise measured by the antenna. This study has shown that the tank is not the origin for the radio events. Nevertheless, electromagnetic simulations showed that the position of the antenna with respect to the tank could influence the radiation pattern and favor the detection of event coming from the south. Finally, the distribution of the signal with the distance from the shower axis shows an exponential decrease supporting a coherent emission. The excess of detection of radio events from southern direction also confirms a geomagnetic origin of the emission but this effect is enlarged by the detector effect.

This first setup has shown the feasibility of the coincident detection with the surface detector of the Pierre Auger Observatory in the VHF band. It has raised experimental issues such as the importance of a steep filtering and the influence of the tank on the antenna pattern. A second demonstrator has been developed to overcome these effects and to improve the sensitivity.

Microwave

The developments in the microwave band were triggered by the measurement in beam experiment of an emission between 1.5 and 6 GHz from a shower of particles. The purpose of EASIER in this band is to confirm the possibility of detection in the microwave band and to evaluate if the parameters measured in laboratory, F_{ref} and α of Eq. 5.1.1 are identical in extensive air shower condition.

After a noise survey at the Pierre Auger site, the C-band [3.4-4.2]GHz was chosen for its atmospheric transparency and the availability of low cost commercial equipment. The antenna we used is a feed horn equipped with an integrated Low Noise Block which amplifies and shifts the RF signal at frequencies between 0.95 and 1.75 GHz. The RF signal is then fed to a power detector and adapted to the Auger SD electronics to obtain a dynamic range of a factor 100. In April 2011, a first installation of one hexagon, i.e. seven surface detectors, led to the first detection of an air shower in the GHz range. This success triggered the installation of 54 more units one year later.

An important work on calibration has been carried out to determine the sensitivity of the detector, defined by the minimum flux detectable. The sensitivity reads:

$$F_{signal} = \frac{k_B \cdot T_{sys}}{A_{eff}(\theta, \phi) \cdot \sqrt{\tau \cdot \Delta\nu}} \quad [\mathrm{W/m^2/Hz}] \tag{0.0.3}$$

with $k_B T_{sys}$ the noise power density, $\Delta\nu$ the frequency bandwidth, τ the time of integration of system and A_{eff} the effective area of the antenna. The effective area is imposed by the required field of view. T_{sys} was measured by different means to around 50 K, i.e. compatible with the detection of MBR as parameterized in [7]. We performed also a calibration of the complete detector on site using an external source carried by an octocopter and flying above EASIER setup. The calibrated power from the source allowed us to estimate our level of noise. It indicated a level of sensitivity in the proper range for MBR detection even if large systematic uncertainties prevented us from reporting a precise number.

The microwave detectors have been running in a stable way up to now. The data analysis performed allows us to report four unambiguous radio detections. The origin of these signals is still under investigation. The short distances from the antenna to the shower axis (≤ 300 m) support a coherent emission origin and the mechanism could indeed be due to a geomagnetic effect, like in the VHF band. However, due to propagation effect in a medium with a refractive index greater than one, even an isotropic emission is greatly enhanced at short distance.

To disentangle the possible mechanisms of emission, we developed a detailed simulation chain. The particle profile of an extensive air shower is simulated and the microwave emission is estimated using the parameters measured in [7]. The propagation effects due to the refraction index are accounted for. The antenna is simulated according to the calibration measurements and a specific electronic simulation was implemented.

The comparison between simulation and the detected events is being finalized. Conclusions are difficult to draw on the small data set of radio signals. Nevertheless, the non detection at large distances will allow us to set limits on the isotropic MBR flux.

Outlook

The presented development of radio detectors in VHF and microwave band showed the possibility and the assets of the coincident detection with the surface detector of the Pierre Auger Observatory.

The installation of a first prototype in the VHF band led to the detection of 36 events in approximately 4 months of operation. The exponential decrease of the lateral distribution of the radio signal at ground supports a coherent emission beamed forward around the shower axis. With the current sensitivity, this limits the distance of detection for vertical showers to around 200 m.

In the microwave band, we developed and installed in total 61 radio detectors at the Pierre Auger Observatory site. We reported the first detections of air showers in the C-band. However, if the expected emission mechanism, the MBR, is emitted isotropically, the events observed seem to indicate a beamed emission just as in the VHF band.

The original purpose of EASIER is to achieve the detection of radio emission from air showers at distances of the order of 1 km. Until now, this distance is limited to 200 m by the radiation pattern of the emission mechanism. Improvements of the sensitivity are underway to possibly explore other emission mechanisms.

Bibliography

[1] M. Fukushima, Proc. UHECR12, CERN.

[2] The Pierre Auger Collaboration, Nucl. Instrum. Meth. **A523** (2004) 50.

[3] H.R. Allan, Prog. in Element. Part. and Cos. Ray Phys., **10** (1971) 171.

[4] D. Ardouin *et al.*, Nucl.Instrum.Meth., **A555** (2005) 148-163.

[5] A. Haungs *et al.*, Nucl.Instrum.Meth., **A604** (2009) S1-S8.

[6] J. Kelley, Proc. 32nd ICRC, Beijing, China, **3** (2011) 112,

[7] P. W. Gorham *et al.*, Phys. Rev. **D78** (2008) 032007.

Contents

Chapter 1

Ultra High Energy Cosmic Rays

The discovery of cosmic ray is now more than a hundred years old. It is usually attributed to Viktor Hess in 1912, who reported an increase of ionization rate in air with higher altitude during a manned balloon flight [1].

Earlier experiments on ionization in air at sea level had shown a ionization rate that was attributed to natural radioactivity. Thus, results of Hess, later confirmed by Kolhörster [2], established that a radiation was issued not from the ground but rather from the atmosphere. The study of this radiation continued further with other balloon flights and measurements under water. The conclusion remained the same, the ionization rate evolution is best explained by "cosmic ray".

During the 1930s the proof was made that these particles were charged [3] and the observation of an excess of events from western direction demonstrated that most of them were positively charged [4, 5]. Meanwhile, detectors had improved too, and electroscopes replaced by Geiger Müller particle counter. A breakthrough was accomplished by Bothe and Rossi, in the 30s, as they developed coincidence setup. This new technique allowed the observation of an increase of coincidences between three distant counters when a plate of lead was placed above them [6]. This was the first observation of what Rossi called a "shower" of particles. A little later in 1939, with an improved timing resolution for coincidence, Pierre Auger and collaborators were able to make coincidence between counters 300 m apart, demonstrating then the existence of extensive shower of particles in air [7]. Auger and collaborators inferred an energy of $\simeq 10^{15}$ eV for the particle initiating the shower. They estimated the number of particles, assumed an average energy of 10^{8} eV per particle and accounted for a factor of ten in ionization losses. This very high energy led them to raise fundamental questions about the origin of cosmic ray and the mechanism that leads to such energies. These questions are expressed by Pierre Auger in the conclusions of [7]: "One of the consequence of the extension of the energy spectrum of cosmic rays up to 10^{15} eV is that it is actually impossible to imagine a single process able to give to a particle such an energy".

Since then, Cosmic Rays (CR) have been extensively studied. They are now defined as ionized nuclei coming from outside the solar system with an energy larger than 10^{9} eV (1 GeV) and that can extend to more than 10^{20} eV. At the highest energies, we will refer to as Ultra High Energy Cosmic Rays (UHECR). The differential energy spectrum of cosmic ray, shown in Fig 1.1, reports measurements of the flux by several experiments over almost 10 decades in energy.

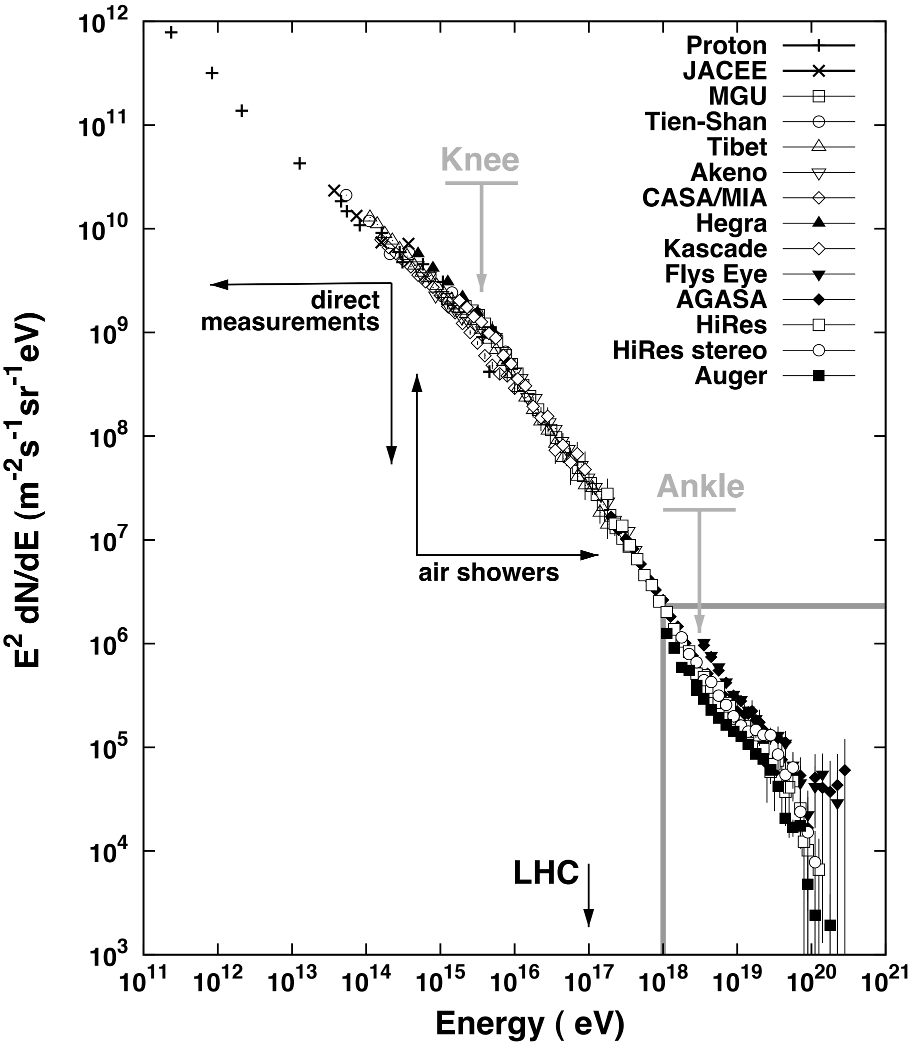

Figure 1.1: Differential energy spectrum of cosmic rays above 100 GeV as measured by the experiments mentioned in the upper right corner (from [8]). It is multiplied by E^2, in gray are pointed the position of the cosmic ray knee and ankle (see text).

The energy spectrum demonstrates an almost featureless decrease with energy with a power law shape, $dN/dE \propto E^{\gamma}$. This energy dependence indicates a non thermal phenomenon at the acceleration site. A first explanation was given by Fermi in 1949 [9]. He described a process in which cosmic rays are accelerated by “collision against moving magnetic field” in the Galaxy and gain at each interaction an amount of energy $\Delta E \propto E$. This model was extended later to diffusive shock acceleration in astrophysical objects like Super Novae Remnant (SNR) and yields naturally to an inverse power law spectrum with a spectral index similar to the one observed. But to reach energy up the 10^{20} eV one needs to find the appropriate astrophysical object likely to accelerate cosmic ray with such energy.

Beyond the overall regularity of the spectrum, three main features are visible. Before 4×10^{15} eV, the spectrum falls with an index of $\gamma \simeq -2.7$ and steepens above with $\gamma \simeq -3.1$. This change of slope, called the *knee* is followed at higher energy by the *ankle*, a flattening above 4×10^{18} eV. At the very end of the spectrum above $3 - 4 \times 10^{19}$ eV, up to the years 2000, data of different experiments yielded to contradictory results: some reported a strong cut off of the flux the other a spectrum falling with a constant index. This tension is now solved since the data of the most recent observatories confirm a steepening of the flux. How can these features be interpreted ? Are they related with the production process or to the source distribution or propagation effects ?

Because of the sharp decrease of the flux, the rate of events in an energy bin decreases by a factor 50 to 100 per decade leading to a rate of less than one particle per km^2 per century above 10^{20} eV. As a consequence, cosmic rays above around 10^{15} eV cannot be detected directly with satellite or balloon born detectors as at lower energy since the flux is too low to detect enough particles in a reasonable amount of time. Instead, they are detected through the shower they induce in air. Observatories covering a large surface or volume of detection are operated on earth, the atmosphere serving as a giant calorimeter. Such indirect detection necessitates a constant atmosphere monitoring and a precise understanding of interaction of ultra high energy particles with air molecules.

Thus, the cosmic ray physic field embraces astrophysics to point possible sources of acceleration and evaluate the interaction of CR during their propagation in space but also high energy particle physics to study their interaction in atmosphere, and addresses challenge in detector development.

We will first address the question of production and propagation of UHECR, then we will give a simple model of air shower development and deal with the main methods used to their detection. We will give in the next section a more precise insight on the Pierre Auger Observatory, its detection methods and its experimental results. The last part is a short description of the current models proposed to explain the observational data at ultra high energy.

1.1 UHECR production and propagation

The question raised by the observation of UHECR is naturally how they are accelerated. Moreover, to be able to interpret the observational data one has to account for propagation effects undergone by UHECR during their transport to the Earth.

Acceleration mechanism

In 1949, Fermi proposed an acceleration mechanism based on the scattering of cosmic rays on interstellar magnetized clouds. As they enter the magnetized cloud, charged particles are bent and eventually ejected away. In this process the CR energy remains unchanged in the frame of the cloud because only magnetic force are involved, but if we consider the frame in which the cloud is moving, the CR energy is changed. The gain in energy is found to be $\Delta E \propto \beta^2 E$ where $\beta = V/c$ the velocity of the cloud. This mechanism was attracting since it yields naturally an inverse power law energy spectrum as observed but according to the mean velocity and distribution of clouds this process is not suited to explain the cosmic ray acceleration.

It was extended to what is called the diffusive shock acceleration [10]. The acceleration is achieved by the movement of a charged particle back and forth between the upstream and the downstream region of a shock wave. For instance a supernova explosion is known to come together with such expanding shock. Particle with a Larmor radius smaller than the dimension of the shock remain in the acceleration source and gain energy at each cycle. The resulting energy gain is proportional to β the velocity of the shock rather than β^2 in the case of the mechanism of acceleration originally proposed by Fermi. The maximum energy reachable by a charged particle is:

$$E_{max} = \beta Z e B r_s \tag{1.1.1}$$

where β is the speed of the shock, Ze the charge of the particle, B the ambient magnetic field and r_s the shock radius. The magnetic field and the dimension of the astrophysical object are the limiting factors. Note that, in case of acceleration in medium in relativistic motion with respect to the Earth and a particle escaping in direction of the Earth, the maximum energy is increased by the Lorentz factor. For typical value of super novea of type II, the maximum energy is $E_{max} \sim Z \times 10^{14}$ eV [11]. More recent estimates find an energy an order of magnitude larger [12], and accounting for mechanisms of interaction between magnetic field at source and the accelerated particle can enhance this value [13], thus becoming compatible with the knee region energy.

To reach higher energies up to 10^{20} eV, other astrophysical objects are proposed. They are gathered in the classic Hillas plot (Fig. 1.2, left) as a function of their magnetic field and dimension. The astrophysical objects can be potential sources if they lie above the line corresponding to the specie to accelerate above 10^{20} eV. The remaining candidates are Active Galactic Nuclei (AGN) and FRII galaxies, Gamma Ray Burst (GRB) or neutron stars.

A more exotic mechanism was also proposed, in this mechanism super massive particles decay producing quarks and leptons, which in turn produce ultra high energy photons, neutrinos and a small fraction of protons. These models in which no acceleration mechanism is required are called top-down models.

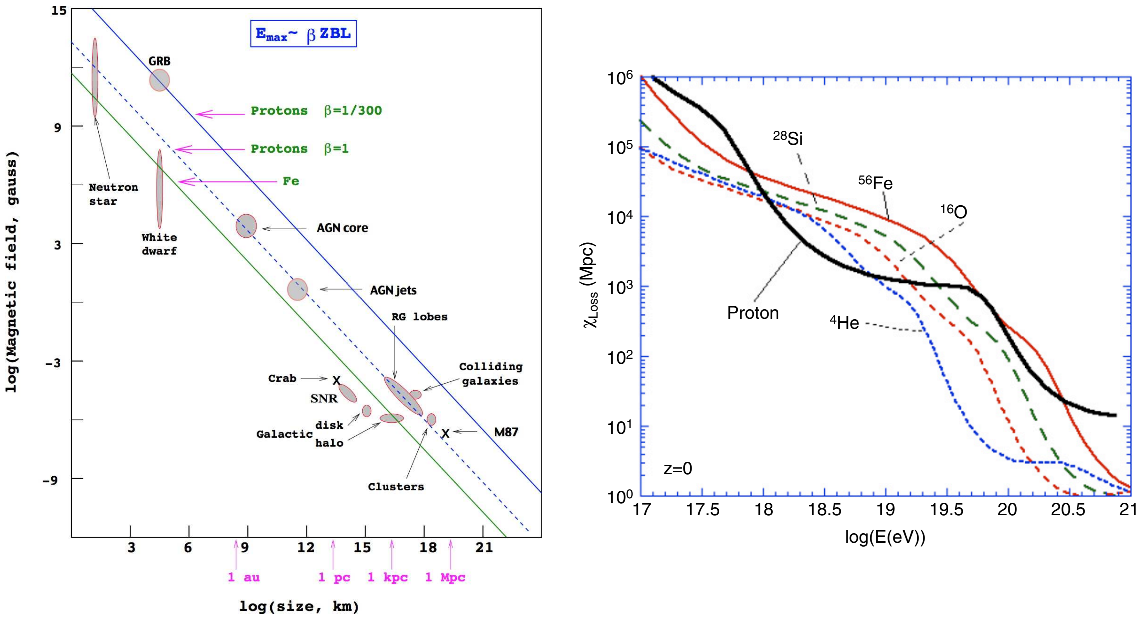

Figure 1.2: Left: Hillas plot collecting the source candidate as a function of the dimensions and magnetic field characteristic of the source. (taken from [8]). Right: Loss length as a function of energy for protons and nuclei (from [14]).

Propagation

Once possible sources are pointed out, one has to evaluate how the propagation of cosmic ray from their production site will affect their flux on Earth. Indeed, soon after the discovery of the Cosmic Microwave Background [15] it was noticed by Greisen [16] and by Kuzmin and Zatsepin [17] that the interaction of ultra high energy protons with CMB photons exceeds the threshold of pion production:

$$p + \gamma \rightarrow N + \pi \tag{1.1.2}$$

Where N can be a proton or a neutron and consequently the pion can be neutral or positively charged. Ultra high energy neutrons undergo the same type of interaction. In the Lab frame the energy in center of mass reads:

$$\sqrt{s} = \sqrt{m_p^2 + 2E_p\epsilon_\gamma(1 - \cos\theta)} \tag{1.1.3}$$

with E_p and ϵ_γ the proton and photon energy and θ the angle of collision. In a frontal collision ($\cos\theta = -1$) and with a mean CMB photon energy of $< \epsilon_\gamma >= 6.3 \times 10^{-4}$ eV, the energy threshold of proton is found to be $E_p \simeq 10^{20}$ eV. This threshold is actually lower, around 3×10^{19} eV because of the CMB photons with energy higher than $< \epsilon_\gamma >$.

This effect is referred to as the GZK effect. For nuclei, the dominant process above 10^{19} eV is the photo disintegration on CMB and infrared background due to giant dipole resonance [18]:

$$A + \gamma \rightarrow (A - 1) + N \tag{1.1.4}$$

where A is the nucleus of mass number A and N is either a proton or a neutron. The energy at which this interaction occurs depends on nuclei mass and is comparable to the GZK threshold

for iron nuclei.
In addition, CR lose their energy via the pair production : $A + \gamma \rightarrow A + e^- + e^+$ where A can be a proton or a nucleus. This interaction occurs typically around $10^{18.4}$ eV for a proton and at higher energy for nuclei. The energy loss length for protons and nuclei are depicted in Fig. 1.2 (left). It defines the length scale on which a particle loses its energy and thus delimits the distance from which a cosmic ray can be produced and still reach the earth with the corresponding energy. Note the short length due to the GZK effect constraining the sources of cosmic rays with an energy observed above 10^{20} eV to be in a 100 Mpc horizon.[1]

---

[1] a parsec (pc) is a distance unit used in astronomy. It corresponds to 3.26 light-years.

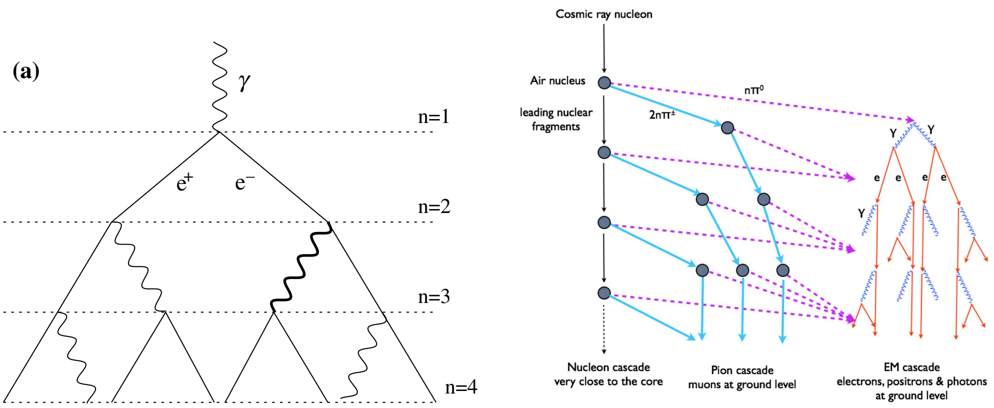

Figure 1.3: Sketch of the development of a simplified electromagnetic cascade (left) and hadronic cascade (right). Respectively taken from [19] and [8].

1.2 Extensive Air Showers

The detection of the highest energy CR is achieved through the observation of the cascade of particles they induce in the atmosphere. When entering the atmosphere, from the interaction of the primary CR with atoms in air, secondary particles are produced which in turn interact and achieve the process of particle production again. In this way an air shower develops in the air in competition with ionization losses undergone by the shower particles. For instance, a primary CR with an energy of $E = 10^{19}\,\mathrm{eV}$ induces billions of secondary particles. After giving the basic models to describe the EAS development, we describe the main detection techniques used in the current experiments.

Model of development

We describe a simple analytical model of shower development in the case of electromagnetic cascade (induced by a electron, positron or a photon) and its extension to hadron induced shower.

Electromagnetic shower The model was introduced by Heitler in [20] to describe electromagnetic cascade i.e. shower induced by photons, electrons or positrons. It assumes a fixed distance step of interaction and cross sections independent of energy. The distances, or depths, are considered as the amount of traversed matter along the particle path and they are expressed in g/cm^2. At each step, photons produce an electron-positron pair, and electrons (or positrons) radiate half their energy on one Bremsstrahlung photon. The scheme of such development is given in Fig. 1.3 for a photon primary. The distance of interaction is then $d = \lambda_r \ln 2$ where $\lambda_r \simeq 37\,\mathrm{g/cm^{-2}}$ in air is the radiation length for Bremsstrahlung process. The development stops when particles have a critical energy E_c^{em}, at which losses in ionization dominate over the particle production. This energy is reached after n_c steps when the number of particles is:

$$N_{max} = 2^{n_c} = E_0/E_c^{em} \tag{1.2.1}$$

with E_0 the energy of the primary particle. The number of steps to reach the maximum is then $n_c = \ln(E_0/E_c^{em})/\ln 2$ and its depth is given by:

$$X_{max} = n_c \lambda_r \ln(2) = \lambda_r \ln(E_0/E_c^{em}) \tag{1.2.2}$$

With this simple consideration, the Heitler model points out two important behaviors of an electromagnetic cascade:

- the number of particles at maximum of development, N_{max}, is proportional to the primary energy
- the depth of this maximum, X_{max}, depends logarithmically on energy

More realistic simulations confirm the behavior of these parameters for electromagnetic cascade. They show however that Heitler's model overestimates the total number of particles at maximum by a factor two or three mainly because the attenuation is not accounted for, and that the ratio photon to electron is underestimated since more than one Bremsstrahlung photon is emitted by electrons at each interaction length.

Hadronic shower At ultra high energy, the CR are mainly nuclei. The previous model was extended for hadron initiated shower by Matthews in [19]. In that case, it is assumed that each hadronic interaction produces a number N_{ch} of charged pions and $N_{ch}/2$ of neutral pions. The relevant interaction distance is now $\lambda_I \ln 2$ with λ_I the hadronic interaction length. The charged pions interact with molecules of air and fuel the hadronic channel while each neutral pion decays immediately into two photons initiating electromagnetic cascades as it is depicted in Fig 1.3 (right). The particle production ends when the decay of charged pions into muon starts to dominate. Thus, along the development of an hadronic shower, three components are present: the hadronic, the electromagnetic and the muonic one. For a primary proton of energy E_0, after n interaction lengths, the number of charged pions is $N_\pi = N_{ch}^n$ with an energy $E_\pi = E_0/(\frac{3}{2}N_{ch})^n$. At a critical energy E_c^{had}, when the decay length of the charged pion becomes smaller than the interaction length in air, the hadronic channel stops to develop. The number of steps to reach this stage is given by $n_c = \frac{\ln(E_0/E_c^{had})}{\ln(\frac{3}{2}N_{ch})}$. At this stage, it is assumed that all the pions decayed into muons resulting in a muon number of $\ln N_\mu = \ln N_\pi = n_c \ln N_{ch}$, or :

$$\ln N_\mu = \frac{\ln(E_0/E_c^{had})}{\ln(\frac{3}{2}N_{ch})} \ln N_{ch} = \beta \ln(E_0/E_c^{had}) \text{ with } \beta = \frac{\ln N_{ch}}{\ln \frac{3}{2}N_{ch}} \tag{1.2.3}$$

$$\Rightarrow N_\mu = \left(\frac{E_0}{E_c^{had}}\right)^\beta \tag{1.2.4}$$

The multiplicity N_{ch}, the number of charged pions at each interaction, is taken in [19] to be 10 from accelerator measurements. The value of the exponent β is then 0.85, showing the non linearity of the number of muons with the primary energy. Concerning the electromagnetic part, the total energy taken away from it, E_{em}, can be calculated by subtraction of muon energy, E_{had}, from the primary energy :

$$E_{em} = E_0 - E_{had} = E_0 - N_\mu E_c^{had} \Rightarrow \frac{E_{em}}{E_0} = 1 - \left(\frac{E_0}{E_c^{had}}\right)^{\beta-1} \tag{1.2.5}$$

For a primary energy of $E_0 = 10^{14}\,\text{eV}$ the electromagnetic component takes away $\simeq 70\%$ of the total energy, and this value rises up to 90% for $E_0 = 10^{17}\,\text{eV}$.
The depth for which the electron and photon number is maximum, is more delicate to obtain. In principle one should sum the contributions of each electromagnetic sub-shower, however accounting only for the first interaction simplifies the treatment and keeps the main properties of X_{max} but its absolute value will be under evaluated.
The depth of maximum is given by :

$$X^p_{max} = X_0 + X^{em}_{max} \tag{1.2.6}$$

where the depth of first interaction is $X_0 = \lambda_I \ln 2$ and λ_I the proton air interaction length. If at the first interaction, the incoming proton doesn't transfer its entire energy by just a portion K_{el} of its kinematic energy to $\frac{1}{2}N_{ch}$ neutral pions, their decay yields N_{ch} photons with an energy $E_0/(3N_{ch})$. These photons initiate an electromagnetic cascade that reach their maximum according to Eq. 1.2.2. Then X^p_{max} writes down :

$$X^p_{max} = X_0 + \lambda_r \ln\left(\frac{E_0(1-K_{el})}{3 \cdot N_{ch} \cdot E^{em}_c}\right) \tag{1.2.7}$$

Now if we want to extend the problem to heavier nuclei than a proton, we can introduce the superposition approximation that states that a shower initiated by a nucleus of mass number A and an energy E_0 behave like a superposition of A showers initiated by nucleons of energy E_0/A. In this approximation, the shower size, increasing linearly with the primary energy remains the same, but the depth of maximum becomes :

$$X^A_{max} = X_0 + \lambda_r \ln\left(\frac{E_0(1-K_{el})}{3AN_{ch} \cdot E^{em}_c}\right) = X^p_{max} - \lambda_r \ln A \tag{1.2.8}$$

and the number of muons :

$$N^A_\mu = A(\frac{E_0}{AE^\pi_c}) = A^{1-\beta} N^p_\mu \tag{1.2.9}$$

The simple parameterization described above and the superposition model assumption, allow us to point out interesting features on hadronic showers:

- at sufficiently high energy (above $10^{17}\,\text{eV}$) most of the primary energy is carried by the electromagnetic part.
- the depth of shower maximum, X^p_{max}, is driven by the first hadronic interaction and the development of the first electromagnetic cascade.
- X^A_{max} varies logarithmically with the mass number A of the primary.
- the number of muons varies with $A^{1-\beta}$ where $\beta \simeq 0.85$.

Nowadays, air shower description is done by means of Monte Carlo simulations. They account for much details neglected in the previous models like the energy dependence of the cross section and the inelasticity of each process. They rely on accelerator measurements but adopt different extrapolation at energies above the TeV ($= 10^{12}\,\text{eV}$) scale in center of mass. We show the evolution of the number of particles as a function of the atmospheric depth for two simulated air showers induced by a proton and an iron primary at $10^{19}\,\text{eV}$ in Fig. 1.4 (left).

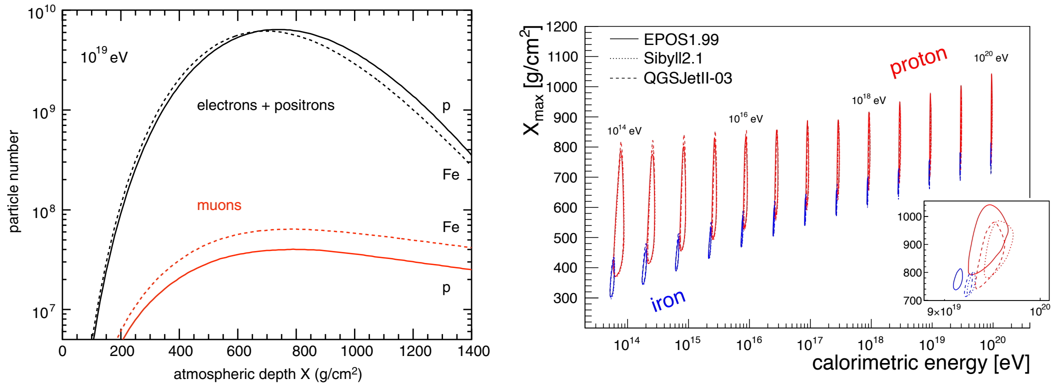

Figure 1.4: Left: Number of particle for a simulated proton and iron induced air shower(from [21]). Right: Depth of shower maximum as a function of the calorimetric energy for proton and iron primary. The contour lines include 90% of the simulated showers (from [22]).

At the shower maximum, the electromagnetic part contains more particles by two orders of magnitude than the muonic part and decrease exponentially after the maximum whereas the number of muons decreases much more slowly with the traversed matter. Furthermore, it confirms the dependence of the number of muons with the primary mass. In Fig. 1.4 (right), the simulated shower maximum is shown as a function of energy for both proton and iron primary. The increase of X_{max} with energy is approximately logarithmic as expressed in Eq. 1.2.2 and for the same energy iron induced shower reach their maximum higher in the atmosphere (at smaller X_{max}). The dispersion of X_{max} is mainly driven by the fluctuations of the first interaction. The smaller dispersion for iron can be seen as a consequence of the superposition model too, since the X_{max} for an iron induced shower is the superposition of $A = 56$ nucleon showers, the fluctuations on the mean are reduced by a factor nearly $\sqrt{A}$. Note that with increasing energy, the calorimetric energy, i.e. the energy transferred to the electromagnetic component, tends to the primary one and exhibits low shower to shower fluctuation above $\sim 10^{17}$ eV.

Detection techniques

An air shower event is characterized by a shower front crossing the atmosphere at approximately the speed of light until hitting the ground. The shower front can be composed of billions of particles and spread over an area of several km^2. The observation of the air shower is made by collecting the particles at ground or by detecting their interactions in the atmosphere. Since the cosmic ray flux is extremely low, air shower observatories need to cover a large area or a large volume of detection. We describe here the main methods employed in the last constructed observatories.

Air shower array Following the original detection technique set up by the pioneers, air showers are generally detected by arrays of particle detectors. Their layout and the altitude of the observatory are chosen depending on the primary energy to be studied. Particle detectors of air shower arrays sample the shower front at ground and measure the lateral distribution of particles at one stage of the shower development. From this information, the shower core location can be retrieved, and the measurement of arrival time of particles in the triggered detectors allows the reconstruction of the arrival direction. Regarding the detector itself, if the historic ones were electroscopes or Geiger Muller counters, nowadays they are replaced by scintillators or Water Cherenkov Detectors (WCD).

Scintillators, when placed on the ground, measure essentially the electromagnetic component. They can also be buried in ground so that the electromagnetic part is absorbed and only muons are detected. Scintillators were first used at Volcano Ranch [23], then at AGASA (Akeno Giant Air Shower Array) [24] and are now the elemental detector of the surface array of Telescope Array [25].

A Water Cherenkov Detector is a tank with a reflective inner surface filled with pure water. When charged particles enter the tank, Cherenkov light is emitted in the water and, often after reflections on the tank's wall, is collected by photo-multipliers looking downward in the water. WCD were first used at Haverah Park and are now extensively used at the Pierre Auger Observatory. Deployment of WCD is more complicated than scintillators: they require pure water and are very heavy (for instance the Pierre Auger Observatory tanks are filled with $12\,\mathrm{m}^3$ of water). But they are sensitive to muons, electrons and photons (via pair production in the water for the photons) and they present a non zero effective area at large zenith angles making them able to detect horizontal showers.

The surface detectors measure the shower development only at one stage, thus the energy of the EAS cannot be directly estimated. Indeed the energy estimation rely either on air shower simulations if these detectors are instrumented alone either on cross-calibration with detector able to measure the energy. Surface detector array can be sensitive to the primary mass if the two main components of the EAS, muonic and electromagnetic are measured separately.

Cherenkov light The charged particles of the shower traverse the atmosphere at relativistic speed. In particular, electrons above the threshold of 21 MeV produce a Cherenkov emission beamed in the forward direction in an angle $\theta_{Ch} \simeq 1.4^\circ$ in air. In several experiments, like AIROBICC [26] or TUNKA [27], an array of photo-multipliers pointing towards the sky measure the lateral distribution of the Cherenkov light at ground. The distribution of light decreases exponentially with distance up to $\simeq 120\,\mathrm{m}$ then exhibit a break and falls steeply at larger distances. The slope within the 120 m is found to be related to the height of the shower maximum and the intensity beyond 120 m is related to the calorimetric energy.

Because of the limited lateral extension of the Cherenkov light at ground, dense arrays are required. Moreover, the operation of photo-multipliers is possible only during the night reducing the statistics of events. For these two reasons, this technique is mainly used at energies below $10^{17}\,\mathrm{eV}$.

Fluorescence light When crossing the atmosphere, the shower particles lose their energy in ionization of the molecules in air. Consequently, the excited nitrogen molecules emit photons, mainly in the UV band, between 300 and 420 nm. Contrary to Cherenkov light, the fluorescence light is emitted isotropically. The fluorescence yield (the number of photons emitted per energy deposited) depends on pressure, temperature and electron energy. Assuming a constant density and a constant energy loss of the electrons per path length, one can give a rough estimate at ground level pressure of around 4 photons per electron per meter. Recent measurement of the fluorescence yield have been conducted in accelerator and can be

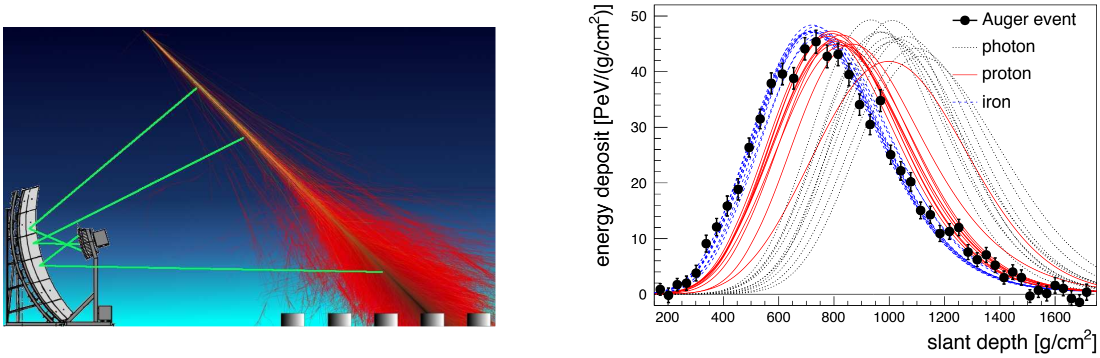

Figure 1.5: Left: sketch of a Fluorescence detector (from [8]). Right: Auger FD event together with simulation for different primaries (from [22]).

found in [28]. As the number of electrons in an air shower can reach several billions, the total number of photons emitted during a path length of several hundreds of meters is of the order of 10^{12}. If the air shower is distant of 20 km, the expected photons flux is only $\simeq$ 200 per square meter. Hence a large collection area is needed to detect distant showers and reach a sufficient exposure.

The idea of using fluorescence light was first raised in 1962 by Suga [29]. After an unsuccessful try in the mid 60s by Greisen and his group, the first detection of the fluorescence light from EAS was reported in 1970 by Tanahashi and collaborators [30] and the first fully functional detector, named Fly's Eyes, installed at Dugway (Utah) began to take data in 1981. Currently, the Pierre Auger Observatory and Telescope Array use this technique in complement to their particle detector array, allowing a cross calibration of the surface detector. A sketch of a fluorescence telescope is shown in Fig. 1.5 (left): the emitted light from the air shower is focussed by large area mirrors onto a camera made of photo-multipliers.

The isotropic distribution of the emission makes this technique suitable to observe the shower development along the atmosphere. Since the fluorescence light is directly proportional to the energy deposit of the shower in the atmosphere, the energy deposit as a function of the atmospheric depth can be directly measured. An example of such profile is shown in Fig. 1.5 (right), together with simulations for different primaries. The longitudinal profile provides then an estimation of the primary energy and the depth of maximum development. A precise estimation of these quantities is submitted to correction due to diffusion and absorption of light and pollution by other contributions such as Cherenkov light. The low duty cycle of about 10% is imposed by the condition of operation with clear moonless night and this is the main limitation of this technique at ultra high energy when the flux of CR is very low.

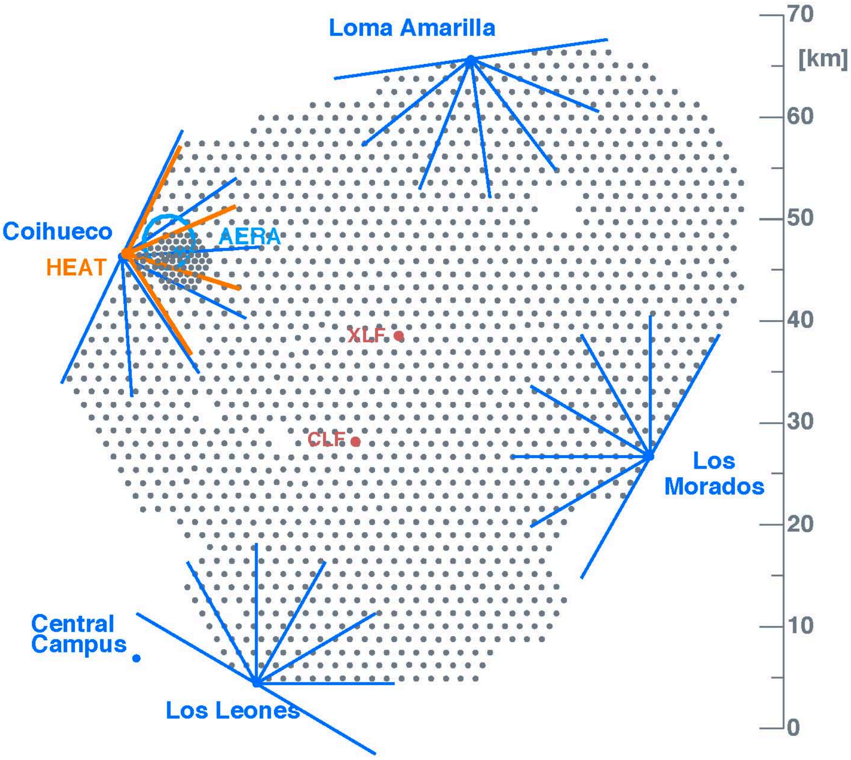

Figure 1.6: Layout of the Pierre Auger Observatory surface detector array (dots), and the five fluorescence detectors, the lines indicate the field of view of each telescope. The central campus outside of the array is located in the town of Malargüe.

1.3 The Pierre Auger Observatory

The Pierre Auger Observatory is a giant cosmic ray observatory located in the western Argentina near the town Malargüe in the province of Mendoza. It was designed to study cosmic ray flux, arrival direction and composition above 10^{18} eV. The Pierre Auger Observatory gathered these last years the largest statistics at ultra high energy. After giving an insight of the detector operation and its performances, we will review the latest experimental results and put them in the light of the current models.

EAS detection at the Pierre Auger Observatory

The Pierre Auger Observatory combines two complementary detection techniques: a surface detector array (SD) and fluorescence telescopes (FD).

Fluorescence detector There are in total 27 fluorescence telescopes at the Pierre Auger Observatory grouped in five sites and overlooking the surface detector array as illustrated in Fig. 1.6. Four detector stations, Coihueco, Loma Amarilla, Los Leones and Los Morados

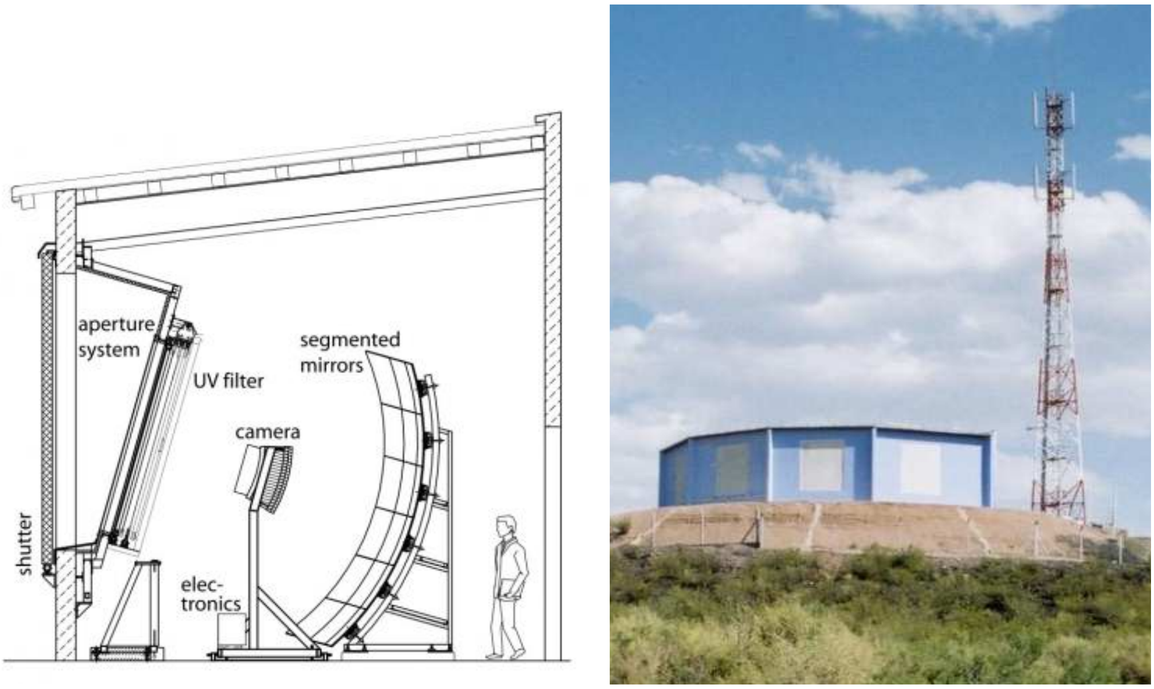

Figure 1.7: Left: Scheme of one FD telescope (from [31]). Right: Picture of Los Leones FD station, with next to it the telecommunication tour. (from [32]).

contain each six telescopes, and each telescope is equipped with a 12 m^2 mirror focusing the UV light from EAS to a 440 pixels camera (Fig. 1.7 (left)). The field of view of one telescope is 30 °×30 ° in elevation and azimuth and so that the six telescopes per station cover 180 ° in azimuth as depicted in Fig. 1.7 (right). A fifth station, HEAT station in Fig. 1.6, comprises 3 additional telescopes that can be tilted to higher elevation angle to study air showers at energies down to below 10^{17} eV.

As the shower crosses the atmosphere, the emitted photons reach the telescope and the triggered pixels form a track in the camera. The reconstruction of the EAS is a two steps process. First, the sequence of triggered pixels fixes the plane containing the shower axis and the detector (named SDP in Fig. 1.8 (left)). Next, the timing information of the pixels t_i from a direction χ_i is used to reconstruct the shower axis in this plane, i.e. the parameters χ_0, the angle between the shower axis and the horizontal line in the SDP, R_p, the closest distance from the shower axis to the telescope and t_0, the time along the shower axis at which R_p is reached. It is retrieved with the equation:

$$t_i = t_0 + \frac{R_p}{c}\tan(\frac{\chi_0 - \chi_i}{2}) \tag{1.3.1}$$

The reconstruction can be performed when the shower is observed only by one FD site, called monocular event, but some degeneracy can remain in the parameters χ_0 and R_p. This degeneracy is broken in case of hybrid event, i.e. if the shower has also triggered the surface detector, or stereo event, i.e. observed in two FD sites. The geometric reconstruction is then improved. A detailed description of the detector components and the reconstruction of FD events are reported in [31].

After the geometric reconstruction, the observed fluorescence light as a function of time is

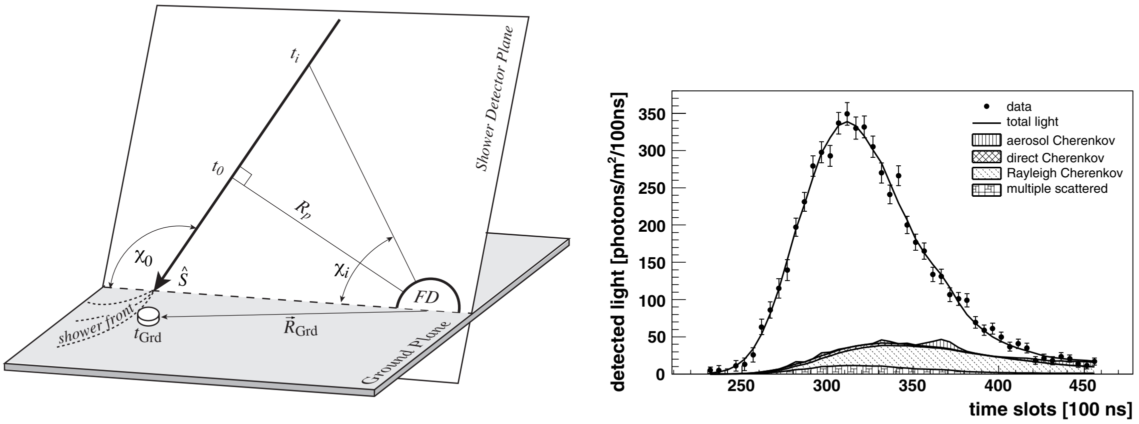

Figure 1.8: Left: Scheme of an air shower event observed by the fluorescence telescope and the parameters used in the geometric reconstruction (see text). Right: Different contribution light source in the light profile reconstructed with the FD. (From [31]).

converted into an energy deposit as a function of the atmospheric depth. First, the light attenuation from the shower to the telescope is estimated, then one needs to disentangle all contributing light sources: fluorescence light, direct and scattered Cherenkov light and multiple scattered light. An example of a shower profile reconstructed with FD is shown in Fig. 1.8. The deposit energy profile is then fitted with a Gaisser-Hillas function:

$$N_e(X) = N_{max}\left(\frac{X - X_0}{X_{max} - X_0}\right)^{(X_{max}-X_0)/\lambda} \exp\frac{(X_{max} - X)}{\lambda} \tag{1.3.2}$$

where X_{max} and N_{max} are the depth and the number of particles at shower maximum, X the atmospheric depth and X_0 and λ two free parameters of the fit. The calorimetric energy is obtained by integration of the fitted function along the atmospheric depth. Corrections for the energy carried by neutrinos and high energy muons and not converted into calorimetric energy, the "invisible energy" is obtained now with an empirical parameterization based on hybrid events. The systematic uncertainties on the energy estimation amount to 14%, the main contributions arise from the fluorescence yield, the atmosphere monitoring, the absolute calibration of the telescopes, the reconstruction of the longitudinal profile and the invisible energy estimation.

The maximum of the shower development is also retrieved from the shower longitudinal profile. The resolution on this measurement depends on the geometry of the air shower event but also on the atmospheric conditions. For instance for the mass composition studies a resolution of the order of $20\,\mathrm{g/cm^2}$ is typical.

Surface detector The surface detector is an array of 1660 stations covering $3000\,\mathrm{km}^2$ of water Cherenkov tanks (one is pictured in Fig. 1.9) arranged in a triangular grid of 1.5 km spacing, its layout is illustrated in Fig. 1.6.

When the shower front reaches the ground, the charged secondary particles (mainly electron, positron, photons and muons) deposit their energy and produce a Cherenkov radiation in the water. This radiation is collected by three photo-multipliers looking downward in the water. The raw data are the Flash Analog to Digital Converter (FADC) traces sampled from the

Figure 1.9: Surface detector unit in the pampa amarilla.

PMTs signal. An example of trace is shown in Fig. 1.11. A further description of the technical details of the SD unit of Auger will be given in chapter 2.

Each station is equipped with a local electronics and performs the two first levels of trigger. The first one called T1 is issued if the signal in the tank crosses a threshold. The rate of T1 is approximately 100 Hz. The second level trigger T2 requires more strict conditions, it requests either a higher threshold on the amplitude of the signal or a condition in its duration (Time Over Threshold). The T2 is sent to the Central Data Acquisition System (CDAS) and if at least three nearby stations reached the same trigger level in a certain time interval, a T3 is issued. The CDAS requires then the full traces of the T2 stations and the surrounding ones with the T1 condition. From this level the data are stored in the central acquisition. The T4 condition checks if the position of the stations and their relative trigger timing are compatible with an air shower event. Finally, T5 is a quality trigger, it insures a reliable reconstruction of the event. It requires that the event was not on the border of the array, or that no inactive station was involved in the event. The full efficiency is reached at energy above 3×10^{18} eV [33].

The time delay between coincident triggered detectors is used to reconstruct the shower front and the arrival direction of the primary cosmic ray. The angular resolution is a function of zenith angle and the multiplicity of stations. It is better than 3° at 10^{18} eV and better than 1° above 10^{19} eV.

To estimate the energy, the lateral distribution of deposited energy in the detectors is fitted with a lateral distribution function (LDF). An example of the lateral distribution of signal in a SD event is depicted in Fig. 1.10 together with the fitted LDF. In this figure, the unit for the signal is the VEM (Vertically Equivalent Muon), it is the average charge produced by a muon penetrating vertically and centrally the tank. It is adjusted online in each tank and provide a common reference level between tanks. The deposited energy at an optimal distance from the shower axis is taken as the energy estimator. At this distance, the statistical fluctuations from particle counting and shower to shower fluctuations are minimized. It depends on the energy range and the spacing of the array and is about 1000 m in Auger's case.

The lateral distribution of the signal at ground is dependent on the zenith angle. Indeed,

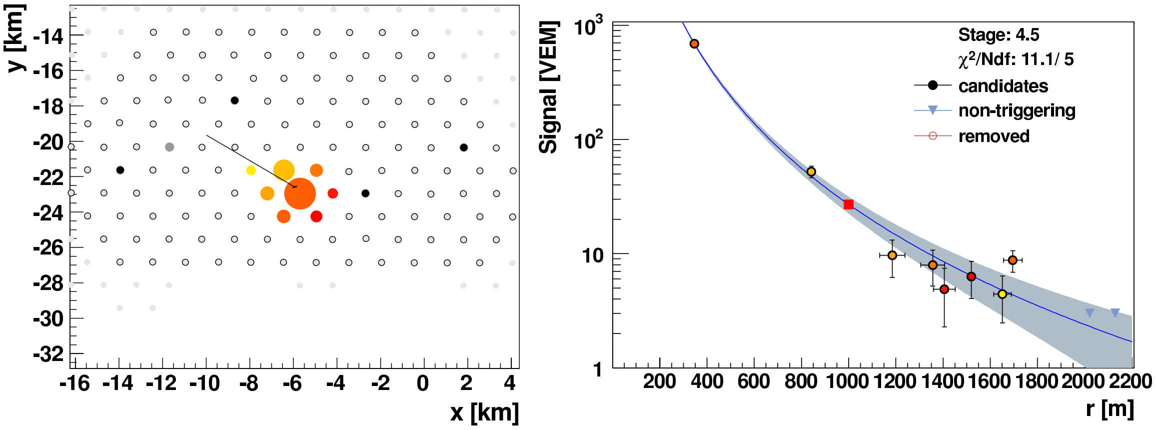

Figure 1.10: Left: Footprint of a SD event. The color code represent the arrival time (early tanks are yellow, late ones are red). Right: Lateral distribution of the signal at ground fitted with a LDF function. The red square is the signal at 1000 m, the energy estimator.

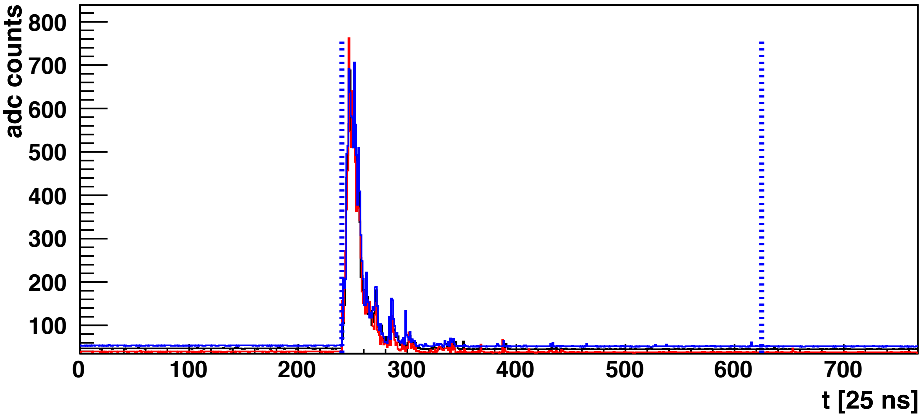

Figure 1.11: Example of a trace acquired with Auger SD unit. The three plain lines correspond to the three PMTs.

inclined showers are in a more advanced stage of development than vertical ones when reaching the ground and their signal is thus attenuated. When estimating the energy, this effect is accounted for using an empirical method, the Constant Intensity Cut (CIC). The basis of this method is to consider the flux isotropic, i.e. in local coordinate independent of the zenith angle when integrated over a large time period. The attenuation function, CIC(θ) is computed with data to normalize the flux in such a way. To estimate the absolute energy the signal at 1000 m, $S(1000)$ is first converted into the signal from a shower with a reference zenith angle of 38 °, S_{38}, according the CIC method:

$$S_{38} = \frac{S(1000)}{CIC(\theta)} \tag{1.3.3}$$

Then S_{38} is converted into the shower energy using the following transformation:

$$E = aS_{38}^{b} \tag{1.3.4}$$

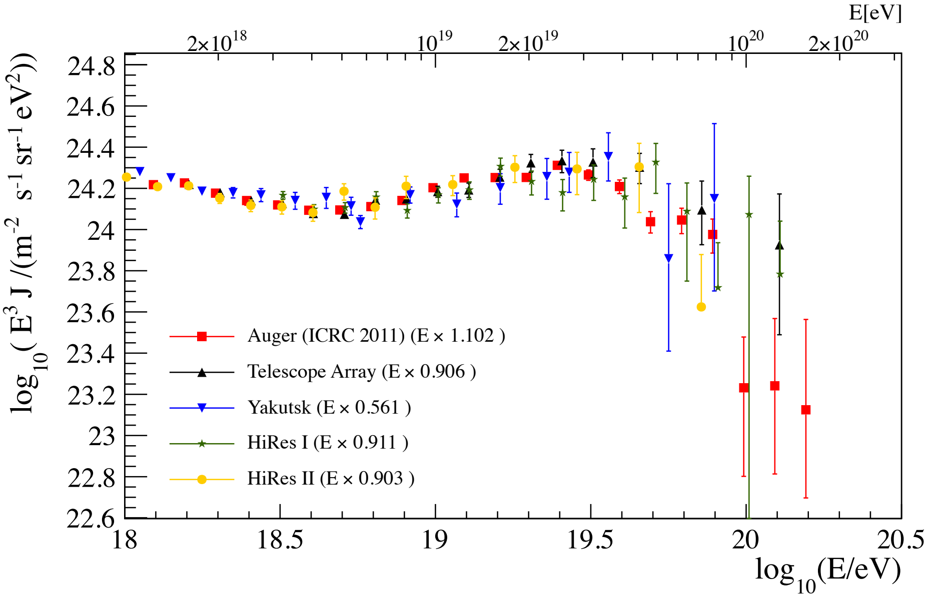

Figure 1.12: Compilation of spectra published by Auger, Telescope Array, Yakutsk and HiRes(I and II). The rescaling in energy is indicated in the lower left corner. From [34].

where coefficient a and b are given by the calibration curve using hybrid events. The independent measurement of energy of these events by the FD and SD allows the cross calibration. The absolute energy scale is given by the fluorescence measurement and has thus a systematic uncertainty for 14%.

Experimental results

Energy spectrum The compilation of energy spectra showed in Fig. 1.1 exhibit the overall regularity of the decrease of the cosmic ray flux. We examine here further the features above the knee energy. At the highest energies, above 10^{17} eV, one can observe two main features. Firstly a flattening of the spectrum, the ankle, has been measured at $\log_{10}(E_{ankle}) = 18.61 \pm 0.01\,\mathrm{eV}$ in Auger data. Secondly, a clear cut-off at the end of the measured spectrum is observed. A broken power law fit on Auger spectrum sets the change of index from -2.6 to -4.3 and the energy at which the flux has fallen by one half in case of extrapolation of the original power law at $\log_{10}(E_{cut-off}) = 19.61 \pm 0.03\,\mathrm{eV}$. The deviation from a single power law was established with a statistical confidence of more than $20\,\sigma$. In Fig. 1.12 are illustrated the energy spectra measured by Auger, Telescope Array, Yakutsk and HiRes. After a normalization within their respective energy systematic uncertainties, the spectra agree very well together.

Mass composition

The determination of mass composition, ideally on an event by event basis or by separation of sub samples of elemental group may point more structures and constrain models. A complete review on mass composition measurements, problematic and interpretation can be found

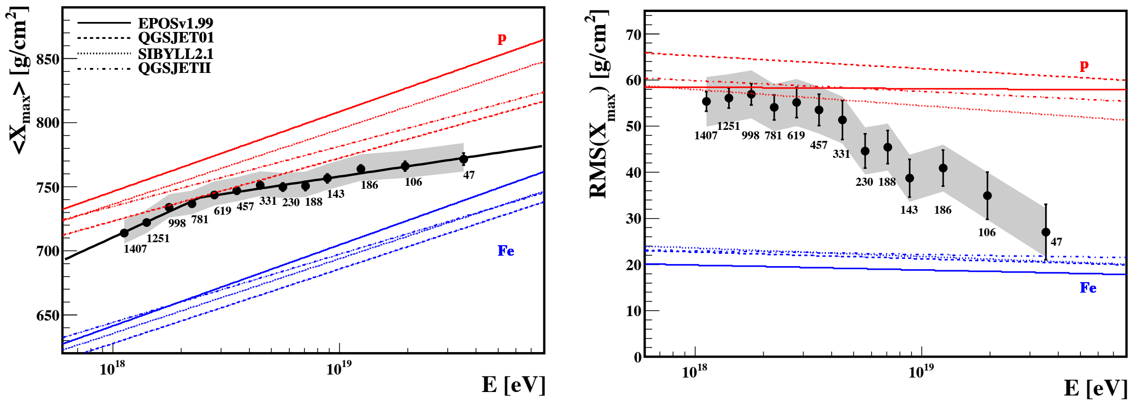

Figure 1.13: Left: Mean X_{max} (Left) and $RMS(X_{max})$ (right) measured with fluorescence detector in Auger data as a function of energy. The lines represent the expectation from simulation with several hadronic models and case of pure proton or iron. Systematic uncertainties are indicated with the gray bands. (from [35]).

in [22].

The model of hadronic shower presented before and especially the superposition model showed that two main observables were sensitive to the primary mass. For the same energy, a light primary penetrates deeper in the atmosphere and the number of muons at ground is smaller with respect to an heavy primary.

On the experimental point of view, optical detectors, fluorescence or Cherenkov light detector, are directly sensitive to X_{max} but are operable only around 10% of the time. Ground arrays can deduce indirectly parameters sensitive to shower development from the measurement of particles at ground and operate with a 100% duty cycle. They are however usually less precise.

The distribution of the depth of maximum development for a given energy is a mass indicator through its two first moments. The evolution of $< X_{max} >$ as measured with the fluorescence telescopes in Auger is plotted as a function of energy in Fig. 1.13 (left) with the expected value from air shower simulations with different hadronic models for pure proton or iron primary. Auger data show a light composition around the ankle energy and indicate a trend toward heavier primary with increasing energy. It is noteworthy that two other important observatories, Telescope Array and HiRes quote a mean X_{max} compatible with protons from 2×10^{18} eV to around 5×10^{19} eV. The comparison of data analysis methods, results and interpretation on mass composition studies of these current experiments can be found in [36]. The second moment of the X_{max} distribution is complementary to the mean, especially in case of mixed composition. Indeed, from the superposition model we saw that an heavier composition would lead to smaller fluctuation of X_{max} than a light one. But in case of mixed composition, for instance of two species, the spread of the distribution is also given by the mutual separation of $< X_{max} >$ that can result in larger fluctuations than if each one of them is taken separately. The measured $RMS(X_{max})$ in Auger data reported in Fig. 1.13 (right) exhibits a trend towards heavy elements above $10^{18.5}$ eV.

Other shower observables can provide information on the average composition. For instance, Auger's surface detectors are sensitive to both electromagnetic and muonic components, and the study of the time distribution of the traces allow us to extract information on the muon content. Using FADC traces of surface detector far from the core, thus dominated by muons,

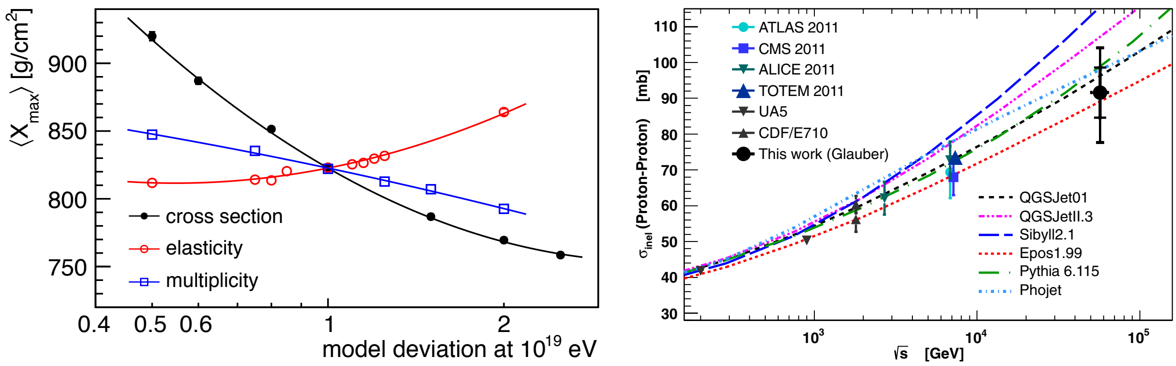

Figure 1.14: Left: Sensitivity of $< X_{max} >$ with changes of cross section, elasticity and multiplicity in SYBILL hadronic model for a proton of 10^{19} eV (from [22]). Right: Proton-proton cross section deduced from the proton-air cross section measurements with Auger data [37].

the Muon Production Depth (MPD) technique converts the time distribution in traces into distance of production of the muons in atmosphere. This technique yields informations on the longitudinal development of the hadronic component of the air shower [35].

Also, as the muons are expected to travel in straight line whereas the electron to scatter in atmosphere, they populate more the early part of the FADC traces. When a non vertical shower reaches the ground, the detectors around the core sample a different "age" of the shower, the detector upstream sees a younger shower than the one downstream. The asymmetry in azimuthal angle of the rise time in the FADC traces is found to be related to shower development. By performing first this study with hybrid events (detected by both the surface detector and the fluorescence detector) one can correlate the sensitive variable with X_{max} and then apply this method with only SD events. Note that these methods, relying on particle detector allow a larger statistics and give composition measurements above $10^{19.5}$ eV. Surface detector based methods with Auger data yield a light composition at $10^{18.5}$ eV and exhibit a trend to a heavier one above.

Hadronic interaction

The description of first interactions of the shower particles in atmosphere has two main goals. Firstly, the interpretation of the measurement of mass sensitive parameters is achieved thanks to the comparison with air shower simulations. The precise determination of the nuclear composition of cosmic ray requires then the correct simulation of shower development. Since most of interactions in shower development occur with low momentum transfer (soft interactions) perturbative QCD (Quantum ChromoDynamics) cannot be applied. Instead, phenomenological model are used based on measurements at accelerators and their extrapolation. Recent data from LHC (Large Hadron Collider), allow to extend the experimental knowledge to an energy of 14×10^{12} eV in center of mass corresponding to $\sim 10^{17}$ eV for a fixed target experiment such as a cosmic ray interacting in atmosphere. Above these energies models rely on extrapolation. As an illustration, in Fig. 1.14 is depicted the impact of the modification of cross section (black full circle), elasticity (red open circle) of interaction and multiplicity (blue open square), on the shower $< X_{max} >$. A change of a factor two in cross section can shift the $< X_{max} >$ by more than 50 g/cm^2. Knowing

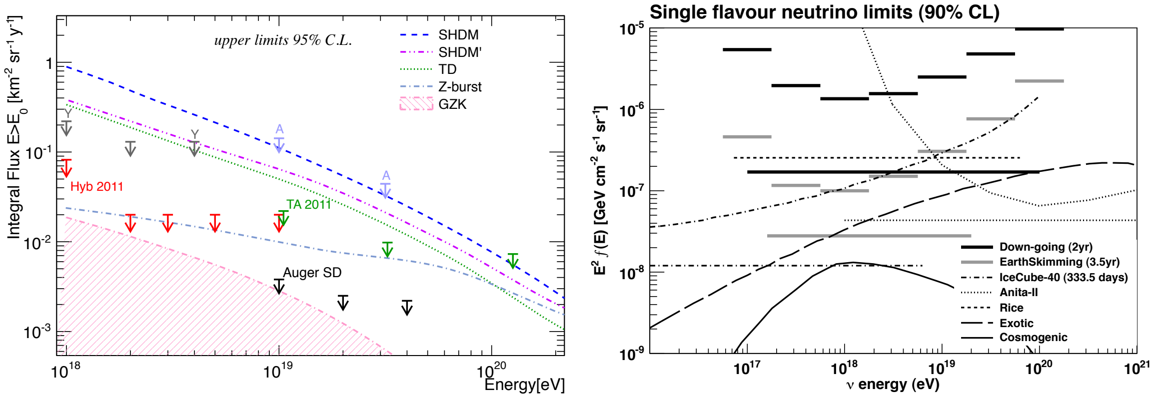

Figure 1.15: Left: Photon flux limit measured estimated with Auger data together with expected flux for exotic models and GZK photon. Right: Neutrino flux limit reported by Auger, IceCube Anita and Rice compared to the expected flux of cosmogenic neutrinos and produced from exotic models. (Both from [39])

that the separation between proton and iron is less than 100 g/cm^2, the hadronic interaction parameters are crucial to interpret correctly the mass composition measurements.
Furthermore, the cosmic ray flux is a unique ultra high energy beam and offers the possibility to study interaction at collision energy in center of mass up to $\sqrt{s} \geq 50$ TeV, well beyond the current accelerators possibilities. The proton-air cross section has been measured with Auger cosmic ray events [37] with energy from 10^{18} to $10^{18.5}$ eV corresponding to an average energy in center of mass of 57 TeV. The study is performed at an energy where mass measurement indicate a light composition. Then the proton-air cross section is extracted from the shape of X_{max} distribution and selecting the most deeply penetrating air showers. Proton proton cross section, shown in Fig. 1.14 can be deduced based on Glauber model [38] and agrees with extrapolation from accelerator measurements.

Photon and neutrinos

UHECR are known to be mainly protons or heavier nuclei. Secondary particles from interactions they undergo during their production or propagation can point to their origin. For instance, in the GZK process, charged pions decay in neutrinos, and neutral pions decay in two photons.
When entering the atmosphere, photons interact inducing an electromagnetic cascade which is expected to penetrate deeper than hadron induced shower of the same energy (see section 1.2). Moreover, above 10^{19} eV the LPM (Landau-Pomeranchuck-Migdal) effect decreases the pair production cross section, further increasing the depth of shower maximum. So X_{max} measurements are well suited to discriminate hadronic from electromagnetic shower. In addition, SD observables like the radius of curvature of the shower front can be used to discriminate between hadronic or photon air shower.
No photon event have been observed so far by any experiments and upper limits to the flux are thus derived. Limits given by Auger data are shown in Fig. 1.15 with the flux expectation for model accounting for GZK effect and more exotic models.
In the same way, GZK process or top down models are expected to produce neutrinos, but

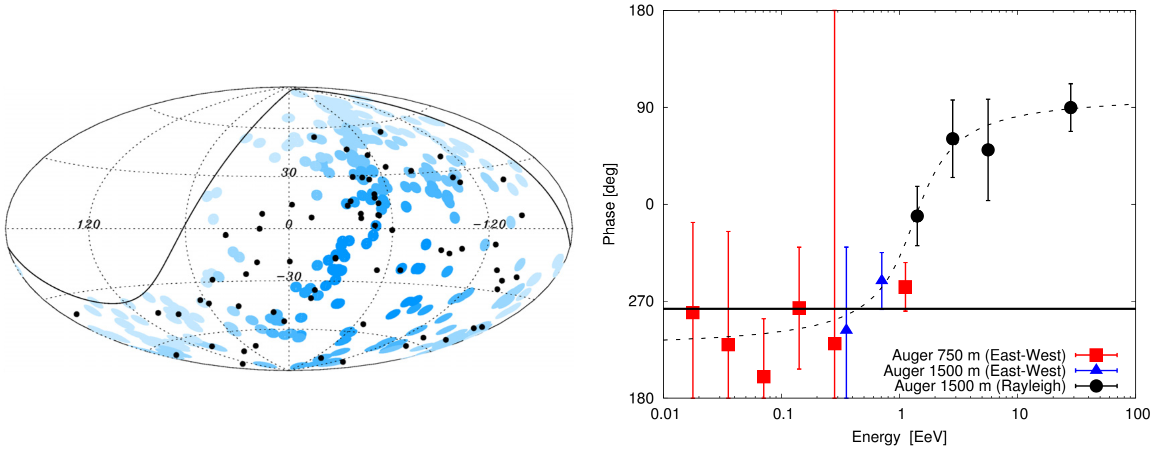

Figure 1.16: Left: Sky map (in Aitoff-Hammer projection of the sky in galactic coordinates) of events above 55×10^{19} eV (black dots) with the sources reported in the Veron-Cetty Veron catalogue (blue dots), the shades of blue represent the relative exposure of the Pierre Auger Observatory in the corresponding direction. (from [46]). Right: Phase of the first harmonic of the development in Rayleigh analysis of the right ascension of events as a function of energy. (from [47])

contrary to photons, they undergo no interaction during their propagation to Earth and the distance they can cover is only limited by adiabatic losses.

All flavors of neutrino reach the Earth with an equal probability because of oscillation, and can either interact with atmosphere (down going neutrinos) or in the crust of the Earth (up-going neutrinos). In Auger data, the signature for a neutrino event is a very inclined event produced by a young shower, i.e. developed close to the ground by contrast with inclined hadronic shower that traversed lots of matter before reaching the ground. Constraints on the topology of an air shower event are put to admit it as a neutrino candidate. For instance, the Pierre Auger Collaboration imposes that the footprint of an event on the surface detector array to have a certain ellipticity set by Monte Carlo simulations. The traces themselves are used to distinguish between young showers, with a trace waveform spread in time, and old showers whose content, mostly muonic, produce a short and sharp signal in the water Cherenkov detectors [40].

Dedicated observatories like IceCube [41] or Antares [42], instrument respectively large volume of ice and water to obtain a large exposure. In Fig. 1.15 (right) is illustrated the neutrino flux limits quoted by Auger, IceCube [43] and Anita [44] and Rice [45] experiments together with the flux expected for cosmogenic neutrinos, and exotic models.

Anisotropies

Cosmic ray anisotropy search may help at spotting either point source or region of CR production. The angular scale on which anisotropy is expected depends on the Larmor radius of the CR that can be written as:

$$r_L = 100 \left(\frac{1}{Z} \frac{E}{10^{20} eV} \left(\frac{B}{10^{-9} G} \right)^{-1} \right) [Mpc]$$

Calculations with random extragalactic magnetic field of magnitude of the order of nG and coherence length of 1 Mpc, yield an angular deviation of around 2 ° for a proton from a 20 Mpc distance [48]. Such small scale of angular deviations open the possibility of tracking back sources for light composition and for sources close enough. Auger data provided a signature for a correlation between the arrival direction of events with energy above 5.7×10^{19} eV with sources of the Veron Cetty Veron catalogue [49]. In the first published result [50], 20 out of 27 events were found to be within 3.1 ° angular distance from AGN within distances lower than 75 Mpc. This correlation has become weaker now and has stabilized at a level of $(33\pm5)\%$ compared to 21% for isotropic expectation. The sky map of the selected events the sources for the correlation studies are presented in the sky map Fig. 1.16 (left).

At lower energy one cannot track back directly sources because of the scattering of particles on the galactic magnetic field. However, anisotropies at larger angular scales are expected if source distribution is not isotropic in the Galaxy. Moreover, if cosmic rays escape from the Galaxy with increasing energy, because of a larger Larmor radius, this may be also visible through structure in the arrival direction distribution. The level of expected anisotropy in this case is of the order of a few % for protons. Since the flux of cosmic ray observed in any direction is distorted by the coverage function of the observatory, it is critical to control accurately both the coverage function and any systematic uncertainties influencing the counting rate above a fixed energy threshold, especially when searching for anisotropies with relative amplitudes down to the % level. Detailed studies performed in Auger data can be found in [51]. Upper limits of 2% at 99% confidence level on a dipole component in the equatorial plane have been derived for energies around 10^{18} eV [52] and no deviation from isotropy were found in dipole or quadrupole search in both declination and right ascension. But an interesting feature was observed: right ascension of the dipole direction are smoothly aligned with energy and point toward the galactic center below 10^{18} eV. In Fig. 1.16 is reported the phase of the first harmonic of the distribution of arrival directions in right ascension of cosmic rays measured in Auger. The phase at low energy corresponds to the direction of the Galactic center represented by the black horizontal line.

1.4 Models at ultra high energy

Top down models were considered until the last decade as potential mechanisms to produce UHECR. Most of them have been ruled out by the limits on photons and neutrinos in particular given by Auger data.

To explain the spectral features observed on Earth and the mass composition, current models adopt a source distribution, assume a composition at the source and account for propagation effects.

Around the knee region, cosmic ray are believed to be of galactic origin. They are assumed to be accelerated by the shock wave produce by Super Novae Remnants (SNR). This idea was raised by Baade and Zwicky [53] and later by Ginzburg and Syrovatskii [54] on the argument that only 5 to 10 % of the kinetic energy of the SNR converted into cosmic ray acceleration would be enough to explain the energetic content of galactic cosmic rays. The common explanation for the knee is related to the limited acceleration in galactic sources.

At ultra high energy, cosmic rays are in contrast expected to be of extragalactic origin, firstly because astrophysical sources within our Galaxy are not likely to produce them but also because arrival distribution of cosmic rays above 10^{19} eV don't show the strong anisotropy that would induce close sources. The region around the ankle energy is expected to be the transition region between the Galactic and the extra galactic origin of cosmic rays. Currently three main models are proposed to explain the observational results at ultra high energy:

the ankle model In this model the ankle is assumed to be a transition from Galactic to extragalactic origin of cosmic rays [55]. The end of the Galactic spectrum is dominated by iron composition, and an extragalactic proton component arises at the ankle energy.

The measurements of a light composition from 10^{18} to $5{\times}10^{18}$ eV is in contradiction with the heavy Galactic component expected, and the trend toward heavier primaries do not support the extragalactic proton component. Moreover, in frame of this model, anisotropies are expected below the transition because of anisotropic distribution of galactic sources and the loss of confinement. Thus, the limits on the dipole structure at energies around the ankle may discard in the future this model.

the dip model This model, proposed in [56], assumes a dominance of extragalactic protons already at $E = 10^{18}$ eV. The ankle is explained to be part of the dip created by the e^+/e^- production by interaction of proton on CMB. The cut off is a consequence of the pion photo-production.

This model is in agreement with the spectral shape observed between 10^{18} and 10^{19} eV. It is also more compatible with mass composition measurements, as it explains the increase of $< X_{max} >$ from 10^{17} to 10^{18} eV with the extragalactic proton component. However, it is not compatible with a heavy composition at higher energy as deduced with the Auger X_{max} data.

the disappointing model In this model cosmic ray below the ankle are already dominated by extragalactic protons. The ankle feature is in fact the upper limit of acceleration of extragalactic proton. At higher energy, the composition is expected to be dominated by nuclei accelerated to an energy proportional to their atomic number Z. The cut off of the spectrum is attributed to an exhaustion of sources. This model predicts no GZK cut-off and

no cosmogenic neutrinos.
It was actually proposed in [57] to explain Auger spectrum and composition but there remains difficulties to explain the ankle shape.

We saw that, at ultra high energy, results of different observatories agree on an ankle feature around 4×10^{18} eV and a cut off at the end of the spectrum. The interpretation in term of source model and propagation is not clear yet. If most of the top down models were excluded, it remains still three main scenarios. If the spectral features can be explained by these scenarios, we see that the mass composition together with anisotropy measurements can support or discard the different models.
Currently, the mass measurements are performed mainly with optical measurements with a limited duty cycle. The goal of the developments presented below is to extend the mass composition measurement to a 100% duty cycle using radio technique and to do it on an event by event basis rather than with a statistical analysis done up to now .
We describe in the following chapter how an extensive measurement of the composition help in a consistent understanding of the air shower measurements presented above and how the radio technique and its implementation with EASIER could reach this goal.

Chapter 2

EASIER

EASIER With EASIER, Extensive Air Shower Identification using Electron Radiometer, we intend to detect extensive air shower radio signal in a complementary way to the Pierre Auger surface detector. The radio detector is integrated with the water Cherenkov tank, and while the latter triggers at the passage of particles at ground, the former is recording the radio emission from the air shower. The measured radio profile will provide a calorimetric measurement of the electromagnetic shower and two key informations for mass discrimination: firstly the depth of shower maximum development directly related to the primary composition, secondly and more indirectly the muonic signal at ground deduced by subtraction of the electromagnetic component to the total signal recorded by the particle detector.

We first describe the scientific motivation for a combined detection of particles at ground and the shower development with a large duty cycle. Then we report a status of the radio detection in the two frequency bands explored by EASIER and justify the detection principle. This will lead us to the definition of the necessary characteristics of the detector in the last section.

2.1 Scientific motivation

As stressed out in the first chapter, some fundamental questions remain open in the overall picture of UHECR. An extensive measurement of composition above 10^{19} eV would be of great help for a coherent interpretation of the current results. Moreover, it would enhance our capability to address fundamental question on particle interaction and transport at the highest energies.

Current methods of detection access to mass sensitive parameters on a statistical basis. On the one hand fluorescence technique allows a precise measurement of the electromagnetic cascade development. The distribution of the depth of maximum development at a given energy supplies two indicators of mass through the average and the standard deviation. However, the fluorescence light from air showers can only be detected during 10% of the time and its diffusion in atmosphere depends largely on weather conditions imposing a constant monitoring and reducing even more the duty cycle. On the other hand, the surface detector is indirectly sensitive to mass as it samples the shower only at one stage of development. Recent studies could extract indirect observables to access the time evolution of the shower with the surface detector, for instance the time distribution of the FADC trace can be used to infer the azimuthal asymmetry of the signal rise time in the SD or the muon production depth [58] that both carry information on the longitudinal development. These observables allow to reach higher energies than FD measurements because of the SD large duty cycle. However, in both cases, the shower to shower fluctuations prevent the estimation of the primary mass on an event by event basis.

A better constrain on the primary mass is obtained with the measurement of the longitudinal development together with another mass sensitive observable such as the number of muons at ground. The additional information carried by a concomitant measurement of these observables would allow an event by event mass assignment and therefor progress to be made on the following issues:

– mass composition and hadronic interactions
  A combined measurement of electromagnetic evolution and the muonic content at ground would constrain the composition of the primary based on the intuitive idea, also supported by most up to date simulation, that light primary nuclei induce deeply penetrating and muon poor showers whereas heavy ones lead to shallow and muon rich showers. Simultaneous measurement of these two anti-correlated observables will supply a separation power between light and heavy nuclei on an event by event basis. Moreover, as X_{max} and S_μ are sensitive to parameters such as cross section, multiplicity and inelasticity of the first interactions, a deviation from this anti-correlation would indicate the presence of new phenomena at the highest energies.

– Cross section:
  Nowadays, the study of the interaction of the cosmic ray beam with the atmosphere nuclei remains the unique way to reach collision energies above tens of TeV in center of mass. Latest published results on proton-air cross section [37] reported a measurement at 57 TeV well above the LHC maximal collision energy. The performed analysis relies on the X_{max} distribution shape, and the uncertainties that would induce a mixed composition requires stringent cuts on this distribution. The separation power provided by the simultaneous measurement of X_{max} and S_μ will improve the proton purity of

the data set, while a 100% duty cycle will allow to access cross section measurement at $\sqrt{s} = 100\,\text{TeV}$ or more.

- Neutrino and photon:
  If present at the highest energies, photons and neutrinos are known to be rare events. Their search requires a precise characterization of the air shower to distinguished them from nuclei induced shower. Indeed, the shower induced by a neutrino interaction in air or earth is expected to be nearly horizontal and dominantly electromagnetic. In contrast, an horizontal shower induced by a nuclei is in an old stage of development when reaching the ground, and is muon dominated. In current analysis the tagging of the “young showers” is achieved thanks to severe conditions on the signal shape. A direct measurement of the shower age would extend the angular range where a neutrino shower would be unambiguously discriminated from an hadronic one. In the same way, ultra high energy photons, whose main features are a deeply penetrating and purely electromagnetic shower, could be more efficiently distinguished from hadronic background with a measurement of electromagnetic cascade with a 100% duty cycle. In fact, photon search is now performed either with the limited hybrid data set or using SD events after selection procedure reducing sensitivity. A detection of ultra high energy photon or cosmogenic neutrino would be a clear signature of GZK effect.

- Anisotropies and magnetic fields.
  Finally, the measurement of shower development at the highest energies would allow to correlate their arrival direction with catalogues of nearby sources accounting for different mass composition. As the magnetic field deflection increases linearly with the atomic number Z, a subsample of light primary showers would enhance the power of correlation. Moreover, if acceleration mechanisms at source are rigidity dependent, with the simultaneous observation of primary mass and energy, one could determine acceleration limits as a function of mass and relate them to spectral features. Let us point out also that information on galactic and extragalactic magnetic field could be retrieved relating the angular scale of correlation with mass.

In the current configuration, the surface detector of Auger samples the total particle signal at ground. The longitudinal development is not directly measured and the muonic component at ground is mixed with the electromagnetic one. It has been stated [59] that after the shower maximum, the EAS development is the same for all showers. One can understand intuitively this behavior noticing that after the number of particles in the shower can rise up to 10^{10} at the maximum development, the collective behavior can be described globally only with a few parameters like the geometry of the shower, its energy and the depth of maximum development. In experimental terms, the collected signal at ground can be parameterized with universal functions of these variables. For instance in reference [60] the total signal at ground is expressed as follow :

$$S(E,\theta) = S_{em}(E,\theta,< X_{max} >) + N_{\mu}(E) \cdot S_{\mu}(\theta,< X_{max} >) \tag{2.1.1}$$

where S_{em} and S_{μ} are universal functions (i.e. independent of hadronic interaction models and of primary mass) of the parameter mentioned above and N_{μ} is the normalization of the muon number at ground. Given the parameterization above and the reconstruction of an air shower by the SD, a measurement of the longitudinal development would entail the recovery

of the muon number as well.
The radio detection is a promising technique since it may give access to the electromagnetic cascade development with almost 100% duty cycle.

2.2 State of the art of radio detection

VHF band

Electromagnetic emissions in VHF band from cosmic ray air shower were detected almost 50 years ago in 1965 by Jelley and collaborators [61]. It was first suggested that the Cherenkov emission, already detected in optical domain could be also detectable at lower frequencies. In 1962 Askaryan [62] pointed out that in dense medium, the negative charge excess arising from the accumulation of Compton scattered electrons and positron annihilation could lead to a coherent Cherenkov emission at lower frequencies than optical ones. The first experiment was installed at the Jodrell Bank Radio Observatory and operated 72 receivers tuned at 44MHz in an array of $1800\,m^2$ in coincidence with three Geiger-Müller counters. It successfully detected cosmic rays in that band. Several experiments were operated in the following decade, at different frequencies from a few MHz to 3 GHz. In parallel, another possible mechanism due to charge separation in the earth magnetic field was suggested. It was already noticed by Askaryan and further developed by Kahn and Lerche [63] that the deflection of positive and negative charged particles of the shower could lead to an electric dipole and a transverse current. Firstly, particles of opposite charge emit a radiation in opposition of phase that cancels out, however if they are separed in space the phase difference is shifted by a factor d/λ where d is the distance of separation and λ the wavelength of observation. As the charge separation increases or the wavelength of observation decreases, the cancellation disappears. Secondly, from the constant deflection of the charged particles at each generation in the air shower arises a transverse current acting as a source of magnetic field. When this element of current is moving faster than the speed of light in the considered medium, a shock wave is produced and the radiation is amplified. Regardless of the mechanism, a coherent emission occurs only if the characteristic length of the shower front are small compared with the wavelength of observation. The calculation made by Kahn and Lerche with a simple model showed that the dominant process should be the transverse current. A review by Allan [64] in 1971 gives an overall picture of the radio detection at that time on the experimental point of view as well as theoretical. On the experimental side, during the 1960s several experiments detected radio pulses at frequencies ranging from a few MHz to hundreds of MHz. The radiation mechanism could be tested comparing the rate of detection with the orientation of the arrival direction with the direction of geomagnetic field. Some polarization measurement were also performed and most of the experiments agreed on a geomagnetic origin. The coherence of the emission, i.e. its dependence with the shower size is more difficult to figure out since other geometrical factors come also into play, different experiments found either almost no dependence with the number of particle N, either an incoherent emission $E \propto N^{1/2}$ or a coherent one $E \propto N$.
Allan summarized the results obtained from the radio experiment operated at Haverah Park in the following expression of the electric field :

$$E_\nu = 20\,\left(\frac{E_p}{10^{17}}\right)\,\sin\alpha\cos\theta\exp\left(-\frac{R}{R_0(\nu,\theta)}\right)\;\mu\mathrm{Vm}^{-1}\mathrm{MHz}^{-1} \tag{2.2.1}$$

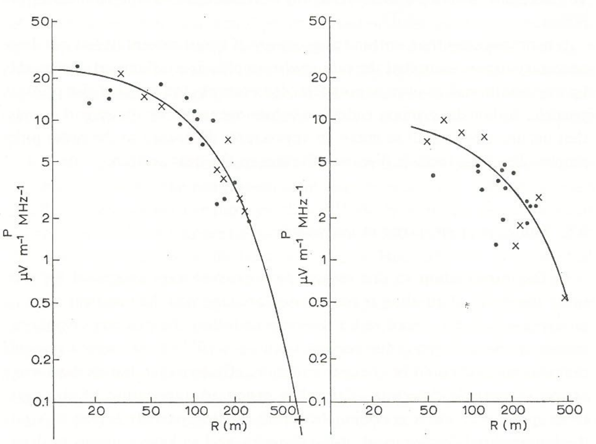

Fig. 24. Normalised radio pulse amplitude, P, at 55 MHz as a function of distance R from the shower axis. The normalisation is carried out assuming the amplitude is proportional to the total shower energy E_p and to the sine of the angle made by the shower axis with the earth's magnetic field. The ordinate gives the field strength in $\mu V\, m^{-1}\, MHz^{-1}$ for a shower of total energy 10^{17} eV moving perpendicular to the earth's field.
(a) zenith angle $\theta < 35°$; ● shower energy $10^{17} < E_p < 3 \times 10^{17}$ eV, × shower energy $3 \times 10^{17} < E_p < 10^{18}$ eV, + $E_p = 1.5 \times 10^{19}$ eV.
(b) zenith angle $35° < \theta < 50°$; × showers with $35° < \theta < 42°$, ● showers with $42° < \theta < 50°$.

Figure 2.1: from [64]

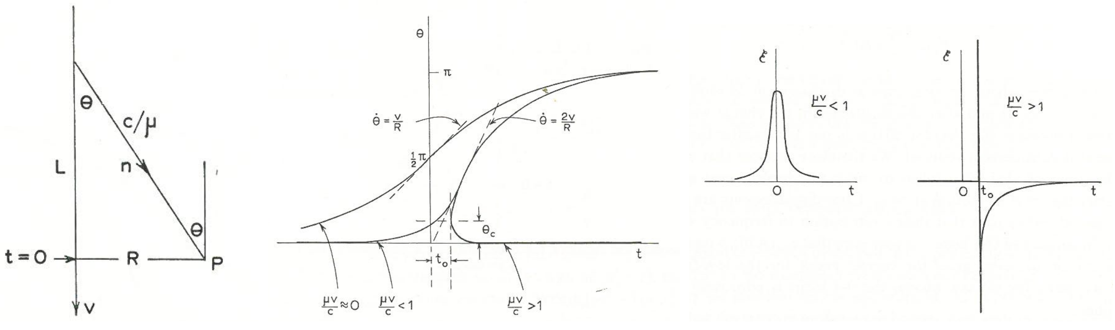

Figure 2.2: Left : The charge e is moving at velocity v. Middle: apparent angle of observation as a function of time for $\mu v/c << 1$, $\mu v/c < 1$ and $\mu v/c > 1$. Right: electric field wave form for $\mu v/c < 1$ and $\mu v/c > 1$.(from [64]).

where α is the angle between arrival direction and geomagnetic field direction, θ the zenith angle, R the distance to shower axis. The parameter R_0 was found to be (110 ± 10) m at the frequency $\nu = 55\,\mathrm{MHz}$ and with rather vertical shower $\theta \leq 35°$. By measuring the ratio of the two polarizations N-S and E-W, it was proved that the dominant emission mechanism was dependent of the geomagnetic field. It is represented in Eq. 2.2.1 by the term $\sin\alpha$. The electric field is found to be proportional to energy and its lateral distribution, shown Fig. 2.1, to decrease exponentially. It was also noticed that the factor R_0 increases with the zenith angle but also as the frequency of observation is reduced. To understand qualitatively these experimental results, Allan gives an intuitive derivation of the electric field produced by an air shower and observed at ground.

We first derive the electric field for a test charged particle and then we see how a more realistic situation modifies it. Based on the formula given in Feynman's lecture [65], the electric field radiated by a electric charge in motion reads :

$$E = \frac{e}{4\pi\epsilon_0 c^2} \cdot \frac{d^2\theta}{dt^2} \tag{2.2.2}$$

where $\frac{d^2\theta}{dt^2}$ is the angular acceleration of the charge e as it would appear to an observer where the field is evaluated. This formula stresses the importance of geometry in the electric field observed. For a test particle and a simple geometry as shown in Fig 2.2 left, taking the refractive index into account, the time the observer in P receives the radiation emitted at t_{em} from the source coming from the angle of observation θ reads:

$$t = t_{em} + \frac{r}{c/\mu} = -\frac{L}{v} + \frac{r}{c/\mu} = -\frac{R}{v\tan\theta} + \frac{R}{(c/\mu)\sin\theta} \tag{2.2.3}$$

where μ is the refractive index and the origin of time of emission is taken when the particle is at the same height as the observer (i.e. $t_{em} = -L/v$). It is clear from this equation that for an observer on the particle track and under the condition $v = c/\mu$ all the radiation emitted along the track arrives at the same time t = 0. The evolution of θ as a function of time retrieved from Eq. 2.2.3 is plotted in Fig 2.2 right. In the case $\mu v << c$ the bearing of θ is following $\tan\theta \propto 1/t$. For air shower the speed of the shower front is close to c, in that case the signal is compressed in time, the radiation from a wide range of θ is seen in a short time interval. One should notice the interesting behavior for a refractive index greater than 1, in this case, the radiation observed at a given time arises from two different parts of the particle track (shower development) and the second derivative of θ or the electric field diverges at the Cherenkov angle. The corresponding pulse shape, is shown in the same figure in the right hand plot. In this simple model, the electric field pulse is a delta function because a finite electric field reaches the observer in an infinitely small time interval.

To account for a more realistic situation, the simple model presented above has to be replaced by a vectorial summation over the shower particles individual fields. In the case of geomagnetic deflection, the changes in apparent angle are aligned with the direction of the Lorentz force and sums up arithmetically and Eq. 2.2.2 becomes :

$$E = -\frac{1}{4\pi\epsilon_0 c^2} \cdot \sum e \cdot \frac{d^2\theta}{dt^2} \simeq -\frac{1}{4\pi\epsilon_0 c^2} \cdot \sum \cdot \frac{d^2[N|e|(\theta_+ - \theta_-)]}{dt^2} \tag{2.2.4}$$

In that case, the electric field evolves with the number of particles and the angular separation of positive and negative charges as seen from the observer. In addition, in realistic condition the shower front has a physical extension caused by the lateral scattering and longitudinal lag of particles that depend on their energy distribution. Here has to come into play a realistic model of shower development. However, one can understand that the electric field pulse shape will be driven by the evolution of $n \cdot \theta = N|e|\ (\theta_+ - \theta_-)$ at the beginning of the shower development where the second derivative is maximum as shown in Fig 2.3. A shower observed near the Cherenkov angle will induce a short and intense pulse and the compression in time will also increase the frequency seen by the observer. The length of the total pulse on the other side limits the low frequencies present in the electric field pulse. We can now understand qualitatively that the pulse shape and its spectral features depend not only on the shower characteristics like its energy and its depth of maximum development but also on the angle from where it is observed.

The important decrease of the electric field with the distance in addition with the influence of many parameters on it, made the prospects for this technique rather pessimistic. Moreover,

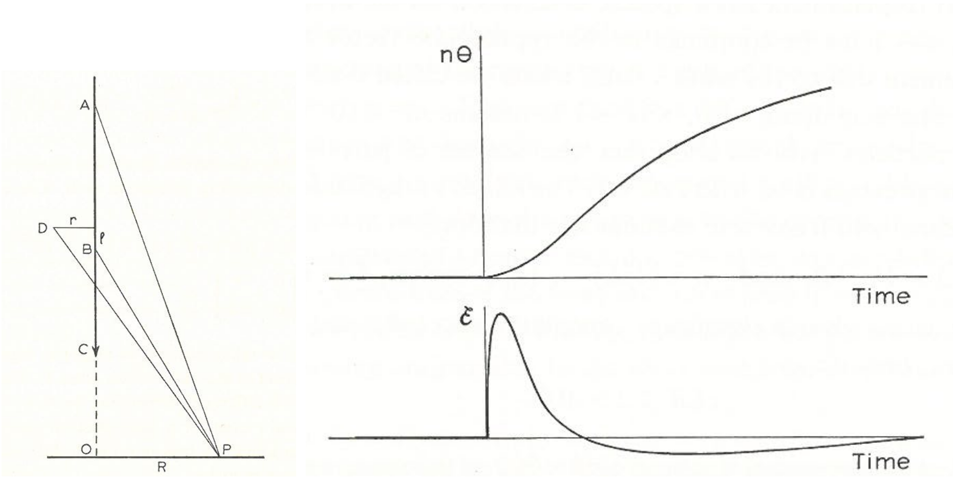

Figure 2.3: Left : Vertical air shower. due to lateral dispersion and longitudinal lag of the shower particle the observer sees radiation from the different part of the shower at the same time. Right: Evolution of the quantity responsible for the electric field at ground. The kink at t = 0 is smoothed out due to a realistic shower development. The corresponding pulse don't show anymore a δ function shape.

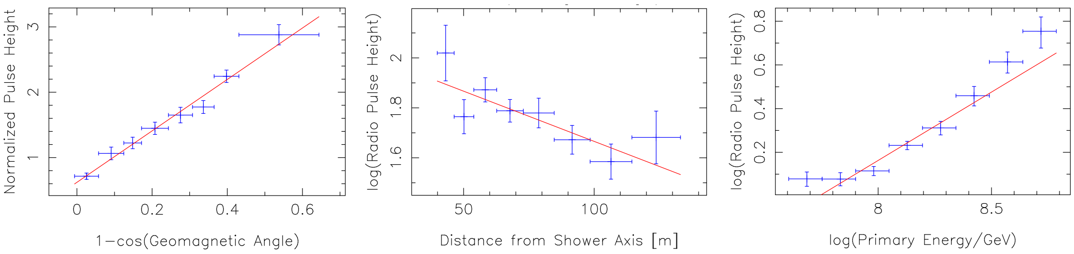

Figure 2.4: Calibration results in [69] in LOPES. Normalized pulse height as a function of geomagnetic angle, distance to shower axis and energy. The parameters are fitted separately, the normalization is done dividing by the fits of other parameters.

the development at that time of other techniques such as fluorescence detection made the development of radio detection of secondary importance.

A renewed interest was raised at the beginning of years 2000 with the need for an increased aperture at ultra high energy and the progress in low noise electronics and data processing. Compared to the pioneering experiment of the 1960s, the modern experiments, like CODALEMA [66] or LOPES [67,68] operate with a larger bandwidth between the AM band and FM band. Some important progress have been made also in amplification electronics and data processing capabilities. CODALEMA has known several phases since 2003. Installed in a radio protected environment in Nancay (France) it is now composed of an array of 24 short active dipoles antenna operating in coincidence with 17 plastic scintillators. CODALEMA is also operating a stand alone array of 60 radio detectors covering 1.5 km^2. Each detector is composed of a dual polarization butterfly antenna and a embedded electronics. LOPES (LOFAR PrototypE Station) uses also an external particle trigger from the KASCADE array. It has been operating since 2003 and in its last upgrade is composed of 30 tripole antennas, thus measuring the 3 polarizations of the radio signal. At the Pierre Auger Observatory, an

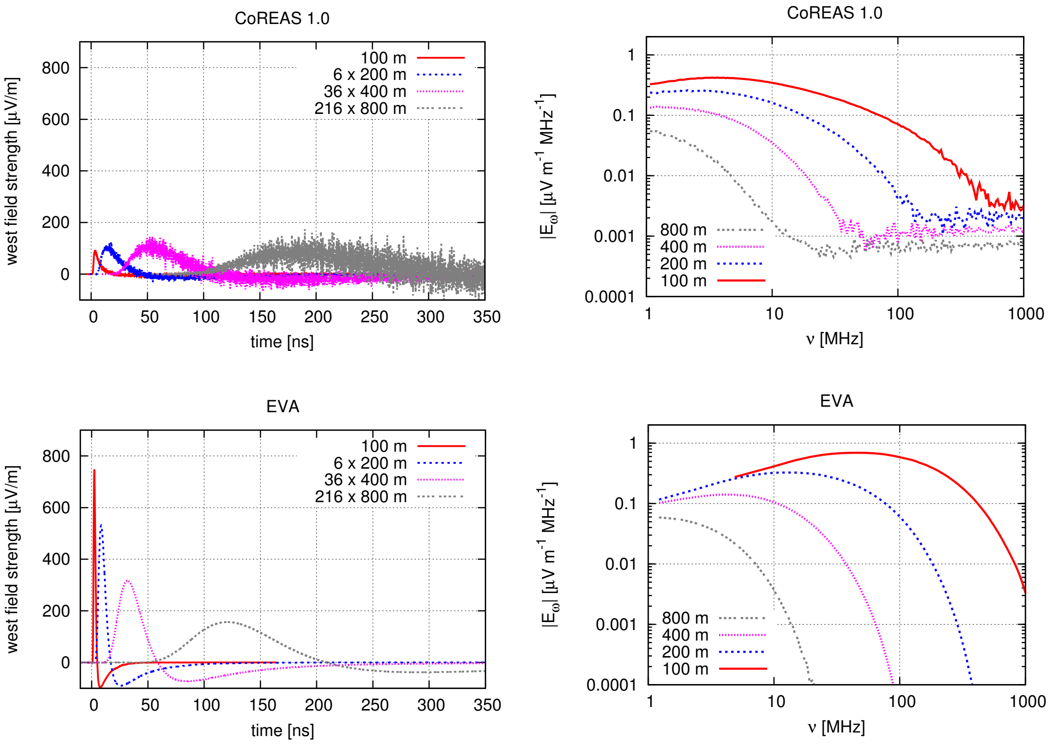

Figure 2.5: Electric pulses and spectra for a proton induced vertical shower of 10^{17} eV at different distances and for a two different models CoReas and EVA (in [71]).

effort was lead to built an array of stand-alone radio detector, the most recent upgrade, to be completed in 2013, is an array of 161 dual polarized antenna self triggered and covering 20 km^2.
The forementioned experiments have confirmed some of the bearing predicted by theory and hinted by the first experiments, namely a dominant emission mechanism induced by the geomagnetic field and exponential decay of the electric field with the distance to the shower axis. Fig 2.4 collects LOPES parameterization results showing separately the influence of the parameters pointed out in Allan's formula. Recently, the contribution of the charge excess mechanism was also detected in AERA data thanks to polarization studies and in CODALEMA data measuring a shift between the core location reconstructed by particle detector and radio detector. The latest experimental results in the VHF band can be found in [70].
Along with the development of experimental techniques in detectors and data analysis, progress in simulation have been performed too. The most recent algorithm uses either a "microscopic approach" applying classical electrodynamics equation to shower particles without assumption on the underlying emission mechanism, or a "macroscopic approach" where the field is calculated from features of the air shower such as current, net charge or dipole moment. A review and comparison of these recent works can be found in [71]. In general, the microscopic models agree with each other but a quantitative difference is found between microscopic and macroscopic model especially close to the shower axis. Fig 2.5 illustrates simulations of the electric field pulse and spectrum at different distance from the

shower axis and for two different models CoReas [71] and EVA [72]. The qualitative pulse shape corresponds to the one calculated with the simple model by Allan, close to the shower axis the electric field is compressed into a short pulse and the spectrum extends at higher frequencies.

In conclusion, the early experiments showed the presence of an emission from EAS leading to a pulse in the VHF band. The most recent ones, with enhanced technologies in acquisition and data post processing, could characterize this pulse signal and compare it with complete simulations. In both cases the dominant emission process was found to be of geomagnetic origin and the lateral extension of the electric field measured to fall exponentially with the distance to shower axis because of a loss of coherence. For this reason the size of the radio arrays remained too small to be able to study the signal at the highest energy. The need of a large aperture to reach the highest energies and the characteristics of the observed signal at lower energies lead to two different options: on one side the installation of a large array able to self trigger on radio information. This path is followed by the AERA setup. It requires a dense spacing to obtain a signal large enough to trigger on and to be efficient at all angle knowing the geomagnetic effect on the radio signal. Moreover, the transient noise is important in this band and is a source of spurious events therefore advanced functions of triggering are needed to select physical events. The other possibility, followed by EASIER is to equip with radio detector an existing particle detector taking advantage of the trigger it delivers. The asset of this method is to lower the required signal to noise ratio to use a radio signal, since there is no need to trigger. Nonetheless this method requires a signal sufficiently intense from the air shower at large distance i.e. where the coherence is lost.

Microwave band

At higher frequencies, the spectrum of air shower emission from individual particle is expected to fall down. However, it was noticed that free electrons, products of ionization induced by the air shower, could interact with neutral molecules of air and produce continuum Molecular Bremsstrahlung Radiation (MBR). This radiation would be unpolarized and emitted isotropically, thus would be a tracker of the shower development in the atmosphere just as the fluorescence emission in the optical domain. Two experiments, one at Argonne Wakefield Accelerator (AWA) and one at the Standford Linear Accelerator Center (SLAC), described in [73] were carried out to figure out if this emission had sufficient intensity to be detected in air shower experiments. In these two experiments, whose setup is illustrated on scheme Fig 2.6 left, a shower is induced by an electron beam in an anechoic chamber and the microwave radiation is detected by antennas. This measurement requires a great care to limit radiation from the electron beam itself. The intensity detected and averaged over 100 shots in the band 1.5 - 6 GHz is shown Fig 2.6 right, it extends out to more than 60 ns above the noise level. As the transit time of the shower in the chamber is less than 4 ns, the origin of the emission is assumed to come from the cooling of the plasma induced by the passage of the shower.

The power recorded in the receivers was found to increase quadratically with the beam energy. The quantitative interpretation of the signal observed is difficult. Indeed, the emission depends on the electron velocity distribution in the plasma. On one side, a suppression of the radiation due to destructive interference in the radiation zone can lower the total emission and is velocity dependent. On the other side, several enhancements of the emission can occur

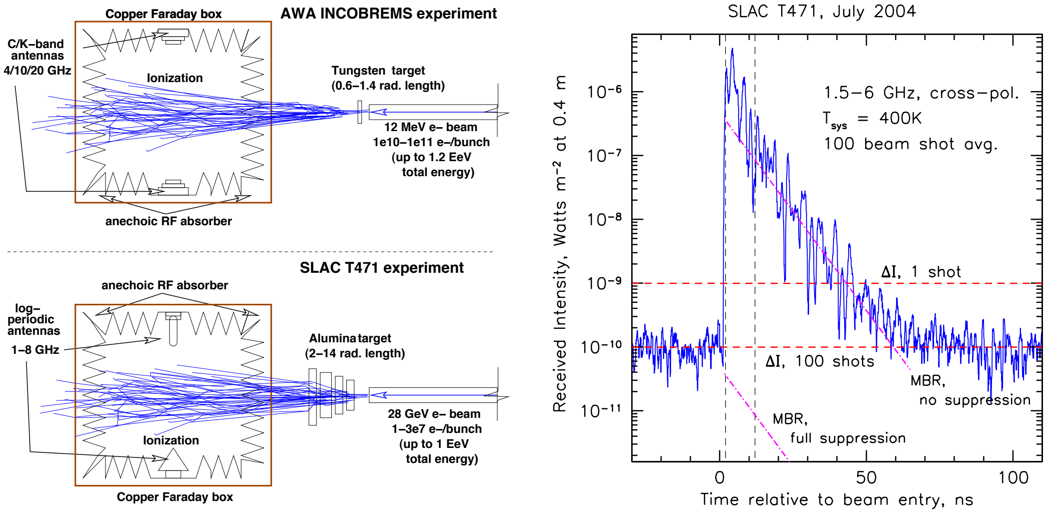

Figure 2.6: Left: setup of AWA and SLAC experiments. Right: Intensity of microwave signal detected after the passage of showers.

because of a non thermal distribution of the electrons of the air shower.

Based on the measured signal in beam experiment, the signal measured was scaled to air shower parameters. The expected flux density from an air shower of energy $3.36 \cdot 10^{17}$ eV at 10 km away from the receiver is found to be $I_{exp} = 2.77 \cdot 10^{-24}$ W m^{-2} Hz^{-1} [73]. In the case of a quadratic scaling with energy, the signal of an air shower above 2 EeV would be easily detectable. Even is the case of a linear scaling, it is stated that a 30 EeV air shower could be observed at $\simeq 20$ km with a radio telescope. This exciting result triggered several detector developments, starting with AMBER [73] (Airshower Microwave Bremsstrahlung Experimental Radiometer) first installed at the University of Hawaii, it is now operated at the Pierre Auger Observatory at the Coihueco fluorescence building. The radio sensitive part is an off-axis parabolic dish viewed by 4 dual band (C-band 3.4-4.2 GHz and Ku-band 10.9-14.5 GHz) and dual polarized horn antenna and 12 other C-band single polarized horn antenna. AMBER uses a modified version of the surface detector trigger at the T3 level to perform a fast reconstruction of the possible air shower and retrieve the time at which the shower crossed its field of view. The corresponding radio data are recorded.

The MIDAS experiment [74, 75] (MIcrowave Detection of Air Showers) is also an imaging radio telescope. It is equipped by a 5 m parabolic dish and a 53 pixels receiver camera. MIDAS detector, first took data at the University of Chicago, and is now installed at the Pierre Auger Observatory. MIDAS group has developed a trigger based on a first level trigger on each pixel and a second level trigger searching for air shower pattern. The microwave efforts at the Pierre Auger Observatory are described in [76]. Another prototype, installed at the KASCADE Grande site, named CROME [77] for Cosmic Ray Observation via Microwave Emission, is also a radio telescope working in the C-band.

In parallel, two beam experiments were setup to confirm and characterize the emission observed in SLAC experiment: MAYBE (Microwave Air Yield Beam Experiment) [78] at Argonne National Laboratory uses a electron beam below the Cherenkov threshold to prevent Cherenkov radiation from the beam, and AMY (Air Microwave Yield) at the beam test facility of the National Laboratory of Frascati which uses as an electron beam a LINAC, similar to the

one used in SLAC experiment. For the moment, the results were not confirmed, particularly the quadratic scaling with energy was not observed with MAYBE [79].
The emission in microwave band observed in SLAC had an intensity that once scaled to air shower can be detectable. The underlying process is not yet fully understood and the spectral features of this emission are not measured. The confirmation of an isotropic emission would lead to the development of a new technique of EAS observation. However, recent beam experiment didn't reach the same conclusion as the first ones. The uncertain value of flux coming from air shower and its dependence with energy makes a coincident detection crucial to determine the characteristics of this emission. In this scope the principle of EASIER is well suited. Firstly the combined detection with the SD lowers the signal to noise ratio needed to claim a detection. Secondly, as EASIER observes the shower from the ground, if the emission is not completely isotropic but beamed in the forward direction of the shower, it remains detectable. The key parameter is once again the maximum distance at which a radio signal can be detected.

2.3 EASIER Detector

We saw the assets of a combined detection on the physics point of view as it lead to a multicomponent information on the shower, but also on the technical side because it permit to avoid triggering issues. We present here the general requirements of the EASIER detector led by its integration in the surface detector unit of Auger.

Auger SD unit

The EASIER radio system is integrated into the surface detector units of the Pierre Auger Observatory. Integration represents a clear asset but sets also constraints in terms of mechanical integration, electromagnetic compatibility and acquisition.
The SD station, pictured in Fig. 2.7, is a cylindrical tank made of polyethylene plastic with a base of 3.6 m diameter and a height of 1.55 m. Inside, a liner is filled with 12 tons of purified water (of resistivity 5-15 MΩcm). The Cherenkov light produced at the passage of particles in the water is collected by three 9 inches PMTs (Photonis XP1805). The PMT base has two outputs, one from the anode (low gain channel) and the other one from an amplifier connected to the last dynode (high gain channel). The overall gain ratio between the two outputs is around 32 and they are both transmitted to the acquisition electronics. The electronics, located under a metallic dome on top of the tank, is composed of a Unified Board (UB) which is a motherboard with CPU and memory that performs all the logics between the Front End, the time tagging and the communication unit. PC operating at The local electronics perform the local triggering, and transmit the data trough the communication antenna to the closest FD stations which in turn transmits them to the central acquisition. The SD station is powered by a 24 V battery charged by two solar panels. The power supply of the station is controlled by a specific electronic board, the Tank Power Control board, (TPCB).

Mechanics The EASIER mechanics has to fit into the components already on the tank. The top of the tank presents little flat surface area. The EASIER mechanical installation will have to take advantage of this surface or to be installed on the side of the tank.

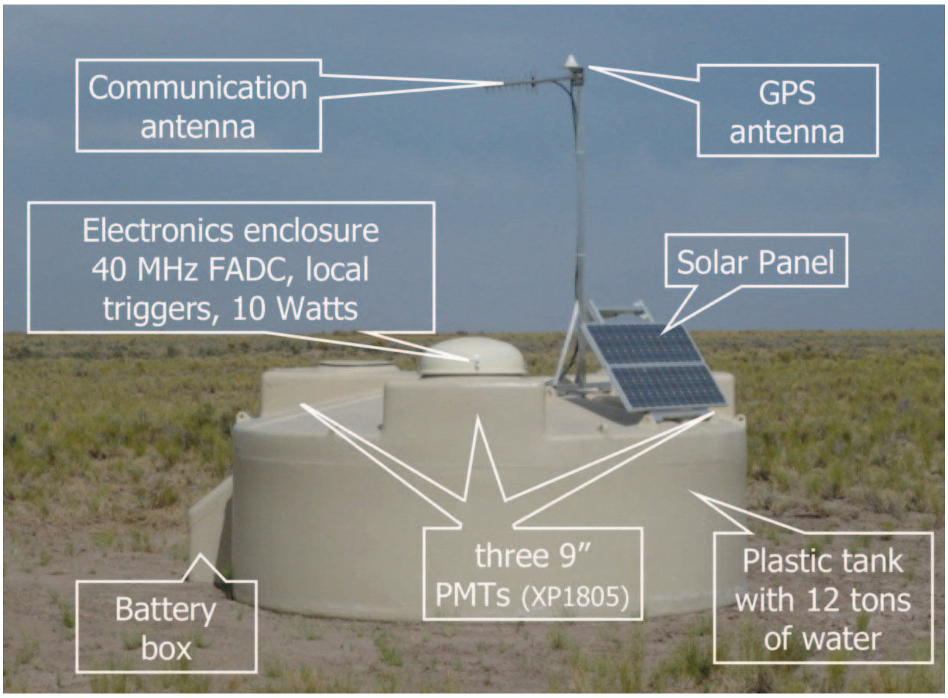

Figure 2.7: Surface detector unit and its different elements. (from [80]).

Electromagnetic Compatibility The electromagnetic compatibility is crucial in the coincident detection. The station elements which are likely to influence the radio detection by emitting either continuous noise or pulses are:

- the PMTs: the accelerated electrons inside the PMTs are expected to radiate.
- the cables: when a SD event occurs, the current in the cable may radiate for instance if a connection is not well shielded.
- the electronics: the processor of the UB operates at 100 MHz and the Flash ADC sample at a frequency of 40 MHz. Note that the electronics boards are enclosed in a metallic shielding (cf Fig. 2.8 (right)) and lay under a metallic dome.
- the SD antenna: the communication link is operated at around 900 MHz.

Moreover, the sensitive part of EASIER will be an antenna, and if it is placed at a distance of the order of the wavelength of observation from the surrounding objects, the latter are likely to modify the shape of the radiation pattern.

Acquisition and data The acquisition is performed by the Front End board (FE). The six inputs acquire the negative signal from the anode and the dynode of the three PMTs. The FE input connection is a coaxial SMA female. It is followed by an input Bessel low pass filter with a cut-off frequency of 20 MHz. An inverter mounting performs an amplification by a factor -1/2 before entering the sampling stage. Strictly speaking the acquisition is achieved by 10 bits FADC with a sampling rate of 40 MHz. Their input dynamic, [0 -1]V, sets the

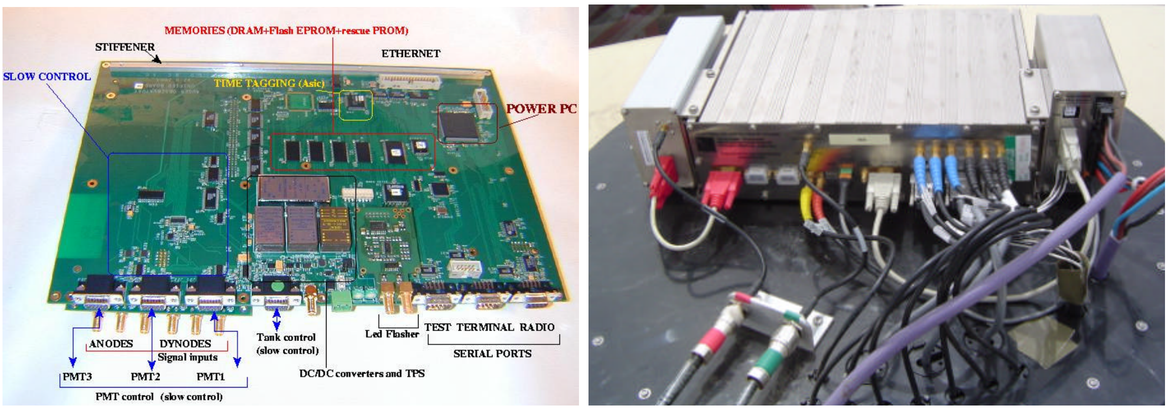

Figure 2.8: Left: Picture of the Unified Board of SD local electronics. Right: Auger SD electronics elements as installed on site, enclosed in a metallic shielding. At the left hand side: the communication module, at the center: the UB, at the right hand side: the TPCB.

dynamic range of the Front End input to [-2 - 0]V.
EASIER signal will replace the anode signal of one PMT. It will have to fit into this dynamic range. Moreover, the sampling frequency prevents us from recording directly the radio high frequency signal therefore the RF signal will be first transformed in its envelope.
When an SD event has reached the trigger level T3, the six traces of the PMTs are stored in the central acquisition. The EASIER trace will replace one of them and thus have the same characteristics: 768 time bins of 25 ns and digitized on 1024 ADC counts. Moreover, a stream of monitoring data of the tank is recorded every 6 minutes. Useful variables such as the temperature, the power consumption and baseline value will be a great asset to check the good integration and operation of EASIER system.

EASIER system

The general scheme of the EASIER detector is sketched on Fig 2.9. The radio signal is detected by an antenna in one polarization, amplified and filtered, then a power detector integrates the power in the selected bandwidth and provides its envelope. A linear transformation will follow so that the final output matches the front end input range of the SD acquisition electronics. The radio signal will use one of the FADC channel originally assigned to a PMT low gain output and the power will be supplied by the Auger SD battery. This setup is adjustable for different frequency bands with few changes and has been applied in the VHF band [30-80]MHz and the C-band [3.4 - 4.2]GHz. We describe here the common concerns for the two different frequency bands, the specific issues will be developed in dedicated chapters.

Antenna The antenna is the sensitive part of the EASIER detector, we list here the main parameters we will focus on to build the prototype and characterize it.
Field of view
The nominal goal is to observe the shower profile of the highest energy air showers ($E \geq 10^{19}$ eV) from a distance of 1 km. The depth of maximum shower development at these energies is measured to be $\simeq 750\,\mathrm{g/cm^2}$ [35] i.e. ~ 2.6 km for a vertical air shower. As the Pierre Auger Observatory site is at an altitude of around 1400 m, the angle required is thus

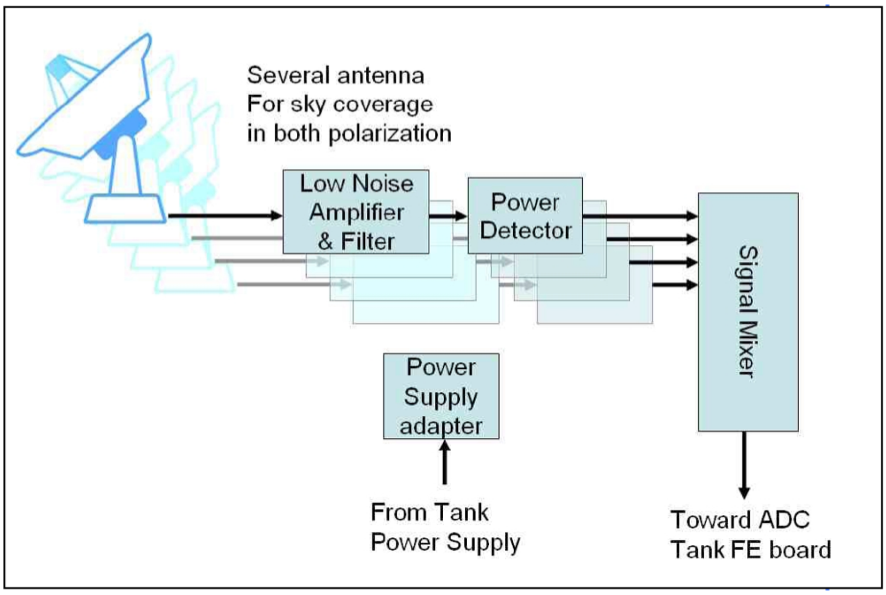

Figure 2.9: Left : functional scheme of EASIER

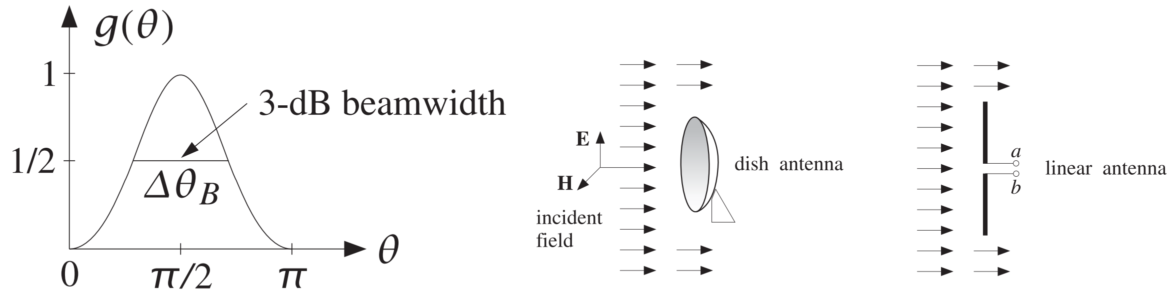

Figure 2.10: Left: Scheme of the half power beam width. Right: Scheme of the effective area and length of an antenna. (both scheme are taken from [81]).

around 40 °. So the half power beam width defined as the angle such that the gain of the antenna is a half of the maximum, has to be of the order of 80 °.

Effective area or effective length

A receiving antenna extracts an amount of power from an incident flux. The power intercepted can be related to the incident flux introducing an effective area or an effective length when the conversion from electric field to voltage is considered.

$$P_{out} = A_{eff} \cdot F_{in} \text{ and } V_{out} = L_{eff} \cdot E_{in} \tag{2.3.1}$$

The effective area or length is dependent on the angle of reception and on the frequency. The scheme in Fig. 2.10 (right) illustrates the fact that only a part of the incident flux is collected by the antenna. The effective area or length are crucial quantities to recover the incident signal. For a lossless antenna, it is related to the gain G of the antenna through:

$$G(\theta, \phi) = \frac{4\pi A_{eff}(\theta, \phi)}{\lambda^2} \tag{2.3.2}$$

where λ is the wavelength.

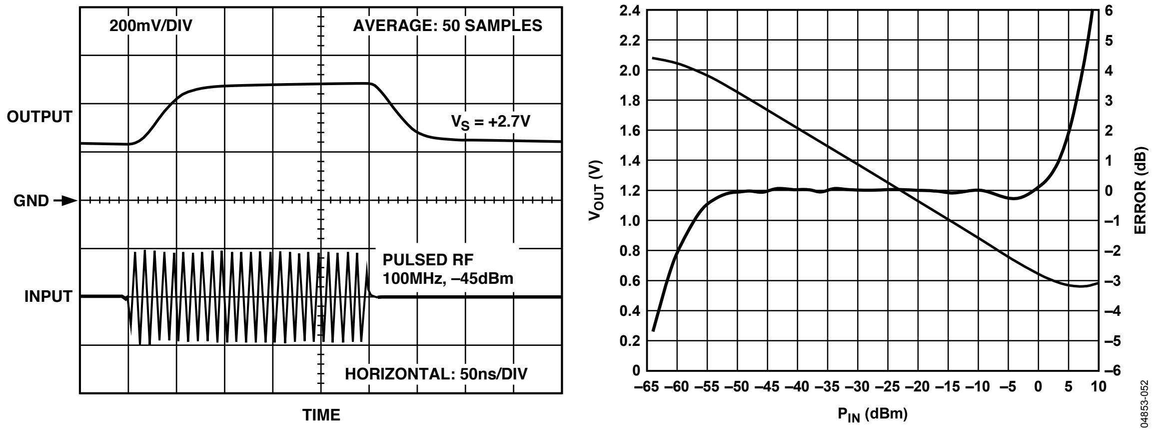

Figure 2.11: Left: Typical response of a power detector to a sine waveform pulse. Right: Typical characteristic curve of a power detector.

Filter The filtering is crucial in EASIER setup. As the signal is integrated over the whole band and no offline filtering can be performed, it is necessary to select a clean band. Some radio frequency band are known to be used for telecommunication. For instance FM band and AM band are used for radio broadcast. But other contribution from local emitter can also pollute the band and require first a survey to determine their frequency.

Amplifier The amplitude at the output of the antenna is expected to be very low. An amplification is needed to recover a signal that can be processed by usual electronic device. The crucial parameter of an amplifier is the noise the amplification can add to the signal. It is quantified by the ratio of input and output signal to noise ratio called the noise figure: $F_{sys} = SNR_{out}/SNR_{in}$. If the electronics system is composed of several stages, the total noise figure is the sum of the noise figures of each stage weighted by the previous gains :

$$F_{sys} = F_1 + \frac{F_2 - 1}{G_1} + \frac{F_3 - 1}{G_1 \cdot G_2} + ... + \frac{F_n - 1}{G_1 \cdot G_2 ... G_{n-1}} \tag{2.3.3}$$

This equation states that provided that the gain of the first amplifier is large enough, the noise of the following stages is negligible.

Power detection The acquisition of EASIER is performed by the Auger SD FADC with a sampling rate of 40 MHz. The reception band is either the VHF band or the microwave one so the RF signal needs to be transformed in its envelope that can be sampled at lower frequency. This operation is performed by a logarithmic amplifier [82]. The output of this device is a voltage proportional to the logarithm of the input power. A typical response of a logarithmic amplifier to a sine wave input is represented on Fig 2.11 (left) and a typical characteristic is shown in Fig. 2.11 (right).

Remark on units We will widely use the decibel units:

- the dB to compare two powers: $X[dB] = 10 \log_{10}(\frac{P_1}{P_0})$
- the dBm unit is a power in dB with $P_0 = 10^{-3} Watt$

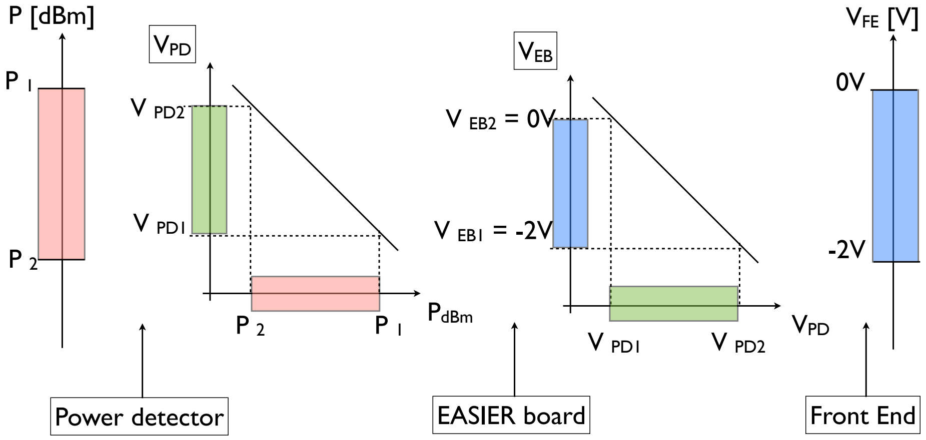

Figure 2.12: Scheme of operation of the different part of EASIER electronics chain. From an initial power dynamic range $[P_1 - P_2]$ to the input of the front end.

EASIER board The final output of the EASIER detector has to fit into the Auger SD front end. The voltage input range is [-2 ; 0]V. The signal from the power detector has to be adapted to adjust the input power dynamic range ($[P_1$ - $P_2]$ in Fig. 2.12) and the baseline level to this input voltage range as indicated in Fig. 2.12. The output of the power detector V_{PD} is:

$$V_{PD} = a \cdot P_{dBm} + b \;\; [V] \tag{2.3.4}$$

An electronics board is designed to perform a linear transformation so that its output, V_{EB}, is:

$$\text{output of the EASIER Board: } V_{EB} = c \cdot V_{PD} + d = a \cdot c \cdot P_{dBm} + c \cdot b + d \;\; [V] \tag{2.3.5}$$

The gain c is set such that the input power dynamic range is $\Delta P_{dBm} = \frac{2}{a \cdot c \cdot}$. The offset d is chosen to place the baseline between [0 ; -2]V. The last stage of EASIER acquisition chain is actually the Auger front end electronics. It is composed of a 20 MHz low pass filter, an amplifier with a gain $G = -0.5$ and 10 bits ADC sampling at 40 MHz. The transformation performed by the Auger front end are:

$$\text{output of the Front End amplifier: } V_{ADC} = -0.5 \cdot V_{EB} \;\; [V] \tag{2.3.6}$$

$$\text{output of the ADC : } ADC = V_{ADC} \cdot 1023 \;\; [ADC\ counts] \tag{2.3.7}$$

At the end, the trace in ADC counts is proportional to the logarithm of the input power.

Power supply board The power supply is provided by the tank power supply, an electronic board is designed to share the power between the different active parts of EASIER electronics. As the nominal power delivered by the solar panel is 10 W, and the tank elements like PMT and electronics use only 7.5 W, our goal was to design a system consuming less than 2 W.

Chapter 3

VHF band

Early experiments have already detected radio signal emitted from air shower in the VHF frequency band [64]. More recent setups with improved electronic and data processing facilities have been studying the origin and characteristics of this signal [70]. Because of the low extension of the radio signal, it has always necessitated a dense array of detectors, and has never been exploited on very large areas. The principle of EASIER in the VHF band is to take advantage on both the new development in radio detection and the facilities of the Pierre Auger Observatory to study the radio signal emitted by air shower with energy above 10^{18} eV. By using the trigger of surface detector and focusing on the ultra high energies, we hope to detect a radio emission that could extend at larger distances than previously measured.

We present in this chapter, the assembling of the EASIER setup in the VHF band, then its installation at the Pierre Auger site. In a third part we describe the resulting data: the detection of radio event and an analysis of their characteristics.

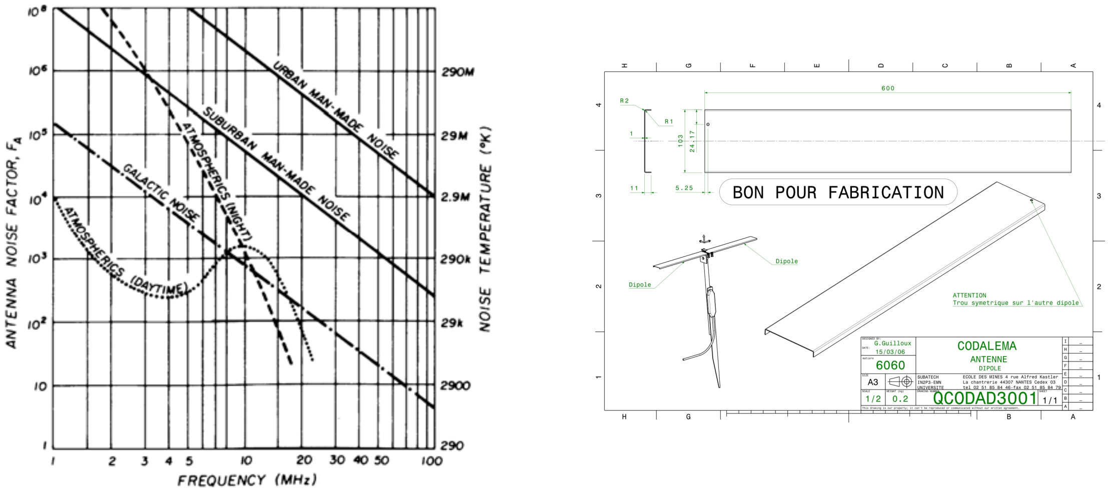

Figure 3.1: Left: Contributions of noise background in noise temperature for natural source (galaxy and atmosphere) and human source. Right: Fat dipole industrial design.

3.1 Detector

The VHF band is well utilized in communication and most of the electronics devices include electronic clocks at these frequencies. Moreover, at low frequency ($\nu \leq 30\,\mathrm{MHz}$) the background noise can be modulated by atmospheric effects. As an illustration we show in the digram 3.1 the different noise contributions between 1 and 100 MHz. In principle, in a radio quiet environment, the limiting noise comes from the galactic thermal emission. Also, it is clear from this figure that in urban condition, with a noise three orders of magnitude larger than in radio quiet condition, no complete test can be performed easily in real conditions for instance in Paris. Test in Faraday cage can be done however, given that the characteristic wavelength in VHF band is of the order of a few meters, the size of the cage must be of this order of magnitude to performe reliable test.

We relied on the sensor developments performed by the CODALEMA experiment [83]. The CODALEMA collaboration developed an active antenna for the purpose of radio detection of air showers. This setup was installed in a radio protected site in Nancay (France) and later at the Pierre Auger Observatory site. It has proven to have an excellent efficiency in the configuration set up by CODALEMA. In the case of EASIER, the setup will be different from the original one because of the constraints imposed by its integration with the Water Cherenkov detector. We will have to face two specific concerns related to the installation of the sensor on the tank:

- the SD electronics placed on the tank is likely to radiate noise and impair the sensitivity.
- as the wavelengths considered are of the order of a few meters, the power pattern can be influenced by surrounding objects. In particular, the amount of water in the SD tank, and solar panels or communication antenna placed on the tank.

Our setup is composed of a fat dipole antenna and a preamplifier both developed for the CODALEMA experiment, followed by an adaptation level specific to EASIER.

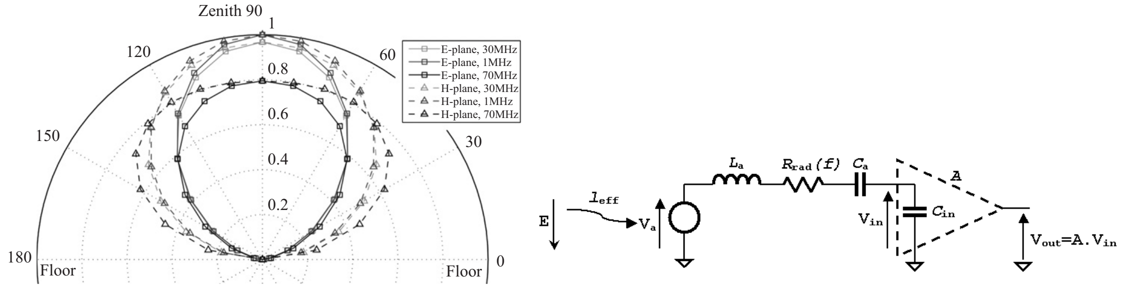

Figure 3.2: Left: Normalized gain of the fat dipole in E-plane and H-plane (from [83]). Right: Electronic equivalent circuit of the active antenna. (from [84]).

Antenna and Amplifier The combination of the antenna and the LNA constitute an active antenna meaning that the amplifier impedance is adapted to compensate the loss of the antenna at frequencies far from the resonance resulting in a wide band of reception.
The antenna is a dipole made of two aluminum blades of 0.6 m each and 0.1 m wide, they are separated by a gap of 0.01 m . The drawings of the radiator are shown in Fig. 3.1 (right). The simulated power pattern of the dipole is shown Fig. 3.2 (left), it exhibits a half power beam width of 90 ° and 120 ° respectively in the E-plane (defined as the plane containing the electric field vector (in our case the dipole direction) and the antenna boresight) and the H-plane (defined as the plane containing the magnetic field vector (orthogonal to the dipole direction) and the antenna boresight). This field of view characteristics are well suited for the EASIER purposes. The pattern is simulated for a dipole placed horizontally at 1.2 m above a perfect conducting ground. The pattern is given by the geometry of the antenna but it is also shapped by interferences of waves reflected by the ground. The pattern is thus expected to change if the detected wavelength is comparable to the distance from the dipole to the ground or if the conductivity characteristics of the ground change.
The main purpose of the active antenna choice is to obtain an approximately flat response with the frequency. The electronic equivalent circuit of the antenna and amplifier system is depicted in Fig. 3.2 (right). In that scheme, the antenna is represented by a voltage generator and a series circuit R_{rad}, L_a, C_a. The effective length, defined as the ratio of the voltage at the output of the antenna with the incoming electric field depends on the gain pattern of the antenna and the radiation resistance as:

$$L_{eff} = \frac{c}{\nu}\sqrt{\frac{R_{rad}(\nu)G(\theta,\phi,\nu)}{120\pi^2}} \tag{3.1.1}$$

Then, the transfer function of the amplifier is given by:

$$H(\nu) = \frac{Z_{in}(\nu)}{Z_{in}(\nu) + Z_a(\nu)} \tag{3.1.2}$$

The product of the effective length and the transfer function determines the factor between the incoming electric field and the voltage at the output of the LNA. The input impedance of the amplifier is mainly capacitive, so to obtain a transfer function independent of the frequency, the terms in Eq. 3.1.2 need to evolve the same way with frequency, i.e. the antenna impedance has to be mainly capacitive too. This characteristic is obtained by means of the important width of the dipole's blades with respect to dipole wires for instance. Moreover, according

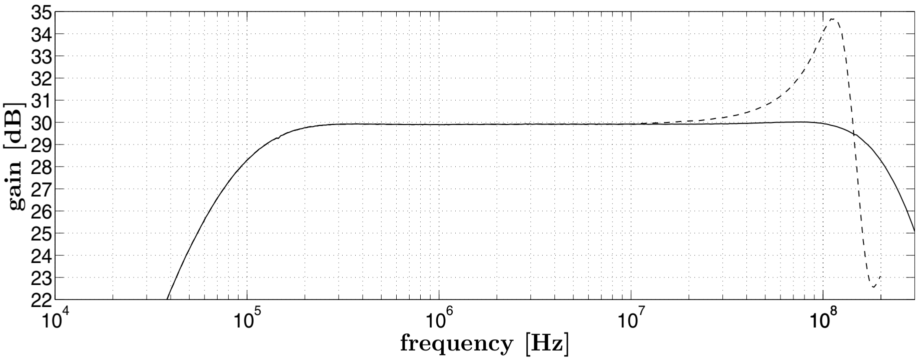

Figure 3.3: Transfer function of the set antenna + amplifier (from [84])

to Eq. 3.1.2, the higher the capacitance, the higher the transfer function. This justifies the choice of a fat dipole with respect to a usual dipole made of conductor wires.

The amplifier was especially designed for the purposes of cosmic ray detection, with a constraint of low noise, wide bandwidth and fast response [84]. It is composed of three differential amplification stages (in differential mode, i.e. not referenced to the electrical ground). It is then followed by a "balun" (BALanced UNbalanced) to make the signal asymmetric, i.e. referenced to the electrical ground. The measurement of the amplifier gain is shown in Fig. 3.3, it was performed replacing the antenna impedance by a capacitance (solid line). Then an independent measurement of the antenna impedance allow to calculate the actual gain calculated from the combination of the antenna and the LNA (shown in dotted line Fig. 3.3). The overall gain is 30 dB and is flat from 200 kHz to 100 MHz for the amplifier alone. When the antenna impedance is taken into account, the gain increases near the antenna resonance frequency at $\nu_0 \simeq 113\,\mathrm{MHz}$. In the design of the LNA, a special care was taken to keep a low noise level. Noise measurements were performed once again replacing the antenna by an equivalent capacitance of 10 pF, the noise induced by the LNA is found to be less than $1\,\mathrm{nV}/\sqrt{\mathrm{Hz}} \simeq 1500\,\mathrm{K}$ for frequencies larger than 10 MHz, thus lower than the galactic noise. The power consumption is 0.25 W and it can be supplied by a voltage from 6 to 12 V.

This setup was first used in CODALEMA in Nancay and later at the Pierre Auger Observatory in the framework of the Radio Auger project. So the noise background condition was already tested and we can then estimate the background noise expected with the spectrum presented in Fig. 3.4. The EASIER setup imposes us to select a clean band. This band, in red in Fig. 3.4, is between 30 and 80 MHz. The noise density in this band after amplification by the LNA is lower than -125 dBm/Hz.

EASIER board As described in chapter 2, the EASIER electronics has to fulfill three main functions: select a clean band, transform the high frequency signal into its power envelope and adapt it to fit the input dynamic range of the SD front end.

The physics requirements for the board are imposed by the background noise level, the amplification factor of the LNA and the expected signal from air showers. To establish the electronic requirements we first choose a limited frequency range: the chosen frequency band is filtered with a pass band filter from 30 to 80 MHz. In this band the spectrum after amplification shows a noise density of -127 dBm/Hz, which, once integrated over the frequency

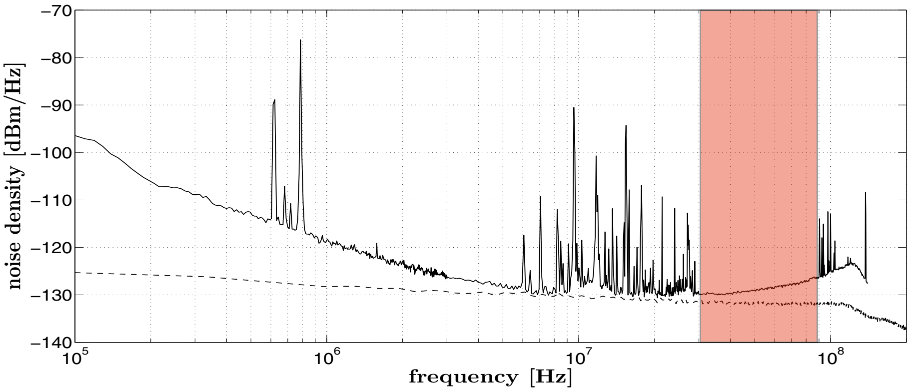

Figure 3.4: Spectrum recorded at Malargüe. The shaded area represents the clean frequency band operable for EASIER. The dashed line is a spectrum taken replacing the antenna by a dummy impedance, it is then the amplifier noise.

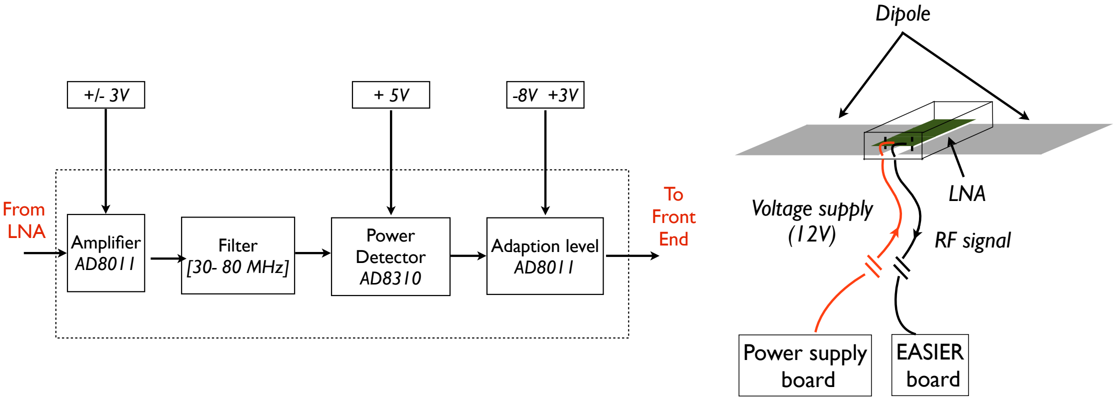

Figure 3.5: Left: Functional diagram of the EASIER board. Right: Scheme of the complete setup

band results in a total power of approximately -50 dBm.

This radio frequency signal has to be adapted to fit into the Auger FADC with the wanted dynamic range. To do so, an electronic board was designed, its main functions are summarized in Fig. 3.5. The first amplification stage, by amplifying the signal from the low noise amplifier (LNA) set the size of the dynamic range. The following filters select the clean bandwidth. Then, the power detector Analog Device AD8310 [85] was chosen because it is suited for VHF frequencies and the background noise level is well in its dynamic range. Its calibration curve taken from the constructor's data sheet is given Fig. 3.6 (left). With its nominal configuration , its slope is $S = 24\,\mathrm{mV/dB}$ and 80 dB of dynamic range are covered at output voltages from 0.5 to 2.5 V. We decided to set the background noise level at 1/4 of the final dynamic range and to allow $\simeq$ 30 dB (a factor 1000) for the signal from air showers. This value sets the requirements for the electronic board: an input power of -50 dBm results in -0.5 V at the output of the EASIER board and the slope is set to 20 dB/V. The last amplification stage sets an offset to place the background signal at $V_{bkg} = -0.5V$, corresponding to one fourth of the front end input. The calibration curves in Fig. 3.6 (right) measured at several frequencies

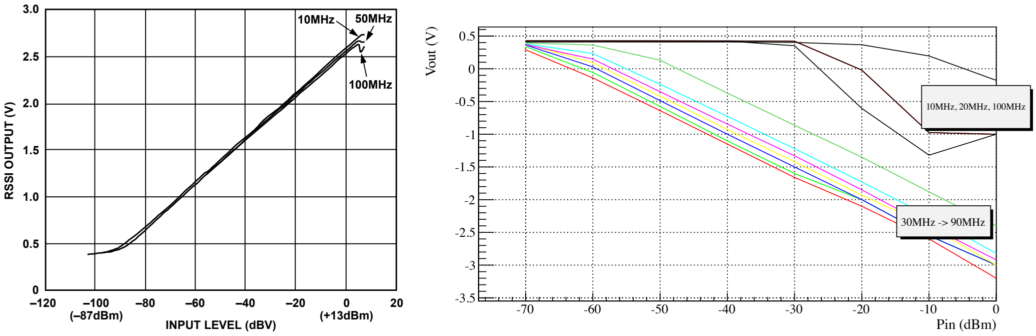

Figure 3.6: Left: Calibration curve of the power detector AD8310 extracted from the data sheet. Right: Calibration curves of the EASIER board at frequencies from 10 to 90 MHz.

represent the output voltage of the EASIER board as a function of the input power. The effect of the filter is clearly seen and in the middle of the band, at 50 MHz, the dynamic range extends from -60 to -20 dBm on the range of 2 V as expected. The calibration relation is :

$$P_{dBm} = 20 \cdot V_{EB} - 60 \tag{3.1.3}$$

with $V_{EB} \in$ [-2 ; 0]. Or in ADC counts:

$$P_{dBm} = 3.9 \times 10^{-2} \cdot ADC - 60 \tag{3.1.4}$$

with ADC $\in$ [0 ; 1024]
A power supply board was also implemented to feed the LNA and the active component of the EASIER board.

Complete setup In a first version of the setup, a metallic box containing the LNA, the power supply board and the EASIER board, was placed just above the dipole. In fact, the metallic box created a parasitic capacitance with the dipole and the signal was highly attenuated [86]. In the definitive version the metallic box is replaced by a plastic one containing uniquely the LNA placed above the dipole and one metallic box containing the two other electronic boards. A scheme of the complete setup is shown in Fig. 3.5 (right) or in Fig. 3.9 once installed on site.
All the boards were tested and calibrated, and the response of the complete detector was tested only qualitatively because of noise conditions. Seven complete setups with radiator, LNA and EASIER board were shipped to Argentina at the end of year 2010.

Figure 3.7: Elements of mechanical assembly of the dipole and the mast.

3.2 Installation

In February 2011, we proceeded to the installation of seven prototypes at the Pierre Auger Observatory. The shipped material was first assembled on site. The mechanic assembling to integrate the antenna with the tank was chosen with the help of the local mechanics. The dipole is placed on top of a 3 m plastic pole with a plastic screw (cf Fig. 3.7), the LNA directly connected to the blades of the dipole (cf Fig. 3.5 right) is just above them in a plastic box. Two cables are connected to the LNA box, one to feed the power supply to the amplifier, the other one is conducting the signal output of the LNA to the EASIER board.

Tests and modifications As it was mentioned before, the frequency band from 1 to 200 MHz is very noisy, especially in city environment. The setup could not be tested completely in Paris for this reason. Once we assembled a complete setup, we tested it near the assembly building of the Observatory campus which is in the town of Malargüe. As the noise background level was still orders of magnitude higher than expected in the Pampa, we made some tests in a container serving as a Faraday cage. The first test we performed revealed an important resonance at the resonance frequency of the antenna (see Fig. 3.8). In principle, this frequency is filtered however the LNA has an upper limit input power to operate nominally. The resonance was suspected to arise from radiation of elements of the setup such as connection or cables. To attenuate this spurious ray, we brought two main improvements :

- we soldered directly the signal cable to LNA board (in the original setup the LNA was connected to the electronic boxes with two cables, one from the LNA to the plastic box and a second one from the plastic box to the electronic box, thus with an additional connection)
- we shielded the cables transporting the RF signal with flexible metallic pipe.

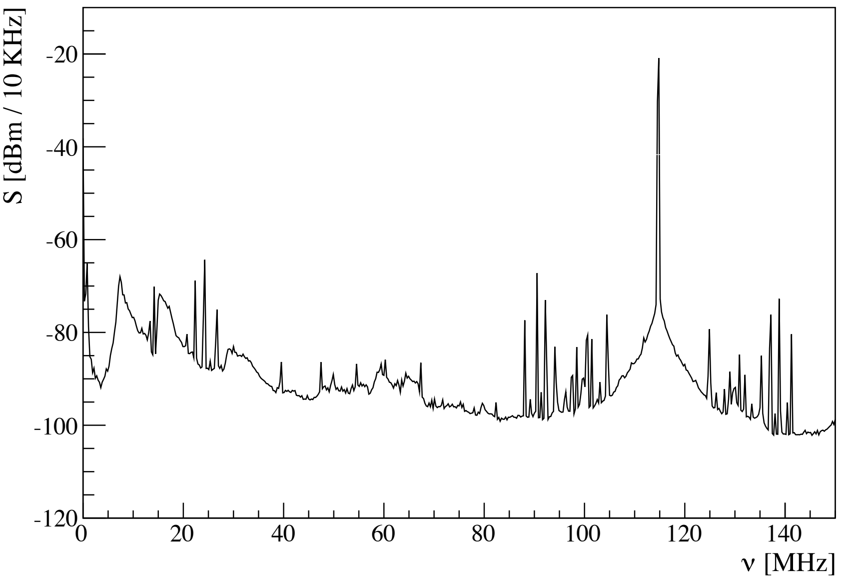

Figure 3.8: Spectrum recorded in a container showing the resonance peak just above 110 MHz.

We decided to test the whole setup about ten kilometers away from the city. The resulting spectra were almost free from any peaks in the chosen bandwidth and the background noise level was approximately the one expected i.e. $\simeq -125\,\mathrm{dBm/Hz}$. These results made us confident in the possibility to install finally the setups in the field.

First installation We installed the first setup on the tank Vieira (LsId: 433) on the 1^{st} of March 2011 . The final setup once installed is shown in Fig. 3.9. The spectrum recorded during the installation shown in Fig. 3.10 in red, as expected, an almost flat noise background between 30 and 80 MHz of density around $-125\,\mathrm{dBm/Hz}$ (or -85 dBm/10kHz).

On figure (3.10 left) is also represented in black a spectrum recorded when a computer was on the tank showing once more the necessity to get rid of any noise source to perform reliable tests. The zoom of the spectrum in Fig. 3.10 (lower panel) shows first that two peaks at 67.5 and 80 MHz of amplitude around 10 dB above the noise remain in the selected band, they will pollute the data. Second at each side of the selected band important peaks are present, therefore if the filter slope is not steep enough they may still bring a contribution in the integrated signal.
The six other detectors were installed in the following week. The date of activation for the seven installed setups are reported in Table 3.1 and their locations are depicted on the map Fig. 3.11.
All the dipoles were placed with an East West polarization. This is justified by the expected emission mechanism, the geomagnetic effect.
Soon after the installation we had the confirmation of the proper functioning of the detector as a clear event was detected in the radio channel just a few days after its installation.

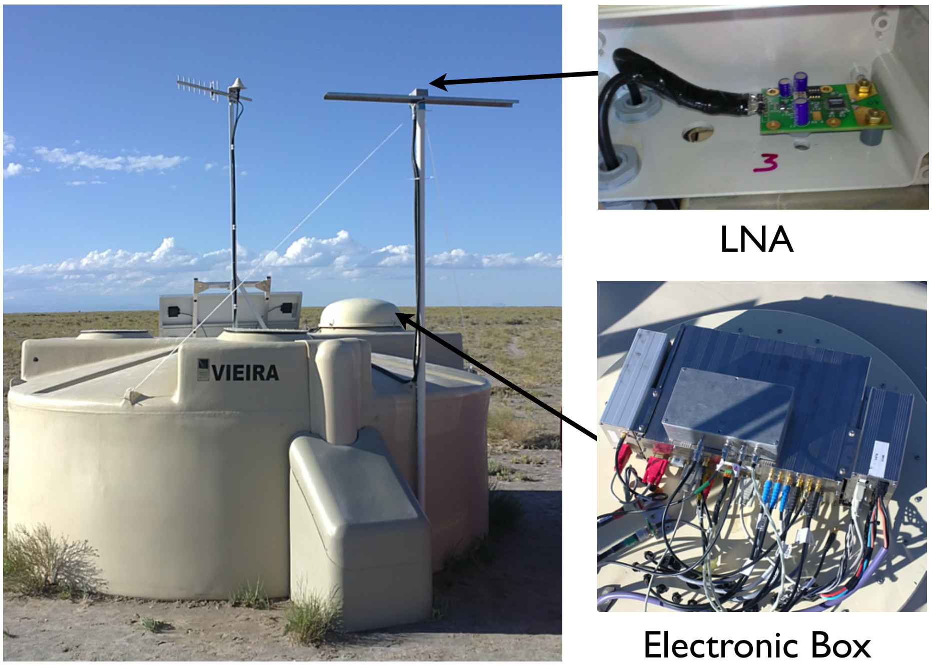

Figure 3.9: Final setup installed on the tank Vieira. The mast is tied with nylon cables. The amplifier (LNA) on top of the dipole has two cables soldered directly on it, one plugged to the power supply board, the other one to the EASIER board. Both of these board are located in a metallic electronic box placed under the dome where the SD acquisition electronic is placed too.

Tank		Start of the Antenna	
ID	Name	Date	GPS
433	Vieira	2011/03/01 21:00	983048415
432	Juan	2011/03/04 22:00	983311215
427	Domo	2011/03/05 18:00	983383215
384	Chape	2011/03/05 19:00	983386815
385	Popey	2011/03/05 20:00	983390415
431	Orteguina	2011/03/05 22:00	983570415
422	Luis	2011/04/15 12:00	986904015

Table 3.1: List of tanks equipped with MHz antenna.

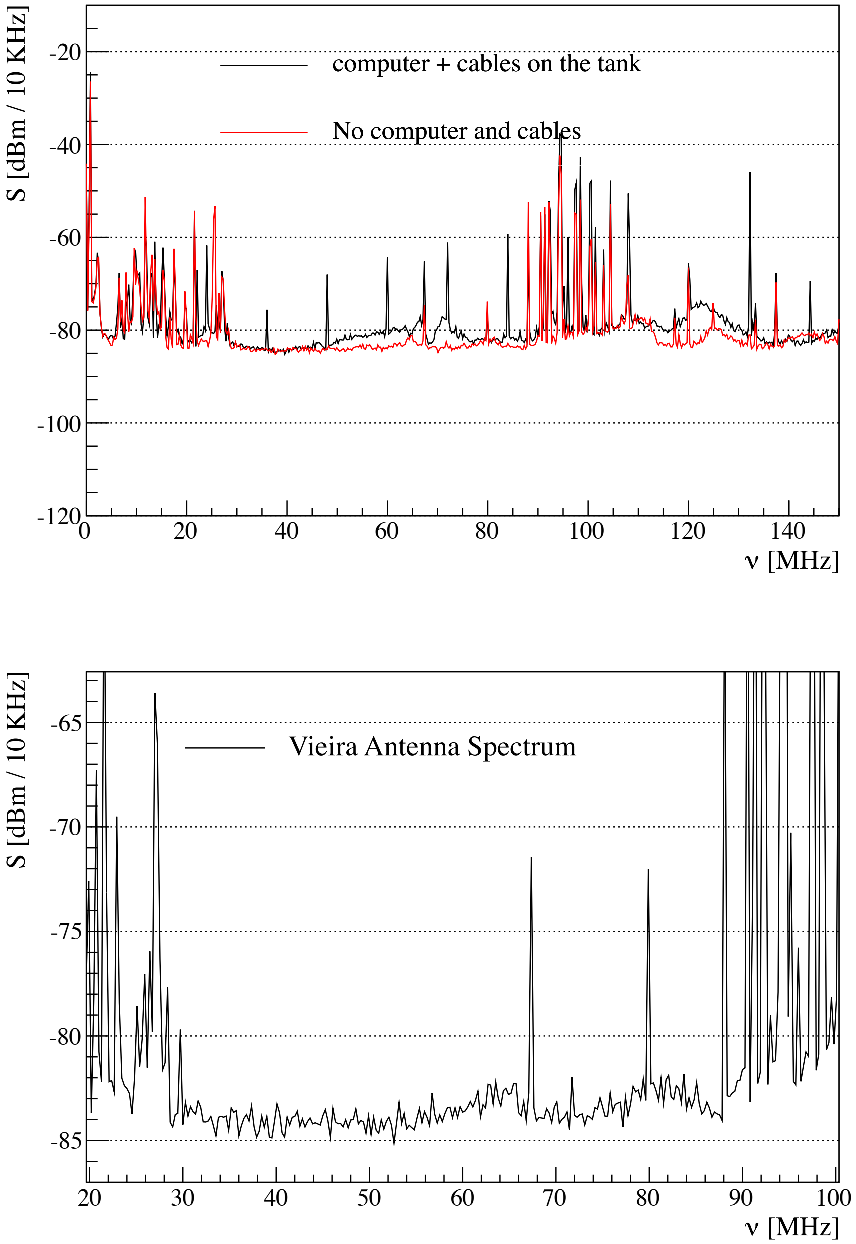

Figure 3.10: Upper panel: Spectra recorded with the setup installed on Vieira tank. The black one was recorded with computer nearby the tank, the red one when source of noise were kept away. Bottom panel: Spectrum zoomed around the EASIER band (30-80 MHz)

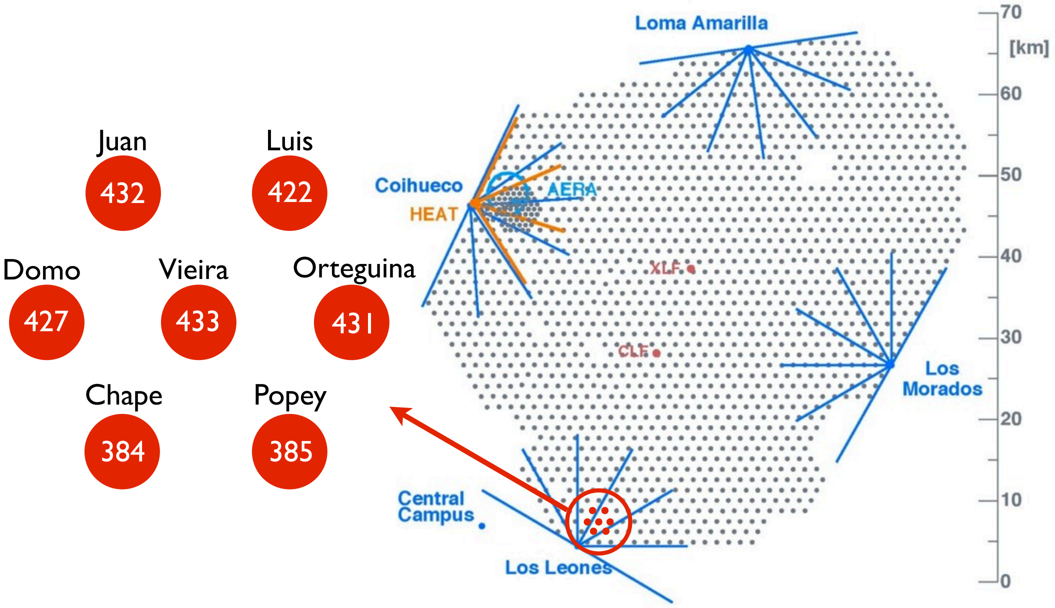

Figure 3.11: Location of the VHF hexagon centered on Vieira tank

3.3 Data Analysis

The seven VHF setups installed in March 2011 operated until November 2011 when they were decommissioned. During this period, not all the recorded data are exploitable. We present first a selection of the data set, then the method of selection of radio events and finally we discuss the origin of these detected radio events.

Data set

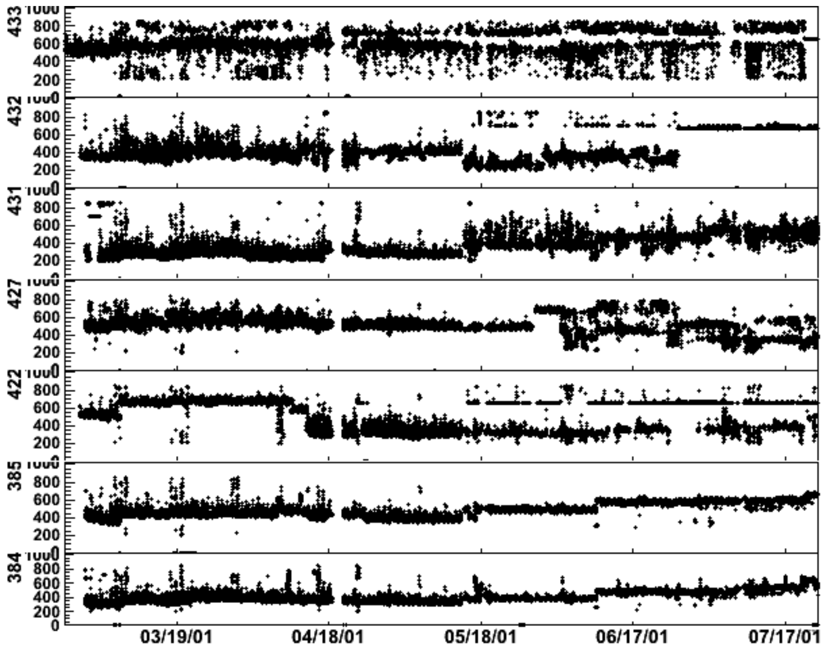

Figure 3.12: Baseline as a function of time over the time of operation of the VHF setup.

Monitoring data allow us to follow the behavior of EASIER detectors over an important time period. One can see in Fig. 3.12 the evolution of the baseline as a function of time during five months of operation. For the stations 384, 385, 422 and 431, the baseline increases by steps appearing at the same moment for the four of them. Such simultaneous behavior can be explained by RFIs that were not present at the time of the installation and appeared in the area of these antennas. The three others don't show a peculiar behavior for the first months. However, every antenna seem to have suffered of the local winter (months of June to September) when some failure appear. Indeed, the antennas were decommissioned in November 2011 and some of them were broken lying on the ground. We suspect a too important wind load of the dipole to be the cause of the failure of the antennas. We should also precise that just before the installation many soldering were redone and some of them may have also broken. In particular, two 5 m cables are soldered directly on the LNA, one supplying the power for its functioning, the other to transport the RF signal and the weight of these cables may have broken the solderings.

In this analysis, the time period considered starts from the installation date and ends the 19^{th} of June 2011. The data of the antenna on station 422 are not included in the data stream because the PMT was malfunctioning thus the traces from it are not kept in the data

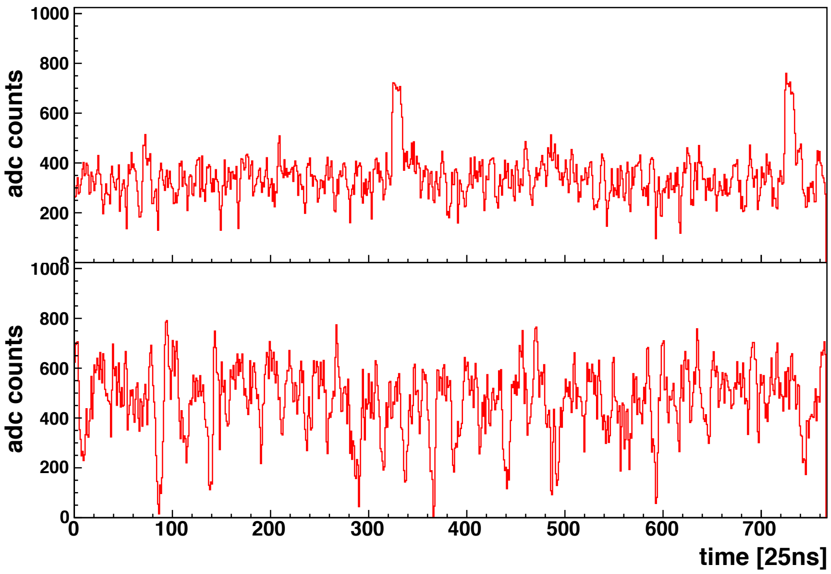

Figure 3.13: Example of rejected traces. Up: regular peaks on the station 432. Down: Important fluctuations of the radio trace.

production. During this period 970 events have a reconstructed energy and at least one of 7 stations, on which a VHF EASIER antenna is installed, has triggered. The resulting data set is composed of 1748 available traces for radio signal search. Despite the difficulties, during the period of good operation of the antennas, we recorded a total of 36 unambiguous radio events, we further detail the procedure of event selection below.

Event selection

Even if the radio environment is quiet in the Pampa, some radio traces can show some clear episodic perturbation when the baseline and its fluctuations are much larger than usual. Some malfunctions, like a brutal increase of the baseline can be detected thanks to the monitoring data in Fig. 3.12. A further look at the radio traces bring more detail on the origin of these malfunctions. We show for instance two traces in Fig. 3.13 with a specific behavior. The trace in the upper panel exhibits peaks at regular time intervals. The origin of these peaks is likely to come from the EASIER electronics itself and appears constantly in the data of the detector 432. The trace in lower panel of Fig. 3.13 exhibits a strong modulation. This may be due to a close intermittent emitter. The event selection criteria we present are chosen to exclude this kind of trace and to select potential radio pulses correlated with EAS. The event selection is performed in four steps:

- For each available trace, the distribution of amplitude in ADC counts is fitted with a Gaussian distribution and the mean and the standard deviation are extracted.
- a cut is applied to keep traces with a mean $\in [100 , 800]$ ADC counts and the standard

deviation $\in [0\ ,\ 150]$ADC count. This insure a good estimation of the mean and remove trace with too large fluctuations. 5% of the traces are rejected by this cut.

- the maximum of the trace is required to be within ± 4 times bins around the arrival time of the particles in the tank.
- the amplitude of the maximum is required to be more than 250 ADC counts above the baseline corresponding to a power around a factor of ten above the background noise.

selection criteria	number of traces	selected %
All traces	1748	100
mean $\in [100\ ;\ 800]$ && $\sigma \leq 150$	1655	95
excluding tank 432	1405	80
maximum ≥ 250 ADC	99	5.7
time coincidence	36	2.1

Table 3.2: Selection criteria and their efficiency on radio traces.

Table 3.2 reports the cut efficiency on the radio traces. We show an example of event for which a signal was found in three antennas in Fig. 3.14 shown together with a PMT signal to indicate the start time of the particle arrival. The radio events show a characteristic pulse shape of a few time bins long, i.e. no more than 200 ns. The characteristics of the air shower that led to the selected radio events are shown in the histograms in Fig. 3.15 in red compared to the distribution of the events detected by the SD. Events from a few 10^{17} eV up to more than 3×10^{19} eV were detected in radio. The distances to shower axis are concentrated in the lower values under few hundreds of meters. The arrival direction leading to radio event don't follow the distribution of the air shower detected by the SD array. Indeed it exhibit an excess of detection for EAS events with a large zenith angle and a southern direction. This effect is explained in the next paragraphs.

Origin of the observed events

We discuss in this paragraph on the origin of the radio events selected above. We present first a study performed in [87] that eliminates the possibility that the radio event originate from the tank noise in the VHF band. We discuss then the possible origin mechanism that give rise to the events and their arrival direction distribution.

Noise from the tank It was pointed out in introduction of this chapter that the good functioning of the EASIER setup is subjected to its integration to the SD tanks and the non influence of the latter on the former. As a matter of fact, one of the main concern was that the radiation emitted by the SD electronics, the PMTs or the cable conducting the PMT signal could be detected by the EASIER antenna and lead to spurious events. A study was performed making use of the LED (Light Emitting Diode) system originally utilized for the calibration of the PMT of the water Cherenkov tank. The LED system simulates the Cherenkov light of the particles in the water tank and causes a fake event. We can thus estimate the noise induced only by the tank elements on the antenna.

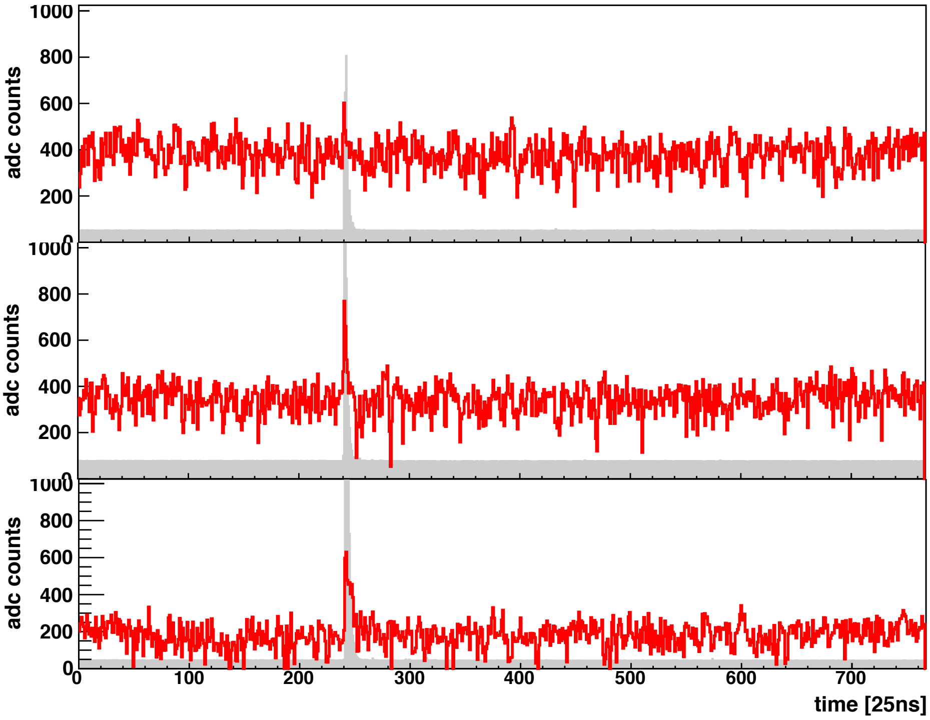

Figure 3.14: Example of a threefold event (Id: 11748502). In grey is represented the trace of one PMT and in red the radio trace in adc counts.

However, the LED cable itself was found to emit noise detected by the EASIER antenna. The method to cancel it is to record separately the noise induce by both the tank elements and the LED and then by switching off the PMT high voltage, record the noise induced solely by the LED system. The noise induced by the tank is obtained by subtraction. Moreover, we can vary the intensity of the light emitted by the LED to check if there is any correlation between the PMT charge and the radio signal. In real events, the intensity of light in the tank depends on the shower energy and the distance from the tank to the shower core. The results are reported in Fig. 3.16 for 5 antennas. The Y-axis represents the amplitude of the maximum radio signal in units of baseline, i.e. the signal to noise ratio (SNR), in this case, it is in fact the difference of SNR when the PMTs were on and when they were off. A fixed number of 5 was added first to prevent from negative signal to noise ratio and be able to plot it in log scale. The X-axis represent the light in the tank and is expressed in $VEMcharge$ which is the integral of the signal in the PMTs. Except for important value of LED intensities, corresponding to cosmic ray event very close to the station, the noise induced by the tank is compatible with zero. The radio signals induced by air shower events presented before are shown in the same figure. All of them are above the noise induced by the tank at the corresponding particle signal proving that the signals observed are not spurious.

Anisotropy of detection efficiency The distributions shown in Fig. 3.15 point to an excess of radio events detected from inclined shower and coming from southern direction. It is more evident on the plot in polar coordinate in Fig. 3.17 (left), where the red dots represent the radio event and the black open circles air shower events selected but without radio event.

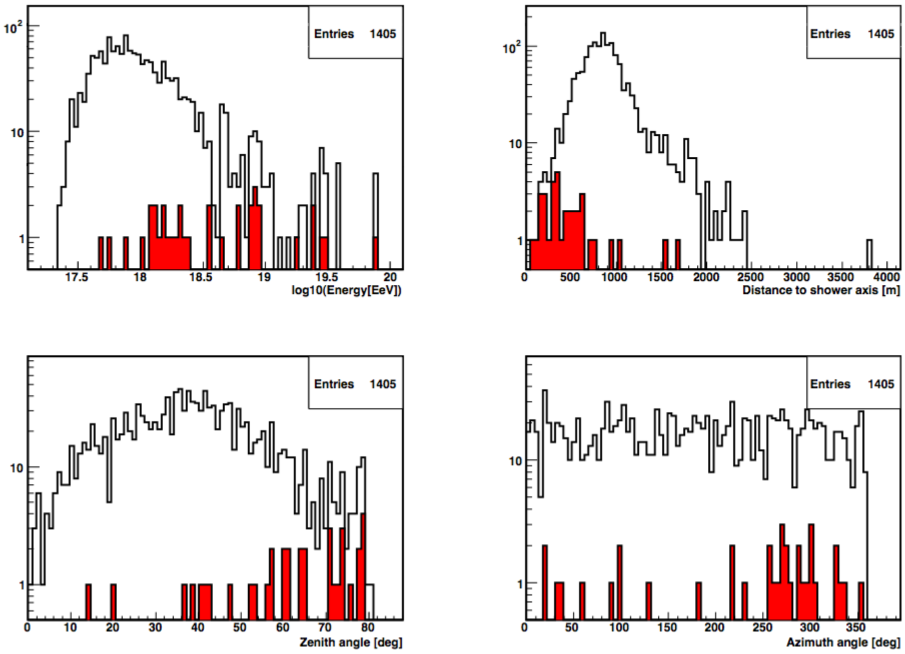

Figure 3.15: Distribution of the energy, distance of station to shower axis, zenith angle, azimuth angle of the air shower event selected. The distributions in red represent the characteristics of the radio events.

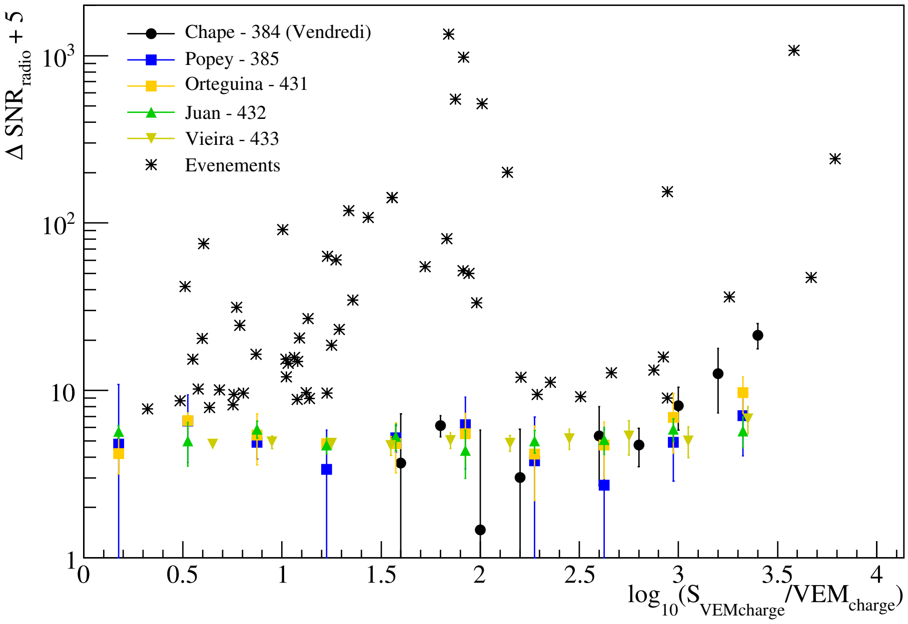

Figure 3.16: Difference of SNR induced by the tank when LED and PMTs are on and when PMT are off. The stars represent the signal to noise ration induced by air shower radio events

This excess is consistent with two expected effects, one is related to the emission mechanism and the other to the detection setup.

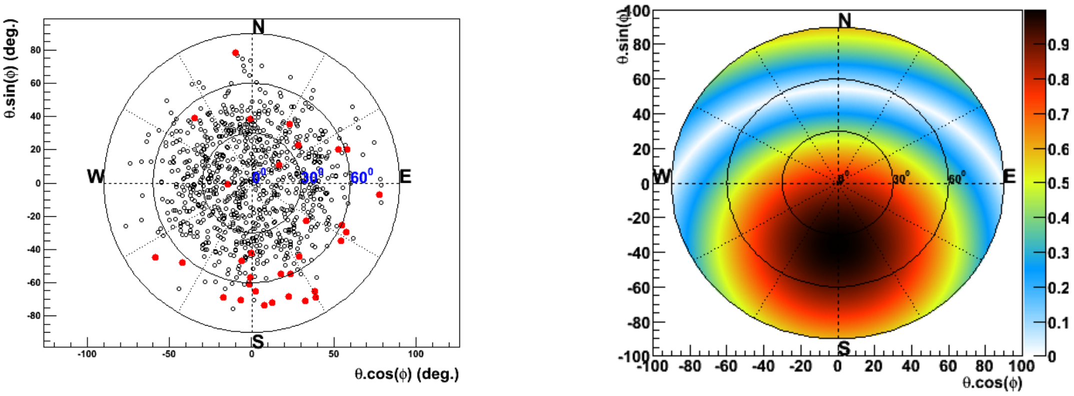

Figure 3.17: Left: Arrival direction of radio events recorded compared to the air shower event non associated with radio events. Right: Intensity of the geomagnetic effect ($[\vec{v} \times \frac{\vec{B}}{\|\vec{B}\|}]_{EW}$) as a function of the arrival direction

Results from other radio detection experiments demonstrated that the dominant emission mechanism is related to the geomagnetic effect of separation of the charged particles in air showers. The expected electric field issued from this mechanism is mainly proportional to the cross product $\vec{v} \times \vec{B}$, where $\vec{v}$ is the unitary vector defined by the shower axis, and $\vec{B}$ the geomagnetic field in Malargüe. According to the International Geomagnetic Reference Field [88], $\vec{B}$ is defined by a total intensity of $24\,\mu T$, a declination D = 2.90 ° and a Inclination of I = -35.67 °. The projection of the cross product on the East-West axis as a function of the arrival direction is plotted in Fig 3.17 (right). The geomagnetic effect is expected to be maximum for air shower coming from the south (270 °) and with an zenith angle between 30 ° and 40 °.

Another effect has to be accounted for to explain the excess in Fig. 3.17 (left). It is related to the pattern of the antenna which is modified due to its position with respect to the tank. The dipole response in presence of the water tank has been simulated with the Ansoft's 3D electromagnetic simulation software HFSS [89]. The antenna gain patterns at three frequencies, 30, 50 and 70 MHz are shown in Fig. 3.18. If at 30 MHz the pattern is regular and looks like the expected one, at higher frequency the pattern become highly anisotropic and a lobe pointing in the southern direction (negative y in Fig. 3.18) participate to excess of detection in this direction. The voltage at the output of the antenna, V_{out} is related to the electric field via :

$$V_{out} = L_{eff} \cdot \|\vec{E}\| \cdot \cos\psi \qquad (3.3.1)$$

where $\cos\psi$ is the polarization vector of the incoming electric field, and the effective length $L_{eff} \propto \sqrt{G(\theta, \phi, \nu)}$. The excess of detection can be explained by the combined effect of the geomagnetic field and the anisotropic gain pattern. The amplitude of this combined effect is shown in Fig. 3.18 (bottom panel) and matches qualitatively the results presented in Fig. 3.17 (left).

Lateral distribution of the radio signal The important parameter for the study of the UHECR is the maximum distance of detection. It determines the minimum spacing needed for an array of detectors.

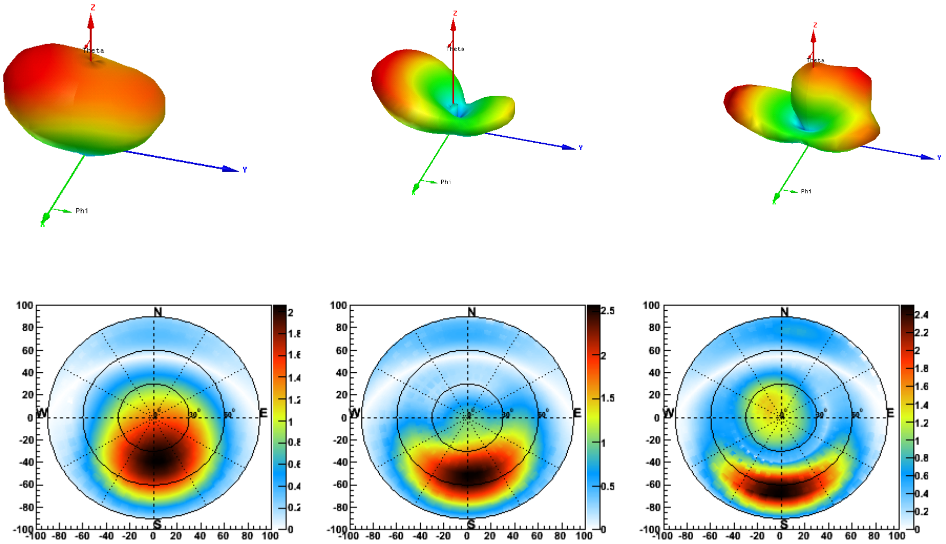

Figure 3.18: Dipole antenna pattern simulated with HFSS in realistic condition at 30 (left), 50 (middle) and 70 MHz (right)

The maxima of the detected radio signals are plotted as a function of the distance from the antenna to the shower axis in Fig. 3.19. The Y axis is the maximum electric field deduced from the radio signals, normalized by the air shower energy and the projection on East West direction of the cross product $\vec{v} \times \vec{B}$. The error bars are the standard deviation of the trace. The calibration of the system necessitates the knowledge of $L_{eff}(\nu)$, $G(\theta, \phi, \nu)$ and the transformation factor induced by the EASIER electronics which depends also of the frequency (cf Fig. 3.6). The overall calibration relation, from the electric field to the voltage is not known precisely enough, so the amplitude is calculated relatively to the baseline of the trace and is reported in arbitrary units.

One can notice a bulk of events decreasing exponentially with the distance. The exponential decrease is consistent with Allan's formula in Eq. 2.2.1 and later results from CODALEMA or LOPES experiments and suggest a coherent process. The characteristic distance of the exponential decrease is found to be approximately 200 m. One can also notice also four outliers (in red in Fig. 3.19) with an amplitude of a factor ten above the bulk of events. One possible explanation for these large amplitudes is the amplification of the radio signal during stormy conditions, but no for the moment we haven't drawn any conclusion on these events.

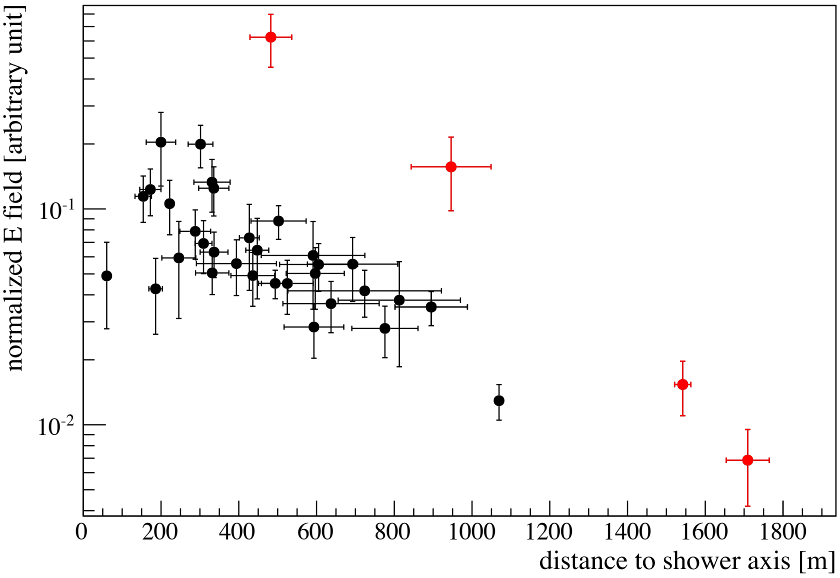

Figure 3.19: Lateral distribution of the electric field as a function of the distance from antenna to the shower axis. The electric field is normalized with the shower energy and the projection on the antenna polarization direction of the vector $\vec{v} \times \vec{B}$.

3.4 Outcome of the first prototype and further developments

First setup We constructed and installed an array of seven radio detectors at the Pierre Auger Observatory operating in coincidence with the surface detector. The detection of cosmic rays in coincidence with the Auger SD tank was proven to be possible and efficient. However, this first prototype had several deficiencies. Firstly some electronic connections were found to be fragile. Secondly, the wind load of the antenna was found to be too important for the conditions at the Pierre Auger site. Thirdly, the position of the antenna on the tank influenced the power pattern preventing us from deriving a reliable absolute calibration of the complete detector, and making the efficiency of detection anisotropic. We also realized the difficulties in instrumenting this frequency band. The noise conditions even in the Argentinian pampa are evolving and emitters in the selected band can appear after the deployment.
Despite these issues, EASIER detectors in this band managed to detect 36 radio events. Their characteristics are consistent with the detection by other experiments of a beamed emission dominated by a geomagnetic effect. However, with this first prototype, we couldn't succeed in the detection of vertical events at distances larger than 200 m. Two main paths are being investigated: first the analysis method presented may be improved with a more thorough data processing. An analysis and a filtering of the noise would allow to lower the detection threshold. Secondly we developed a new prototype taking advantage of the experience we gained.

second setup The second setup was developed in order to respond to the requirements set by the first setup experience. The overall setup remained unchanged, but some improvements were brought. We followed the evolution of CODALEMA in the sensor part. The antenna is still an active antenna but is now a butterfly antenna in reference to its shape (see Fig. 3.20). Its design was chosen to optimize its sensitivity between 30 and 80 MHz [90]. The comparison of the effective length of the fat dipole and the butterfly antenna is shown in Fig. **??** (left). The LNA remained the same but the cable transporting the RF signal is now shielded to avoid its radiation and amplification (one of the problem we had during the first installation). As noticed in the spectrum taken during the installation of the first setup, the initial selected band (30 and 80 MHz) was too wide and peaks were present into this band. The filtering was improved by ordering a filter designed specifically for our purposes. The specifications for the filter design were a steep cut of the frequencies below 30 MHz and above 60 MHz. A loss of 40 dB is reached at 3 MHz out of the selected band.
A special care was also taken to insure no electronic noise arises from the EASIER electronic itself and the two electronic boards (the power supply board and the EASIER board) are now separated to ensure that no radiated noise from the first can interfere with the second. The picture in Fig 3.20 (right) shows the two electronic boxes. They are connected with a cable equipped with ferrite to filter any low frequency modulation from the power supply board to the EASIER board.
Five detectors were installed in March 2013, the position of the antenna on the tank was chosen to keep symmetric lobes according to simulation results including the water tank and the solar panels . The antenna is now placed at the center of the tank at 1.5 m above the water. Up to now, on the five antennas installed, only two are operating correctly. The failure of the others are under investigation.
With this second prototype our goal is to be sensitive to a possible isotropic emission

Figure 3.20: Left: Butterfly antennas installed on a water Cherenkov tank. Right: picture of the two electronic boxes.

mechanism or in case of non detection to set limits on such emission. Its description will be the subject of another thesis.

Chapter 4

Detector developments and sensitivity in microwave band

In the microwave band two setups were installed at the Pierre Auger Observatory surface detector. The first one, a prototype hexagon was deployed in April 2011 and the second one, an extension to 61 detectors, in April 2012.
We describe here first the different steps we followed in the detector development. From the noise survey carried at the very beginning of the project to the installation of the first setup and then its extension. We detail then the calibration of the detector electronics performed both in laboratory and on site and extract an absolute calibration of the system. In a third part of this chapter, we give the important parameters to estimate the performance of the detector and describe the efforts we made to measure them.

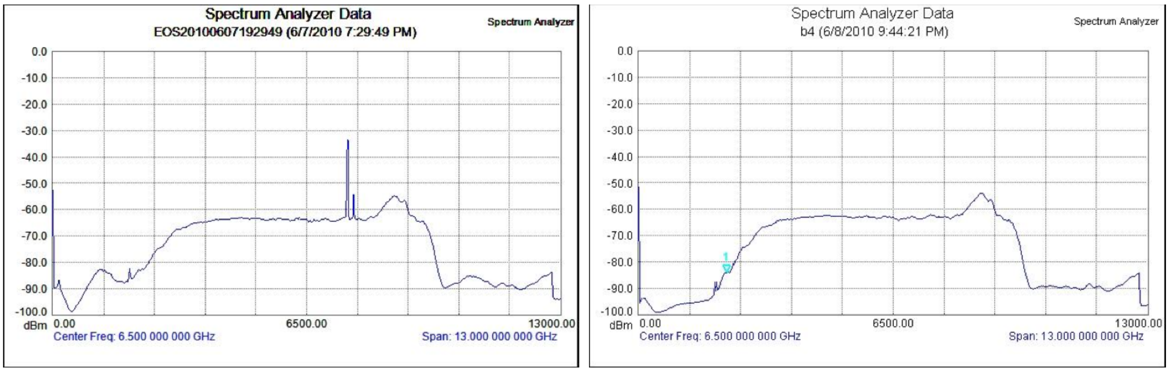

Figure 4.1: Noise survey. Left : spectrum taken a the FD building Los Leones. Right : Spectrum taken on the tank Vieira.

4.1 Detector developments

Noise survey

A noise survey was carried out to estimate the noise pollution in the microwave band at the Auger site. The survey was achieved with an ultra wide band [2 - 18]GHz spiral antenna circularly polarized, and two cascaded low noise amplifiers AM48 L4003 of 38 dB of gain each, a nominal bandwidth of [4 - 8]GHz and a noise figure of 2 dB. We performed the survey where the first prototype is planned to be installed, i.e. in front of the Los Leones FD building. In Fig 4.1 are illustrated the spectra recorded on the roof of the FD building Los Leones (left), and on the tank Vieira (right) which is situated close to Los Leones. Two peaks between 7.5 and 7.8 GHz from the FD communication are present near Los Leones and disappear if the antenna is placed far enough from the FD building. From the spectra, the frequency band [3 - 9]GHz exhibits no peaks when the antenna is placed in the array. In this large band, the C-band (3.4-4.2 GHz) is an interesting choice. This band was originally chosen for satellite broadcast because of the good propagation of in atmosphere at these wavelengths. Therefore, this band is adapted for us for physical reasons, and in addition the antenna and the amplifier are already developed for commercial purposes and can be found really inexpensive. This band is chosen for the first setup of EASIER.

Setup components

Overview of the setup A scheme of the complete setup is presented in Fig. 4.2. In the scheme, the blue blocks represent the EASIER components, whereas the pink ones are Auger SD components. The red connections feature the radio signal lines and the dashed line the power supply circuit.
The setup is largely composed of commercial equipments assembled together.

- The antenna we chose is a TV satellite antenna, it is already equipped with a high gain amplification. On the same line is carried the power supply for the amplification and the output signal.
- the bias Tee split the radio signal and the power supply voltage.

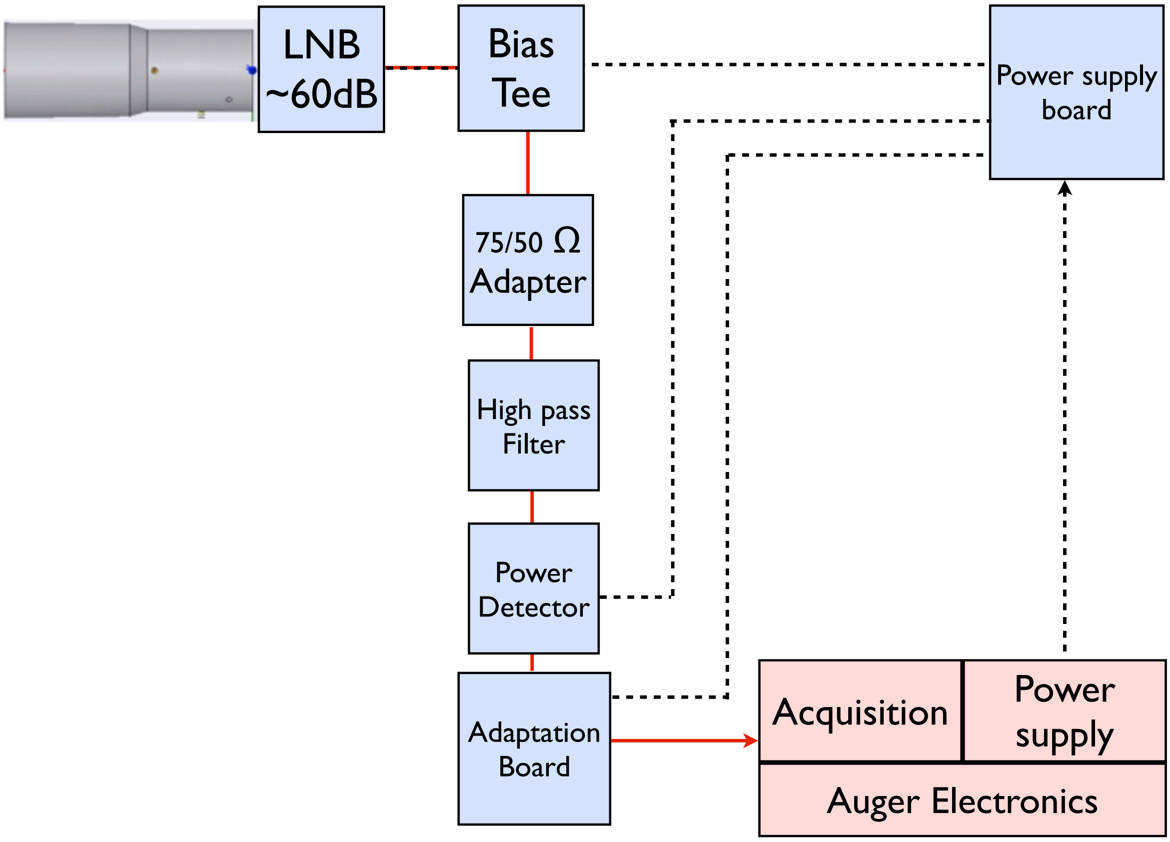

Figure 4.2: Scheme of the complete detector microwave band

- the impedance adapter adjusts an impedance of 75 Ω, standard in TV equipment, to 50 Ω widely used in RF electronics component.
- the high pass filter is added to get rid of any low frequency modulation
- the power detector integrates the RF signal in its power envelope.
- the adaptation board accommodates the right dynamic range to fit into the Auger acquisition.
- the power supply board derives a part of the Auger surface detector power and feeds it to the active element of EASIER.

Antenna The antenna chosen for the first setup is a Golden Interstar GI-301SC. These commercial products embed also the amplifier, they are composed of a feed horn antenna and of a Low Noise Block. A picture of the LNBF used for the first setup is shown Fig. 4.3 (left). The receiving part is the metallic cylinder, a wave guide, it is used to collect the electromagnetic waves from the free space. The dimensions of the cylinder set the frequency band. The radiator itself is placed at the bottom of the waveguide an is a quarter wave monopole antenna. The signal collected is fed to the LNB. It is first amplified by a large factor,

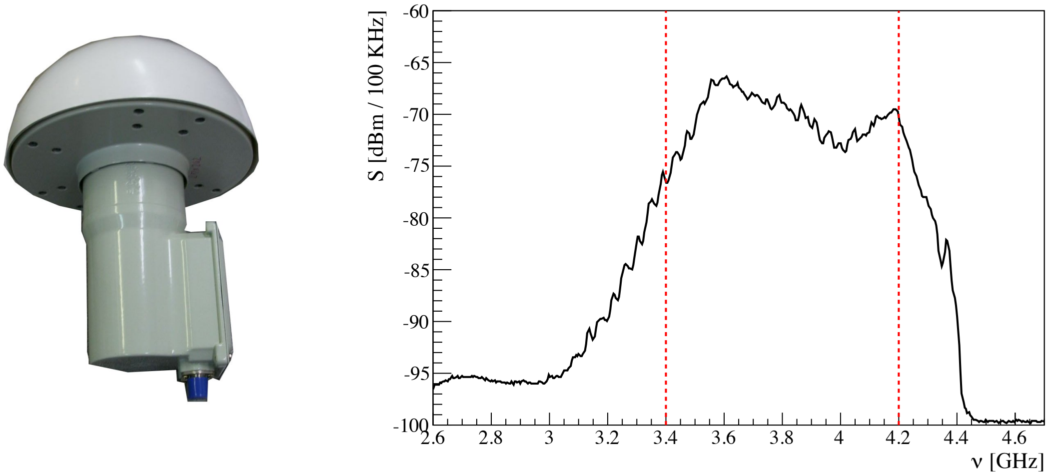

Figure 4.3: Left: Picture of LNBF GI 301SC with its scalar ring and radome. Right: Spectra of the 7 first antenna installed. The Y axis is the power integrated on 100 kHz band. The red dashed lines set the boundaries of the nominal bandwidth.

then the signal is mixed with fixed frequency signal from a local oscillator at $f_{LO} = 5.15$ GHz to shift the signal at lower frequencies. This shift is performed for two reasons, at lower frequencies the electronics is less expensive and the signal suffers less attenuation through the cable. From a collected signal at frequency f_C the operation of mixing generates two signals, one at the frequency sum $f = f_{LO} + f_C$ the other at the frequency difference $f = f_{LO} - f_C$. The signal at higher frequency is filtered and the reception band is shifted from [3.4-4.2]GHz to [1.75-0.95]GHz. The signal is transmitted on a coaxial F connector on a 75 Ω load.
As the power supply of the active part of the LNBF goes also through the same connector than the RF signal, an element named a Bias Tee is needed to separate the RF signal from the DC component.
Then the impedance of the RF signal line is adapted from 75 Ω to 50 Ω which is the impedance of following stages.
In order to reduce the backward lobes, and to enlarge the field of view of the antenna, we mounted a scalar ring. The comparison of patterns in these two cases is presented further in section 4.3. A radome made of fiberglass protects the antenna from rain. A typical spectrum recorded at room temperature is shown in Fig. 4.3 (right). The bandwidth is approximately [3.4 - 4.2]GHz and the spectrum is not flat showing variations of gain with the frequency up to 5 dB in this band.

Power detector The power detector returns a low frequency, almost DC, voltage whose value is proportional to the input power is log scale. In this band, the power detector, Analog Device AD8318 [91], was chosen for its large bandwidth and wide dynamic range. The company Minicircuit markets this electronic chip embedded in a board already with connectors on it. We chose this device Minicircuit ZX47-50 [92] for convenience. Its picture and typical characteristic supplied in data sheet are shown in Fig. 4.4.

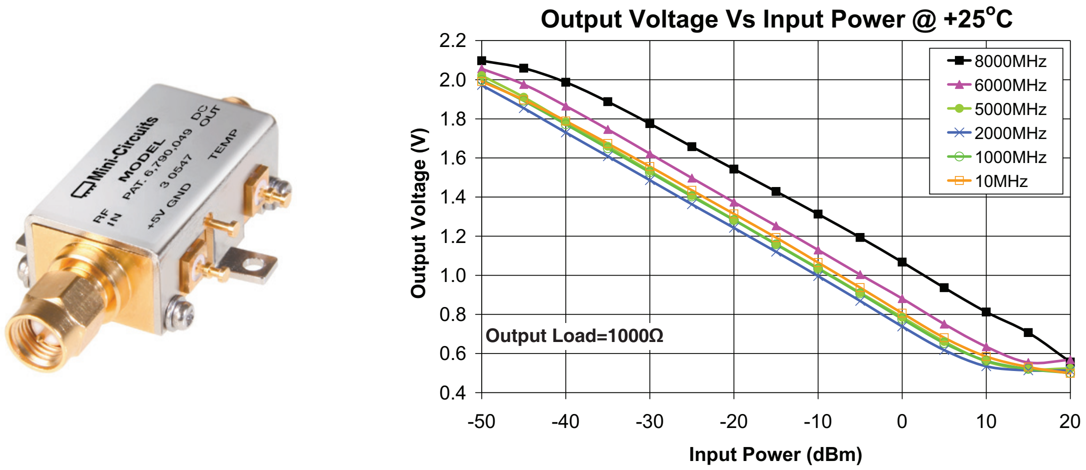

Figure 4.4: Left: picture of the power detector. Right: supplied calibration curve from 10 MHz to 8 GHz (from [92]).

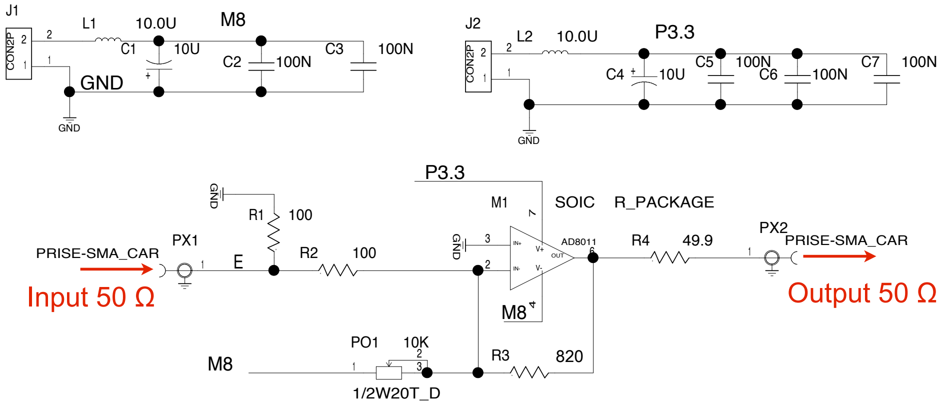

Figure 4.5: EASIER board scheme, see text

Adaptation board The adaptation board is designed to transform the signal at the output of the power detector so that it fits the front end input range and covers the required dynamic range. As the variations of the mean noise power and the expected signal are uncertain, it was chosen to cover 20 dB in power and we foresaw an adjustable voltage offset. The main functionalities of the EASIER board are an amplification with a fixed gain and the addition of an adjustable voltage offset controlled by a variable resistance. The electronic circuit is shown Fig. 4.5. The gain is set by the ratio $-\mathrm{R3}/\mathrm{R2} = -8.2$, the offset is taken from a stable voltage (M8) and is modified with the adjustable resistor P01. The sum of the amplified signal and the offset are then divided by a voltage divider $\mathrm{V}_{\mathrm{out}} = (\mathrm{R}_{\mathrm{coax}}/(\mathrm{R4} + \mathrm{R}_{\mathrm{coax}})) \cdot \mathrm{V}_{\mathrm{in}}$. As the output impedance is $R_{coax} = 50\,\Omega = R_4$, the signal is divided by 2 and the final amplification factor is -4.1.

Power supply board The power supply board is designed to distribute the power from the SD TPCB (Tank Power Control Board) to the active elements of EASIER. The voltage

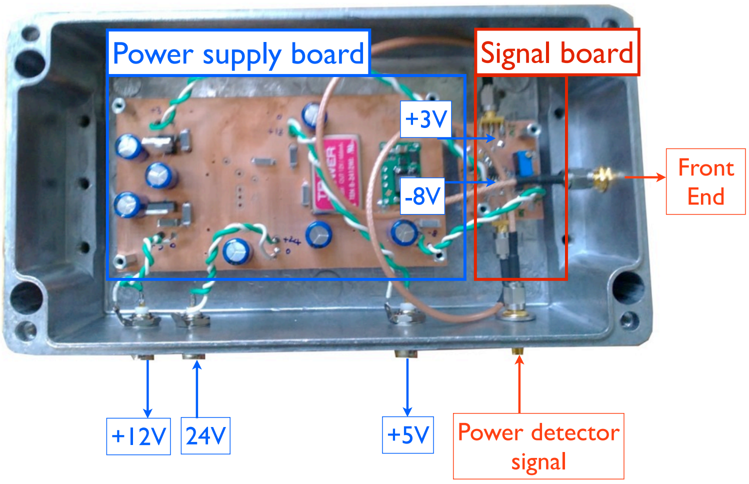

Figure 4.6: EASIER boards in their metallic box.

level delivered by the TPCB is converted to :

- +12 V to the LNBF
- +5 V to the power detector
- +3 V to the EASIER Board
- -8 V to the EASIER Board

The nominal voltage delivered by the TPCB is 24 V, but can vary under the variations of the power delivered by the solar panels. The two EASIER boards, are shown in a metallic box in Fig. 4.6. The prototypes were developed at LPNHE and 8 units were wired at the laboratory too. The picture and description of the electronic box is shown in Fig. 4.6.

Installation of the detectors

The first setup installed is a complete hexagon (7 detectors) centered on the tank Nene (local station ID: 342). The location of the EASIER detectors, in front of the FD building Los Leones, was chosen for a hybrid measurement of air showers, i.e. SD, FD and EASIER.

Installation The first installation was carried out the 3rd week of April 2011. The date of installation are reported in Appendix B. It is centered on the station Nene (342), surrounded by Bastille (333), Concorde (332), Magali (344), Leandro (341), Jose Maria (419) and Paloma (343).
The antennas and electronic boxes were brought in luggage to Malargüe. The mechanical part to integrate the radio detector with the SD tank was found on site. It consists of a

plastic pipe with one side driven in the ground and the antenna attached at the other side with the main lobe pointing to the zenith. Before the installation in the fields we tested the operation of the detector at several stages of the electronics chain:

- recorded a spectrum with a spectrum analyzer at the output of the antenna
- measured the voltage after the power detector, and after the adaptation board with a portable oscilloscope
- recorded FADC traces after the whole acquisition chain, i.e. when the detector is in place and connected to the SD electronics

EASIER detectors operate in slave mode with respect to the SD station and thus traces are recorded only when a T3 trigger is issued. The T3 trigger are issued only a few times per day because it requires a coincidence between three SD detectors. To be able to test the complete chain of detection during the installation, without waiting for the data production, a dedicated software was developed. It is a modified version of the local trigger that is uploaded in the control board of the SD station and records the FADC traces when a T2 (a local trigger with a 20 Hz rate) is issued.

The first step in the installation is to test the integration of the mechanical and electronic setup with the tank. We performed this first test on the tank Jamie next to the assembly building in Malargüe. We detected strong pulses with a power larger than 10 dB above the noise level shown in Fig. 4.7 (left) with a large rate. To understand the origin of these pulses we made several measurements:

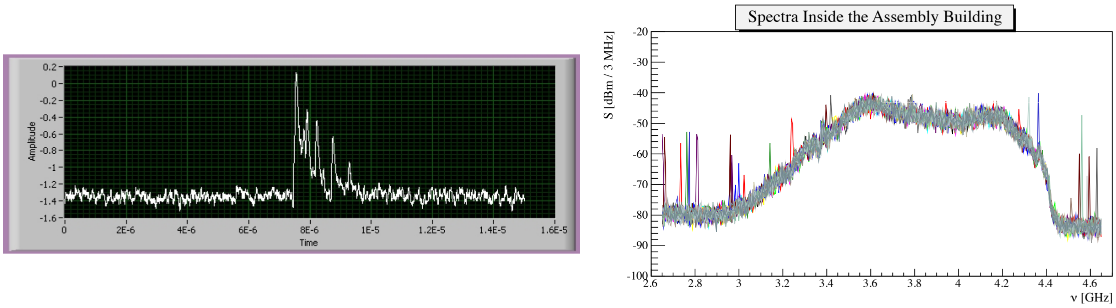

Figure 4.7: Left: Pulse observed after the power detector next to the assembly building. Right: superposition of spectra taken inside the assembly building. The spectra were taken with the spectrum analyser on the *peak mode* option (cf Appendix A).

- we supplied the electronics with a fixed power supply (and not the power supply board): we still observed some pulses.
  ⇒ The pulses don't arise from a radiation of the power supply.
- We disconnected the antenna : the signal was then really different but we still observed some pulses.
  ⇒ The pulses may arise from a bad ground isolation, i.e. if a transient signal is captured by the metallic part of a circuit element like the power detector, and if this part is not well linked to the ground, then a signal can appear.

- we recorded spectra of the antenna inside the assembly building that exhibits lots of peaks at various frequencies (cf. Fig 4.7(right)).
  ⇒ the noise in the environment of the assembly building is important and transient pulses may come from electronic devices emitting at these frequencies, or communication link.

We decided to link the electrical ground of the power detector to the ground of the power supply board. We also tapped the electronics elements to the box with conductor tape to insure a continuity of ground. With this shielding, the pulses remained frequent. We concluded that their origin can be caused by transient noise from the human activity. We have decided to test if in the pampa the noise would disappear with the first complete installation. We prepared eight sets ready to install (seven to be installed and one spare).
The first installation in the fields was carried out the 15^{th} of April on the tank Paloma. The process for the installation is in four steps:

1. **mechanics installation:** the plastic pole with the antenna at its top is driven into the ground and tied to the tank. The electronic box is placed on the SD electronic box.

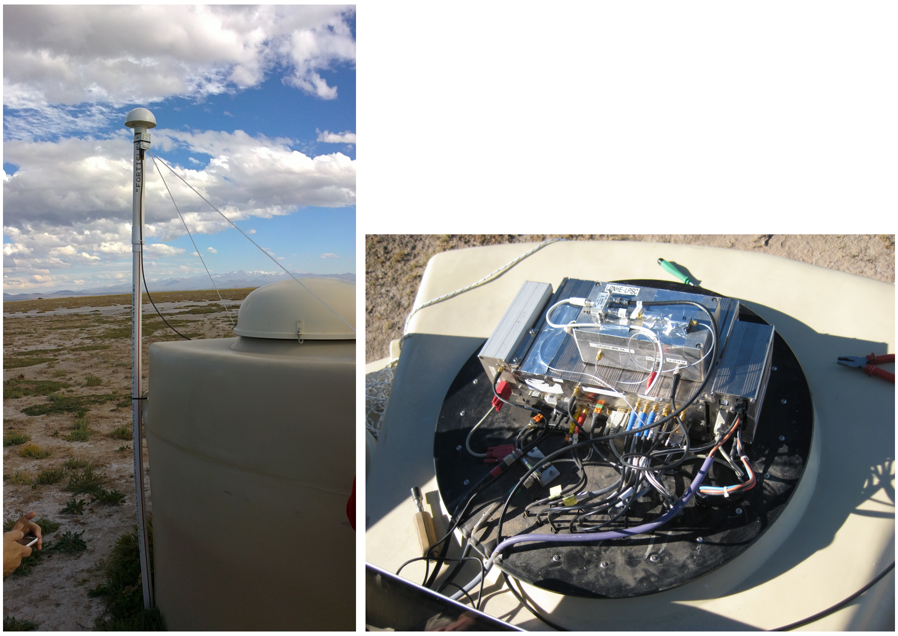

Figure 4.8: Left: antenna integrated with the SD tanks. Right: EASIER electronics box on top of the SD electronics.

2. **spectrum acquisition:** we recorded spectra with the spectrum analyser on *peak mode* to check if the place is noiseless. The superposition of spectra in Fig. 4.9 do not show the peaks as it was observed in the previous tests.
3. **noise level measurement:** the noise level is measured after the power detector to have an absolute reference of the noise.
4. **offset adjustment:** the voltage after the EASIER board is measured and the offset is adjusted to -1 V the middle of the input dynamic range of SD FADC.

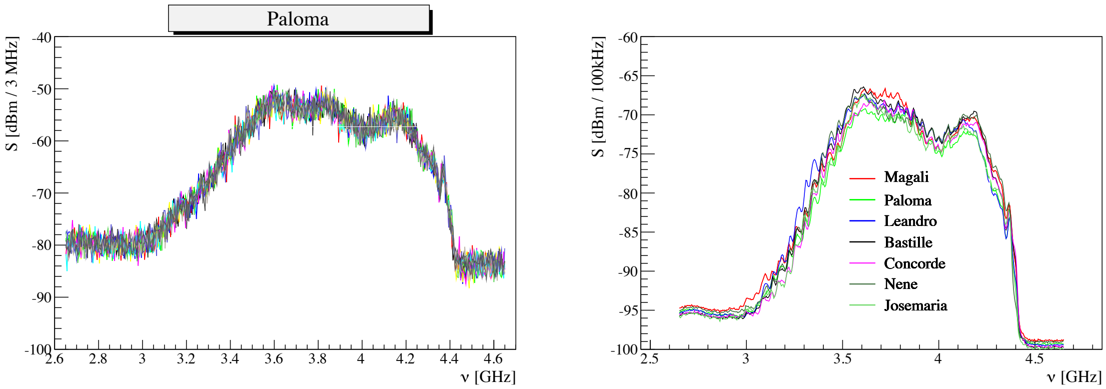

Figure 4.9: Left: Superposition of spectra recorded during the installation (here on Paloma tank). The spectrum analyser option is *peak mode*. No peaks are detected compared to the spectra taken at the assembly building (cf. 4.7). Right: Spectra during the installation of the seven prototypes. The spectra analyser option is *RMS mode*

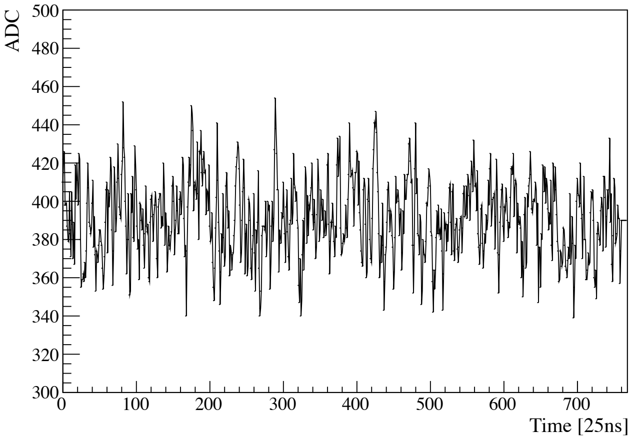

Figure 4.10: Monitoring power trace in ADC counts

5. **check of the complete installation:** FADC traces are recorded on the UB in order to have a final calibration between the noise level and the mean level in ADC counts.

In the next three days, the other six antennas were installed following the same process. The spectra taken of each antenna at the installation in RMS mode are shown in Fig. 4.9.

First data

Monitoring The first setup has been running in a stable way up to now for more than two years. In the first months a specific trigger, recording random data every 10 or 20 minutes, was set to be able to check the trace itself rather than just the mean parameters supplied by the SD monitoring. A typical radio trace of background noise is represented in ADC counts Fig 4.10 and the variation of the baseline during one week is shown in Fig 4.11 (left). The daily modulation is of the order of 100 ADC or 2 dB and it is not completely understood.

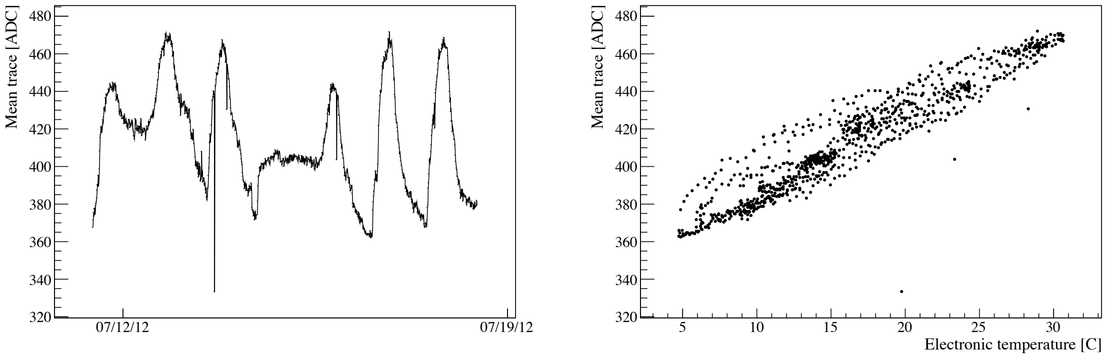

Figure 4.11: Left: variation of the baseline in ADC counts over one week for station Nene. Right: the baseline as a function of SD electronic temperature

A clear correlation with the SD electronics temperature can be seen Fig. 4.11 (right). Most likely the LNB gain has a variation with the external temperature.

First GHz signal observed On the 30th of June 2011 at 3:17 o'clock an air shower with an energy of (13.9 ± 1.3) EeV and a zenith angle of (29.7 ±0.3) degrees has triggered the surface detector. The impact point on ground, $(\text{easting}, \text{northing}) = (465012 \pm 42, 6077615 \pm 50)$ m, is well contained within the GHz hexagon. Los Leones was shut down at the time of this event, due to strong wind. The footprint on the array and the reconstructed lateral distribution function are illustrated in Fig. 4.12. Nene was the station closest to the shower axis at a distance of (136 ± 40) m.The uncertainty on the distance of the stations to the shower axis gives a large uncertainty on the estimation of the expected GHz signal. The recorded traces for Nene from the low gain of the PMTs together with the recorded GHz signal are illustrated in Fig. 4.12. There is a clear time coincidence between the GHz signal and the signal produced by the air-shower particles. The GHz signal is up to two bins in advance of the PMT signal, corresponding to a time advance of 25 to 50 ns.

The radio signal is very likely from the air shower origin and not a noise coming from the tank for two main reasons:

- the radio signal appears before the signal of particle in the FADC trace. The GHz signal is up to two bins in advance of the PMT signal, corresponding to a time delay of 25 to 50 ns. The transit time of a single photo-electron in a EMI9350 8" tubes (slightly smaller than SD ones) is 70 ns with a dispersion of about 7 ns [93]. We expect a larger delay in the Auger PMTs. We measured the response time of the mini-circuit power detector to be about 35 ns. Assuming that the amplifier chains and cables introduce roughly the same time delay in both systems we obtain an expected time delay of the PMT pulse w.r.t. the GHz pulse of at least 35 ns.
- we checked on other SD events that the particle signal was not related to the radio signal. The amount of light in the water Cherenkov detectors and thus the intensity in the PMT and the cable that follow can be excluded as an origin of the microwave signal observed.

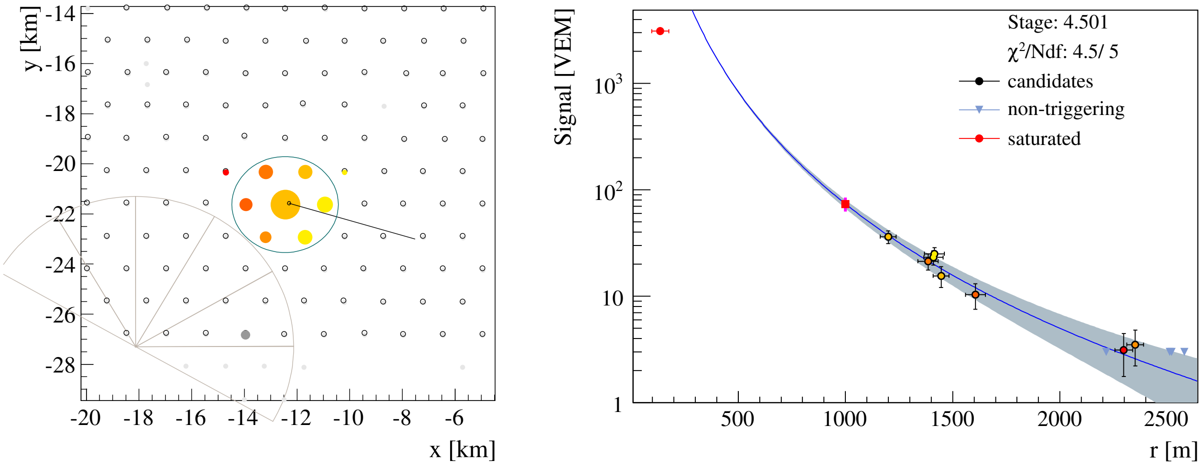

Figure 4.12: (left) Footprint on the array. The ellipse surrounds the GHz hexagon. (right) Lateral distribution function.

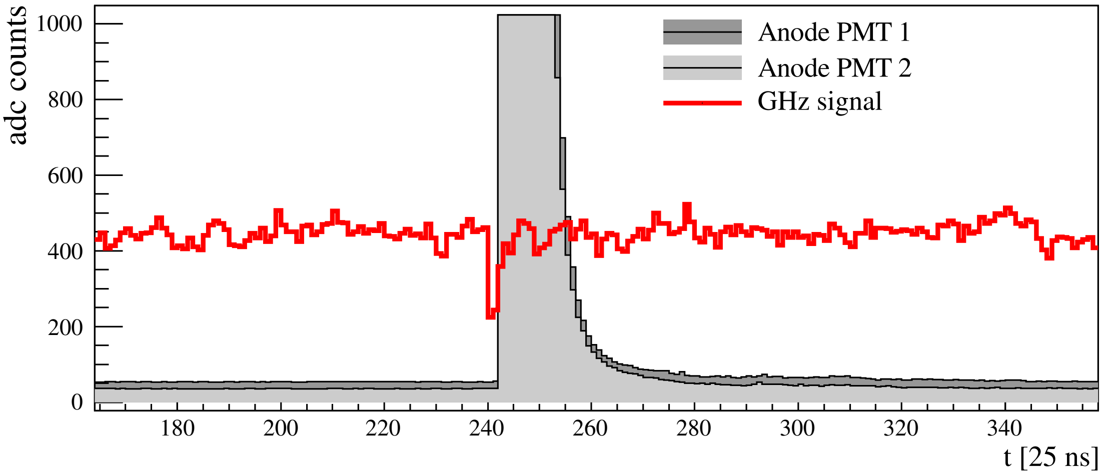

Figure 4.13: FADC traces from the anodes of the PMT 1 and PMT 2 together with the GHz trace.

The recorded signal is the first detection of an air shower emission in the C-band. The interpretation on the origin of the emission is difficult because the distance from the antenna to the shower axis is small. The observed pulse could arise from an isotropic signal enhanced by time compression or from a coherent signal as observed in the VHF band. For a more detailed discussion, see chapter 5. To confirm this detection, and to characterize the signal observed, we decided to extend the EASIER GHz array to 61 units. The system being mainly of commercial origin, and rather inexpensive, the assembling of 60 more units was made in less than six months.

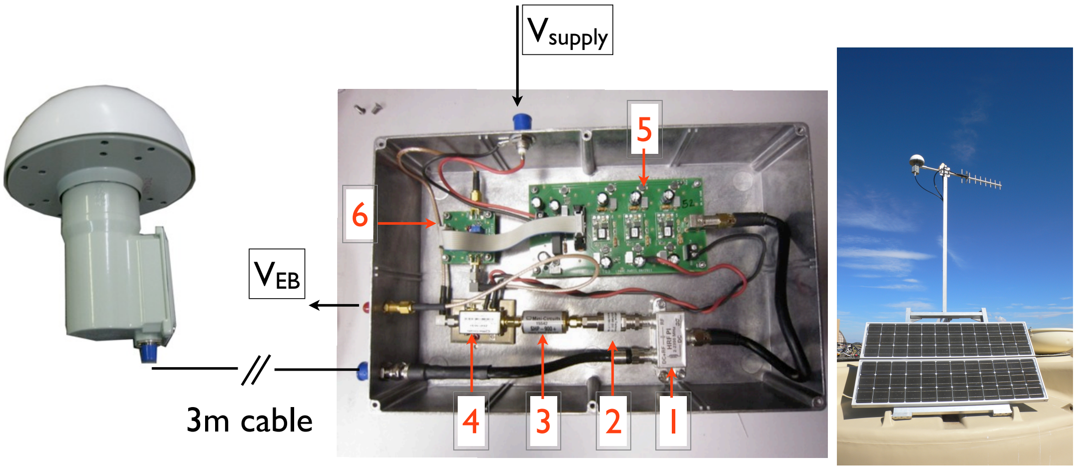

Figure 4.14: Left: electronic box of the 2nd GHz setup. The output of the LNBF is P_{in}, the voltage V_{out} is the radio signal transform by the electronic chain : 1: Bias tee; 2: 75-50Ω adapter; 3: high pass filter; 4: power detector Minicircuit ZX 47-50; 5: power supply board; 6: EASIER board. Right: Picture of the mechanical installation of EASIER antenna for the second setup

EASIER61

The extension of the EASIER array was carried out around one year after the first installation, in April 2012. 54 new detectors were installed with an improved mechanical integration. The first seven detectors remained unchanged apart from change in the attachment to the tank. The times of deployment are given in Appendix B.

Setup In the EASIER61 setup, just a few changes with respect to the first hexagon configuration have been made and we will describe them next.
The antenna, a commercial TV satellite LNBF, has the same design but the model is now a WS international ESX241.
The power detector underwent an important change. The commercial version of the ZX 47-50 is a power detector with a capacitor at its output. This capacitor is meant to filter the noise at the output of the logarithmic amplifier but makes the power detection less sensitive to short pulses due to a longer rise time. We decided to remove this capacitor on new detectors. The signal electronic board was not changed at all and the power supply board was slightly modified. All the electronic items are now integrated in a metallic box (cf Fig. 4.14), the RF chain, the power detector and the electronic boards. 60 boxes were prepared at LPSC (Grenoble) and checks and calibration were made at LPNHE (Paris).

Location The completed hexagon of 61 detectors covers now an area of 193.5 km^2. This is the largest radio array in the C-band. In Fig 4.15 (left) it is illustrated the location of the radio array at the Pierre Auger Observatory. Regarding the polarization of the antenna, the array has 33 antennas oriented to have a North-South polarization, and 28 East-West. Their layout is illustrated in Fig 4.15 (right).

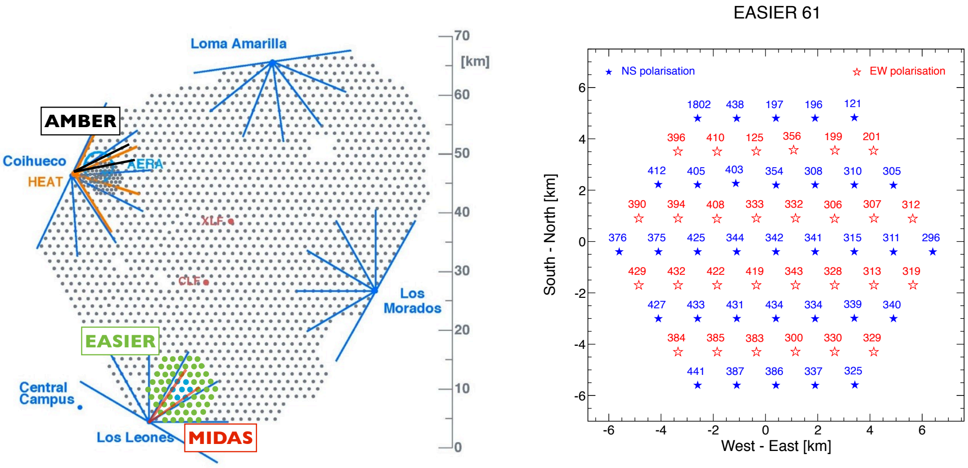

Figure 4.15: EASIER GHz arrays. Left : EASIER GHz arrays into the Auger array, in blue the first setup installed in 2011, in green the extension completed in 2012. The field of view of the other microwave detection prototypes (MIDAS and AMBER) are also displayed Right : polarization distribution of the complete array

Mechanics The mechanical integration was simplified, it consists now of a pipe that is fixed to the support of the SD communication antenna (see picture in Fig 4.14 (right)), and the EASIER antenna is held by a bracelet . This simplification allowed us to install the 54 detectors in 5 days with two teams of two persons.

After the installation of a few detectors, we realized that the radio baseline was dependent on the voltage supplied by the SD batteries. The EASIER design did not include a voltage regulator on the power supply board. The SD battery voltage, which is the source of power for EASIER, has daily variations as well as seasonal ones because of the modulation of the power delivered by the solar panels. It can vary from $\simeq 23\,\mathrm{V}$ to $30\,\mathrm{V}$. When the voltage at the input of the power supply board varies from the nominal value of $24\,\mathrm{V}$, the $-8\,\mathrm{V}$ output varies and since the offset added to the radio baseline is directly related to this voltage (cf Fig. 4.5) the radio baseline was strongly dependent on the changes of battery voltage. The resulting variation on the radio baseline can lead to saturation of the FADC and to a reduction of the dynamic range available for the microwave signal.

We had to find a fast solution and with material available in Argentina. To circumvent this problem, we added a $24\,\mathrm{V}$ regulator in each box. This device insures an output voltage of $24\,\mathrm{V}$ if the input voltage is larger than $\mathrm{V_{th}} = 24 + \mathrm{V_{drop\_out}}$. The chosen model is LM7824 with a drop out voltage of approximately $1.5\,\mathrm{V}$. This was the model with the smallest $V_{\mathrm{drop\_out}}$ available near Malargüe. An example of the measured regulated voltage is shown Fig. 4.16 (left) and the radio baseline as a function of the input voltage in the same figure (right). The regulated voltage is slightly different from $24\,\mathrm{V}$ and is stable above $26\,\mathrm{V}$ while still depending on the battery voltage below. This variation will be corrected for in the calibration procedure.

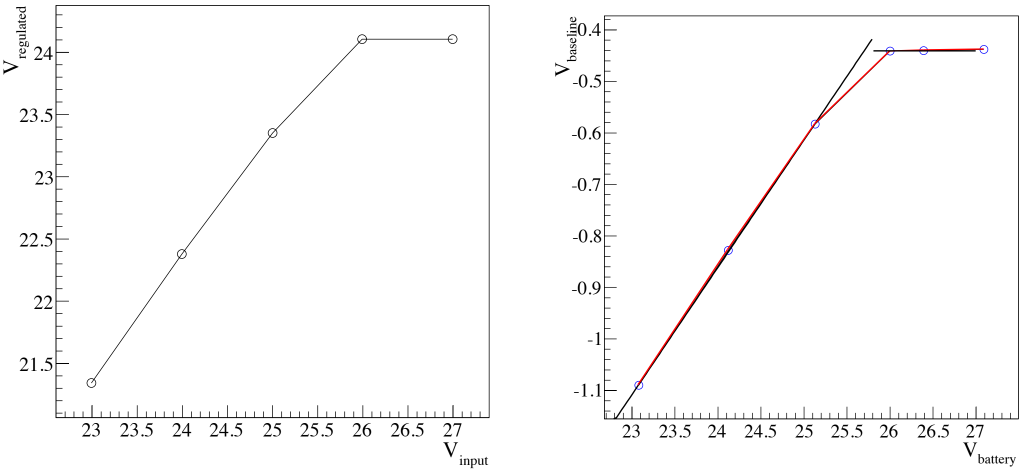

Figure 4.16: Left : Regulated voltage as a function of supplied voltage. Right: Output of the EASIER board as an function of supplied voltage.

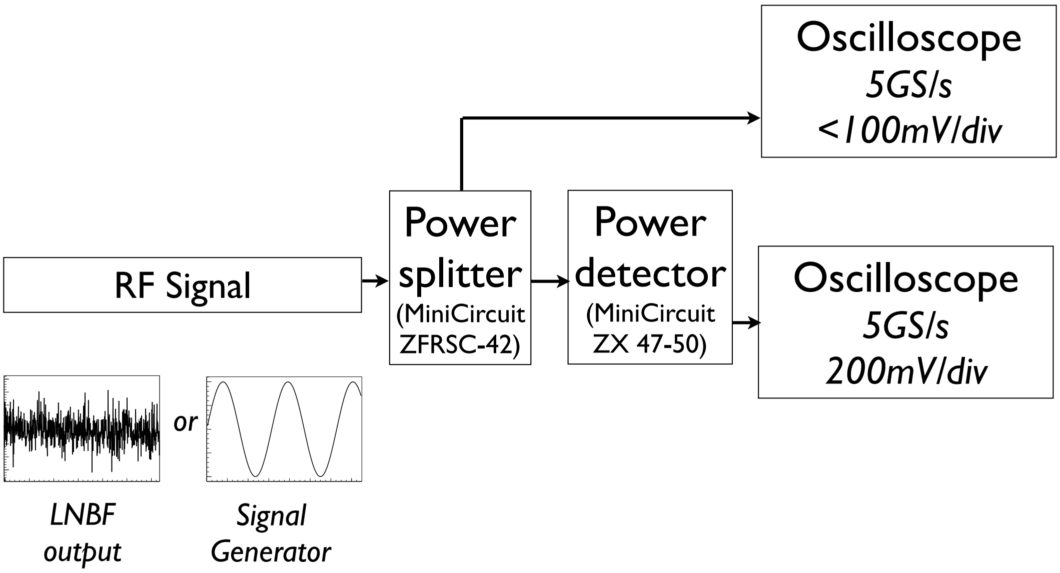

Figure 4.17: Setup for the calibration of the power detector.

4.2 Electronics calibration

In this section, I will describe the measurements performed in the laboratory in order to calibrate and understand the detector response.

Power detector

The power detector transforms the RF signal into a DC voltage and thus is one of the most important element in the electronic chain. The data-sheet of the power detector Minicircuit ZX47-50 supplied by the constructor shows that the characteristic function is dependent on the signal input frequency as shown in Fig. 4.4 (right) and thus we measured in a first step its response as a function of the frequency. The calibration curves are given for input sine wave at frequencies from 10 to 8000 MHz in steps of 1 GHz. EASIER antenna output is between 950 and 1750 MHz and is approximately a white noise with a flat spectrum.
We characterized the power detector in the frequency range of EASIER with the setup shown in Fig. 4.17. First the signal generated is a sine wave at different frequencies and amplitudes, the signal is split with a power splitter Minicircuit ZFRSC-42 [94] before the power detector and one part, the RF signal, is acquired by the oscilloscope the other is fed to the power detector and then recorded. The oscilloscope is a Lecroy sampling at 5 GHz with a resolution of 8 bits. The RF power is computed on a 50 Ω impedance, $P_{RF} = V_{RMS}^2/50$. The RF power and the voltage output of the power detector are averaged over the trace of 2 μs. The

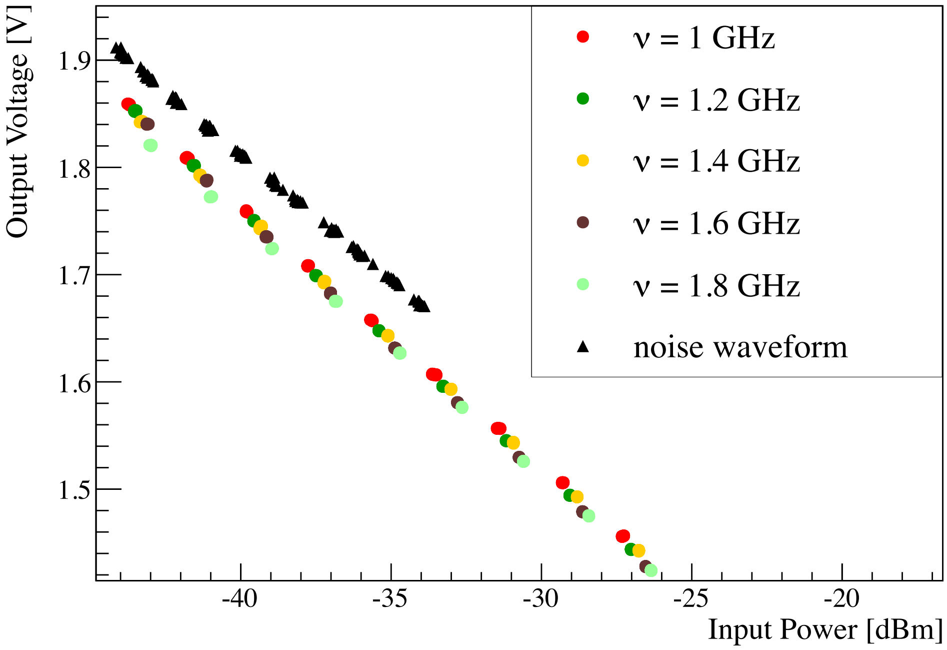

Figure 4.18: Calibration curves for sine waves and noise.

calibration curves of sine waveform input are shown in colored dots in Fig. 4.18. They are well in agreement with each other one the spanned frequency band.
Then the sine wave signal is replaced by the output of a LNBF, followed by an adjustable attenuator. By this mean, we can characterize the response of the power detector to the same type of noise as in real condition. The calibration curves of one power detector for the noise input are represented by the black triangles in Fig. 4.18 . The calibration curve for an input sine wave at 1 GHz and for a noise waveform input can be described by:

$$\text{sine at 1 GHz: } V_{\text{PD}} = -0.0244 \cdot P_{\text{dBm}} + 0.789\ V \qquad (4.2.1)$$

$$\text{noise waveform: } V_{\text{PD}} = -0.0234 \cdot P_{\text{dBm}} + 0.877\ V \qquad (4.2.2)$$

The slope is slightly different and the intercept differs by about 100 mV. The calibration of the rest of the electronics was mainly performed with sine waveform, whereas the physical signal detected by the antenna is a noise waveform. We will account for the different calibration curves in the next paragraph.

Power detector + EASIER board

The output of the electronic chain of EASIER is a linear function of the logarithm of the input power. Thus to characterize this transformation we measured the slope defined in Eq. 2.3.5 and the offset that sets an absolute scale. The slope of the EASIER board is set with the electronics board gain and was measured in laboratory with sine wave input. The offset is adjustable and was first set in laboratory and then shifted during the installation to accomodate the baseline to the right level in the input dynamic range of Auger electronics.

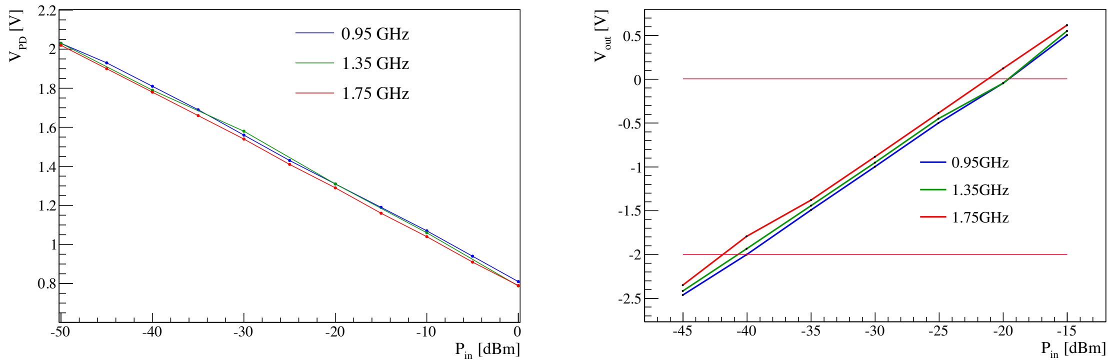

Figure 4.19: Left: Calibration curve of one power detector at three frequencies. Right: Calibration curve of the set power detector and EASIER board. The horizontal red lines shows the dynamic range determined by the Auger SD electronics.

First setup All the power detectors of the first setup were tested. A calibration curve is given in Fig. 4.19 at three different frequencies: 950, 1350, 1750 MHz. The mean fitted slope of the eight tested power detectors (seven installed + one spare) at the same three frequencies is found to be $S_{\mathrm{PD}} = -0.0245\,\mathrm{V/dB}$. One complete set of electronics was calibrated, the calibration curve of the power detector and the EASIER board are shown in Fig. 4.19. The voltage offset is set so that the output of the EASIER board is -1 V for an input power of -30 dBm at 1350 MHz. Taking the Eq. 4.2.1 we can then retrieve the transformation of the EASIER board:

$$\text{at } 1\,\mathrm{GHz} \text{ and } P_{\mathrm{in}} = \text{-}30\,\mathrm{dBm},\ V_{\mathrm{PD}} = 1.521\,\mathrm{V} \text{ and } V_{\mathrm{EB}} = \text{-}1\,\mathrm{V} \tag{4.2.3}$$

then the calibration formula for the EASIER board only is:

$$V_{\mathrm{EB}} = -4.1 \cdot V_{\mathrm{PD}} + 5.23\,\mathrm{V} \tag{4.2.4}$$

If the input signal is a noise waveform, then V_{PD} is computed with Eq. 4.2.2.
During the installation, the voltage offset was shifted in order to place the noise level at the center of the dynamic range (cf. section 4.1). To obtain a final calibration we have to account for this shift. The absolute power at the output of the antenna is measured with the power detector and calculated with the calibration curve Eq. 4.2.2 for a noise waveform. Then after the shift of the baseline at the center of the dynamic range of the SD FADC, we recorded FADC traces that give us the level of the baseline in ADC counts. The measured power detector voltage, the deduced power and the final level of the baseline are given in Table 4.1. Accounting for the Auger Front End electronics, i.e. a gain of $-1/2$ and a sampling in a 10 bits FADC, the relation between ADC and input power is :

$$\#ADC = -0.5 \cdot 1023 \cdot V_{\mathrm{EB}} \text{ with } V_{\mathrm{EB}} \propto (-4.1) \cdot (-0.0234) \cdot P_{\mathrm{dBm}} \tag{4.2.5}$$

we have :

$$\#ADC = -511.5 \left(\frac{\mathrm{ADC}}{\mathrm{V}}\right) \cdot 0.096 \left(\frac{\mathrm{V}}{\mathrm{dBm}}\right) \cdot P_{\mathrm{dBm}} + ADC_{\mathrm{offset}} \tag{4.2.6}$$

or

$$P_{\mathrm{dBm}} = \frac{\#ADC - ADC_{\mathrm{offset}}}{-511.5 \cdot 0.096} \tag{4.2.7}$$

station	V_{PD} [V]	Power [dBm]	baseline [ADC]
332	1.5	-26.7	499
333	1.51	-27.1	474
341	1.53	-27.9	467
342	1.53	-27.9	477
343	1.57	-29.6	517
344	1.5	-26.7	463
419	1.48	-25.8	467

Table 4.1: Measurements performed during the installation to obtain a final calibration

where #ADC is the number of ADC counts, and ADC_{offset} the offset induced by the power detector and the EASIER board. Thanks to the measurement at the installation we can retrieve ADC_{offset}, they are given for each station in Table 4.2.

station	332	333	341	342	343	344	419
ADC_{offset}	-812	-857	-903	-893	-936	-848	-803

Table 4.2: Offset for the seven first detectors to apply in Eq. 4.2.5

Second setup The calibration of the second setup is more complicated because it depends on the voltage supplied by the battery of the SD. We saw in section 4.1 that the baseline of EASIER electronics is dependent of this voltage. A correct description of the baseline has to account the time dependence of the battery voltage. We first describe the calibration we performed in laboratory and then we explain how we recover the power out of the final trace. The electronics box integrates the whole chain, so its input is suited to the impedance of the LNBF output, a F connector on 75 Ω impedance. In addition, in the same coaxial cable, the DC voltage to supply the LNBF is also transmitted. The signal generator used to perform the calibration has an output impedance of 50 Ω and can be damaged by the DC voltage transmitted through the cable. Thus, we connected an impedance adapter between the signal generator and the box, and to cut the DC component a cable with a capacitor was used. The loss induced by these additional stages is taken into account in the following calibration.
The purpose of the calibration is to check the slope of the EASIER and to set the offset voltage to make correspond the input power to the wanted output voltage. For each box we set the offset voltage so that the middle of the Auger dynamic range ($\mathrm{V_{EB}} = -1\,\mathrm{V}$) corresponds to an input power of -28 dBm, at a frequency of 1 GHz. We measured the output voltage for three different input powers: -18 dBm, -30 dBm and -38 dBm. The calibration curves of the 61 boxes are shown in Fig. 4.20 (left). The distribution of the measured slopes is shown in Fig. 4.20 (right), the average slope is found to be $\mathrm{S} = (0.101 \pm 0.001)\mathrm{V/dB}$. The final calibration of the second setup differs from the first setup, Eq. 4.2.4, only by the offset voltage:

$$V_{EB} = -4.1 \cdot V_{PD} + 5.04\,\mathrm{V} \tag{4.2.8}$$

At the installation we added a voltage regulator to correct in part the effect of the voltage supply on the baseline. We characterized all the boxes once the regulator was added to obtain

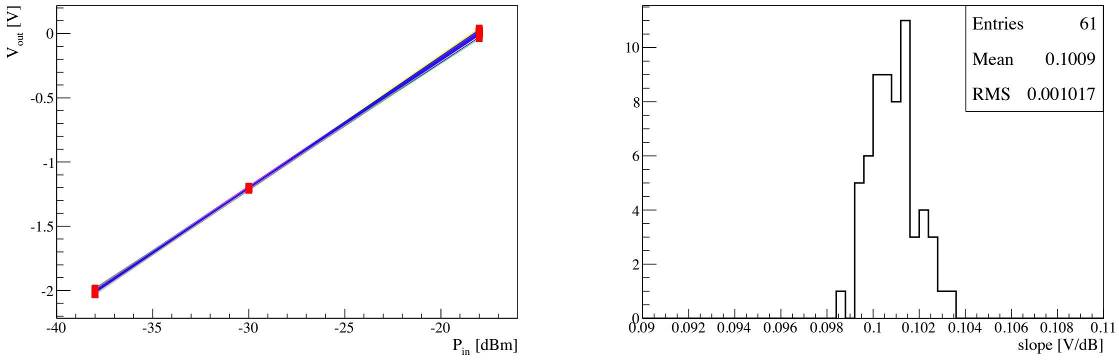

Figure 4.20: Right: Calibration curves of the 61 prepared boxes. Left: Distribution of the slopes

its effect on the original calibration. To recover the laboratory calibration we consider three parameters, the input voltage threshold V_{th} above which the voltage is regulated, the value of regulated voltage V_{reg} and the slope S of the baseline below V_{th}. The response of the EASIER board in Fig 4.16(right) shows that the baseline varies linearly for low values of input voltage. To recover the original output of the EASIER board, we need to add a correction that will depend on the input supplied voltage :

- if $V_{\text{input}} > V_{\text{th}}$: $V_{\text{corr}+} = S \cdot (V_{\text{reg}} - 24V)$

- if $V_{\text{input}} < V_{\text{th}}$: $V_{\text{corr}-} = V_{\text{corr}+} + S \cdot (V_{\text{input}} - V_{\text{th}})$

The response as a function of input supplied voltage was measured for each electronic set. A table with the parameters V_{th}, V_{reg} and S is reported in Appendix B. In addition, the offset set in laboratory calibration was shifted by $V_{\text{shift}} = 600\,\text{mV}$. So at the end the relation between ADC counts and radio power is :

$$\#ADC = -511.5 \left(\frac{\text{ADC}}{\text{V}}\right) \cdot V'_{\text{EB}} = -511.5 \cdot (V_{\text{EB}} + V_{\text{corr}}) \tag{4.2.9}$$

where V_{EB} is the voltage calibrated in laboratory (cf Eq. 4.2.8) and $V_{\text{corr}} = V_{\text{corr}+}(\text{or } V_{\text{corr}-}) + V_{\text{shift}}$. To summarize, to transform the number of ADC counts into a power trace we use equations 4.2.2, 4.2.8 and 4.2.9:

$$P_{\text{dBm}} = \frac{\#ADC}{-511.5 \times 0.096} - \frac{1.44\,\text{V} + V_{corr}}{0.096}. \tag{4.2.10}$$

This power is the result of the background noise amplified first by the antenna gain, then by the LNB gain and attenuated by the adapter 75-50Ω. In order to obtain the power received by the antenna, the LNBF gain has to be accounted for. We do not have a complete characterization of the different LNBFs. As the gain of these detectors can vary by a few dB we will mainly use an estimation of the power relatively to the power of the baseline P_{BL}. The measured power is then:

$$P_{\text{measured}}[\text{dBm}] = P_{\text{BL}}[\text{dBm}] + \frac{\Delta\#ADC}{-511.5 \cdot 0.096} \tag{4.2.11}$$

4.3 Detector Sensitivity

The sensitivity is defined as the minimum microwave flux detectable out of the noise. We present first the expression of the sensitivity for the EASIER detector. Then we present a set of measurements performed to estimate the relevant parameter to compute the sensitivity.

Expression of the sensitivity

Noise fluctuations The noise amplitude sets the limit for a detectable signal. It was shown, for instance in [95] that for an input noise signal with a Gaussian distribution processed by a square law detector, the relation between the mean noise $< P_{\mathrm{noise}} >$ and its fluctuations $\Delta P_{\mathrm{noise}}$ is simply :

$$\Delta P_{\mathrm{noise}} = \sqrt{2} \cdot < P_{\mathrm{noise}} > \tag{4.3.1}$$

When the RF input signal is filtered on a bandwidth $\Delta\nu$ and the output of the square law detector integrated over a time τ for instance with a low pass filter, the standard deviation is lowered by a factor $\sqrt{\Delta\nu\tau}$. In the case of EASIER the input voltage is the LNBF output and the square law detector is the power detector. The output filtering is performed first just after the power detector, and then by the low pass filter of the Auger SD front end. If we account for the factor $\sqrt{2}$ in the integration time:

$$\Delta P_{\mathrm{noise}} = \frac{< P_{\mathrm{noise}} >}{\sqrt{\Delta\nu\tau}} \tag{4.3.2}$$

System temperature In the microwave band thermal noise is the main concern in the detector development. It can be expressed at the output of the amplification stage using the equivalent system temperature, T_{sys} :

$$< P_{\mathrm{noise}} >= k_{\mathrm{B}} \cdot T_{\mathrm{sys}} \cdot G \cdot \Delta\nu \tag{4.3.3}$$

with k_{B} the Boltzmann constant, G the gain of the system, $\Delta\nu$ the bandwidth. T_{sys} is the sum of the antenna noise and the electronic noise temperature.

Antenna temperature The antenna noise temperature is related to the thermal emission of surrounding objects, it is useful to express it as the temperature that would have a black body emitting the same intensity. In the limit of $h\nu << k_{\mathrm{B}}T$ the intensity for a black body is expressed via Rayleigh-Jeans law:

$$B_\nu = \frac{2\nu^2 k_B T}{c^2} \tag{4.3.4}$$

For non black body emission, the same expression is kept replacing the thermodynamical temperature by the brightness temperature $T_{\mathrm{B}} = \epsilon T$. The brightness temperature of the sky at zenith is around 5 K whereas for the ground $T_{\mathrm{B}} \simeq 300\,\mathrm{K}$. To compute the spectral density of power received by the antenna one has to integrate over the solid angle accounting for its gain:

$$P_{\mathrm{ant}} = \frac{k_{\mathrm{B}}}{2} \int_{\theta=0}^{\pi} \int_{\phi=0}^{2\pi} \frac{2\nu^2}{c^2} T_{\mathrm{B}}(\theta,\phi) A(\theta,\phi) \cdot \sin(\theta) \mathrm{d}\theta \mathrm{d}\phi \tag{4.3.5}$$

The factor one half is needed because the black body intensity contains all the polarizations whereas the antenna selects just one. Using the relation between the effective area and the gain ($A_{\mathrm{eff}} = \frac{Gc^2}{4\pi\nu^2}$) and the property of the gain for a loss less antenna:

$$\int_{\theta=0}^{\pi}\int_{\phi=0}^{2\pi} G(\theta,\phi)\cdot\sin(\theta)\mathrm{d}\theta\mathrm{d}\phi = \int_{\theta=0}^{\pi}\int_{\phi=0}^{2\pi} \mathrm{G}_{\max}\cdot \mathrm{g}(\theta,\phi)\cdot\sin(\theta)\mathrm{d}\theta\mathrm{d}\phi = 4\pi \tag{4.3.6}$$

where $g(\theta,\phi)$ is the gain relative to the maximum gain of the antenna, we can express the antenna temperature:

$$T_{\mathrm{ant}} = \frac{1}{\Delta\Omega}\int_{\theta=0}^{\pi}\int_{\phi=0}^{2\pi} T_{\mathrm{B}}(\theta,\phi)\cdot g(\theta,\phi)\cdot\sin(\theta)\mathrm{d}\theta\mathrm{d}\phi \tag{4.3.7}$$

with $\Delta\Omega = \int_{\theta=0}^{\pi}\int_{\phi=0}^{2\pi} g(\theta,\phi)\cdot\sin(\theta)\mathrm{d}\theta\mathrm{d}\phi$
The total power received by the antenna is then:

$$P_{\mathrm{ant}} = k_{\mathrm{B}} T_{\mathrm{ant}} \Delta\nu \tag{4.3.8}$$

Because the brightness temperature of the ground is large, back-lobes have to be well controlled to keep the antenna temperature as low as possible.

Electronics temperature Another contribution of noise arises from the amplification electronics. If the spectral power of noise added by the electronics is N_a, the gain of the device G and the bandwidth $\Delta\nu$, one can define the electronics noise temperature as :

$$T_{\mathrm{e}} = \frac{N_{\mathrm{a}}}{k_{\mathrm{B}} G \Delta\nu} \tag{4.3.9}$$

As noted in the chapter 2, if the gain of the first stage of amplification is large enough, the temperature of the following stages can be neglected.

Minimal flux detectable To estimate finally the minimum flux detectable by our system we compute the flux F_{signal} required to equate the noise fluctuations:

$$P_{\mathrm{signal}} = F_{\mathrm{signal}}\cdot A_{\mathrm{eff}}(\theta,\phi)\cdot G_{\mathrm{LNB}}\cdot\Delta\nu = \frac{< P_{\mathrm{noise}} >}{\sqrt{\tau\cdot\Delta\nu}} = \frac{k_{\mathrm{B}}\cdot T_{\mathrm{sys}}\cdot G_{\mathrm{LNB}}\cdot\Delta\nu}{\sqrt{\tau\cdot\Delta\nu}} \tag{4.3.10}$$

then

$$F_{\mathrm{signal}} = \frac{k_{\mathrm{B}}\cdot T_{\mathrm{sys}}}{A_{\mathrm{eff}}(\theta,\phi)\cdot\sqrt{\tau\cdot\Delta\nu}} \tag{4.3.11}$$

with

$$T_{\mathrm{sys}} = T_{\mathrm{ant}} + T_{\mathrm{e}} \tag{4.3.12}$$

The two main parameters we need to estimate are the effective area and the system temperature. We present now a set of measurements performed on this purpose.

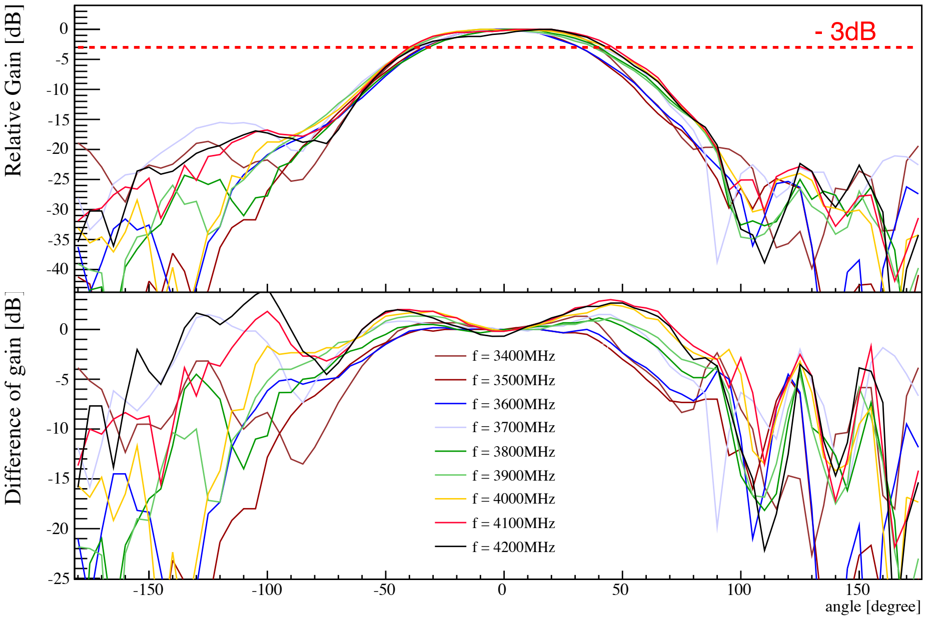

Figure 4.21: Measured relative gain. Upper panel: Pattern of the antenna ESX241 with an attached scalar ring and a radome. Lower panel: Difference of gain of the pattern shown in upper panel with the one of an antenna without scalar ring or radome.

Sensitivity measurements

Power pattern and effective area

The power pattern provides the relative gain, g, of the antenna as a function of the angle. If the antenna is sensitive to very large zenith angle θ, thus detecting the thermal noise from the ground, the antenna temperature is increased significantly. Also the effective area $A_{\text{eff}}(\theta,\phi)$ is directly linked to the power pattern through Eq. 2.3.2. The normalized gain of the antenna ESX241 was measured in an anechoic chamber at the IMEP (Institut de Microelectronique Electromagnetisme et Photonique) at Grenoble. The pattern was measured for the antenna with the scalar ring and the radome (shown in Fig. 4.21 in the upper panel) and without scalar ring or radome. The difference of these two measurement is shown in the lower panel of Fig. 4.21. The opening angle is widened and the backlobes reduced by up to 25 dB.
The maximum gain of the antenna can be calculated using relation 4.3.6. We find for frequencies from 3.4 to 4.2 GHz a mean gain of $G_{max} = 8.75$ dB. From the maximum gain the angular effective area is calculated as follows:

$$A_{eff}(\theta,\phi) = \frac{\lambda^2 \cdot G_{max} \cdot g(\theta,\phi)}{4\pi} \tag{4.3.13}$$

The effective area are represented in linear scale in Fig. 4.22.

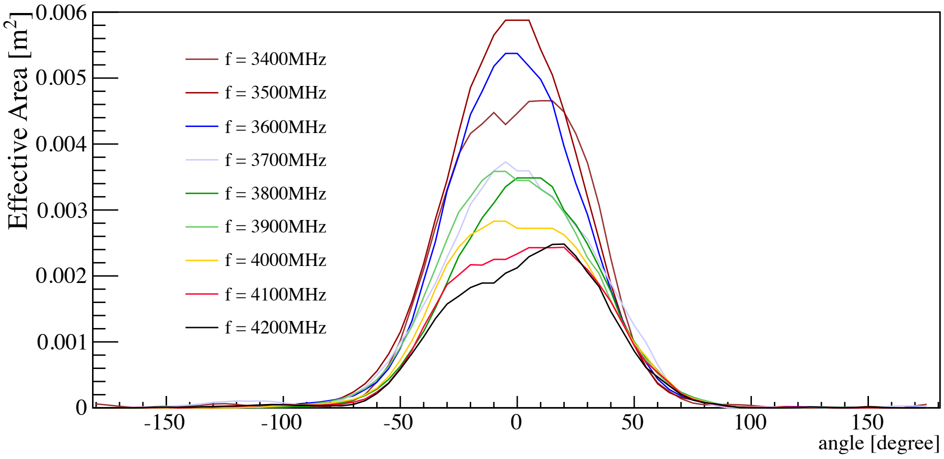

Figure 4.22: Calculated effective area at frequency from 3.4 GHz to 4.2 GHz.

Noise temperature measurements

Noise temperature measurement of a Device Under Test (DUT) are usually performed using the Y-factor method [96]. This method is based on the measurement of the response of a DUT to two known noise power references. Their comparison allows us to retrieve the noise added by the DUT. The Y-factor is the ratio $\frac{P_{\text{hot}}}{P_{\text{cold}}}$, where hot and cold refer to higher and lower noise power input. The temperature added by the DUT is then:

$$Y = \frac{P_{\text{hot}}}{P_{\text{cold}}} = \frac{T_{\text{hot}} + T_{\text{DUT}}}{T_{\text{cold}} + T_{\text{DUT}}} \Rightarrow T_{\text{DUT}} = \frac{T_{\text{hot}} - Y \cdot T_{\text{cold}}}{Y - 1} \tag{4.3.14}$$

This method is particularly suited for electronic devices with no loss between the noise source and the DUT. In case of losses of a factor α between the source of noise and the DUT, Eq. 4.3.14 becomes :

$$T_{\text{DUT}} = \alpha \cdot \frac{T_{\text{hot}} - Y \cdot T_{\text{cold}}}{Y - 1} \tag{4.3.15}$$

Following this method, several measurements were undertaken.

Spectrum comparison We apply the Y-factor method to measure the noise induced by the amplification part of the LNBF. The two noise references are thermal noise received by the antenna when looking either at object at room temperature (T_{hot}) either looking at the sky (T_{cold}).

The measurement of hot temperature is performed recording a spectrum when the antenna points toward a microwave absorber. This material absorbs the radiation around it and reemits it as a thermal emission at its physical temperature. Based on Eq. 4.3.7, the antenna temperature when the brightness temperature T_{B} is constant over the antenna pattern yields to an antenna temperature of T_{B}. Then $T_{\text{hot}} = 300\,\text{K}$.

The measurement of the low temperature was performed during the installation in the fields. We recorded a spectrum with the antenna in its definitive position, i.e. pointing toward the sky. T_{cold} is computed with Eq. 4.3.7and the power patterns in Fig. 4.21. The temperature

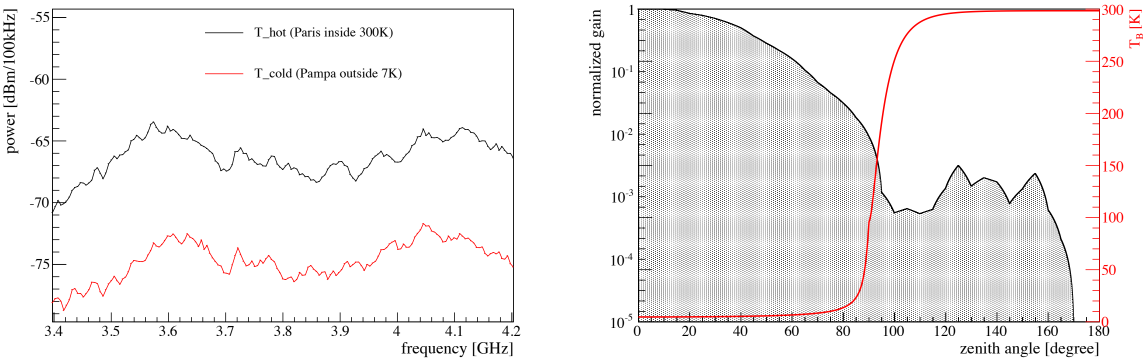

Figure 4.23: Left: Superposition of two spectra recorded at T_{hot} and T_{cold} (see text). Right: Profile of brightness temperature at 2.295 GHz. The normalized gain of the antenna at 3.8 GHz is superimposed.

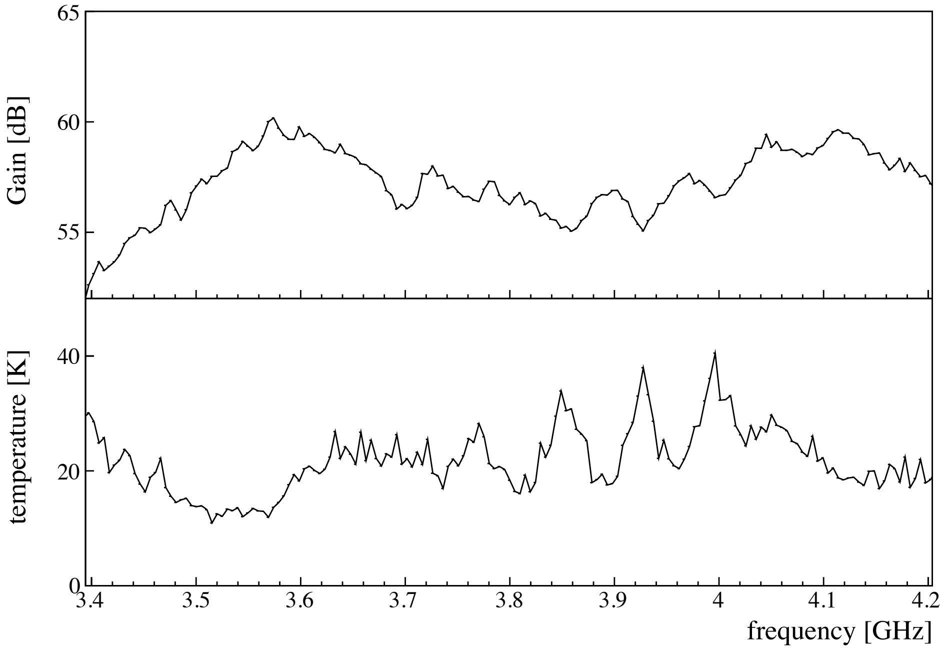

Figure 4.24: Gain and temperature computed for one antenna comparing spectra at T_{hot} and T_{cold}.

profile taken from reference [97] is a parameterization at a frequency $\nu = 2.295$ GHz, close to the one we operate and represented in red in Fig. 4.23 (right). After integration over the solid angle at frequencies from 3.4 to 4.2 GHz, the mean temperature is found to be $T_{\text{cold}} = 7.5$ K. The comparison of the spectra at hot and cold temperature, shown in Fig. 4.23 is a measure of Y-factor. We considered a lossless antenna, however, because of the polarization mismatch between the unpolarized thermal noise and the linear antenna we used Eq. 4.3.15 with $\alpha = 0.5$. For instance, we show in Fig. 4.24 the temperature for one antenna in the lower panel. The gain is deduced from the total power and the temperature, it is illustrated in the upper panel. This measurement was performed for 28 of the 54 ESX241 antennas installed (second setup).

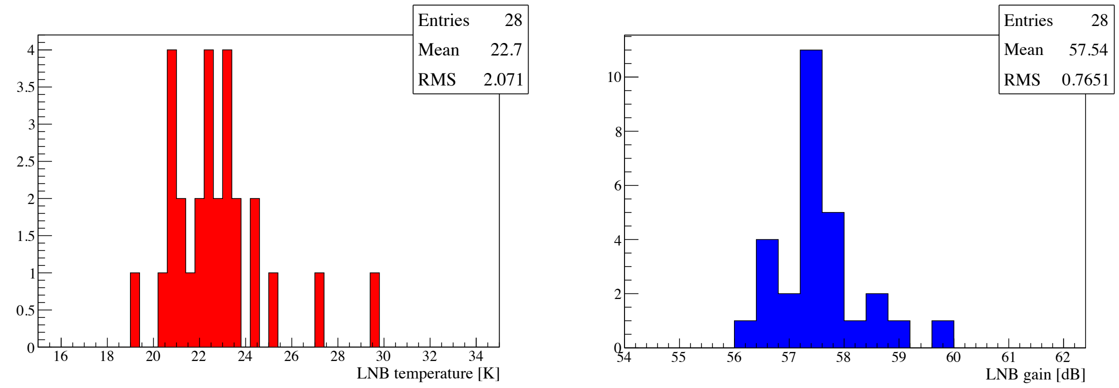

Figure 4.25: Distribution of temperature (left) and gain (right) of 28 LNBF (ESX241)

The distribution of temperature and gain in Fig. 4.25 show a mean temperature of LNB of 23±2 K and a mean gain of 58±1 dB. The total noise temperature, the sum of the antenna temperature and the LNB temperature is then $T_{\mathrm{sys}} = 30\,\mathrm{K}$ for the antenna ESX241.

KIT measurements As mentioned before, other experiments with the same goal as EASIER and using the same type of equipment have been operating. Among them, CROME is an experiment in Karlsruhe at the KASCADE Grande site. They developed a dedicated setup to measure the LNB noise temperature [98]. It is also based on the Y-factor method, but the LNBF are pointing into a cryostat filled with absorber on its inner sides. The hot reference temperature is obtained when the absorber is at room temperature and the cold temperature when the cryostat is filled with Liquid Nitrogen (LN2). The CROME collaboration measured the noise temperature of LNBF GI301SC and ESX241. For the LNBF GI301SC, the temperature measured was really unstable and they found a mean temperature of 91 K but ranging from 40 K to 180 K. ESX241 LNBF were more stable and a LNB temperature of around 25 K was found and is compatible with the 23 K found with room/sky spectrum comparison presented before.

LNB noise measurements with a noise meter A third method to measure the noise temperature of the LNB was performed. The amplification stage of the LNBF ESX241 installed for EASIER61 exists without the feed horn. The LNB DMX211 is only the electronics part and a waveguide as shown in Fig. 4.26 (left). To measure the noise temperature of this part we had available a spectrum analyzer with a noise meter function (Agilent PXA N9030A) and a coaxial noise source (Agilent N4002A). The spectrum analyzer switches automatically on and off the noise source in order to feed the DUT with P_{hot} and P_{cold}. To connect the coaxial noise source to the LNB we used an adapter from a coaxial line to a waveguide. The setup is shown in Fig. 4.26 (right). The resulting noise temperature and the gain as a function of frequency are shown in Fig. 4.27. The mean noise temperature is found to be 201 ± 30 K, i.e. a factor of 10 larger than the one found with the other methods. The reason of this discrepancy is not understood. However the gain is also much lower than the announced one and that measured with other methods. As a matter of fact, the gain of the LNB alone (not taking into account the antenna gain) is expected to be around 60 dB. It is a factor 10 larger

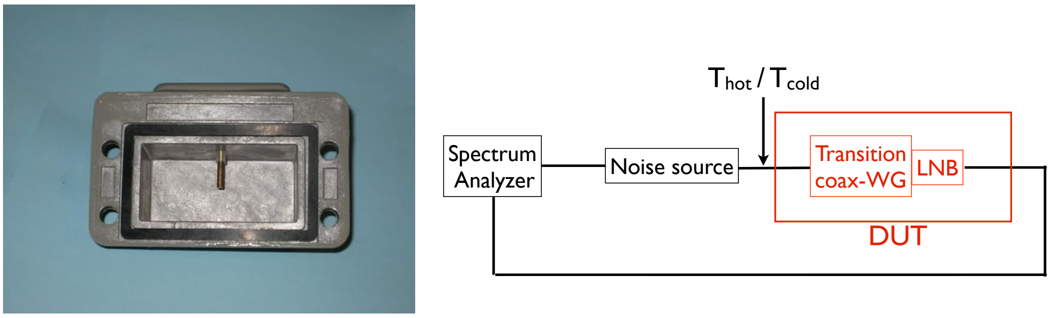

Figure 4.26: Left: picture of the LNB DMX211. Right: setup for the noise measurements

than the one measured. A loss of such factor could explain the high temperature measured thanks to Eq. 4.3.15.

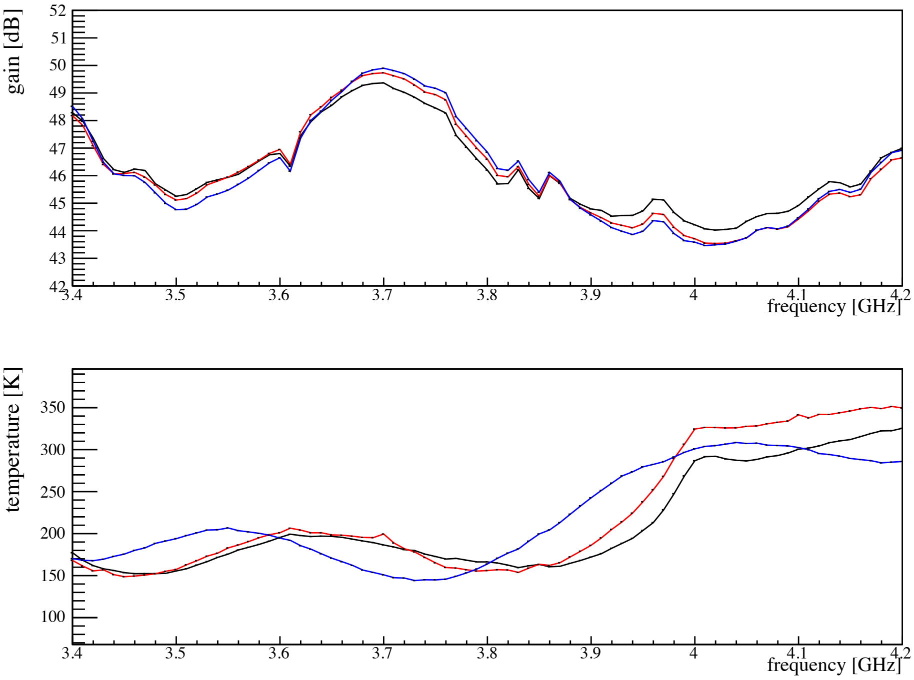

Figure 4.27: Measured gain and temperature of the LNB DMX211 using a noise figure meter.

Calibration with an external source

We performed in November 2011, in collaboration with KIT researchers, a measurement with an octocopter carrying a source emitting sine waves at GHz frequencies and flying above the EASIER antenna located on the tank Jose Maria (LsId 419) in order to obtain an on site calibration of the whole detector. We first describe in detail the experimental setup used for this calibration, then a specific calibration of electronics performed in laboratory required to interpret the data, then we explain the data selection and the analysis to extract the signal of the octocopter out of the noise. Finally, we will exploit the data to reach an absolute calibration of the whole detector in the frequency band [3.65 - 3.95] GHz.

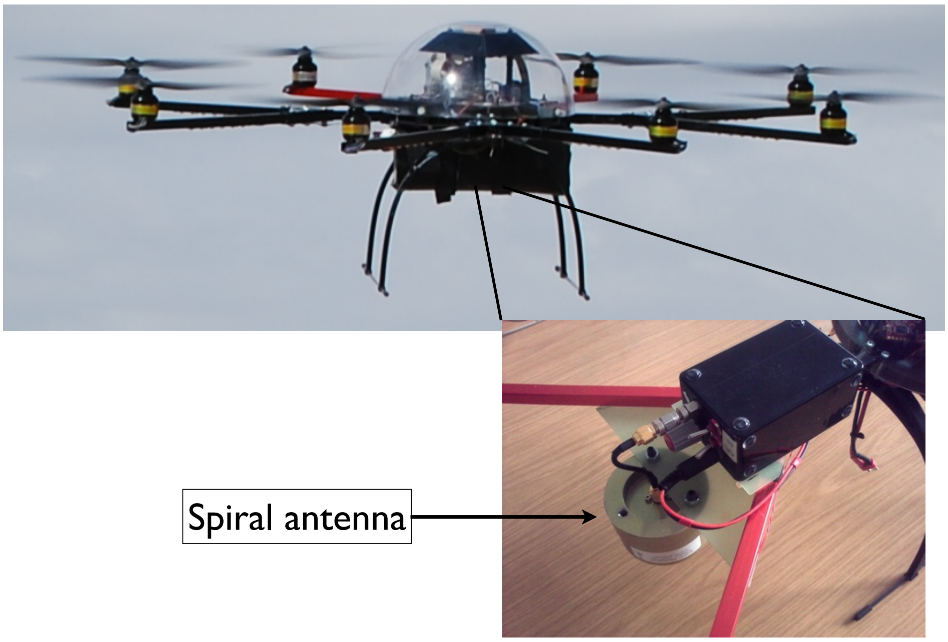

Figure 4.28: Octocopter carrying the source.

Experimental setup

The experimental setup has two components: the EASIER detector and the signal emitter carried by the octocopter which can fly at predefined distances above the EASIER antenna. The EASIER detector was already described in section 4.1, we describe thus only the source and the specific acquisition method.

The source The source carried by the octocopter [99], shown in Fig. 4.28, is composed of a Voltage Controlled Oscillator (VCO) [100], that is a generator delivering a power of ≈7 dBm, depending on the frequency. The frequency of emission is proportional to an input voltage. In our case, it was set to sweep every second from 2.97 GHz to 3.95 GHz during the first 145 ms of each GPS second to stay at 3.95 GHz until 180th ms and then to turn off until the end of

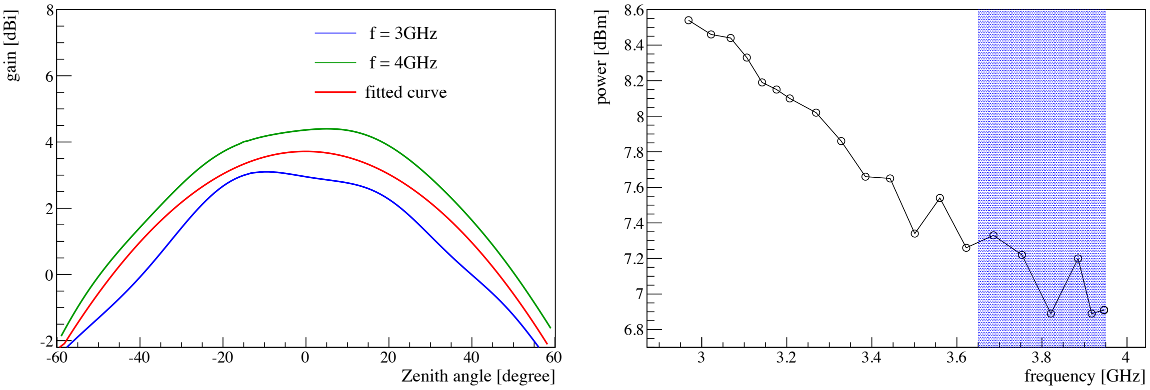

Figure 4.29: Left: The patterns at 3 and 4 GHz of the spiral antenna for the elevation plane. The average, shown in red, is described by a quadratic polynomial. Right: Power delivered by the oscillator as a function of the frequency. The blue band represents the frequency range used for these measurements.

the second. This signal is attenuated by 12 dB and emitted by a spiral antenna circularly polarized whose pattern is known from data sheet at 3 and 4 GHz (see Fig. 4.29). The power emitted by the source is:

$$P_{\text{emitted}} = (\underbrace{P(\nu)}_{\text{oscillator}} - \underbrace{12\,\text{dB}}_{\text{attenuator}} + \underbrace{G_{\text{spi}}(\theta)}_{\text{spiral antenna gain}})\,\text{dBm} \pm \epsilon_{spi} \pm \epsilon_{VCO}$$

.The function $P(\nu)$ retrieved from the oscillator data sheet is shown in Fig. 4.29 and has a systematic uncertainty of $\epsilon_{VCO} = 1\,\text{dB}$. The gain of the spiral antenna, G_{spi}, is taken as the average gain at 3 and 4 GHz, its dependence in zenith angle is approximated by a quadratic polynomial. An uncertainty $\epsilon_{spi} = 0.73\,\text{dB}$, taken as the standard deviation of the difference between curves and the average, is added to the emitted power.
Knowing the distance between the octocopter and the receiving antenna, R, the incoming flux at the receiver becomes:

$$F = \frac{1}{4\pi R^2} 10^{\frac{(P_{\text{emitted}} - 30)}{10}} \pm 1.73\,\text{dB} \tag{4.3.16}$$

The systematic uncertainty attributed to the flux limits the precision on the calibration of the receiver to ±50% .

Remark The frequency scan performed by the VCO is dependent of the ambient temperature. The sweep time at 15 °C is 145 ms but can extend to 160 ms at 35 °C [101]. This effect is not accounted for in the following analysis.

Acquisition The source flew at several distances, and emitted a sine wave at different frequencies. The source and the receiver have absolute GPS time, therefore we can relate the parameters of the source, like position and emission frequency, with the time at the receiver.

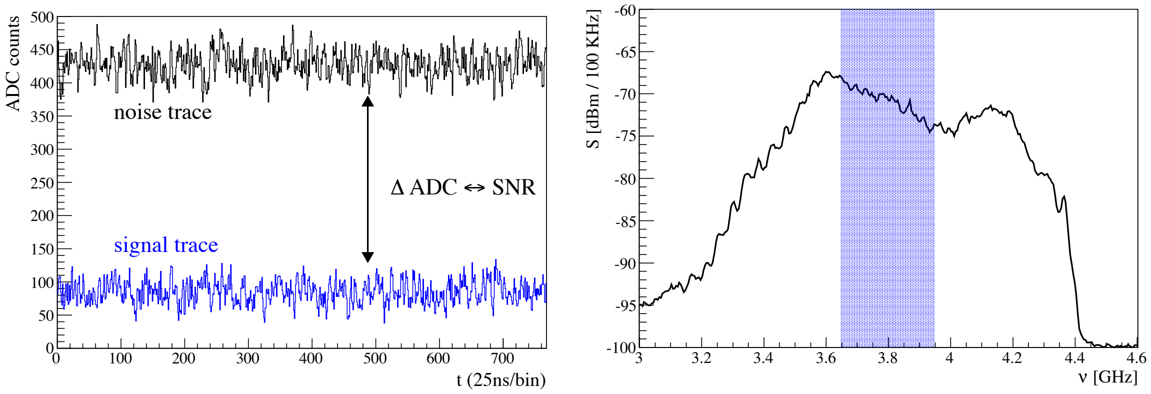

Figure 4.30: Example of a noise trace and a signal trace, a decrease of the mean of the trace represents an increase of power.

We forced the trigger of the local station to write the data from 100^{th} ms to the 150^{th} ms of each GPS second selecting a range of frequency from the source between 3.65 and 3.95 GHz. The selected range, in blue in Fig 4.30 (right), is in the middle of the frequency spectrum of the LNBF.
Example of recorded traces are shown in Fig. 4.30 (left). Due to the electronics chain, the level in ADC counts decreases with the input power. Traces when the source is and is not emitting are compared to estimate the signal to noise ratio. The absolute measure of the signal is then retrieved using the absolute measure of the background noise power.

Specific electronics calibration

The response of the power detector is dependent on the waveform of signal input. The signal received when the source emits is a mixture of a sine signal and a noise waveform signal. To recover the useful signal from the source, we need a calibration for the noise only that gives us the reference power, as given by Eq. 4.2.6 and a calibration in term of signal to noise ratio is also required to retrieve the power added by the source. Such calibration was performed in laboratory.
The setup for this calibration is composed of a signal generator and a spiral antenna as a sine source and a LNBF receiver as source of noise. We record alternately the RF output and the power detector output. We first record 10 traces of pure background noise. Then we emit a sine waveform of increasing power and record for each input power 8 traces. We measured the factor $A_{\rm dB} = 10 \cdot \log_{10}(\ (P{\rm sine} + P{\rm noise})/P{\rm noise}\ )$ as a function of the difference of voltages at the power detector output. We can then estimate the linear signal to noise ratio $SNR_{\rm linear} = P_{\rm sine}/P_{\rm noise}$ knowing that $A_{\rm dB} = 10 \cdot \log_{10}(SNR_{linear} + 1)$. The factor A_{dB} is compared to the difference of voltage it induces at the output of the power detector : $\Delta V_{PD} = V_{PD} - V_{PD-noise}$. We recorded data at three frequencies: 3.4, 3.8, 4.2 GHz and performed a fit with the three frequencies together. The calibration curve is shown Fig. 4.31 together with a second order polynomial fit where we fix the origin point so that $A_{dB} = 0$ for $|\Delta V_{PD} = 0|$. The residuals shown in the same figure are taken as the uncertainties on this calibration.

$$A_{dB} = a \cdot |\Delta V_{PD}|^2 + b \cdot |\Delta V_{PD}| \pm \sigma_{calib} \tag{4.3.17}$$

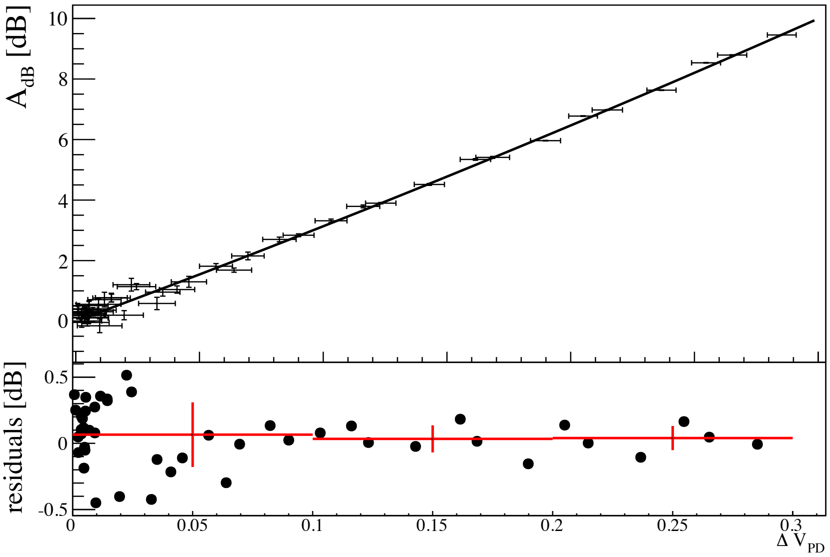

Figure 4.31: Calibration of the parameter A_{dB} with a second order polynomials. The lower plot shows the residuals of the fit.

The fitted parameters are $a = 9.84$ and $b = 30.36$, and the conversion to ADC yields :

$$A_{dB} = 2.23 \times 10^{-6} |\Delta ADC|^2 + 1.45 \times 10^{-2} |\Delta ADC| \pm \sigma_{\text{calib}}[dB] \tag{4.3.18}$$

where $\sigma_{\text{calib}} = 0.25\,\text{dB}$ for $\Delta ADC < 210$ and $\sigma_{\text{calib}} = 0.1\,\text{dB}$ for $\Delta ADC > 210$.

Data analysis

The data set is composed of two different runs corresponding to two different parameter scans: a vertical scan in distance and frequency (Run 1), a scan in frequency at different zenith angle (Run 2).

Data selection The octocopter flew at several distances from the receiving antenna and covered a span of 300 MHz, thus covering different values of gain of the antenna. Given that the noise is at around 450 ADC counts, the dynamic range for the signal is less than 9 dB. Thus for some distances and frequencies, the received flux was larger than the dynamic range of the receiver leading to saturated traces. We define a trace as saturated if more than 10% of the 768 bins are out of the ADC range and for each distance for run 1 (100 m, 150 m, 200 m) or zenith angle for run 2, we select the range of frequency for which there is no saturated trace. For run 2, only 23 on 166 traces are removed and for run 1 the table 4.3 report the selected frequencies and the number of accepted and rejected traces. The scanned parameters of the selected data are shown for the two runs in Fig 4.32. For run 1, the rejected traces are, as expected, at shorter distances and lower frequencies in agreement with the shape of the spectrum in Fig 4.30 (right).

	d $\sim$ 100 m	d $\sim$ 150 m	d $\sim$ 200 m
frequency [GHz]	≥ 3.86	≥ 3.77	≥ 3.68
accepted/rejected	56/42	167/111	177/14

Table 4.3: Statistics of selected traces for run 1.

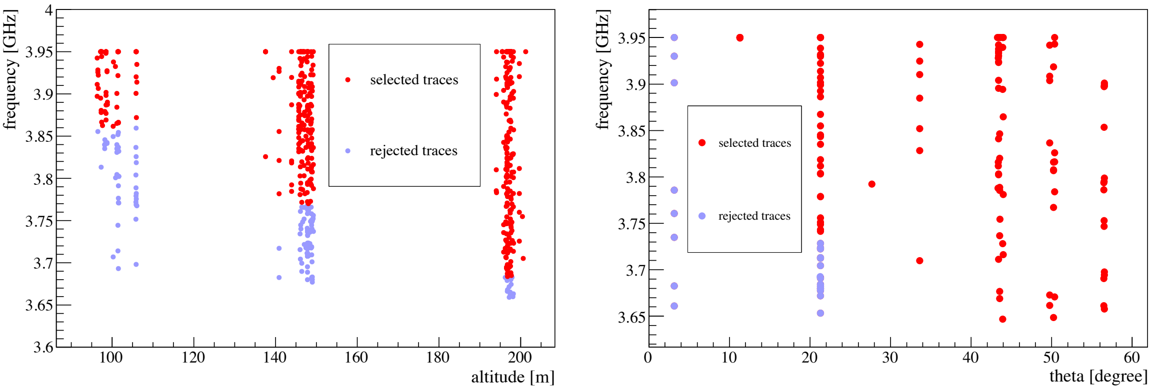

Figure 4.32: Frequency and distance of selected traces (in red) and rejected (in blue) for the 2 runs

From ADC counts to signal power During the calibration a sine signal from the source is added to the noise always present produced by the environment (sky + ground) and the electronics. To extract from the traces the contribution from the source, we will first estimate the noise from traces when the octocopter is not emitting and then we will use the relation 4.3.18 to estimate the signal to noise ratio.

Noise power The noise power is calculated averaging over 7 traces recorded when the octocopter was not emitting and amounts to $< ADC_{\text{noise}} >= 452.6 \pm 1.3 ADC$ where the uncertainty is the dispersion of the mean over the 7 traces recorded. Using the calibration for the noise waveform, this gives :

$$P_{noise} = -25.6\,\text{dBm} \pm 0.1\,\text{dB} \tag{4.3.19}$$

Where an uncertainty of 0.1 dB is added on the power estimation to account for the uncertainty on the electronic calibration.

Sine power To obtain the sine power coming from the source, we average the trace in ADC counts, and then we estimate the parameter A_{dB} with relation 4.3.18:

$$|\Delta ADC| = | < ADC > - < ADC >_{noise} | = 4.1 \cdot 511.5 \cdot |\Delta V_{PD}|$$

The linear signal to noise ratio is given by :

$$SNR_{lin} = 10^{\frac{A_{dB}}{10}} - 1 \tag{4.3.20}$$

and its uncertainty by :

$$\sigma_{SNR_{lin}} \simeq \frac{\ln 10}{10} \sigma_{A_{dB}} SNR_{lin} \tag{4.3.21}$$

We can finally extract the sine part of the signal with the following relation:

$$P_{\text{sine}} = P_{\text{noise}}.SNR_{\text{linear}}$$

The uncertainties are dominated by the contribution from the calibration of the power detector. The power of sine signal recorded by the EASIER receiver is shown in Fig 4.33 as a function of the frequency for the 3 distances covered during run 1.

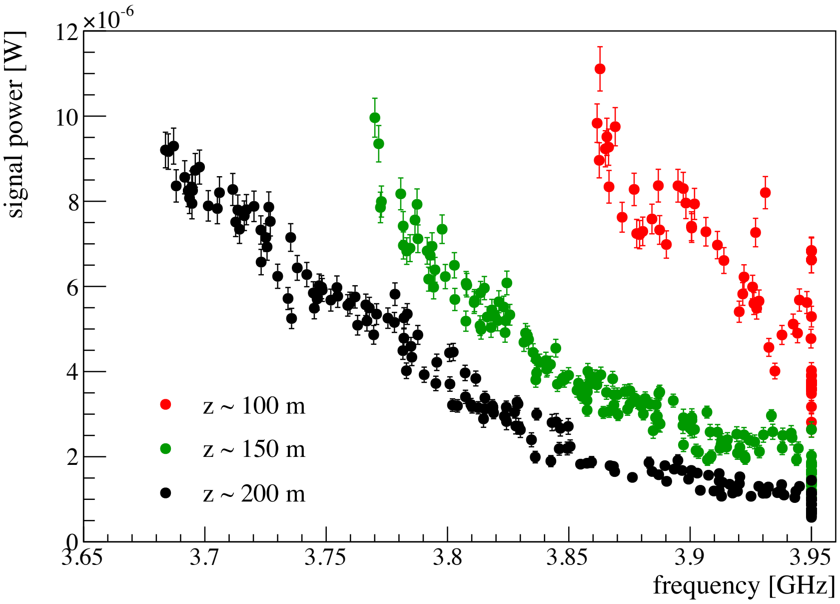

Figure 4.33: Sine power measured as a function of the frequency at z = 100, 150, 200 m

Results

The observed power is the sum of the noise and the signal sent by the source :

$$P_{\text{obs}} = P_{\text{signal}} + P_{\text{noise}} = \frac{P_{\text{emitted}}}{4\pi R^2} \cdot A_{\text{eff}}(\theta,\nu) \cdot G_{\text{LNB}}(\nu) + k_B \cdot \int_{\nu} G_{\text{LNB}}(\nu) \cdot T_{\text{sys}}(\nu)\, d\nu. \quad (4.3.22)$$

where A_{eff} is the effective area of the antenna, G_{LNB} is the gain of the amplifier, and T_{sys} the system temperature defined before. The octocopter measurements can provide us the first part of Eq 4.3.22, while the second part can be extracted by the frequency spectrum in Fig 4.30 (right).

Run 1: distance scan The 3 distances that covered the octocopter during run 1 allow us to test the distance dependency and check the consistency of the method to extract the signal. Figure 4.34 shows the signal power observed as a function of distance at different frequencies. The plain curves are fits of power law k_1/R^{k_2}. Table 4.4 reports the values of the fit showing a decrease of the signal power with an index k_2 ranging from 2 to 2.44. The small uncertainties on k_2 reflect an underestimation of the uncertainties on power signal.

frequency [GHz]	k_2
3.85 - 3.875	2.09 ± 0.033
3.875 - 3.90	2.44 ± 0.04
3.90 - 3.925	2.23 ± 0.034
3.925 - 3.95	2.40 ± 0.041
3.95	2.25 ± 0.03

Table 4.4: Fitted exponent k_2 of the power law function k_1/R^{k_2}

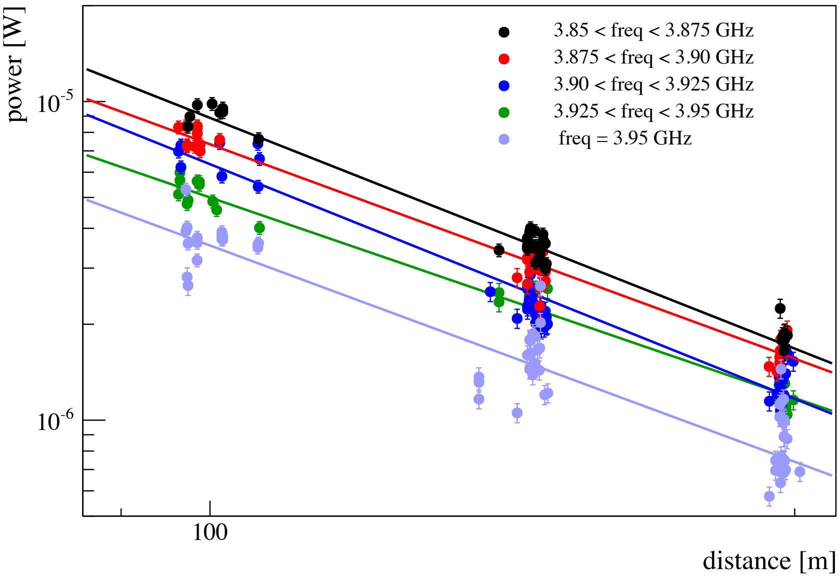

Figure 4.34: Sine power as a function of distance for different frequencies

Contribution in uncertainties of a possible tilt of the octocopter, or the frequency shift of the source are not taken into account in this study.

During Run 1 we scanned the frequency range of 300 MHz at different distances, at a zenith angle close to 0. The signal power recorded is highly dependent on frequency, around a factor 10 in the range explored (see Fig 4.33). This behavior is the combined effect of the frequency dependency of the effective area, the LNB gain and the power emitted by the source.
Once corrected with the expected flux at the receiver (Fig 4.35), we can extract the product $A_{\text{eff}}(\theta = 0, \nu) \cdot \mathrm{G_{LNB}}(\nu) = \frac{\mathrm{P_{sine}}}{\mathrm{F}} \equiv \mathrm{G_{tot}}(\nu)$ which is the global factor to transform the incoming flux for a zenithal angle $\simeq 0$ into a recorded power. The uncertainties on G_{tot} come from the measurement itself and has a additional systematic uncertainty from the flux emitted. In the range of frequency scanned, $G_{\text{tot}}(\nu)$ can be fitted by an exponential function. The mean G_{tot} is retrieved out of the integration of the fitted function over the frequency range :

$$< G_{tot} >_{\nu}= \frac{1}{\Delta\nu} \int_{3.68}^{3.95} A_{eff}(\theta = 0) G_{LNB}(\nu) d\nu \tag{4.3.23}$$

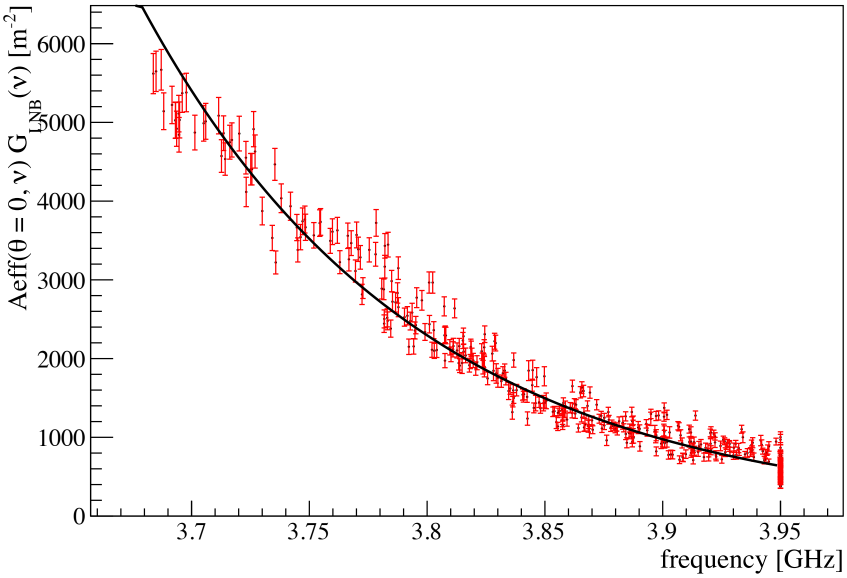

Figure 4.35: Factor $A_{\text{eff}}(\theta = 0, \nu) \cdot G_{\text{LNB}}(\nu)$

The errors on the fit coefficients are propagated on the mean. We obtain:

$$< G_{tot} >_{\nu} = 2499 \pm 285(stat) \pm 1225(sys) \tag{4.3.24}$$

Inferred sensitivity The estimate of the sensitivity is given as the constant flux density, f, required over a frequency band to give an output equal to the noise in this band. We estimate the noise in the band scanned with the octocopter, [3.68 - 3.95]GHz. The contribution of this band to the spectrum in Fig 4.30 (right) is multiplied by the total noise power given in relation 4.3.19.

$$P_{\text{noise}[3.68;3.95]} = 0.32 \cdot P_{\text{noise}} \tag{4.3.25}$$

then the sensitivity f can be calculated from:

$$f \quad \text{such} \quad \text{as} \quad : \Delta\nu < G_{tot} > f = P_{\text{noise}[3.68;3.95]} \tag{4.3.26}$$

The flux density that yield a power equivalent to the noise in this band is found to be :

$$f = 4.02 \cdot 10^{-19} \pm 11\% \pm 49\% \; [\text{W m}^{-2} \text{ Hz}^{-1}] \tag{4.3.27}$$

For comparison, the sun flux density is around 100 times lower than this value. Furthermore, the flux density estimated in [73] for an air shower of $3.36 \cdot 10^{17}$ eV at 10 km is 2.8×10^{-24} W m^{-2} Hz^{-1}. A rough estimate for an air shower of 3×10^{19} eV at 500 m yields to a flux of $\sim 10^{-19}$ W m^{-2} Hz^{-1} accounting for a linear scaling of the flux with energy or a factor 100 larger in case of a quadratic scaling.

The flux sensitivity can also be converted in noise temperature according the following equation:

$$T_{sys} = \frac{f \cdot A_{eff}}{2k_B} \tag{4.3.28}$$

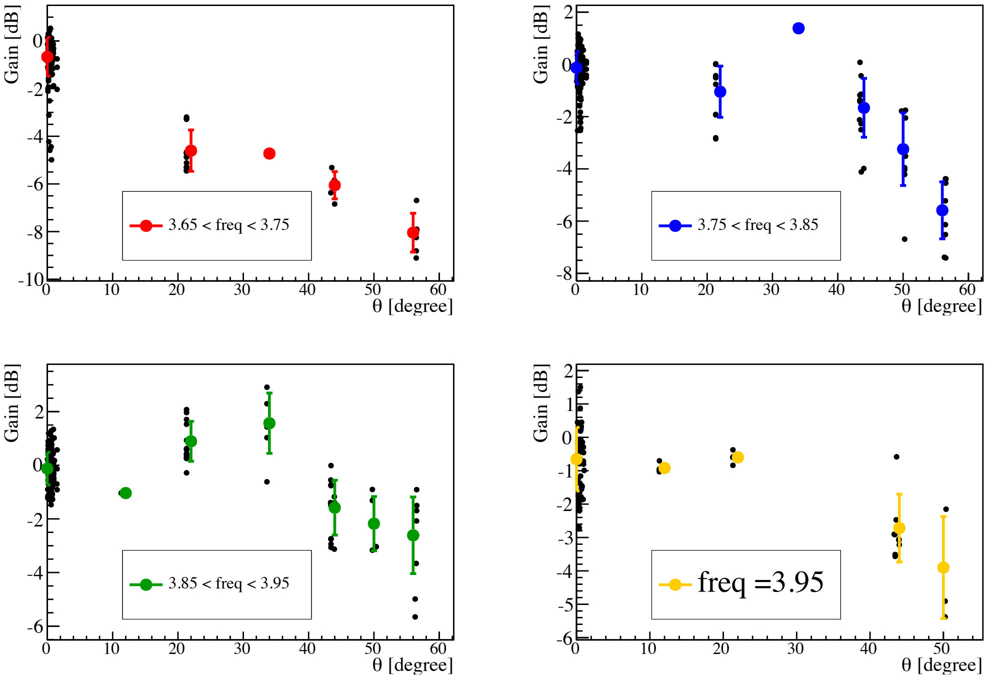

Figure 4.36: Angular pattern relative to the gain at 0 degrees

where the factor two comes from the polarization mismatch between the circularly polarized source and the linearly polarized receiver. We find a system temperature of $T_{\mathrm{sys}} \simeq 51\,\mathrm{K}$. This result is consistent with the noise temperature found before with other methods.

Run 2 : Angular scan During Run 2 we scanned in zenith angle. We can then reconstruct the power pattern of the receiving antenna. We determine the relative gain with respect to the gain at the zenith by dividing the factor $G_{\mathrm{tot}}(\theta, \nu)$ by the fitted function of $G_{\mathrm{tot}}(\theta = 0, \nu)$. In Fig 4.36 it is illustrated the dependency on zenith angle of the effective area for 4 ranges in frequency. The black dots represent the measurements and the colored plain circles the mean in angle bins. The error bars are the dispersion in the bin. From 3.75 GHz to 3.95 GHz the gain is rather constant until 30 - 40 degrees, and the -3 dB opening angle is around 50 degrees. This number is in good agreement with pattern measurements. At lower frequency between 3.65 GHz and 3.75 GHz the gain seems to fall faster with the elevation angle and does not match the measurements. But a large uncertainty of 2 dB, given the spread of the points is present.

Outlook on the octocopter measurements

The set of measurements done with the octocopter allowed us to test and calibrate the whole acquisition chain of the EASIER detector. Two different sets of data, Run1 with a source at fixed angle ($\theta = 0$) and variable distances and Run2 at different zenith angles allowed us to scan various parameters. The product of the effective area times the LNB gain at $\theta = 0$ was measured in the band 3.65 - 3.95 GHz. The comparison of this parameter at different angles

showed an opening angle at -3 dB of around 50 degrees for most of the frequencies scanned in agreement with antenna simulation. The equivalent flux of noise at $\theta = 0$ was determined to be $4.02 \cdot 10^{-19}\,\mathrm{W/m^2/Hz}$ with an uncertainty of 11% and a systematic error of 49%.
The uncertainties of these measurements are large due to the limited knowledge on the flux emitted by the source. These measurements could be improved by scanning the whole frequency band of the receiver or emitting in a wide spectrum a noise signal. The described method can be a complete method of an on site calibration and could give a precise measurement of the system sensitivity at different angle with such improvements.

Chapter 5

Data analysis in microwave band

In the microwave band, EASIER is an array of 61 radio detectors. Seven have been taking data since April 2011, and 54 since April 2012. Its purpose is the observation of the isotropic radiation from air showers produced by Molecular Bremsstrahlung Radiation (MBR). The MBR has been observed in one beam experiment in SLAC in 2008 but the observation in EAS experiments has not been established.
In the previous chapter we reported the characteristics of the EASIER detectors, in particular their ability to detect the MBR emission if the parameters observed in beam are scaled to EAS. However, in this frequency range, other types of emission are likely to be detected. Indeed, the mechanism responsible for the detection of air shower in the VHF band, namely a geomagnetic effect on the shower particles and a charge separation could extend at microwave frequencies.

5.1 Emission mechanisms in the microwave band

Molecular Bremsstrahlung The R&D for experiments measuring EAS in the microwave band were triggered by the results of a test beam experiment in SLAC. These measurements reported the detection in the frequency band [1.5 - 6]GHz of a continuum emission produced by the plasma induced by the passage of a shower in an anechoic chamber. A maximum flux of $F_{\text{ref}} = 4 \times 10^{-16}$ W /m^2/Hz was observed at a distance $d = 0.5\,\text{m}$, from the showers produced by an electron beam of $2.8{\times}10^{10}$ eV. Knowing the beam current, the energy of the equivalent shower is estimated to $E_{\text{ref}} = 3.36 \times 10^{17}$ eV. Then to compute the corresponding flux for an air shower one introduces the following relation:

$$F(t) = F_{ref} \cdot \Gamma \cdot \frac{\rho}{\rho_0} \cdot \left(\frac{d}{R(t)}\right)^2 \cdot \left(\frac{N(t)}{N_{ref}}\right)^{\alpha} \tag{5.1.1}$$

where ρ and ρ_0 are the density of air at the point of emission and at see level where the beam test was performed. The expected emission is also scaled by the number of particles $N(t)$ in an air shower with respect to the number of particles at the maximum development of an EAS with the energy E_{ref}. In the beam experiment, the scaling of the flux was observed to increase quadratically with the beam energy, which is proportional to the number of particles. This was explained by a possible coherent effect in the plasma emission. This coherence is represented by the parameter α. A value of $\alpha = 2$ is expected in case of a full coherence of the emission and $\alpha = 1$ if the emission is non coherent. Γ is the ratio of the distances over which the emission occurs in the anechoic chamber of the beam experiment and in air shower, it is taken as $\Gamma = 4.62$ in [73].

Coherent radiation It was recently pointed out that the mechanism responsible for air shower radiation in the VHF band is likely to extend to higher frequencies [102]. The mechanism of coherent emission of shower particles due to the geomagnetic effect and a charge excess was first studied and expected in the VHF band because the shower front thickness, of the order of 1 m, corresponds to frequencies below 300 MHz. But recent simulation show that the flux produced by this emission can be important at short distance from the shower axis up to the observation band of EASIER. The two components (North- South and East-West) of the simulated electric field produced by an air shower with an energy of 10^{17} eV is shown in Fig. 5.1. The difference of amplitude between the two components is due to the geomagnetic effect. The order of magnitude of the flux from this emission is found to be of the order of tens of μV/m/MHz at 100 m from the shower axis. An electric field spectral density of 0.1 μV/m/MHz represents a power flux of 1.3×10^{-10} W/m^2 once integrated on the bandwidth of EASIER. By comparison, a rough estimate of the MBR flux with equation 5.1.1 yields a power flux around 3 orders of magnitude lower.

The MBR is expected to be produced by the low energy electrons of the plasma induced by the shower front. Thus it is expected to be emitted isotropically. In contrast, a coherent emission produced by the relativistic particles of the shower produces a radiation pattern beamed in the forward direction and is expected to be dominant at short distance from the shower axis, and decrease with distance much rapidly than a isotropic emission as shown in Fig. 5.1. In addition, the MBR is expected to be unpolarized whereas the emission produced

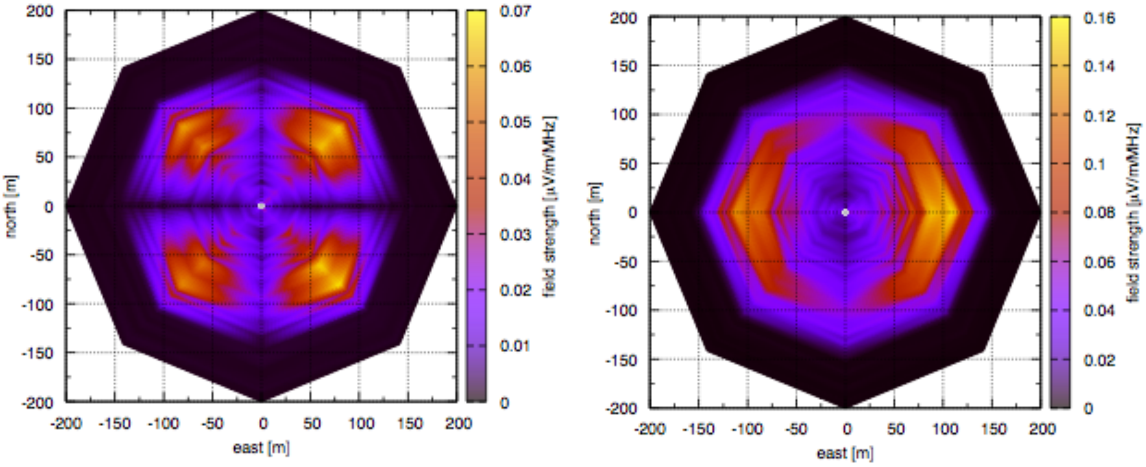

Figure 5.1: Electric field spectral density simulated with CoReas code for an EAS of 10^{17} eV in the band 3.4 - 4.2 GHz. The North South component is shown on the left and the East West on the right. (from [102]).

by the geomagnetic acceleration is expected to be polarized in the $\vec{v} \times \vec{B}$ direction, with $\vec{v}$ the arrival direction of the air shower and $\vec{B}$ the direction of the geomagnetic field. These two parameters, the distance of detection and the polarization, will help in disentangling between the underlying mechanism.

5.2 Event search

We select the Auger data until June 2013. On this data set, we apply the usual quality cut insuring a good reconstruction of the SD event: we ask that the tank with the highest particle signal is surrounded by six active tanks at the moment of the event. In addition we select the events with zenith angle smaller than $60\,^\circ$ and events tagged as lightning are also removed. We apply also a selection on the radio trace. We reject the station if the radio trace has saturated bins, caused by the dependence of the baseline with the supply voltage (see chapter 4). The total number of traces available is 72465, out of which 28787 are from EAS above $\mathrm{E} = 10^{18}\,\mathrm{eV}$ and 842 above $\mathrm{E} = 10^{19}\,\mathrm{eV}$.

The raw radio trace in ADC counts is in logarithmic scale because of the power detector operation. We transformed it first in absolute power in dBm unit according to Eq. 4.2.6, it is then exponentiated to retrieve the microwave power in Watt. As the gain from one antenna to the other is different and is not known with precision we cannot obtain an absolute power scale. To compare the data of all the antennas, we transform the absolute power trace into a trace relative to its mean and its standard deviation. For each point we calculate the relative power:

$$P_{rel} = \frac{P_{abs} - \text{mean}}{\text{standard deviation}} \tag{5.2.1}$$

The trace obtained is thus centered around zero and normalized with the fluctuations of the trace.

Event search The shape, the arrival time and the amplitude of the expected radio signal depend on the position of the antenna with respect to the shower axis. At short distances from the core we expect short pulses approximately in coincidence with the particle arrival time. Fig. 5.2 (left) represents the maximum of each radio trace as a function of the time difference between the start time of the particle signal and the radio maximum time. Three points emerge from the bulk of events[1]. They have a maximum of more than ten times the trace fluctuations and are located in the trace one or two bins (25 to 50 ns) before the start time of the particle signal. These three events are also visible in Fig. 5.2 (right) well beyond the distribution of the other maxima. The characteristics of these three events are gathered in Table. 5.1 and their radio traces in ADC counts and after linearization are shown in Fig. 5.3, 5.4 and 5.5. For these three events the distance from the antenna to the shower axis is less than 300 m and the antenna is oriented in the East West polarization direction. Two events have an energy larger than $10^{19}\,\mathrm{eV}$.

---

[1] a fourth has been detected on the 14th of July with a maximum of more than $25\,\sigma$. It is not shown in this thesis

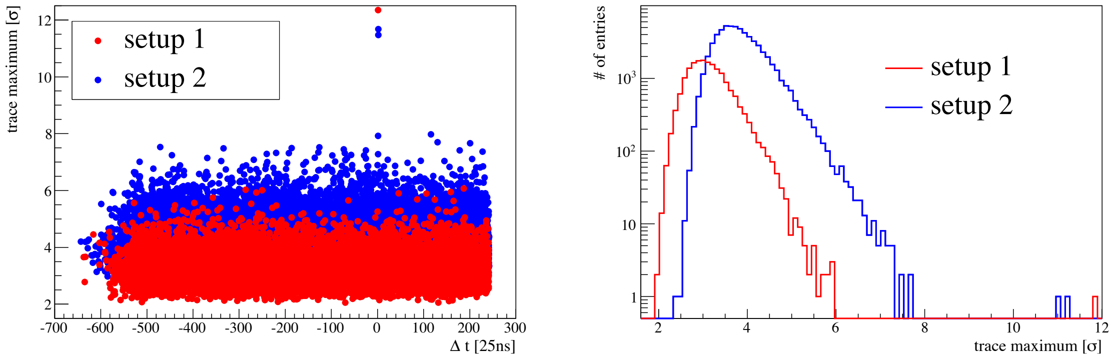

Figure 5.2: Left: Maximum radio signal in the trace as a function of the difference of time bins between the particle signal start time and the time of the maximum radio signal. Right: Distribution of the trace maximum of all events selected. Three events lay well above the bulk of events.

Auger Id	12046376	20830870	21050180
station	342	429	306
date	2011/06/30	2013/01/03	2013/02/07
energy [eV]	$(1.32 \pm 0.12)\times10^{19}$	$(1.71 \pm 0.1)\times10^{19}$	$(2.56 \pm 0.41)\times10^{18}$
zenith [°]	29.7 ± 0.3	55.2 ± 0.1	47.4 ± 0.5
azimuth[°]	343.4 ± 0.8	33.8 ± 0.1	289.4± 0.6
Distance to axis [m]	136 ± 40	268 ± 11	193 ± 15
Δt to trigger	1	2	2
radio maximum [sigma]	11.86	11.23	11.05
polarization	E-W	E-W	E-W
time length [time bins]	2-3	1	1-2

Table 5.1: Characteristics of the three radio events with the maximum well above the noise.

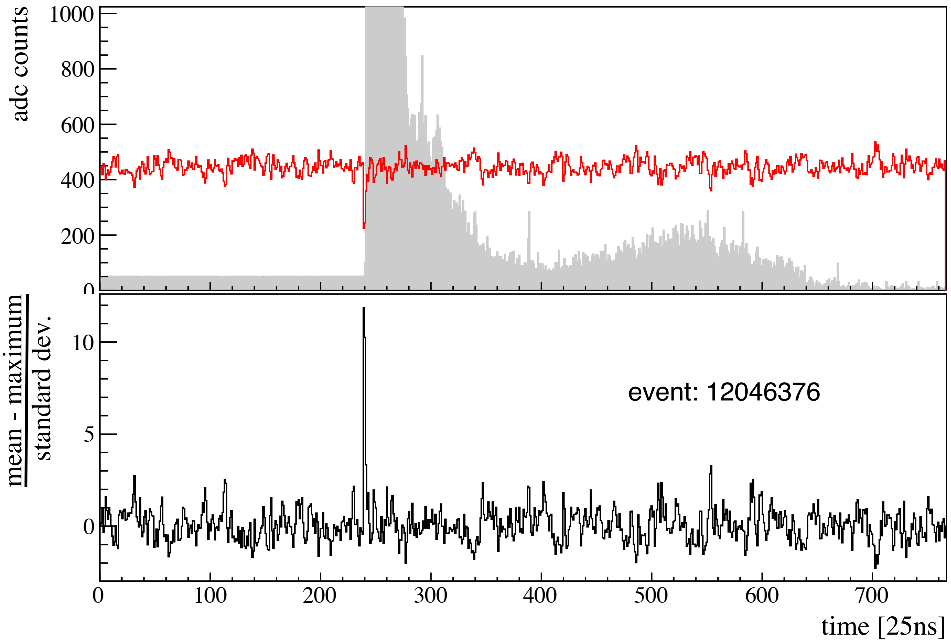

Figure 5.3: Event 12046376

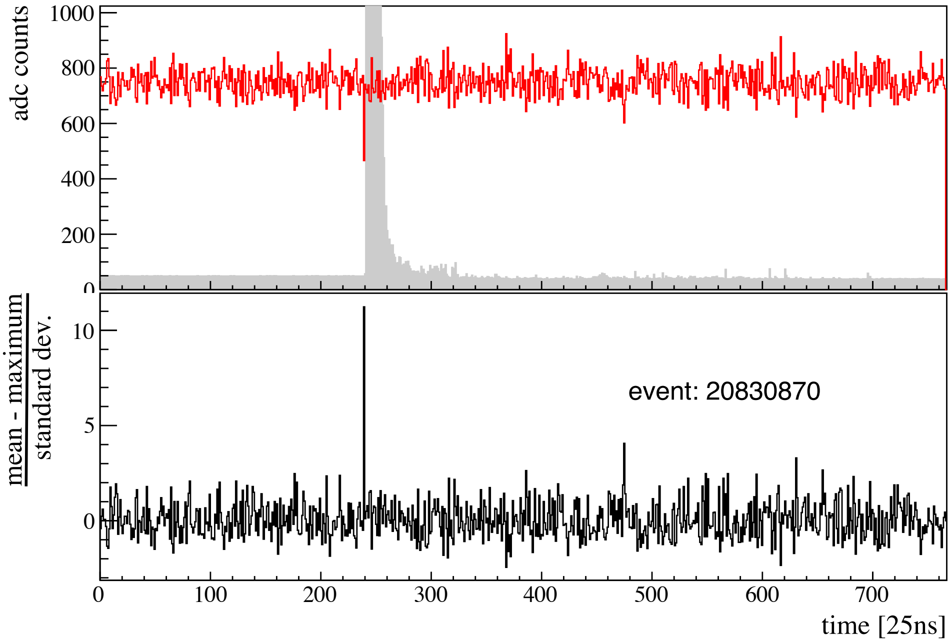

Figure 5.4: Event 20830870

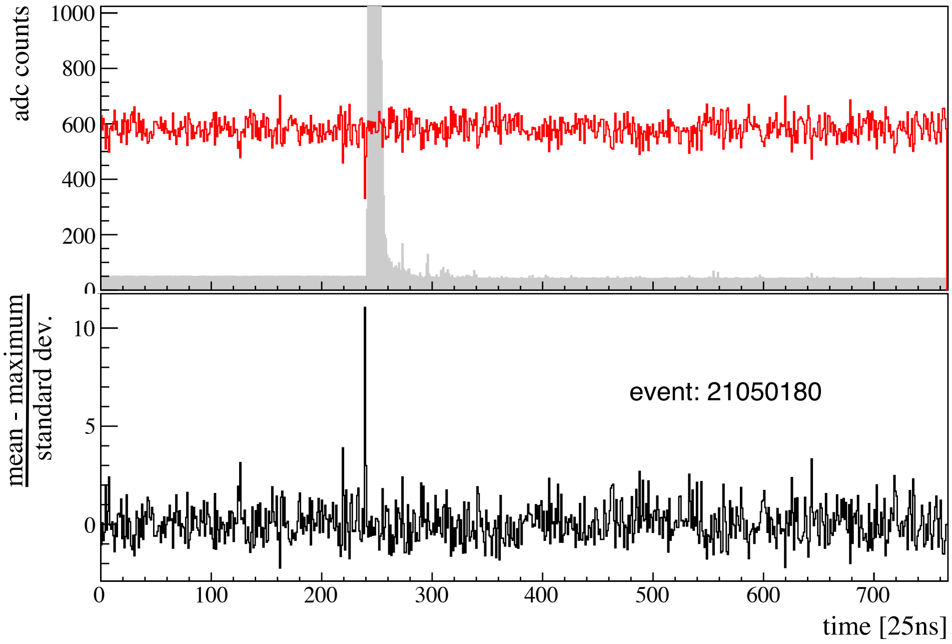

Figure 5.5: Event 21050180

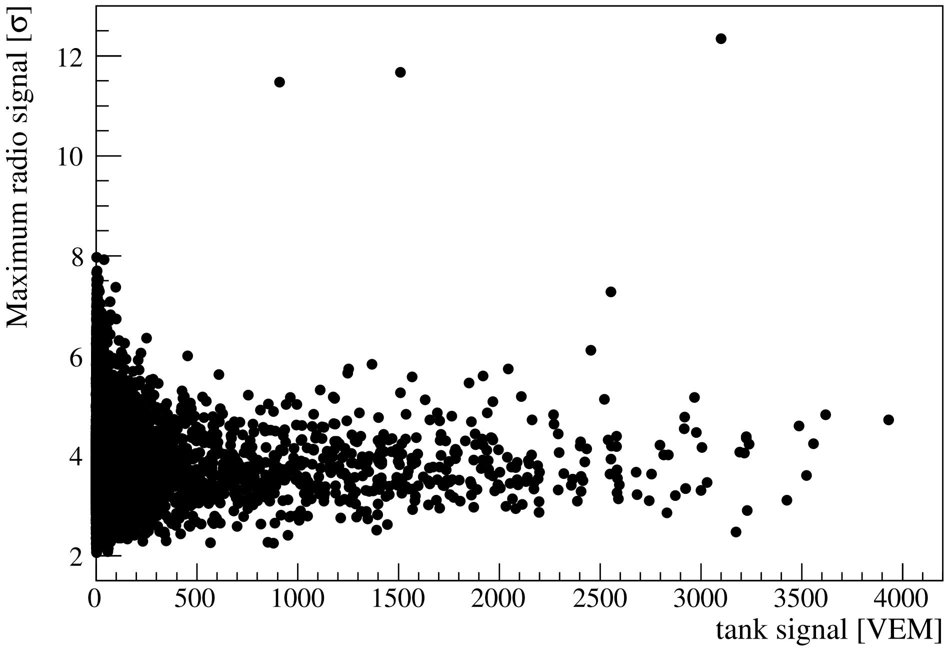

Figure 5.6: Maximum radio signal as a function of the detected light in the water Cherenkov tank in VEM (Vertical Equivalent Muon).

On the origin of the radio signals The surface detector electronics does not operate at microwave frequencies. However, other processes inducing pulse in the radio trace can be imagined. For instance the acceleration of electrons in the phototubes of the surface detector or the current draw associated in cables which occur at the event time. We checked if the radio signals observed are likely to be spurious by comparing the radio maximum signal with the particle signal in VEM in Fig. 5.6. If the radio signal were produced by the tank at the moment of the event, we would expect a correlation between the radio maximum and the particle signal. Fig. 5.6 show no correlation, excluding the tank elements as a source of spurious events.

If the signals observed seem to originate from air shower, the mechanism producing the emission is still unknown. The events characteristics, a short distance from the antenna to shower axis, and short pulse favors a beamed emission. Moreover, the East-West orientation of the antenna that detected the radio signals points to a geomagnetic origin. However, the statistics gathered up to now doesn't allow us to draw firm conclusion. Events 12046376 and 20830870 have an energy above 10^{19} eV, thus we expect them to produce MBR with a sufficient intensity to be detected. Event 21050180, on the other hand, is a much lower energy event and the radio pulse is of the same order of magnitude than the two others.

Moreover, the distribution in Fig. 5.2 is not continuous. The three events are largely above the bulk of events. This could indicate that for these three events, we reached a specific regime. For instance, the coherent emission is known to be maximum at the Cherenkov angle around the shower axis like in the VHF band. And in case of an isotropic emission the radio pulse is also greatly enhanced at the Cherenkov angle simply because, depending on the geometric configuration, the emission of different parts of the shower are detected at the same time.

5.3 Microwave signal simulation

We present here the implementation of the simulation of the radio signal expected in case of an isotropic emission. We will then use these simulations to estimate if the events detected are compatible with such emission, and if the non detection of events at larger distance is compatible with the laboratory measurements presented in [73].
The simulation process is composed of three main parts:

- the microwave signal simulation
- the signal propagation from the point of emission to the antenna.
- the detector simulation, comprising the antenna and the electronics.

Shower simulation The profile simulation method is largely adapted from [103]. In this work, proton and iron showers at different energies from $10^{17.5}$ to 10^{21} eV are simulated with CORSIKA [104]. The obtained profiles are fitted with a Gaisser-Hillas function $N(X - X_1)$ with X_1 the first interaction depth and:

$$N(X) = N_{\max} \left(\frac{X - X_0}{X_{\max} - X_0} \right)^{\left(\frac{X_{\max} - X_0}{\lambda}\right)} \exp\left(\frac{X_{\max} - X_0}{\lambda} \right) \tag{5.3.1}$$

where $N_{\max}$ is the maximum number of shower particles and $X_{\max}$ is the atmospheric depth at shower maximum in g/cm^2. X_0 and λ are shape parameters, with λ related to the particle mean free path. The fit results give a parameterization in function of $N_{\max}$, X_0, X_1, $X_{\max}$, the primary mass and the energy of the shower. The complete description to retrieve these parameters is given in [103].
We used only the mean value of the parameters and their dispersion to simulate the air shower profiles. As an example, we show in Fig. 5.7 the simulated profile of 100 showers of iron and proton at an energy of 10^{19} eV.

Microwave emission The conversion from the particle profile to a microwave power is performed using Eq. 5.1.1. The reference number of particle N_{ref} for a shower of energy E_{ref} is taken from the parameterization in [103] and its value is $N_{ref} = 2 \times 10^8$.
In [73], the expected flux for an air shower of $E_{ref} = 3.36 \times 10^{17}$ at 10 km is found to be $F_{E_{ref}} = 2.77 \times 10^{-24}$ W/m^2/Hz . We simulated the same shower a hundred times to check the consistency of our method. The mean flux is found to be around a factor 1.7 above $F_{E_{ref}}$. This difference is caused by the choice of the reference number of electrons N_{ref}. The distribution of the maximum flux in the trace is shown in Fig. 5.8 (left) and the traces are depicted Fig. 5.8 (right). In order to agree with the estimation of the original paper, we normalize the flux with the corresponding factor (1/1.7).

Signal propagation The microwave power is estimated along the shower axis at each distance in steps of 10 m. As we consider the emission isotropic, to estimate the flux at the detector we first account for a factor $1/4\pi R^2$. Then we consider the compression of the signal that occurs because of the propagation. The radiation from the air shower propagates with

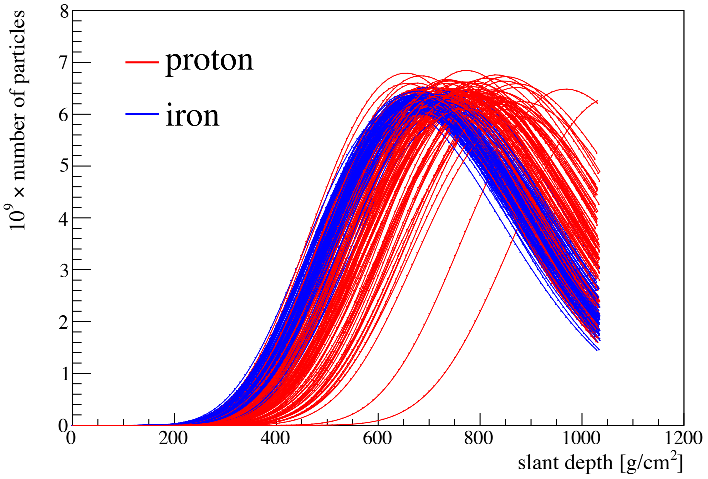

Figure 5.7: Simulated shower profiles for a vertical shower with an energy of 10^{19} eV using the parameterization given in [103].

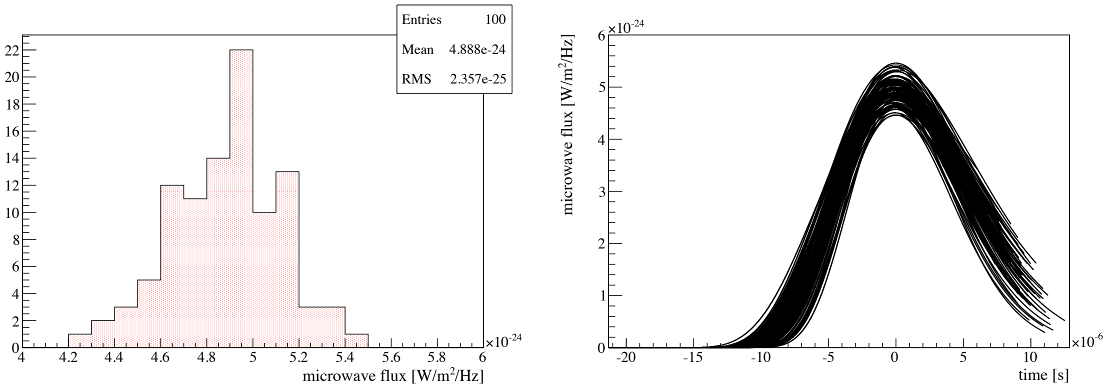

Figure 5.8: Left: Distribution of maximum of flux at ground for the reference shower. Right: Simulated traces of the reference shower, they are all shifted to have their maximum at $t = 0$.

the speed c/n, where n is the refractive index of air, whereas the shower front is assumed to traverse the atmosphere at the speed of light. Because of the delay thus induced and depending on the shower geometry, different parts of the shower can be detected at the same time, enhancing the signal in amplitude and compressing it in time.

To account for this propagation effect, the time of propagation from the emission point to the antenna is calculated at each height of the shower development. For two consecutive steps we compute τ_{up} and τ_{down}, as indicated on the sketch in Fig. 5.9 (left) with :

$$\tau_{up} = \frac{1}{c \sin \alpha_{\text{up}}} \int_{h_{\text{antenna}}}^{h_{\text{up}}} n(h')\,\mathrm{d}h' \quad \text{and} \quad \tau_{\text{down}} = \frac{1}{c \sin \alpha_{\text{down}}} \int_{h_{\text{antenna}}}^{h_{\text{down}}} n(h')\,\mathrm{d}h'$$

The time compression is defined as the ratio of the difference $\Delta\tau = |\tau_{\text{up}} - (\tau_{\text{step}} + \tau_{\text{down}})|$ with the step time along the shower $\tau_{\text{step}} = L_{\text{step}}/c$, where L_{step} is 10 m. In the simple case of a vertical shower with a refractive index of $n = 1$, all the emitted radiation along the shower is detected at the same time for an observer underneath the shower. For an air index different

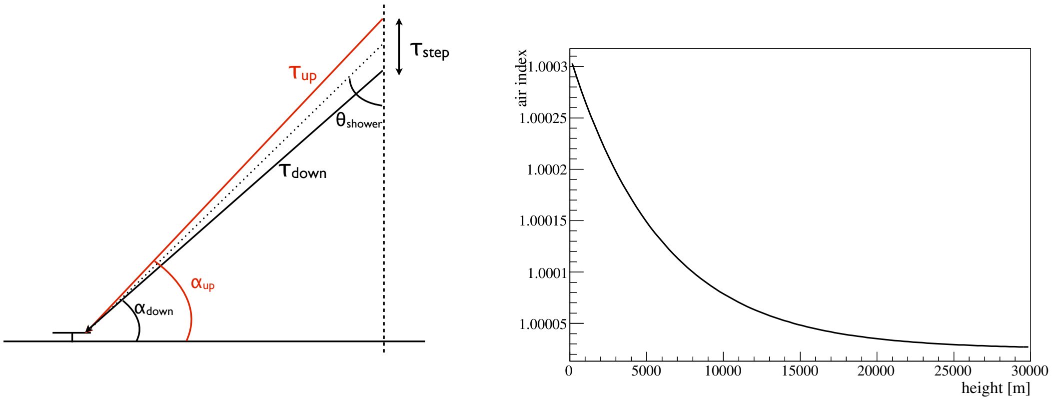

Figure 5.9: Left: Sketch of the propagation of the radiation in air. If $\tau_{up} = \tau_{down} + \tau_{step}$ these two part of the shower are detected at the same time. Right: Refractive index of air as a function of height used in the simulation.

from $n = 1$, the radiation along the shower sum up and give rise to a compression in time of the signal received, at a certain angle. The Cherenkov angle depends on the refractive air index as : $\cos(\theta_{Ch}) = 1/n$.
We take a realistic air index decreasing exponentially with the height. The refractivity defined as N = 10^6(n-1) is parameterized as follow:

$$N = 285 \cdot \exp(-h/5.992 \times 10^3) + 25 \tag{5.3.2}$$

The resulting air index is shown in Fig. 5.9 (right). To illustrate this phenomenon we show in Fig. 5.10 the time compression for different refractive air index as a function of the angle between the emission point and the receiver, called θ_{shower} in Fig. 5.9 (left). For the simulations, the lateral distribution of the particle in the shower front is not taken into account and the emission is simulated as a moving point like source. We mentioned in chapter 2 that under this simplification, the time compression can, in principle, lead to an infinite signal thus non physical. However, because of the finite sampling of the shower in height steps, the signal enhancement cannot be infinite but it is very dependent of the shower sampling when the angle between the emission point and the antenna reaches the Cherenkov angle. The time compression is then overestimated and the resulting trace can be strongly peaked.
As an illustration of this effect, we show in Fig. 5.11 the flux as a function of time for simulated vertical showers at a distance of 300 m (left) and 1000 m (right). The Cherenkov peak can be clearly noticed at 300 m. For sufficiently large distances, the Cherenkov angle is not observed.

Antenna simulation From the simulated profile, we obtain the flux at the detector and the shape of the signal after the propagation in air. To simulate the antenna in the setup we transform the incoming flux into a power through the effective area $A_{\text{eff}}(\theta, \phi)$. In addition, the antenna adds a noise component corresponding to the system temperature T_{sys}.

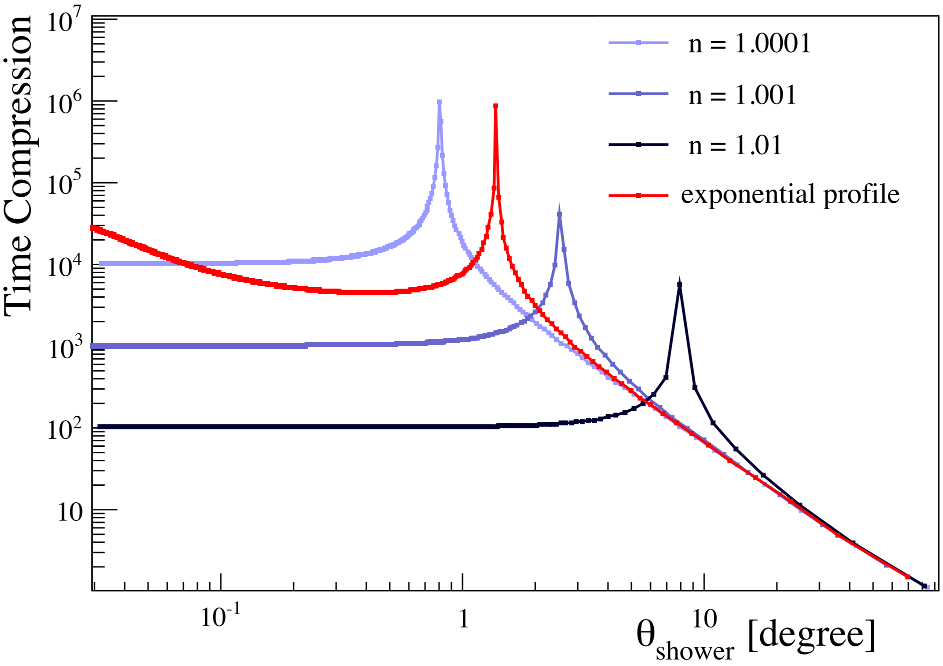

Figure 5.10: Time compression for several constant indices of air and a taking the exponential profile represented in Fog. 5.9 (right).

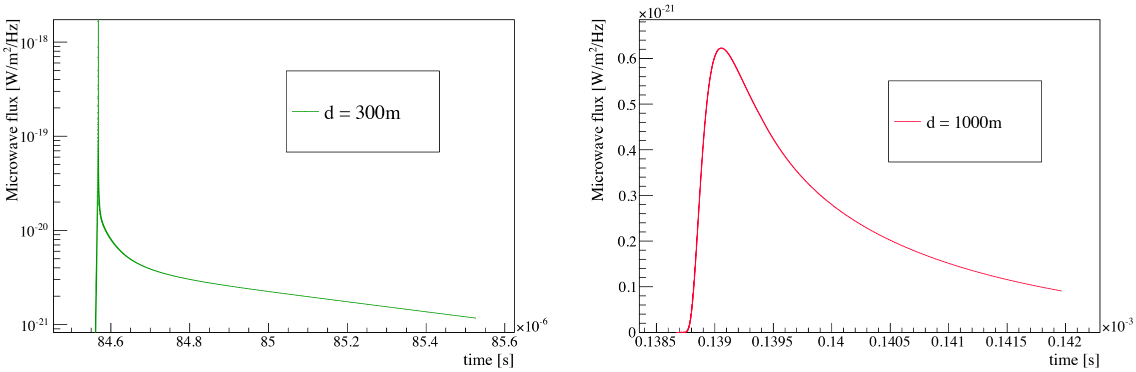

Figure 5.11: Simulated microwave flux for a distance to shower axis of 300 m (left) and 1000 m (right).

The relation between the incoming flux and the power at the output of the antenna before the LNB amplification is simply:

$$P_{\mathrm{S}}(t) = F(t) \cdot A_{\mathrm{eff}}(\theta, \phi) \cdot \Delta\nu \tag{5.3.3}$$

Where we take bandwidth $\Delta\nu = 0.8\,\mathrm{GHz}$. The effective area is taken from the measurements described in chapter 4 at the middle frequency of the range of observation, i.e. at 3.8 GHz. The effective area is assumed to be invariant in azimuth. At the zenith, $A_{eff}(\theta = 0) = 3.8 \times 10^{-3}\,\mathrm{m}^2$ and its dependence in zenith angle is represented in Fig. 5.12 (left).

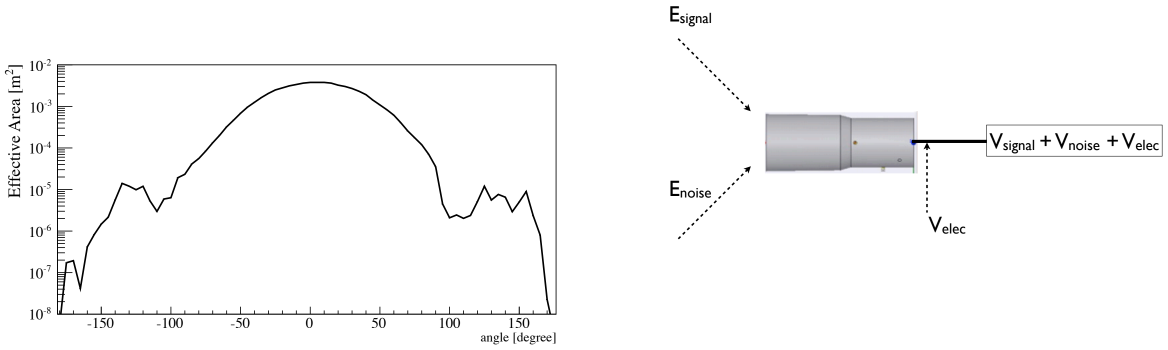

Figure 5.12: Left: Antenna effective area at the middle frequency 3.8 GHz. Right: Scheme of the component of the total signal.

noise temperature The system temperature was described in chapter 4, it represents the noise power received by the antenna and the noise power added by the electronics:

$$P_{\mathrm{N}} = k_{\mathrm{B}} \cdot T_{\mathrm{sys}} \cdot \Delta\nu \qquad (5.3.4)$$

The measurements of sensitivity reported in chapter 4 showed a different system temperature for the two setups installed. For the first one, the system temperature was measured between 40 and 180 K with the Karlsruhe method, and a temperature of around 50 K was deduced from the octocopter measurements. For the antenna of this setup, we will set the system temperature either at 40 K, 80 K or 180 K. For the antennas of the second setup the system temperature was found to be 30 K with the Karlsruhe method and by comparison of spectra, thus it will be set at this value for the simulations.

Radio frequency trace simulation The sum of the noise of the system and signal from EAS is not just the sum of the respective powers. The scheme in Fig. 5.12 (right) represents the different component of the total signal and the place they appear in the setup. The electric fields of the EAS signal (E_{signal}) and the thermal noise (E_{noise}) are added at the level of the antenna and yield a voltage at its output. Then the noise of the electronics amplification, V_{elec}, is also added. These components are at high frequency and have to be summed in voltage (instead of power) to account for their random phase with respect to each other.
To simulate this effect, we adopted the following method: we recorded a reference high frequency trace at the output of one antenna, and we transform $P_S(t)$ and P_N into respectively $V_{\mathrm{signal}}(t)$ and $(V_{\mathrm{noise}}(t) + V_{\mathrm{elec}}(t))$ by scaling this reference trace.
To simulate the noise temperature T_{sys} we scale the trace such that the mean power equates the noise temperature:

$$< P_{\mathrm{N}}(t) >= kT_{\mathrm{sys}}\Delta\nu =< V_{\mathrm{noise}}(t)^2/50 >=< (\beta V_{\mathrm{ref}}(t))^2/50 > \qquad (5.3.5)$$

where β is a constant and the power is calculated on a 50 Ω impedance. We have then a trace of noise identical to the real background noise.
The microwave signal, $P_{\mathrm{S}}(t)$, obtained before is the envelope of the power. To add it to the noise trace we need to transform it in a high frequency trace. We normalize the reference

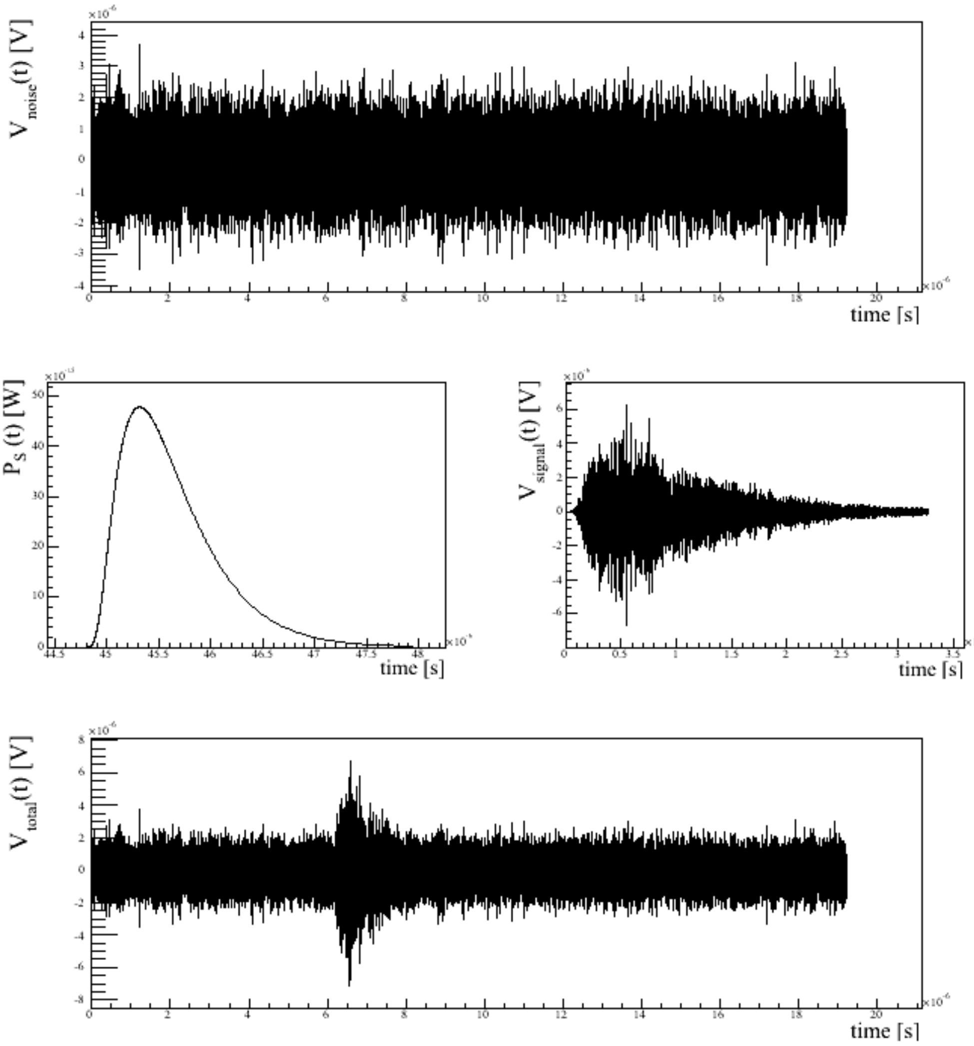

Figure 5.13: Scheme of the component of the total signal.

trace to obtain a waveform $V_{\text{norm}}(t)$ such that $< V_{\text{norm}}(t)^2 >= 1$. Then the microwave signal, $P_{\text{S}}(t)$, is transformed to obtain the high frequency signal trace:

$$V_{\text{signal}}(t) = V_{\text{norm}}(t) \cdot \sqrt{50 \cdot P_{\text{S}}(t)} \tag{5.3.6}$$

The total power is then estimated as:

$$P_{\text{tot}}(t) = \frac{(V_{\text{noise}} + V_{\text{signal}})^2}{50} \tag{5.3.7}$$

We show for instance in Fig. 5.13 such simulation with a low system temperature to make the signal more visible out of the noise. The upper trace is the high frequency noise and the middle part shows the transformation from $P_{\text{S}}(t)$ to $V_{\text{signal}}(t)$. The lower part is the sum of the voltage traces.

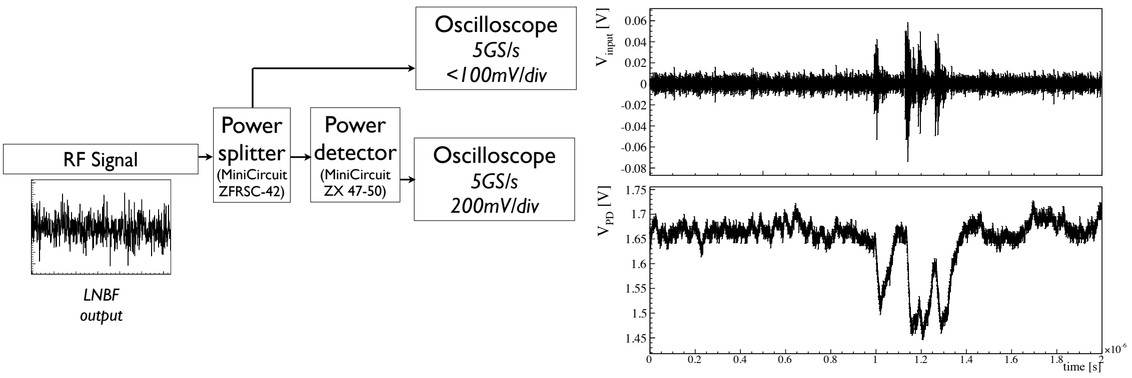

Figure 5.14: Left: Scheme of the setup to record at the same time the high frequency trace and the corresponding trace processed by the power detector. Right: Example of high frequency trace and the corresponding response of the power detector.

Electronics simulation The electronics part is divided in three parts:

- the LNB amplification
- the power detection
- the acquisition shaping and sampling

The high frequency trace is amplified by the LNB gain, but the signal and the noise are amplified with the same factor G_{LNB}. This part is just a multiplication by a factor G_{LNB}.
The power detection is an important part in the setup since the signal is strongly modified at this stage. The high frequency trace is transformed in its power envelope in logarithmic scale. The mean response to a steady signal was already studied in chapter 4 in the electronics calibration section and we present here a method to reproduce the time response of the power detector.
Two power detectors Minicircuit ZX47-50 were tested in laboratory. One of them is equipped with a filtering capacitor like the ones installed in the seven first prototypes, and one has this capacitor removed like the 54 other detectors.
We recorded at the same time the high frequency trace at the output of the antenna and the same signal processed by the power detector in the condition illustrated in Fig. 5.14 (left). To produce microwave pulses with time length of the order of a few tens of nanoseconds, we used an electronic lighter. The spark produced was found to emit such short pulse. We show for instance the response of the power detector to a short pulse in Fig. 5.14 (right). Our goal is to reproduce the power detector curve in the bottom part from the high frequency trace shown in the upper part. We found that the power detector response is well reproduced when performing the three following steps:

1. transform the high frequency trace in dBm units
2. convolve the dBm trace with an exponential function:

$$P_{sim} = (P_{\text{dBm}} * f)(t) = \int_{-\infty}^{+\infty} P_{dBm}(u) \cdot f(t-u) \cdot \theta(u)\, du \tag{5.3.8}$$

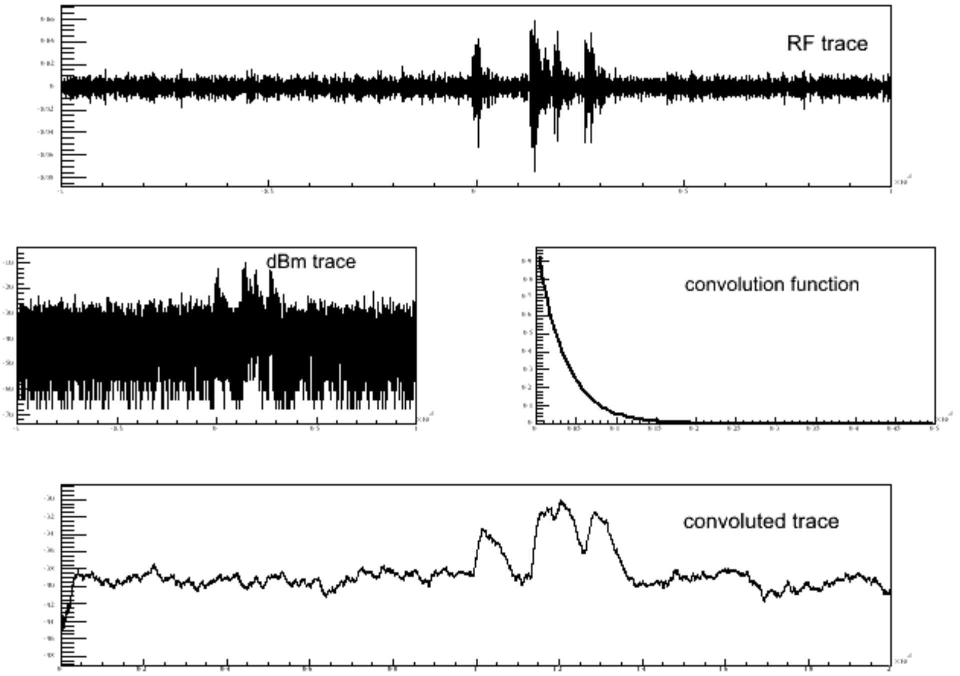

Figure 5.15: Upper panel: original high frequency trace. Middle left panel: trace in dBm unit. Middle right panel: convolution function. Bottom panel: resulting convoluted trace.

where

$$f(t) = exp(-t/\tau)$$

and $\theta(u)$ the Heaviside function to restrain the time to the positive values.

3. transform the convoluted trace in a voltage according the power detector calibration curve.

Step 1 is done by taking for each point: $P_{dBm} = 10 \cdot \log_{10}(P_{watt}/10^{-3})$. An example of high frequency trace and the resulting dBm trace are shown in the upper panel and the middle left panel of Fig. 5.15.

The convolution done in step 2 is done with an exponential function of 500 ns length and sampled with a period of 0.2 ns. The average of the convoluted trace is :

$$< (P_{\mathrm{dBm}} * f)(t) >=< P_{\mathrm{dBm}} > \cdot \int_0^{+\infty} f(t)\, dt \tag{5.3.9}$$

The convolution function is normalized so that the mean of the convolved trace is the mean of the trace in dBm.

Step 3 is performed using the calibration curve of the power detector to transform the dBm trace into a voltage trace. The calibration of these two power detectors gives the following transformation:

$$V_{sim} = k - 0.023 \cdot P_{sim} \tag{5.3.10}$$

In order to match the simulated trace and the real one, we tuned several parameters. We let free the intercept k in Eq. 5.3.10, a time shift and the characteristic time decay of the

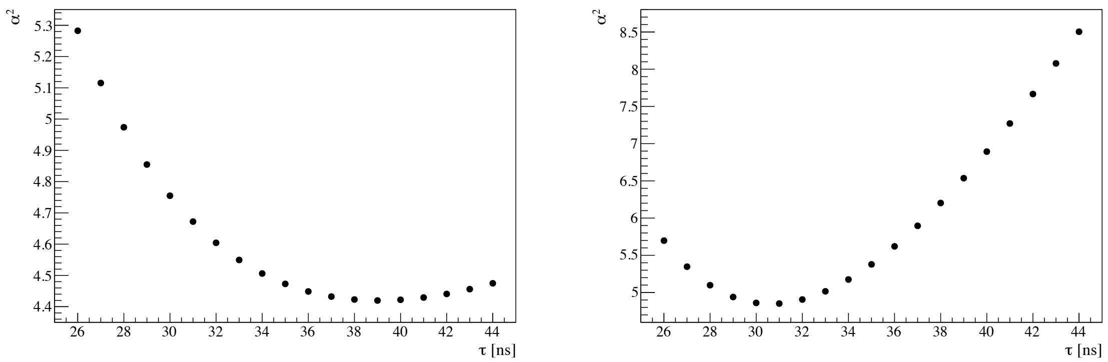

Figure 5.16: Sum of the squared difference between the real and simulated points as a function of the time integration for the noise part (left) and the pulse part (right).

exponential function f. To estimate the best suited parameters, we minimize the square of the difference between simulated and real points ($\alpha^2 = \sum_i (V_{sim}[i] - V_{real}[i])^2$). We performed the minimization in two parts of the trace. The part before the pulse (noise part) and the part around the pulse. For the power detector with capacitor we find that an offset $k = 0.76V$ and time delay of 19 time bins (3.8 ns) minimize α^2 in the two regions (noisy and pulse).

Then for these parameters, the integration time that minimize α^2 is found to be 39 ns for the noise part and 31 ns for the pulse part as shown in Fig. 5.16. We take the average of these two values, $\tau_{capa} = 35\,\text{ns}$, as the power detector time constant. An example of superposition of simulated and real traces is shown in Fig. 5.17 with their difference in bottom panel.
For the power detector without capacitor, the offset is found to be $k = 0.74$, the time delay of 21 time bins, and an integration time $\tau = 5\,\text{ns}$ is found in both parts (noisy and pulse). On the 20 traces that we recorded and simulated, the distribution of their difference (in Fig. 5.19) show a bias on the mean smaller than 2 mV for the power detector with capacitor (3 mV without) and the standard deviation around 10 mV (and 22 mV without), i.e. less than 0.5 dB (or 1 dB without).

The EASIER board is simulated multiplying by a factor 4.1 the voltage at the output of the power detector and adding an offset voltage.
The front end simulation accounts for the low pass filtering at a frequency of 20 MHz and the amplifier gain of -0.5. The simulated trace is then sampled in time (each 25ns) and in amplitude (in 1024 bins).
Note that the value of the offset k in equation Eq. 5.3.10 and the offset added by the EASIER board are not important as long as we consider traces relative to the mean.
To estimate the validity of the electronics simulations, we performed a complete simulation of a shower with an energy of 3×10^{19} eV accounting for different system temperatures. We compare the signal to noise ratio before and after the electronics processing. The traces represented in Fig. 5.20 and are in good agreement in signal shape and in the value of signal to noise ratio. The relative difference between the maximum before the electronics simulation and after is plotted in Fig. 5.21 as function of the original signal to noise ratio. It shows that the maximum after the electronics simulation is larger than the initial one. This is expected since the electronics simulation add fluctuations and we take always the positive ones when searching for the maximum.

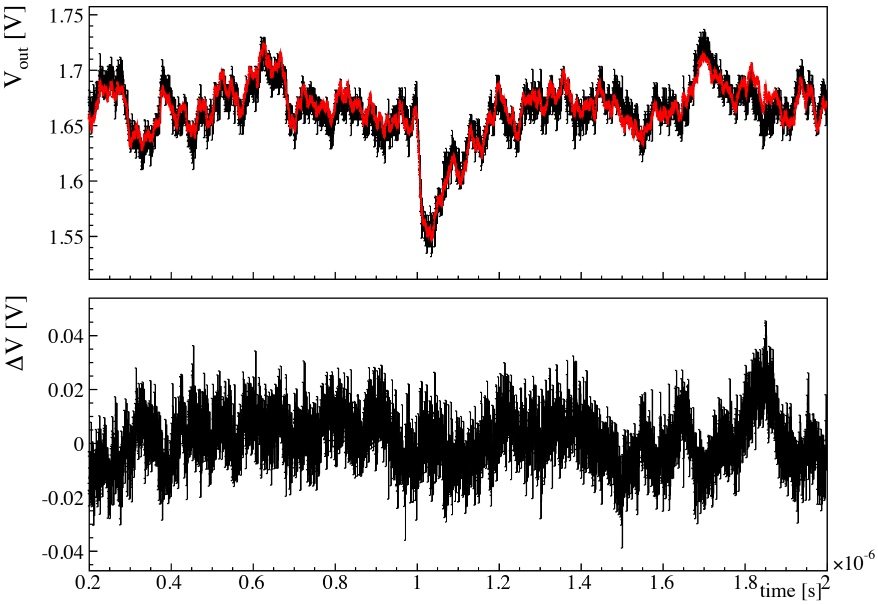

Figure 5.17: Superposition of real power detector trace and simulated one for the configuration with capacitor (see text)

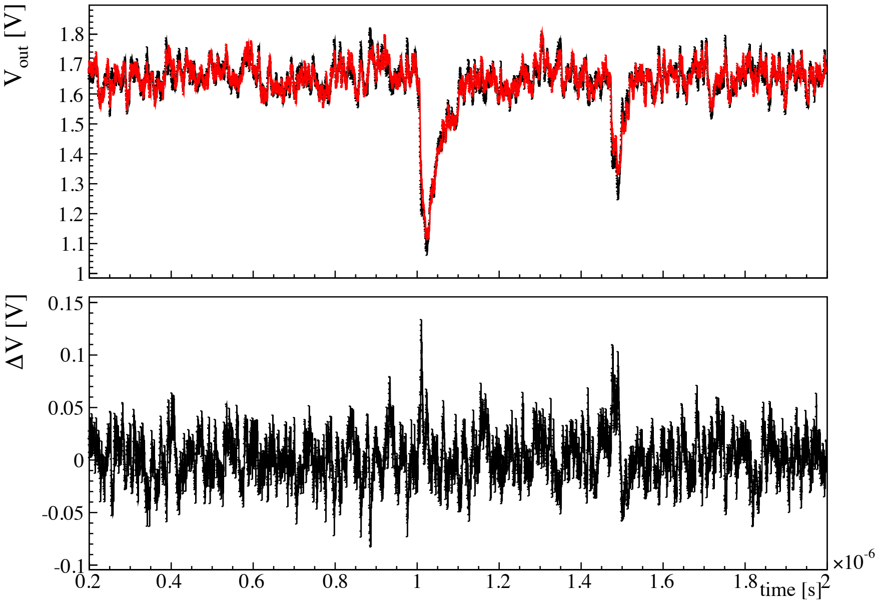

Figure 5.18: Superposition of power detector trace and simulated one for the configuration without capacitor (see text).

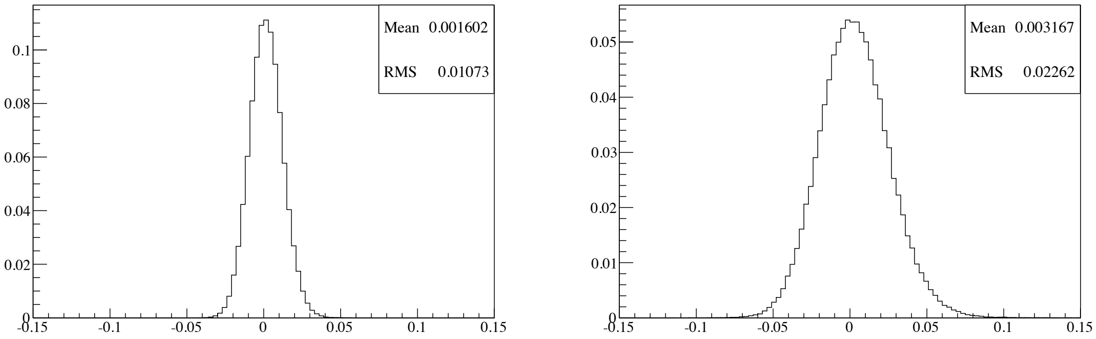

Figure 5.19: Distribution of the difference between simulated point and real ones for the configuration with capacitor (left) and without (right)

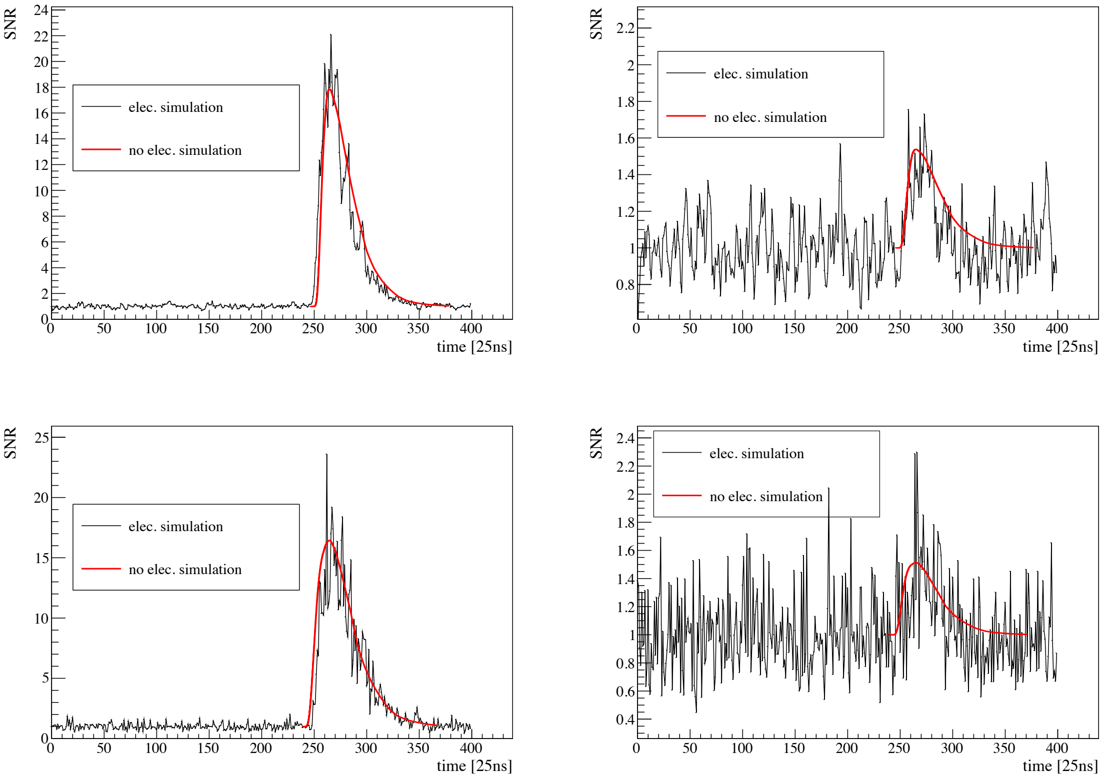

Figure 5.20: Superposition of traces simulated before and after the electronics for the configuration of the first setup (upper panel) and the second (bottom panel)

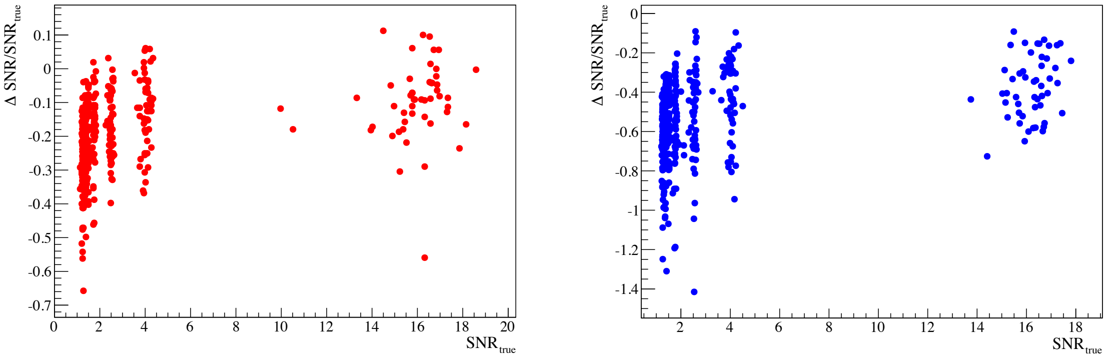

Figure 5.21: Relative difference of the maximum signal to noise ratio before and after the electronics processing for the setup 1 (left) and setup 2(right).

5.4 Comparison data/simulation and interpretation

Simulation of the detected events

We apply the simulation described above to the observed events in order to estimate if these detections can be attributed to an isotropic emission as measured in the SLAC experiment. For each of the three events we simulated 10 showers of proton primary and 10 showers of iron primary. We compare then the maximum of traces and the time width above half of the maximum of simulated pulse and the real ones. In Fig. 5.22, it is illustrated the superposition of the 10 simulated traces with the real event signal to noise ratio for the three radio events detected. Quantitative results are presented in Table 5.2 for proton primary and in Table 5.3 for iron primary accounting for two sets of simulation parameters.

	12036476 (40K)	12036476 (80K)	20830870	21050180
max data	2.8	2.8	3.7	3.2
max sim (F_{ref}, $\alpha = 1$)	2.2 ±0.3	1.6 ± 0.2	1.9±0.1	1.9 ±0.1
max sim (F_{ref}, $\alpha = 2$)	12.4± 4.5	9.2±0.3	6.3 ± 2.1	2.0± 0.2
width data [25ns]	3.1	3.1	1.4	1.7
width sim (F_{ref}, $\alpha = 1$)	11 ± 5	17.2±3	3.4 ± 1.3	4.1 ± 2.5
width sim (F_{ref}, $\alpha = 2$)	4.3 ± 0.4	4.7 ±0.4	1.4 ±0.1	3 ± 1.6

Table 5.2: Maximum, and the width at half height for the events detected in radio and simulation with parameters (F_{ref}, $\alpha = 1$), and (F_{ref}, $\alpha = 2$) where $F_{ref} = 4 \times 10^{-16}$ W/m^2/Hz. For proton primary simulated showers.

	12036476 (40K)	12036476 (80K)	20830870	21050180
max data	2.8	2.8	3.7	3.2
max sim (F_{ref}, $\alpha = 1$)	1.8 ±0.3	1.6 ± 0.2	2.1± 0.3	1.9 ±0.2
max sim (F_{ref}, $\alpha = 2$)	6.5± 1.3	5±1	4.4±1	2.0 ± 0.3
width data [25ns]	3.1	3.1	1.4	1.7
width sim (F_{ref}, $\alpha = 1$)	14± 4	17.1 ± 2	3.3±2.8	2.9 ± 1.2
width sim (F_{ref}, $\alpha = 2$)	4.3±0.7	3.8±0.3	1.4 ±0.1	4.9±4

Table 5.3: Maximum, and the width at half height for the events detected in radio and simulation with parameters (F_{ref}, $\alpha = 1$), and (F_{ref}, $\alpha = 2$) where $F_{ref} = 4 \times 10^{-16}$ W/m^2/Hz. For iron primary simulated showers.

This first comparison between the simulated events and their corresponding real trace show a compatibility in terms of amplitude for the event 12036476 but discrepancy in terms of time length. The two other events show a maximum for (F_{ref}, $\alpha = 1$) lower than the one observed. For the full coherence case, i.e. $\alpha = 2$, simulations yield a signal to noise ratio too large for the events 12036476 and 20830870, but still unsufficient to explain the event 21050180.

Limits on an isotropic emission

The detection of events only at short distances from the shower axis favors a beamed emission as dominant emission process. The comparisons with simulations in the previous section

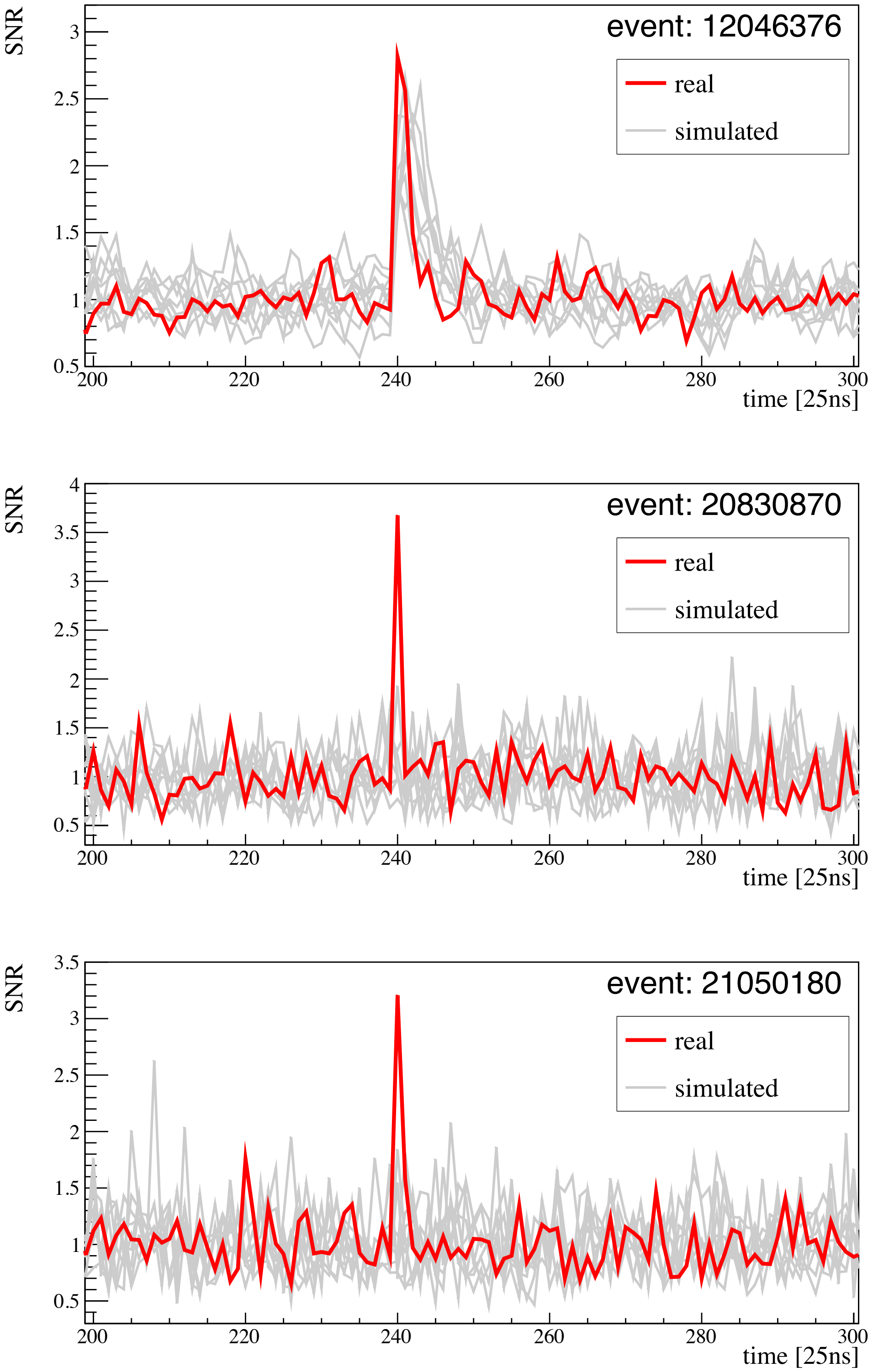

Figure 5.22: Superposition of observed and simulated trace for the three events detected.

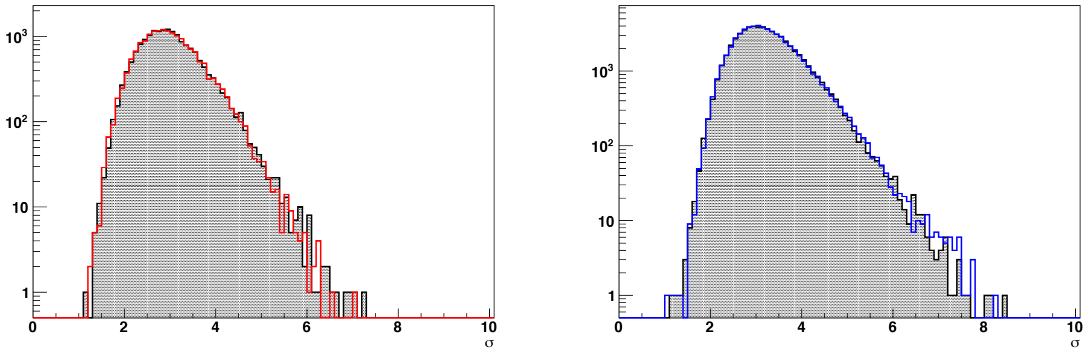

Figure 5.23: Distributions of the maximum in the window [0-150] in black and in color are represented the distributions of the maximum in the interval [230-380].

indicated that these detected events are difficult to explain with an isotropic emission and the parameters of emission tested.

We present here a more general study to estimate limits on the MBR flux. After defining the conditions to accept a radio event, we compare the number of real events detected with simulated events accounting for several emission parameters F_{ref} and α.

As we want to set limits on an isotropic emission, we select only stations with distance to shower axis larger than 300 m. This way, we reduce the possible contribution of a beamed emission in the data.

Then the noise is estimated thanks to the first part of the real traces where no radio signal is expected. The distributions of noise in trace fluctuation unit are shown for the two setups in Fig. 5.23. We find a maximum of $\sigma_{noise1} = 7.2$ for the first setup and $\sigma_{noise2} = 8.4$ for the second.

Then maxima of the radio trace are searched in a time window of 150 time bins around the particle signal start ([230- 380] where the time bin of the signal start is around bin 242). To accept a radio event, we require the maximum of the trace in the window [230-380] to be larger than the maximum noise σ_{noise}. The colored distributions in Fig. 5.23 represent the maxima in the signal window and show that no event is found in the real data with the criteria defined above.

We are interested in pointing limits above 10^{19} eV, therefore we select events above this value. Moreover, the simulated events with a short Cherenkov peak like the one showed in Fig. 5.11 are removed by selecting only the simulations with a half maximum height larger than 100 ns. The system temperature is taken to 180 K for the first setup to be consevative (it is the highest temperature measured in chapter 4). For the second setup, a temperature of 30 K was found with several methods and is thus chosen for the simulation. We scanned the range of parameters $F_{ref} \in [2.5 \times 10^{-17} - 16 \times 10^{-16}]$W/m^2/Hz and $\alpha \in [1 - 2]$ with steps of $\Delta\alpha = 0.1$. In total, the data set is simulated 20 times for proton and iron primary.

The number of events accepted in the simulation has to be compared with the data, i.e. no candidate in a null background. The upper limits are defined as the Feldman Cousins definition [106]. An upper limit with a 95% confidence level is set if more than 3.2 events are accepted in the simulation for a given set of parameters. The limits on the reference flux F_{ref} as a function of the coherence index α are given in Fig. 5.24 for proton and iron primary.

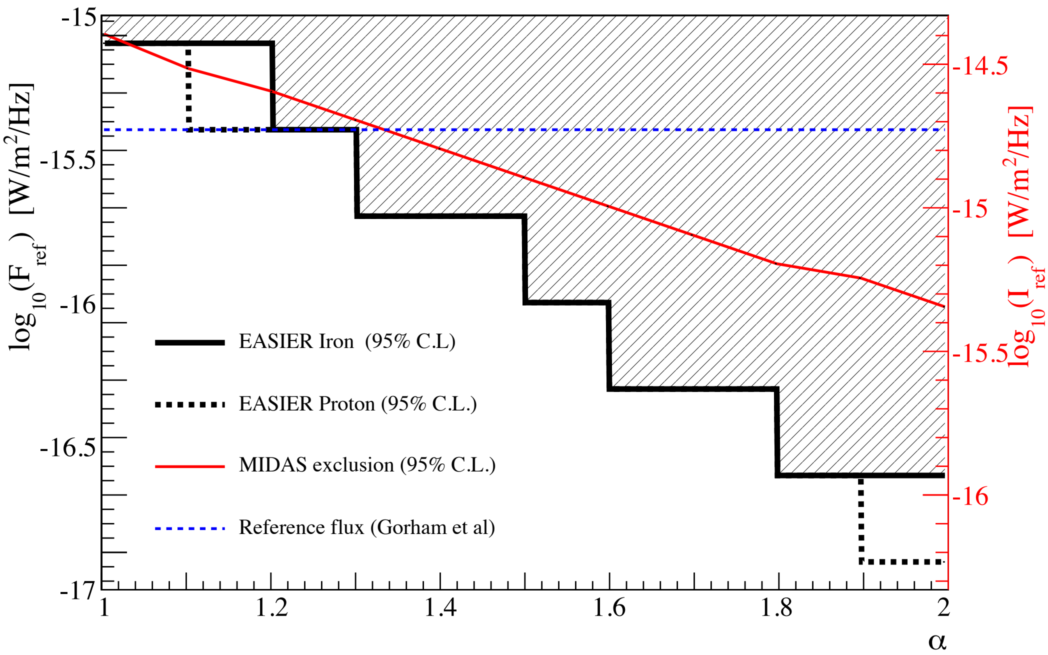

Figure 5.24: Limit set on the parameters F_{ref} and α. The blue dashed line represents the flux measured in [73]. The red line represents the upper limits set with MIDAS detector [105]. The right axis shows $I_{ref} = F_{ref} \times 4.62$.

The reference flux observed in the beam experiment is also depicted with the dashed blue line. This reference flux is excluded for $\alpha \geq 1.2$. The limits found with MIDAS detector are represented with the red line. The limits found with EASIER are comparable for α close to 1 and exclude a wider range of flux at $\alpha \geq 1.3$.

Discussion on the limits on MBR

The limits presented above constrain the parameters the MBR emission F_{ref} and α. The simulations presented include the microwave signal simulation, its propagation and the main detector effects. The results quoted here are found under the assumptions exposed in section 5.3. The number of events may be overestimated mainly because of the following reasons:

- the time compression may be overestimated because the lateral extension of the shower front is not accounted for.
- there remains some uncertainties on the system temperature measurements, they may be larger than the one assumed in the simulations.

The limits found are in agreement with the results of other experiments aiming at the MBR detection from EAS (like AMBER, MIDAS, CROME) or in laboratory (AMY and MAYBE). AMBER is a telescope like experiment instrumented with feed horns antenna in C-band

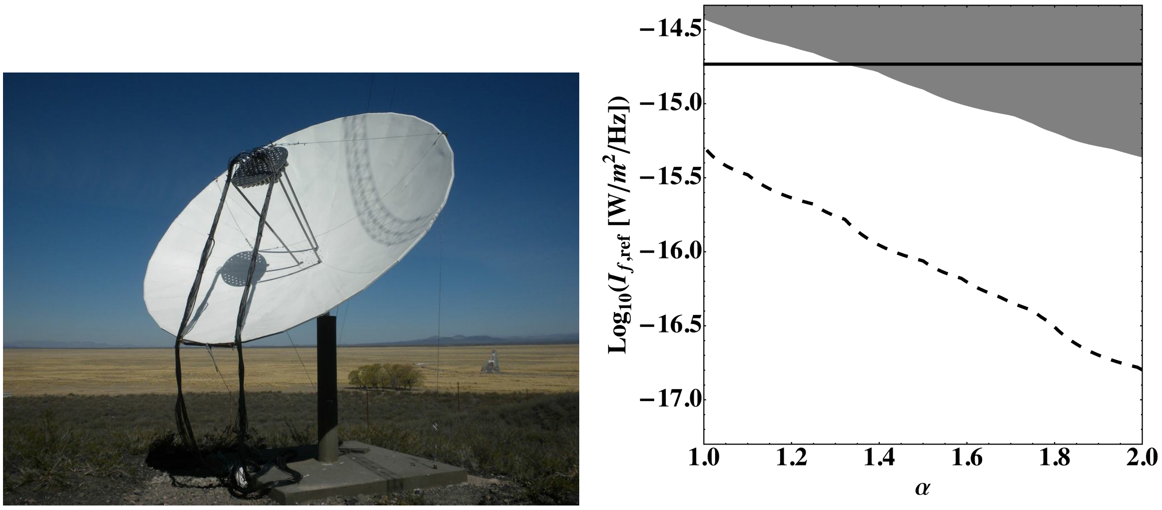

Figure 5.25: Left: MIDAS detector installed at the Pierre Auger site. Right: Limits on the MBR flux estimated with MIDAS (shaded area) as a function of the parameters $I_{ref} = F_{ref} \cdot \Gamma$ and α. The horizontal line represent the reference flux measured in [73].

and Ku-band. It was first commissioned at the University of Hawaii and then installed at the Pierre Auger Observatory. The data showed no radio event detection during the first commissioning neither in the second up to now.
MIDAS is also a telescope like detector, as shown in Fig. 5.25(left). It was first installed at the University of Chicago, and took data for several months in this conditions. The absence of detection in this first run allowed the MIDAS collaboration to set limits on the MBR flux from air shower [105]. The shaded area in Fig. 5.25 shows the exclusion at 95% confidence level of the set of parameters I_{ref} (where $I_{ref} = F_{ref} \cdot \Gamma$ in Eq. 5.1.1) and α .
MIDAS detector is now operating at the Pierre Auger Observatory, in a much quiet environment than in Chicago. The expected limits after one year of operation at the Pierre Auger site are given by the dashed line in Fig. 5.25 (right).
The CROME detector, is composed of a parabolic dish with feed horns at the focus. Unlike MIDAS or AMBER, the dish is oriented towards the zenith thus this setup is sensitive to radiation beamed in forward direction from vertical showers. It is installed at the KASCADE site and operates in coincidence with its air shower surface detector. The CROME collaboration has reported the detection of 30 radio events in the C-band in coincidence with shower of reconstructed energy above 3×10^{16} eV [107]. Fig. 5.26 (left) shows two detected events. An interesting feature is the distribution of the shower cores shown in Fig. 5.26 (right) that led to radio events. The events are represented with square and the simulated electric field with CoREAS code for a vertical iron shower of 10^{17} eV. This simulation code accounts for both the geomagnetic and the charge excess effect. The shower cores position forms a ring structure with a radius of around 100 m as expected in the simulation.
The detected pulses shape and the characteristics of the detected showers indicate a coherent emission beamed around the shower axis.
Two beam tests were conducted in order to confirm the results of the SLAC experiment and to characterize further this emission.
AMY experiment uses an electron beam accelerated by the same type of linac (Linear particle

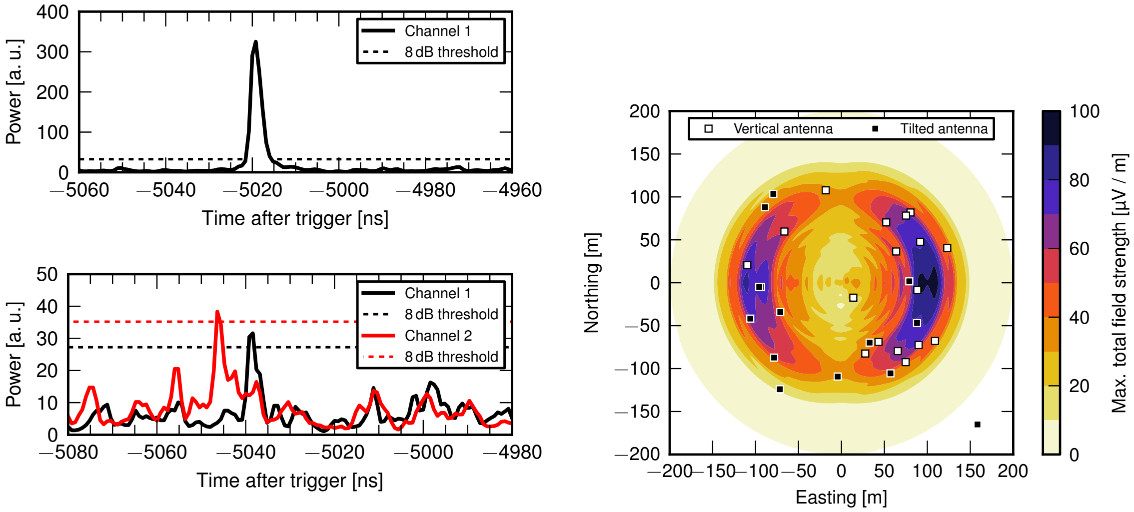

Figure 5.26: Left: Time trace of events detected by CROME experiment. Right: Position of the antenna at which microwave signals were detected with respect to the shower core. The shaded areas represent the amplitude of the simulated electric field with CoREAS code (see text).

accelerator) than in SLAC experiment. The AMY instrument itself is a large anechoic chamber (4 m × 2 m × 2 m) equipped with antennas on its sides. When the electron beam interacts with targets placed before the chamber, a shower of particles is produced and the microwave signal is recorded by the antennas.

The microwave signal recorded was found to be dominated by the Cherenkov emission of particles in particular at the LINAC frequencies. The data analysis of AMY data is underway, and a thorough filtering of the LINAC frequencies will allow the AMY collaboration to set limits on an isotropic emission.

MAYBE experiment utilize an electron beam produced by a Van Der Graaff generator. The energy of the electrons produced is lower than the Cherenkov threshold, thus the measurements are free from strong signal from the beam itself. The results of the runs already conducted are still being analyzed but the first measurements published confirmed the observation of a continuum emission in a large bandwidth from 1 to 15 GHz [79]. However, the dependence of the flux observed with the beam energy is found linear (cf Fig. 5.27) contrary to the results found in [73]. In addition, the absolute reference flux is found significantly lower.

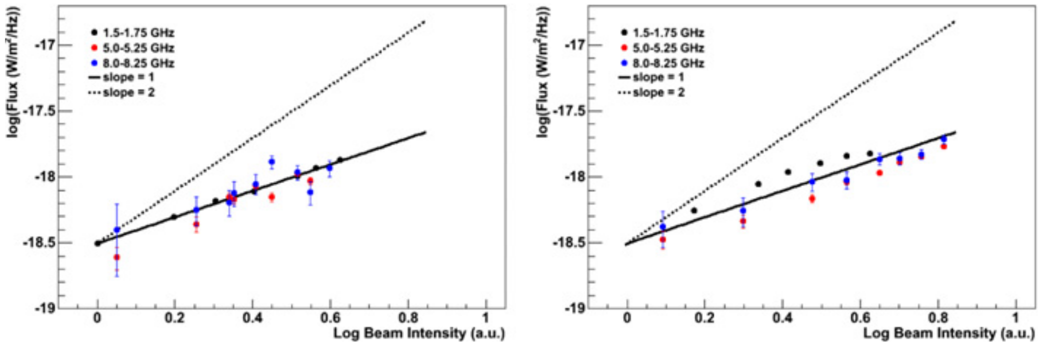

Figure 5.27: Energy dependence of the microwave signal observed in MAYBE experiment for two polarization orientations.

Summary and Conclusions

The aim of my thesis has been to determine the feasibility of the measurement of UHECR mass composition using radio detection technique in coincidence with the Pierre Auger Observatory surface detector. Radio detection setups, in the VHF band (30-80 MHz) and in the C-band (3.4-4.2 GHz), have been developed. In each band, one test hexagon has been installed on site in 2011. It was then extended to 61 units in the C-band and replaced by a new setup in the VHF band in 2012.
I was deeply involved in the R&D phase, in the deployment and installation of the antennas and in data analysis.

My main contributions to the detector developments are:

- the choice of the suitable electronics, in terms of bandwidth and dynamic range.
- the validation and the end-to-end calibration of the detector to accommodate the dynamic range of 40 dB in the VHF band and 20 dB in the C-band.
- the deployment of the detectors in the Argentinian pampa comprising the on site hardware tests and calibration.

In the next step, my work was focused on the determination of the detector sensitivity in the C-band by measuring the system temperature and determining the minimum detectable flux.

- the noise temperature of electronics was measured by two different techniques. The use of a dedicated noise meter yielded a temperature of 201± 30 K. Using a second method, a comparison of spectra in different noise conditions, we obtained a temperature of 23 ± 2 K in agreement with the measurements performed by other groups. The high temperature found with the noise meter compared to other techniques may come from an important loss in the connections of the setup used.
- a measurement of sensitivity was conducted on site using an external calibrated source. The minimum detectable flux has been estimated to be $F = 4 \times 10^{-19}\,\mathrm{W/m^2/Hz} \pm 11\% \pm 50\%$.

The first prototype in the VHF band has been working in stable conditions for four months. I performed a search for radio events in the data set.

- 36 candidates were found with a signal to noise ratio above 10 and in coincidence with the particle signal.
- the amplitude of the electric field detected decreases exponentially with the distance to the shower axis with a characteristic distance of around 200 m for vertical showers.
- the events exhibit a preferred arrival direction, 23 events were reconstructed with a south direction compared to 9 with a north direction. This effect is a combination of the expected geomagnetic contribution and the antenna pattern.

In the C-band, the data analyzed are the combination of the first hexagon data and the additional 54 detectors data. A search for events yielded a total of three event candidates largely above the noise, including the first cosmic ray event ever detected in the C-band. Their amplitudes are all above $10\,\sigma$, two of them have an energy above 10^{19} eV and one below 3×10^{18} eV. The maximum distance of detection is less than 300 m.

In order to interpret the observed events, I developed the entire chain for the simulations, starting from the expected shower profile up to the final data acquisition processing.

- A parameterized air shower particle profile is converted to the microwave power according to the beam measurements reported in [73]. Then the propagation of the signal from its production point to the detector accounts for a realistic refraction index of air and then the signal is fed into the electronics simulations. The lateral distribution of the electromagnetic part of the shower has not yet been included in the simulation chain.
- The power detector response is simulated with a time of integration of 35 ns and 5 ns respectively for the first and the second setup. It is found to describe the power detector response with an uncertainty below 1 dB.
- Using the value of the reference flux observed in beam experiment ($F_{\mathrm{ref}} = 4 \times 10^{-16}\,\mathrm{W/m^2/Hz}$), and a coherence factor $\alpha = 1$ or $\alpha = 2$, the three events observed cannot be reproduced by an isotropic emission.
- Using the events with an energy larger than 10^{19} eV and the detector further than 300 m, an upper limit on the expected flux has been calculated. The present limit, $F_{\mathrm{ref}} \leq 8 \times 10^{-16}\,\mathrm{W/m^2/Hz}$ with $\alpha \geq 1$ is currently the best limit on the MBR emission.

In the C-band, larger statistics of detected events will allow to characterize better the emission. An excess of detection in East West polarized antennas would sign a geomagnetic contribution. The improvement of the sensitivity can be achieved by lowering the noise temperature and by shifting the band of observation at lower frequencies to increase the effective area. A noise temperature reduced by 50% and a central frequency reduced by a factor three would improve the signal to noise ratio by more than a factor 10.

The detection of air showers with EASIER in both bands showed the possibility and the assets of a coincident operation. However, the characteristics of the observed radio pulses and the short distance of detection, point to an emission mechanism beamed around the shower axis, instead of isotropic. In the perspective of the original purpose of EASIER, the observation of the shower longitudinal profile at energy larger than 10^{19} eV, the only observation of these type of emission entail two main drawbacks. First, the short distances of detection prevent from instrumenting a large area, mandatory to be able to detect with sufficient statistic the low flux at ultra high energy. Second, the short length of the pulse makes it hard to extract the information on the longitudinal profile.

The work done during this thesis provides radio data on cosmic rays at the highest energies in two frequency bands. It will serve as a basis to improve further both the detector, to lower the sensitivity, and the analysis, to perform a deeper event search and reach better limits.

Bibliography

[1] V. Hess, *Observations of the penetrating radiation on seven balloon flights*, Physik. Zeitschr. **13** (1912) 1084–1091.

[2] W. Kolhorster Deutsch. Phys. Gesell. Vehr **16** (1914) 719.

[3] J. Clay Amsterdam Proc. **33** (1930) 711.

[4] L. Alvarez and A. Compton Phys. Rev. **43** (1933) 835.

[5] T. Johnson Phys. Rev. **43** (1933) 834.

[6] B. Rossi Z. Phys. **82** (1933) 151.

[7] P. Auger et al., *Extensive Cosmic-ray Showers*, Rev. Mod. Phys. **11** (1939) 288–291.

[8] A. Letessier-Selvon and T. Stanev, *Ultrahigh Energy Cosmic Rays*, Rev.Mod.Phys. **83** (2011) 907–942, `arXiv:1103.0031 [astro-ph.HE]`.

[9] E. Fermi, *On the Origin of the Cosmic Radiation*, Phys. Rev. **75** (1949) 1169–1174.

[10] W. Axford et al. Proc of 15th Int. Cosmic Ray Conf. Plovdiv **11** (1977) 132.

[11] P. Lagage and C. Cesarsky, *The maximum energy of cosmic rays accelerated by supernova shocks*, Astron.Astrophys. **125** (1983) 249–257.

[12] E. Berezhko, V. Elshin, and L. Ksenofontov, *Cosmic ray acceleration in supernova remnants*, J.Exp.Theor.Phys. **82** (1996) 1–21.

[13] S. Lucek and A. Bell Mon. Not. R. Astronom. Soc **314** (2000) 65–74.

[14] D. Allard, M. Ave, N. Busca, M. Malkan, A. Olinto, et al., *Cosmogenic Neutrinos from the propagation of Ultrahigh Energy Nuclei*, JCAP **0609** (2006) 005, `arXiv:astro-ph/0605327 [astro-ph]`.

[15] W. R. Penzias, A.A. Astrophys. J **142** (1965) 419.

[16] K. Greisen Phys. Rev. Lett. **16** (1966) 748.

[17] G. Zapsetin and V. Kuzmin Sov. Phys. JETP Lett. **4** (1966) 78.

[18] F. Stecker and M. Salamon, *Photodisintegration of ultrahigh-energy cosmic rays: A New determination*, Astrophys.J. **512** (1999) 521–526, `arXiv:astro-ph/9808110 [astro-ph]`.

[19] J. Matthews, *A Heitler model of extensive air showers*, Astropart.Phys. **22** (2005) 387–397.

[20] W. Heitler, *"Quantum Theory of Radiation"*. Oxford University Press, 1944.

[21] M. Risse, *Properties of extensive air showers*, Acta Phys.Polon. **B35** (2004) 1787–1798, `arXiv:astro-ph/0402300 [astro-ph]`.

[22] K.-H. Kampert and M. Unger, *Measurements of the Cosmic Ray Composition with Air Shower Experiments*, Astropart.Phys. **35** (2012) 660–678, `arXiv:1201.0018 [astro-ph.HE]`.

[23] J. Linsley, L. Scarsi, and B. Rossi, *Extremely energetic cosmic-ray event*, Phys.Rev.Lett. **6** (1961) 485–487.

[24] N. Chiba, K. Hashimoto, N. Hayashida, K. Honda, M. Honda, et al., *Akeno giant air shower array (AGASA) covering 100-km**2 area*, Nucl.Instrum.Meth. **A311** (1992) 338–349.

[25] T. Abu-Zayyad, R. Aida, M. Allen, R. Anderson, R. Azuma, et al., *The surface detector array of the Telescope Array experiment*, Nucl.Instrum.Meth. **A689** (2012) 87–97, `arXiv:1201.4964 [astro-ph.IM]`.

[26] F. Arqueros et al. Astronomy. Astrophys. **359** (2000) 682.

[27] N. Budnev, D. Chernov, O. Gress, N. Kalmykov, V. Kozhin, et al., *The tunka experiment: towards a 1-km^2 EAS Cerenkov light array in the Tunka valley*, `arXiv:astro-ph/0511229 [astro-ph]`.

[28] AIRFLY Collaboration, M. Ave et al., *Precise measurement of the absolute fluorescence yield of the 337 nm band in atmospheric gases*, Astropart.Phys. **42** (2013) 90–102, `arXiv:1210.6734 [astro-ph.IM]`.

[29] K. Suga in *Proc. 5th Interamerican seminar on CRs, LaPaz, Bolivia*, vol. 2. 1962.

[30] T. Hara, S. Kawaguchi, S. Mikamo, M. Nagano, K. Suga, et al., *Observation of air showers of energies above 10^{18} eV*, Conf.Proc. **C690825** (1969) 361–367.

[31] Pierre Auger Collaboration, J. Abraham et al., *The Fluorescence Detector of the Pierre Auger Observatory*, Nucl.Instrum.Meth. **A620** (2010) 227–251, `arXiv:0907.4282 [astro-ph.IM]`.

[32] I. Mariş, *Measurement of the ultra high energy cosmic ray flux using data of the Pierre Auger Observatory*, . PhD thesis, Universität Karlsruhe, 2008.

[33] Pierre Auger Collaboration, J. Abraham et al., *Trigger and aperture of the surface detector array of the Pierre Auger Observatory*, Nucl.Instrum.Meth. **A613** (2010) 29–39, `arXiv:1111.6764 [astro-ph.IM]`.

[34] M. Fukushima, *Measurement of Ultra-High Energy Cosmic Rays: An Experimental Summary and Prospects*, EPJ Web Conf. **53** (2013) 02002, `arXiv:1302.5893 [astro-ph.HE]`.

[35] Pierre Auger Collaboration, P. Abreu et al., *The Pierre Auger Observatory II: Studies of Cosmic Ray Composition and Hadronic Interaction models*, `arXiv:1107.4804 [astro-ph.HE]`.

[36] E. Barcikowski et al., *Mass Composition Working Group Report at UHECR-2012*, EPJ Web Conf. **53** (2013) 01006, `arXiv:1306.4430 [astro-ph.HE]`.

[37] Pierre Auger Collaboration, P. Abreu et al., *Measurement of the proton-air cross-section at $\sqrt{s} = 57$ TeV with the Pierre Auger Observatory*, Phys.Rev.Lett. **109** (2012) 062002, `arXiv:1208.1520 [hep-ex]`.

[38] R. Glauber, *Cross-sections in deuterium at high-energies*, Phys.Rev. **100** (1955) 242–248.

[39] Pierre Auger Collaboration, J. Abraham et al., *Astrophysical Sources of Cosmic Rays and Related Measurements with the Pierre Auger Observatory*, `arXiv:0906.2347 [astro-ph.HE]`.

[40] Pierre Auger Collaboration, P. Abreu et al., *Ultrahigh Energy Neutrinos at the Pierre Auger Observatory*, Adv.High Energy Phys. **2013** (2013) 708680, `arXiv:1304.1630 [astro-ph.HE]`.

[41] IceCube Collaboration, R. Abbasi et al., *A Search for UHE Tau Neutrinos with IceCube*, Phys.Rev. **D86** (2012) 022005, `arXiv:1202.4564 [astro-ph.HE]`.

[42] ANTARES Collaboration, M. Ageron, *Performance of the First ANTARES Detector Line*, `arXiv:0812.2095 [astro-ph]`.

[43] IceCube Collaboration, R. Abbasi et al., *Constraints on the extremely-high energy cosmic neutrino flux with the IceCube 2008-2009 data*, Phys. Rev. D **83** (May, 2011) 092003.

[44] Anita Collaboration, P. W. Gorham et al., *Observational constraints on ultra-high energy cosmic neutrino flux from the second flight of the ANITA experiment*, Phys. Rev. D **82** (2010) 022004.

[45] I. Kravchenko, A. Hase, D. Besson, S. Graham, Z. Kessler, et al., *Event Reconstruction and Data Acquisition for the RICE Experiment at the South Pole*, `arXiv:0705.4491 [astro-ph]`.

[46] Pierre Auger Collaboration, P. Abreu et al., *Update on the correlation of the highest energy cosmic rays with nearby extragalactic matter*, Astropart.Phys. **34** (2010) 314–326, `arXiv:1009.1855 [astro-ph.HE]`.

[47] Pierre Auger Collaboration, I. Sidelnik, *Measurement of the first harmonic modulation in the right ascension distribution of cosmic rays detected at the Pierre Auger Observatory: towards the detection of dipolar anisotropies over a wide energy range*, Proc. 33rd ICRC, Rio, Brazil (2013) .

[48] A. Achterberg, Y. A. Gallant, C. A. Norman, and D. B. Melrose, *Intergalactic propagation of uhe cosmic rays*, `arXiv:astro-ph/9907060 [astro-ph]`.

[49] M.-P. Veron-Cetty and P. Veron, *A catalogue of quasars and active nuclei: 12th edition*, Astron.Astrophys. **455** (2006) 773–777.

[50] Pierre Auger Collaboration, J. Abraham et al., *Correlation of the highest-energy cosmic rays with the positions of nearby active galactic nuclei*, Astropart.Phys. **29** (2008) 188–204, `arXiv:0712.2843 [astro-ph]`.

[51] Pierre Auger Collaboration, P. Abreu et al., *Constraints on the origin of cosmic rays above* 10^{18} *eV from large scale anisotropy searches in data of the Pierre Auger Observatory*, Astrophys.J. **762** (2012) L13, `arXiv:1212.3083 [astro-ph.HE]`.

[52] Pierre Auger Collaboration, P. Abreu et al., *Search for First Harmonic Modulation in the Right Ascension Distribution of Cosmic Rays Detected at the Pierre Auger Observatory*, Astropart.Phys. **34** (2011) 627–639, `arXiv:1103.2721 [astro-ph.HE]`.

[53] W. Baade and F. Zwicky Phys. Rev. **46** (1934) 76.

[54] V. L. Ginzburg and S. I. Syrovatskii, *The Origin of Cosmic Rays.* Macmillan, London, New York, 1964.

[55] J. Linsley Proc. 8th ICRC, Jaipur, India (1963) .

[56] V. Berezinsky, A. Gazizov, and S. Grigorieva, *Dip in UHECR spectrum as signature of proton interaction with CMB*, Phys.Lett. **B612** (2005) 147–153, `arXiv:astro-ph/0502550 [astro-ph]`.

[57] R. Aloisio, V. Berezinsky, and A. Gazizov, *Ultra High Energy Cosmic Rays: The disappointing model*, Astropart.Phys. **34** (2011) 620–626, `arXiv:0907.5194 [astro-ph.HE]`.

[58] D. Garcia-Pinto, *Measurements of the longitudinal development of air showers with the Pierre Auger Observatory*, in *Proc. 32nd ICRC, Beijing, China*, vol. 2, p. 87. 2011.

[59] A. S. Chou, K. Arisaka, M. D. A. Pernas, D. Barnhill, P. Billoir, A. Tripathi, and T. Yamamoto, *An Universal Description of the Particle Flux Distributions in Extended Air Showers*, in *Proc. 29th ICRC, Pune, India*, vol. 7, p. 319. 2005.

[60] F. Schmidt, M. Ave, L. Cazon, and A. S. Chou, *Applying Extensive Air Shower Universality to Ground Detector Data*, in *Proc. 30th ICRC, Merida, Mexico*, vol. 4, pp. 601–604. 2007. `arXiv:0706.1990 [astro-ph]`.

[61] J. V. Jelley, J. H. Fruin, N. A. Porter, F. G. Weekes, and R. A. Porter Nature **205** (1965) 327.

[62] G. Askaryan, *Excess Negative Charge of an Electron-Photon Shower and its Coherent Radio Emission.*, JETP 14 (441-443) (1962) .

[63] F. Kahn and I. Lerche Proc. Roy. Soc. A-289 (206) (1966) .

[64] H. R. Allan Prog. in Element. Part. and Cos. Ray Phys. **10** (1971) 171.

[65] R. P. Feynman, R. B. Leighton, and M. Sands, *"The Feynman Lectures in Physics Vol1"*. Addison Wesley, 1963.

[66] D. Ardouin, A. Belletoile, D. Charrier, R. Dallier, L. Denis, et al., *Radio-detection signature of high-energy cosmic rays by the CODALEMA experiment*, Nucl.Instrum.Meth. **A555** (2005) 148–163.

[67] LOPES Collaboration, H. Falcke et al., *Detection and imaging of atmospheric radio flashes from cosmic ray air showers*, Nature **435** (2005) 313–316, `arXiv:astro-ph/0505383 [astro-ph]`.

[68] W. Apel, J. Arteaga, L. Bahren, K. Bekk, M. Bertaina, et al., *LOPES 3D - vectorial measurements of radio emission from cosmic ray induced air showers*, `arXiv:1303.7080 [astro-ph.HE]`.

[69] LOPES Collaboration, A. Haungs et al., *Air Shower Measurements with the LOPES Radio Antenna Array*, Nucl.Instrum.Meth. **A604** (2009) S1–S8, `arXiv:0811.1919 [astro-ph]`.

[70] B. Revenu, *Overview of MHz air shower radio experiments and results*, `arXiv:1302.2733 [astro-ph.HE]`.

[71] T. Huege, *Theory and simulations of air shower radio emission*, `arXiv:1301.2135 [astro-ph.HE]`.

[72] K. Werner, K. de Vries, and O. Scholten Astropart. Physics **37** (2012) 5–16.

[73] P. Gorham, N. Lehtinen, G. Varner, J. Beatty, A. Connolly, et al., *Observations of Microwave Continuum Emission from Air Shower Plasmas*, Phys.Rev. **D78** (2008) 032007, `arXiv:0705.2589 [astro-ph]`.

[74] M. Monasor, I. Alekotte, J. Alvarez-Muniz, A. Berlin, X. Bertou, et al., *The MIDAS experiment: A prototype for the microwave emission of Ultra-High Energy Cosmic Rays*, Nucl.Phys.Proc.Suppl. **215** (2011) 63–65, `arXiv:1010.5224 [astro-ph.HE]`.

[75] J. Alvarez-Muniz, E. A. Soares, A. Berlin, M. Bogdan, M. Bohacova, et al., *The MIDAS telescope for microwave detection of ultra-high energy cosmic rays*, `arXiv:1208.2734 [astro-ph.IM]`.

[76] Pierre Auger Collaboration, P. Abreu et al., *The Pierre Auger Observatory V: Enhancements*, J.Phys.Conf.Ser. **375** (2012) 052006, `arXiv:1107.4807 [astro-ph.IM]`.

[77] CROME Collaboration, R. Smida et al., *First results of the CROME experiment*, `arXiv:1108.0588 [hep-ex]`.

[78] M. Monasor et al. in *Proc. 32nd ICRC, Beijing, China*, vol. 3, p. 192. 2011.

[79] C. Williams et al. in *UHECR 2012 - International Symposium on Future Directions in UHECR Physics, CERN Geneva*, vol. 53. 2012.

[80] K.-H. Kampert, *The Pierre Auger Observatory -Status and prospects*, Nucl.Phys.Proc.Suppl. **151** (2006) 393–400, `arXiv:astro-ph/0501074 [astro-ph]`.

[81] S. J. Orfanidis, *"Electromagnetic Waves and Antennas"*. http://www.ece.rutgers.edu/ orfanidi/ewa/, 2002.

[82] E. Nash, *Logarithmic amplifiers explained*, . http://www.analog.com/library/analogDialogue/archives/3303/ask28/logamps.pdf.

[83] D. Ardouin, A. Belletoile, D. Charrier, R. Dallier, T. Gousset, et al., *An active dipole for cosmic ray radiodetection with CODALEMA*, Nucl.Instrum.Meth. **A572** (2007) 481–482.

[84] D. Charrier, *Design of a low noise, wide band, active dipole antenna for a cosmic ray radiodetection experiment*, Antennas and Propagation Society International Symposium **41** (2007) 4485–4488.

[85] http://www.analog.com/en/rfif-components/detectors/ad8310/products/product.html.

[86] S. Gambetta, *Study of the Attenuation of Extensive Air Showers in the Atmosphere and of the Feasibility of Measuring their Radio Signal with EASIER*, .

[87] E. Thiery, *Influence des cuves du detecteur de surface de l Observatoire Pierre Auger sur les antennes MHz d EASIER*, .

[88] http://www.ngdc.noaa.gov/IAGA/vmod/igrf.html.

[89] http://www.ansoft.com/products/hf/hfss/.

[90] CODALEMA Collaboration, D. Charrier, *Antenna development for astroparticle and radioastronomy experiments*, Nucl.Instrum.Meth. **A662** (2012) S142–S145.

[91] http://www.analog.com/en/rfif-components/detectors/ad8318/products/product.html.

[92] http://217.34.103.131/pdfs/ZX47-50+.pdf.

[93] B. Lubsandorzhiev, R. Vasiliev, Y. Vyatchin, and B. A. J. Shaibonov, *Photoelectron backscattering in vacuum phototubes*, Nuclear Instruments and Methods in Physics Research A **567** (2006) 12–16.

[94] http://217.34.103.131/pdfs/ZFRSC-42+.pdf.

[95] T. L. Wilson and H. S. Rohlfs, K, *"Tools of Radio Astronomy 5th edition"*. Springer, 2009.

[96] http://cp.literature.agilent.com/litweb/pdf/5952-8255E.pdf.

[97] T. Y. Otoshi, *"Noise Temperature Theory and Applications for Deep Space Communications Antenna Systems"*. Artech House, 2008.

[98] R. Engel, M. Riegel, R. Smida, and F. Werner. GAP-2013-028.

[99] F. Werner. GAP-2011-048.

[100] http://217.34.103.131/pdfs/ZX95-3760+.pdf.

[101] F. Werner, private communication.

[102] T. Huege, M. Ludwig, and C. James, *Simulating radio emission from air showers with CoREAS*, `arXiv:1301.2132 [astro-ph.HE]`.

[103] F. Salamida, L. Perrone, and S. Petrera. GAP-2005-087.

[104] D. Heck, J. Knapp, J. Capdevielle, G. Schatz, and T. Thouw, *CORSIKA: A Monte Carlo code to simulate extensive air showers*, FZKA-6019 (1998) .

[105] J. Alvarez-Muñiz et al., *Search for microwave emission from ultrahigh energy cosmic rays*, Phys. Rev. D **86** (Sep, 2012) 051104.

[106] G. J. Feldman and R. D. Cousins, *A Unified approach to the classical statistical analysis of small signals*, Phys.Rev. **D57** (1998) 3873–3889, `arXiv:physics/9711021 [physics.data-an]`.

[107] R. Smida, F. Werner, R. Engel, J. Arteaga-Velazquez, K. Bekk, et al., *Observation of Polarised Microwave Emission from Cosmic Ray Air Showers*, `arXiv:1306.6738 [astro-ph.IM]`.

Appendix A: Measuring apparatus

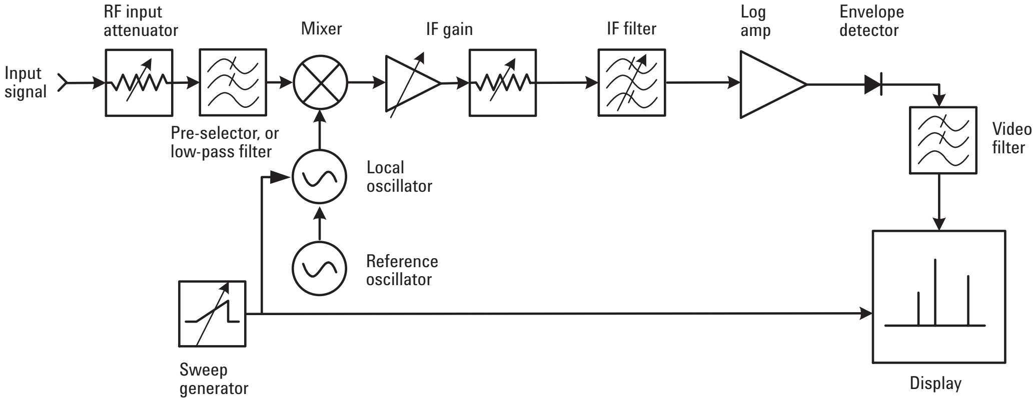

Figure 1: Block diagram of a spectrum analyzer operations

Spectrum analyzer The spectrum analyzer measures the power as a function of the frequency. The block diagram of a super heterodyne spectrum analyzer operation is represented in Fig. 1. To determine the power at a given frequency f_{sig} it mixes the input signal with a local oscillator signal with an adjustable frequency f_{LO}. The result of the mixing yields a signal with all the harmonic frequencies but the two most important are at the sum and the difference of f_{sig} and f_{LO}. The power is measured at the difference, the Intermediate Frequency (IF), by a n envelope detector in a frequency band defined by the IF filter in Fig. 1. A video filter is applied after these operation to smooth the frequency trace.
The main option to choose before doing a spectrum measurement are:

- the bandwidth.
- the resolution, driven by the IF filter or Resolution Bandwidth (RBW).
- the display of the result.

The choice of the bandwidth is clear, and depends on the measurement.

The resolution is the ability on the spectrum analyzer to separate two input sine signal into distinct response. A choice of a small RBW is right to distinguish close peaks.

The result can be displayed in different way depending on the information that one wants to stress. The bandwidth displayed is divided in frequency windows. In each of these window, the measurement displayed is defined by the mode of detection:

- the peak mode: displays the highest power in the window
- the sample mode: displays the instantaneous level at the center of the window.
- the RMS mode: displays the average power in the window.

We used the portable spectrum analyzer Anritsu MS2723. Its main characteristics are a large bandwidth from 9 kHz to 13 GHz and a noise level lower than 140 dBm/Hz over the bandwidth.

(a) Calibration

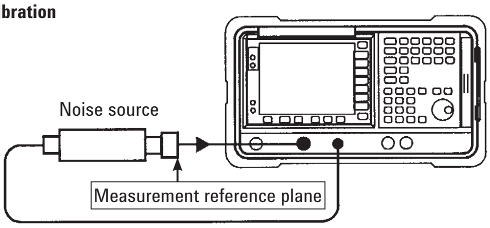

(b) Measurement

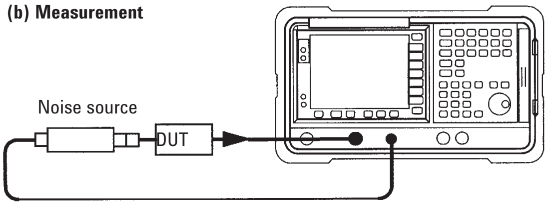

Figure 2: Measurement phase

Noise meter Measurement of noise temperature are widely performed using the Y-factor method. The measurement of the response of a device to two different noise power input allow to deduce the noise induced by the device itself.
A noise meter is an apparatus made for this purpose, it is essentially a spectrum analyzer but in addition it controls a calibrated noise source. The measurement is made when the source is on (large noise power) and compared with the measurement when the source is off.
The setup for this measure is illustrated in Fig. 2. A first phase is needed to calibrate the system, it allow to account for the loss inserted by cables for instance. Then the Device Under Test (DUT) is inserted and the measurement performed.
The noise meter we used is an Agilent PXAN9030A and the noise source Agilent N4002A.

Appendix B: Installation data

We report here useful data for the GHz calibration of first and the second setup. We give the GPS time of installation, the regulated voltage, the threshold voltage and the slope of the regulator for the 54 detectors. The data of two installed detectors are missing.

station	LS id	GPS time of installation
Concorde	332	986997615
Bastille	333	987001215
Leandro	341	986925615
Nene	342	986932815
Paloma	343	986842815
Magali	344	986925615
JoseMaria	419	986914815

Table 4: table of time of activation.

station	LsId	date of installation	electronic box number	V_{cst}	v_{shift}	V_{th}	slope
Aleph	306	1018969215	19	24.1	0.6	25.56	0.26
Noemi	308	1018807215	49	23.98	0.6	25.7	0.25
Adriana	315	1018810815	53	23.96	0.6	25.67	0.24
Gringa	328	1018803615	28	24.06	0.6	25.86	0.24
Gilda	334	1019311215	57	24.08	0.6	25.88	0.24
Selknam	403	1018900815	16	24.05	0.6	25.79	0.24
Camanzo	408	1018983615	31	24.18	0.6	25.96	0.24
Luis	422	1018882815	47	24.04	0.6	25.48	0.26
Tom	425	1018886415	44	23.96	0.6	25.76	0.24
Orteguina	431	1018897215	32	24.36	0.62	25.81	0.25
Gato	434	1018897215	56	24.01	0.6	25.02	0.51
Chaquira	354	1018879215	07	24.05	0.6	25.76	0.25
Scarface	125	1018818015	55	23.9	0.6	25.31	0.25
Benjamin	199	1018976415	19	24.1	0.6	25.56	0.26
Yannick	300	1018796415	41	23.97	0.6	25.69	0.25
Adone	307	1018818015	40	23.9	0.6	25.59	0.24
Osvaldo	310	1018810815	36	23.65	0.6	25.04	0.25
Leonel	311	1018818015	52	24.15	0.6	25.59	0.25
Rula	313	1018807215	38	23.95	0.6	25.36	0.25
Eva	330	1018792815	46	24.41	0.6	25.77	0.26
Santy	339	1019235615	04	23.92	0.6	25.6	0.25
Aime	356	1018818015	50	23.84	0.6	25.23	0.25
John David	375	1018890015	25	23.71	0.6	25.14	0.24
Chuletas	383	1018720815					
Popey	385	1018720815	59	24	0.6	25.8	0.24
Chihuido	394	1018908015	17	24	0.6	25.66	0.24

station	LsId	date of installation	electronic box number	V_{cst}	$v_{shif\ t}$	V_{th}	slope
Barriga	405	1018908015	29	24.07	0.6	25.8	0.25
Hualung	410	1018900815	43	24.1	0.6	25.53	0.24
Juan	432	1018882815	48	23.8	0.6	25.2	0.25
Vieira	433	1018900815	23	23.8	0.6	25.1	0.25
La Caida	121	1018976415	01	24	0.59	25.3	0.25
Montmartre	196	1018972815	15	24.1	0.6	25.8	0.27
Pigalle	197	1018972815	02	24	0.6	25.7	0.25
Andrea	201	1018976415	60	24	0.6	25.6	0.26
Yahima	296	1018814415	09	23.8	0.6	25.11	0.25
Irina	305	1019314815	51	23.9	0.6	25.23	0.25
Leo	312	1018814415	34	23.8	0.6	25.2	0.25
Coca	319	1018814415	33	24.4	0.6	25.9	0.25
Anay	325	1018803615	12	24	0.6	25.7	0.24
Jorge	329	1018803615	06	24.4	0.6	25.9	0.24
Patzu	337	1018792815	21	23.9	0.6	25.3	0.25
Nono	340	1018792815	03	23.8	0.6	25.2	0.25
Daiana	376	1018900815	37	23.9	0.6	25.3	0.25
Chape	384	1018720815	27				
Lauty	386	1018792815	26	23.8	0.6	25.2	0.25
Agustin	387	1018796415	54	24.1	0.6	25.8	0.24
Rachel	390	1018893615	08	23.8	0.6	25.2	0.25
Rehovot	396	1018886415	13	23.7	0.6	25.3	0.24
Quintana	412	1018969215	20	23.7	0.6	25.1	0.26
Domo	427	1018879215	42	23.8	0.6	25.2	0.24
Raul	429	1018875615	10	23.7	0.6	25.1	0.27
Obradoiro	438	1018969215	14	23.9	0.6	25.4	0.25
Alejandro	441	1018789215	35	23.6	0.6	25	0.24
Emiliana Jr	1802	1018893615	39	23.8	0.6	25.1	0.25

Table 5: Table of date of installation and voltage data of the second setup in microwave band.

Romain GAÏOR

EASIER: Extensive Air Shower Identification using Electron Radiometer

La composition des rayons cosmiques d 'ultra haute énergie est une information cruciale pour déterminer leur source. Les techniques actuelles la mesure avec un cycle utile limité a 10%.

Le projet EASIER (Extensive Air Shower Identification using Electron Radiometer) est un système de détection radio intégré au détecteur de surface de l'Observatoire Pierre Auger. L'objectif est la mesure de la composition à hautes énergies (E > 10EeV) par l'observation du profile électromagnétique avec un cycle utile de 100%.

Le principe d'EASIER a été appliqué dans la bande VHF (30-80 MHz) dans laquelle un signal radio cohérent a déjà été observé et dans la bande C (3.4-4.2 GHz) dans laquelle une émission isotrope est attendue.

Une partie importante de cette thèse décrit les développements et la caractérisation des dispositifs expérimentaux dans ces deux bandes.

L'installation de 7 détecteurs dans la bande VHF a permis la détection de 36 événements. Leurs caractéristiques indiquent une émission concentrée autour de l'axe de la gerbe avec une distance caractéristique de l'ordre de 200m pour des gerbes verticales.

Dans la bande C un prototype de 7 unités a permis la première détection d'un signal radio dans cette bande. L'extension à 61 unités porte le nombre de candidats à 4, tous détectés à des distances à l'axe inferieures à 300m. La comparaison avec des simulations a permis d'établir des limites sur les caractéristiques d'une émission isotrope.

Les distances de détection sont contraintes par les mécanismes d'émission observés et restent trop faibles pour remplir les objectifs d'EASIER. Des développements sont en cours pour abaisser la sensibilité des détecteurs dans les deux bandes.

Ultra high energy cosmic ray composition is crucial to determine their source. Current techniques measure it with a limited duty cycle of 10%.

The EASIER project (Extensive Air Shower Identification using Electron Radiometer) is a radio detection system integrated with the surface detector of the Pierre Auger Observatory. Its goal is the measurement of the mass composition at high energy via the observation of the electromagnetic profile of air showers with a 100% duty cycle.

The principle of EASIER was applied in the VHF band (30-80 MHz) in which a coherent signal was already observed and in the C band (3.4-4.2 GHz) in which an isotropic emission is expected.

A large part of this thesis describes the developments and calibration of the experimental setups in both bands.

The installation of 7 detectors in the VHF band led to the detection of 36 events. Their characteristics indicate an emission beamed around the shower axis with a characteristic distance of the order of 200m for vertical showers.

In the C band, 7 detector units were installed and led to the first detection of a radio signal in this band. The extension to 61 units raised the number of candidates to 4, all detected at distances to the shower axis lower than 300m. The comparison with simulations allowed us to set limits on the parameters of an isotropic emission.

The distances of detection are limited by the emission mechanism and are up to now too small to fulfil EASIER goals. Improvements are underway to lower the sensitivity in both bands.